Optimal Shape Design of Turbine Endwalls with CFD

Dipl.-Ing. M. Bugra Akin
Institute of Thermal Turbomachinery and Machine Dynamics
Graz University of Technology

This dissertation is submitted for the degree of
Doctor of Technical Sciences

Assessors
Prof. Dr.techn. Wolfgang Sanz
Prof. Dr.techn. Reinhard Willinger

Graz University of Technology December 2015

Deutsche Fassung:
Beschluss der Curricula-Kommission für Bachelor-, Master- und Diplomstudien vom 10.11.2008
Genehmigung des Senates am 1.12.2008

EIDESSTATTLICHE ERKLÄRUNG

Ich erkläre an Eides statt, dass ich die vorliegende Arbeit selbstständig verfasst, andere als die angegebenen Quellen/Hilfsmittel nicht benutzt, und die den benutzten Quellen wörtlich und inhaltlich entnommenen Stellen als solche kenntlich gemacht habe.

Graz, am ……………………………   …………………………………………………..
(Unterschrift)

Englische Fassung:

STATUTORY DECLARATION

I declare that I have authored this thesis independently, that I have not used other than the declared sources / resources, and that I have explicitly marked all material which has been quoted either literally or by content from the used sources.

……………………………   …………………………………………………..
date   (signature)

Acknowledgements

There are many people I would like to acknowledge who have contributed to this thesis. Some have contributed directly to the work and some have contributed to my personal development as an engineer or as a person. I am going to address these people in chronological order as I have met them.

First I would like to thank Prof. Dr.-Ing. André Bardow. When I met him, he was not a professor yet. He was working on his PhD thesis and I was working for him as a student at the RWTH Aachen. His guidance and knowledge that he shared with me at that time helped me effectively tackle many of the problems that I encountered during my thesis. And the same goes for Dr. Bernd Wickerath. It was when I worked for him at the Institute of Jet Propulsion and Turbomachinery (RWTH Aachen) that I first encountered CFD and one of the biggest challenges associated with it, which is turbulence modeling. But that luckily hasn't been a major part of my thesis. (Instead I would find myself struggling with optimization using CFD. Also quite a challenge.)

Most importantly I would like to thank Professor Dr.-Ing. Reinhard Niehuis, who was head of the Institute of Jet Propulsion and Turbomachinery while I was working there as a student. Without him I would never have been able to start working on this thesis. It is his trust in me that convinced Prof. Dr.techn. Wolfgang Sanz to give me the opportunity to work on this thesis, whom I would also like to sincerely thank for his guidance, all the constructive discussions, his support when I needed it, and his trust which allowed me to conduct my research in the direction I believed it should go. Also I would like to thank Prof. Dr.techn. Reinhard Willinger for accepting to assess the thesis and his thorough revision of it.

I would like to thank Prof. Dr.-Ing. Franz Heitmeir for creating an incredibly positive atmosphere at the Institute of Thermal Turbomachinery and Machine Dynamics as head of the institute that made it a pleasure to work there.

And I would also like to thank Prof. Dr.techn. Jakob Woisetschläger for the many witty discussions regarding science and philosophy, Dr.techn. Andreas Marn and Dr.techn. Emil Göttlich for their support and of course all of my colleagues for all the bitter sweet discussions and the laughs we have shared.

Also I would like to thank the Austrian Federal Ministry for Transport, Innovation and

Technology who funded the project SEIKON3D within the Austrian Aeronautics Program TAKE OFF as well as the German Aerospace Center (DLR) for the permission to make use of the CFD Solver TRACE and their support. The research leading to experimental results used in this study has been partially funded by the European Union within the EU-project DREAM (contract No. ACP7-GA-2008-211861) as well as from the Austrian Federal Ministry for Finance.

Now I would like to mess up the chronological order and thank my mother, who is responsible for a huge part of who I am (the better part). And I would like to thank my ex-girlfriend for being the reason of so many beautiful moments (and no, the thesis had nothing to do with our breakup).

And finally, thank you fate! You are the best teacher, as long as one has faith!

I hope that this work truly contributes to our endeavor as engineers to create solutions fast and effectively!

Abstract

Reducing fuel consumption for energy production is one of the main concerns of the transportation and energy industries due to limited fuel reserves, emissions of pollutants and cost reduction. Both these industries rely heavily on gas turbines for the conversion of energy. The turbine within the gas turbine is responsible for the conversion of the inner energy of the medium into rotational mechanical energy. Current technical achievements have led to the development of the turning mid turbine frame for the turbine that enables shortening it and consequently reducing its weight.

The aerodynamics in the turbine blade and vane rows, specifically the turning mid turbine frame, are dominated by secondary effects causing losses that can be significantly reduced by an appropriate design. There are a number of proposals for design modifications one of which is the non-axisymmetric endwall contour, which is a promising concept to reduce the cross-flow pressure gradient of the boundary layer flow, and thus reduce secondary flows. All such modifications commonly require extensive studies to achieve a design that results in an improvement. An efficient method to effectively achieve design improvements is to parametrize design modifications and systematically test the resulting alternatives.

Computational optimization strategies offer an efficient method to test a huge number of these alternatives and effectively find the optimum of an objective function. A review of current optimization methods is given with the focus on deterministic methods using gradient information. A method for calculating gradient information is provided by the adjoint method. The advantage of the adjoint method is that the computational effort for calculating the gradient of the objective function for the parameters is roughly the same for any number of parameters. The gradient information can be used with a number of optimization methods such as the steepest descent method or quasi-Newton methods.

The adjoint method is demonstrated on the non-axisymmetric endwall contour optimization of a turning mid turbine frame using a quasi-Newton method. The results as well as the challenges associated with the adjoint method are discussed.

The challenges posed by the calculations of the derivatives using an adjoint method led to the development of a simple and effective alternative optimization method that is referred to as a quasi gradient-based optimization method. Its application is demonstrated on the optimization of the same turning mid turbine frame. The results are discussed and compared with those achieved by the former optimization method. The introduced method is desirable due to its simplicity and stability. But it has its own challenges that must be overcome to successfully optimize complex problems with more than one objective function or constraint. Strategies to overcome these challenges are also discussed.

Kurzfassung

Reduzierung des Verbrauchs fossiler Brennstoffe ist eine der Hauptsorgen der Transport- und Energieindustrie aufgrund der begrenzten Reserven, Schadstoffemissionen und Kostenaspekte. Beide Branchen verlassen sich stark auf Gasturbinen für die Umwandlung von Energie. Die Turbine innerhalb der Gasturbine ist für die Umwandlung der inneren Energie des Mediums in mechanische Rotationsenergie verantwortlich. Derzeitige technische Errungenschaften haben zu der Entwicklung des umlenkenden Turbinenübergangskanals für die Strahltriebwerke geführt, der die Verkürzung und damit eine Gewichtsverringerung ermöglicht.

Die Aerodynamik in den Schaufelreihen, insbesondere im umlenkenden Turbinenübergangskanal, wird durch Sekundärströmungseffekte dominiert. Diese verursachen Verluste, die durch eine entsprechende Auslegung wesentlich verringert werden können. Es gibt eine Reihe von Vorschlägen für Designänderungen zur Verlustverringerung. Die nicht-rotationssymmetrische Seitenwandkonturierung ist ein vielversprechendes Konzept, um den Druckgradient der Querströmung in der Grenzschichtströmung, und damit Sekundärströmungen, zu reduzieren. Üblicherweise erfordert es umfangreiche Studien, um ein Design zu erzielen, das zu einer wesentlichen Verbesserung führt. Eine effiziente Methode, um Designverbesserungen zu erzielen, ist Änderungen zu parametrisieren und die daraus resultierenden Alternativen systematisch zu testen.

Rechnergestützte Optimierungsstrategien bieten effiziente Methoden an, um eine große Anzahl dieser Alternativen zu prüfen und erfolgreich das Optimum einer Zielfunktion zu finden. Ein Überblick der aktuellen Optimierungsverfahren wird mit dem Fokus auf deterministische Methoden, die Gradienten der Zielfunktion einsetzen, präsentiert. Ein Verfahren zur Berechnung der Gradienteninformation ist das adjungierte Verfahren. Der Vorteil des Verfahrens ist, dass der Rechenaufwand für die Berechnung des Gradienten der Zielfunktion für jede Anzahl von Parametern in etwa gleich bleibt. Die Gradientinformation kann mit einer Reihe von Optimierungsverfahren, wie beispielsweise der Methode des steilsten Abstiegs oder dem Quasi-Newton-Verfahren verwendet werden.

Das adjungierte Verfahren wird an der nicht-rotationsymmetrische Seitenwandkonturoptimierung eines umlenkenden Turbinenübergangskanals unter Verwendung eines Quasi-Newton-

Verfahrens demonstriert. Die Ergebnisse sowie die Herausforderungen, die mit dem adjungierten Verfahren in Zusammenhang stehen, werden diskutiert.

Die Herausforderungen bei der Berechnung der Gradienten unter Verwendung des adjungierten Verfahrens führten zur Entwicklung eines einfachen und wirksamen Optimierungsverfahrens, das als ein quasi-gradientenbasiertes Optimierungsverfahren bezeichnet wird. Seine Anwendung wird an der Optimierung des gleichen umlenkenden Turbinenübergangskanals demonstriert. Die Ergebnisse werden diskutiert und mit den Ergebnissen der zuvor gehenden Optimierung verglichen. Das vorgestellte Verfahren ist aufgrund seiner Einfachheit und Stabilität vorteilhaft. Aber es stellt auch Herausforderungen, die überwunden werden müssen, um komplexe Probleme mit mehr als einer Zielfunktion oder mit zusätzlichen Einschränkungen erfolgreich zu optimieren. Strategien zur Überwindung dieser Herausforderungen werden ebenfalls diskutiert.

Contents

List of Figures

List of Tables

Nomenclature

Abbreviations

CC	Combustion Chamber
CFD	Computational Fluid Dynamics
DNS	direct numerical computation
FDM	Finite Differences Method
GHG	greenhouse gas
GMRES	Generalized Minimal Residual Method
HPC	High-Pressure Compressor
HPT	High-Pressure Turbine
ITD	Intermediate Turbine Duct
ITTM	Institute of Thermal Turbomachinery and Machine Dynamics
LPC	Low-Pressure Compressor
LPT	Low-Pressure Turbine
RANS	Reynolds-averaged Navier-Stokes
SA	Spalart-Allmaras
SST	Shear Stress Transport
TMTF	Turning Mid Turbine Frame
TTTF	Transonic Test Turbine Facility

Roman Symbols

$\mathbf{U}$	vector of state variables
$\mathbf{u}$	velocity vector
$\mathbf{x}$	design vector
e	specific total energy
f	objective function
g, h	constraint functions
I	objective function
k	thermal conductivity, turbulent kinetic energy
N, M	basis functions
p	pressure
Q	heat source term
q	heat conduction
R	penalty multiplier, gas constant, equation of state
r	B-spline surface
Re	Reynolds number
S	momentum source term, strain rate magnitude
T	B-spline surface
u	velocity in x-direction
v	velocity in y-direction
w	velocity in z-direction
x	random variable

Greek Symbols

α	step size (matrix)

γ	intermittency
Δ	difference operator, scale factor
δ	limiter, Kronecker delta, difference operator
κ	heat capacity ratio
μ	molecular viscosity
ρ	density
τ	stress tensor
Ψ	vector of adjoint variables
Ω	vorticity
ω	turbulent dissipation rate

Subscripts

n	time step

Superscripts

l	lower
u	upper

Chapter 1

Motivation and Background

One of the main aims of the transportation and energy industries is to reduce the amount of fuel consumed without compromising the energy output. Three main concerns motivate this development objective. Firstly, there are limitations to the availability of fossil fuels; even though new reserves are being found sporadically it is undisputed that they will run out eventually. Estimates predict that the current reserves will run out before the end of the century. To lessen our dependency on fossil fuels a search for alternatives and simultaneously an effort to cut down on consumption have been initiated. The second concern is the problem of global warming which is becoming more acute continuously. The main cause for global warming lies in the anthropogenic emission of greenhouse gases. Carbon dioxide is one of the greenhouse gases which is a byproduct of burning fossil fuels and more than 50 % of the released greenhouse gases is CO_2 due to fossil fuel usage (Fig. 1.1). Nearly two-thirds of the global CO_2 emissions in 2012 were by the electricity and heat generation (42 %) and transport (23 %) sectors (Fig. 1.2). Mostly road transport is responsible for the emissions caused by the transport sector. Although aviation makes up only a small part of transport emissions international air transport grew by 80 % in the 22 years from 1990 to 2012. The European Commission ranks it as one of the fastest-growing sources of greenhouse gas emissions. And last but not least, reducing fuel combustion is an important and effective measure to cut down operational costs.

Both the transportation and energy industries rely heavily on gas turbines for the conversion of energy. And in modern aviation the most common type of gas turbine used is the turbofan engine. Figure 1.3 shows the main components of such an engine. Its operating principle is fairly simple. Air is sucked in through the fan with a slight pressure rise. Part of this air enters the engine core and the other part enters the by-pass channel. The pressure of the core flow is raised further as it passes through the low-pressure compressor (LPC) . An intermediate compressor duct guides the core flow from the LPC to the high-pressure compressor (HPC) .

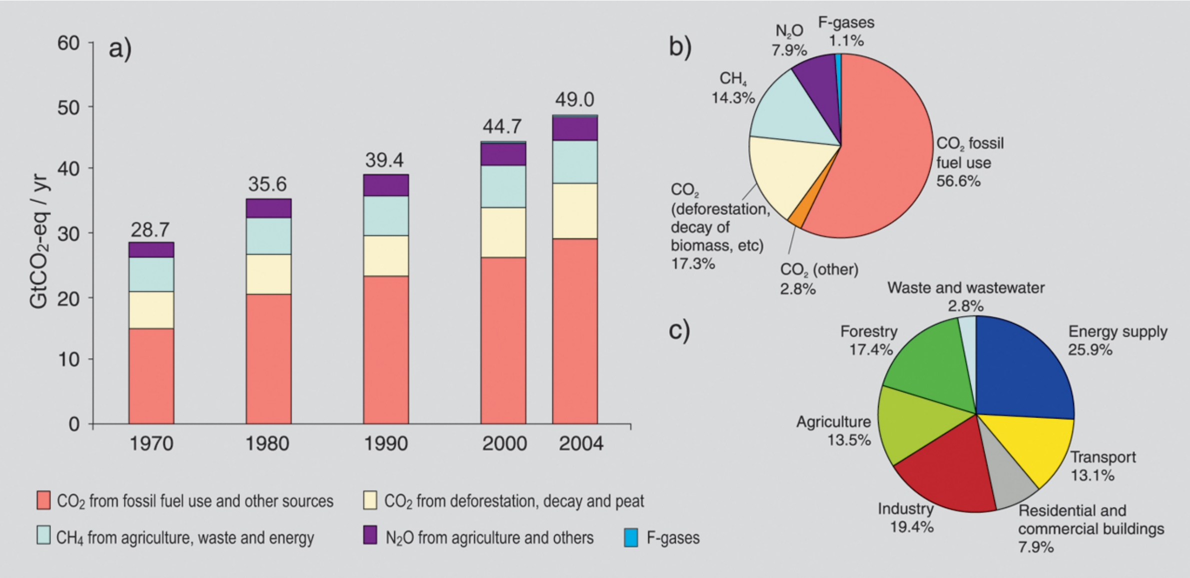

Figure 1.1: **(a) Global annual emissions of anthropogenic GHGs from 1970 to 2004. (b) Share of different anthropogenic GHGs in total emissions in 2004 in terms of CO2-eq. (c) Share of different sectors in total anthropogenic GHG emissions in 2004 in terms of CO2-eq. (Forestry includes deforestation.) IPC (2007)**

At the exit of the HPC air reaches the engine maximum pressure with advanced engines using pressure ratios of up to 45:1. In the combustion chamber (CC) fuel is injected into the highly pressurized air and ignited to increase the air temperature to the engine maximum which is around 1800 K for modern engines. The hot pressurized fluid then enters the high-pressure turbine (HPT) to transfer energy to the rotating shaft through the expansion of the fluid. The fluid is diffused through the intermediate turbine duct (ITD) before it enters the low-pressure turbine (LPT) where it is expanded again to transfer more work. The turbine shown in Fig. 1.3 is a two-spool engine such that the high-pressure turbine drives the high-pressure compressor and the low-pressure turbine drives the fan and low-pressure compressor. After the LPT the core flow exits through a nozzle creating a jet which mixes with the by-pass air before leaving the engine to create thrust and thus push the engine and aircraft forward.

The depicted machine for the realization of this fairly simple operating principle is not at all simple. Aircraft engines constantly push the limits of our engineering capabilities. In fact, they are the driving force behind much of our technical understanding and improvement as we try to travel faster and further more efficiently and reliably. As high pressure and temperature increase the thermal efficiency of an engine, engineers always try to develop materials that can withstand extremely high temperatures, but already turbine engines incorporate cooling concepts to allow operation at temperatures beyond the melting points of current materials. Lower exit velocities decrease engine noise and increase propulsive efficiency so that current

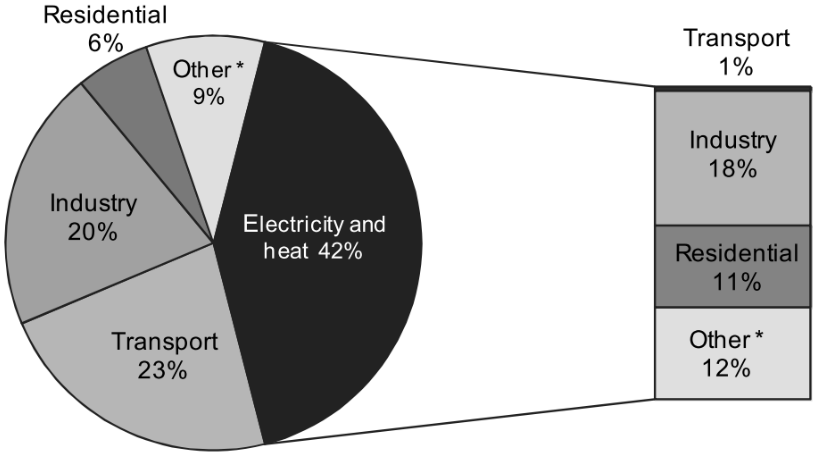

Note: Also shows allocation of electricity and heat to end-use sectors.

* Other includes commercial/public services, agriculture/forestry, fishing, energy industries other than electricity and heat generation, and other emissions not specified elsewhere.

Figure 1.2: **World CO_2 emissions by sector in 2012 (IEA (2014))**

development strides towards increasing by-pass ratios, hence increasing radial offset between the high-pressure and the low-pressure systems. And a lighter engine is more efficient simply because less weight has to be carried. This leads to new designs with shorter or even reduced number of components as technical achievements allow additional and improved functionalities for single components.

The development trend of high radial offset and shorter designs for intermediate turbine ducts are named aggressive design concepts. The diffusive duct can also be equipped with struts that can be used to turn the flow and thus eliminate the first stator row of the low-pressure turbine and reduce weight further. And another weight reduction can be achieved by designing these struts to carry the engine mount load, which is usually realized by carrying structures downstream of the LP turbine. Then the ITD has to be equipped with rigid struts that can withstand the strain due to the load. In this case, the ITD becomes a diffuser that guides the flow from the high-pressure turbine to the low-pressure turbine, a turbine frame that supports the rear bearing load and the first stator row of the low-pressure turbine that turns the flow. This is the concept of the turning mid turbine frame (TMTF).

The main challenge of the TMTF is its complex 3D flow structure due to the usually high turning angle and the low aspect ratio of the struts. A highly unsteady inflow from the HPT adds to the complexity of the flow. Reducing losses in the TMTF is a field of intensive research and involves passive or active methods. Active methods refer to techniques where the control power is provided by external sources. These methods may increase or decrease

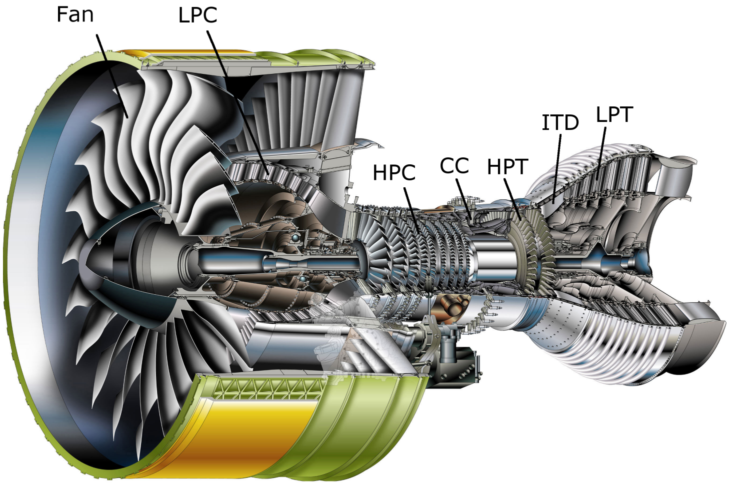

©2014 Engine Alliance

Figure 1.3: **GP7000 two-spool turbofan engine**

mass flow, e.g. boundary-layer suction. Passive methods refer to techniques such as changing the geometry of boundary contours to improve the flow path where additional power supply in not required. The changes to the boundary contours include modifications to the blade geometry such as leaning or curving the blades or endwall contouring. Finding the right endwall contour, leaning, curving or even blade profile requires optimization strategies to ensure the minimization of aerodynamic losses.

To investigate the fundamental flow physics in aggressive intermediate ducts and develop new concepts in 2004 the EU 6th Framework Program project AIDA[1] was launched. It focused on the investigation of the fundamental flow physics in aggressive intermediate ducts. More aggressive concepts were developed and evaluated both in test facilities and with computational fluid dynamics (CFD) . And in 2008 the European project DREAM[2] was launched which was supported by 44 partners from 11 European countries as well as Turkey and Russia. One of the focuses of the DREAM project was the investigation of innovative systems. Within this focus a work package investigated novel structures for mid turbine frames. The Institute of Thermal Turbomachinery and Machine Dynamics (ITTM) of Graz University of Technology was one of the project partners involved in this specific work package. In the project much insight into the flow structures in the TMTF was gained which lead to concepts for its improvement in respect to aerodynamics and aeroacoustics.

In 2011 the TAKE OFF project SEIKON3D was started at ITTM which was funded by the Austrian Federal Ministry for Transport and Technology. The objective of the project

---

[1] Aggressive Intermediate Duct Aerodynamics for Competitive and Environmentally Friendly Jet Engines, contract number: AST3-CT-2003-502836

[2] valiDation of Radical Engine Architecture systeMs, contract number: ACP7-GA-2008-211861

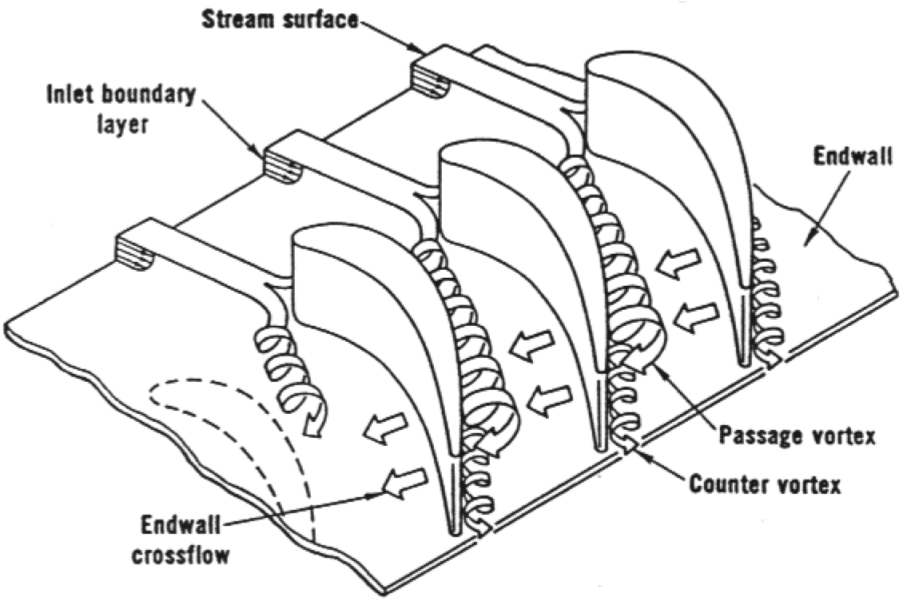

Figure 1.4: **The 3D separation of a boundary layer entering a turbine cascade (Langston (1980))**

was to develop a software tool for the CFD optimization of turbine endwall contours. The results presented in this thesis are from investigations conducted within the framework of this project. These investigations led to the development of a new optimization strategy which will be introduced and discussed in terms of performance and complexity.

In the following introduction to the various aspects of loss phenomena and their counter measures the next section deals with secondary flow phenomena in a turning mid turbine frame which is followed by a review of the effort to reduce loss caused by secondary flows. Then contour parametrization techniques are shortly discussed. Consequently, optimization strategies will be reviewed.

1.1 Secondary Flow

The flow in turbomachinery blade rows deviates considerably from an idealized flow structure that follows the boundary surfaces. It is dominated by complex 3D flow phenomena that are caused by the curvature of surfaces, pressure gradients in the flow path and gaps between the components. Research has been conducted since the 50s to understand the nature of these 3D structures. The findings till 1984 are summarized by Sieverding (1984). In 2001 Langston (2001) took up the effort and summarized the results of investigations conducted between 1984 and 2001.

The basic flow through a plane cascade has been fairly well studied. Figure 1.4 shows the dominant secondary flow structures in a linear cascade. The inlet boundary layer on the

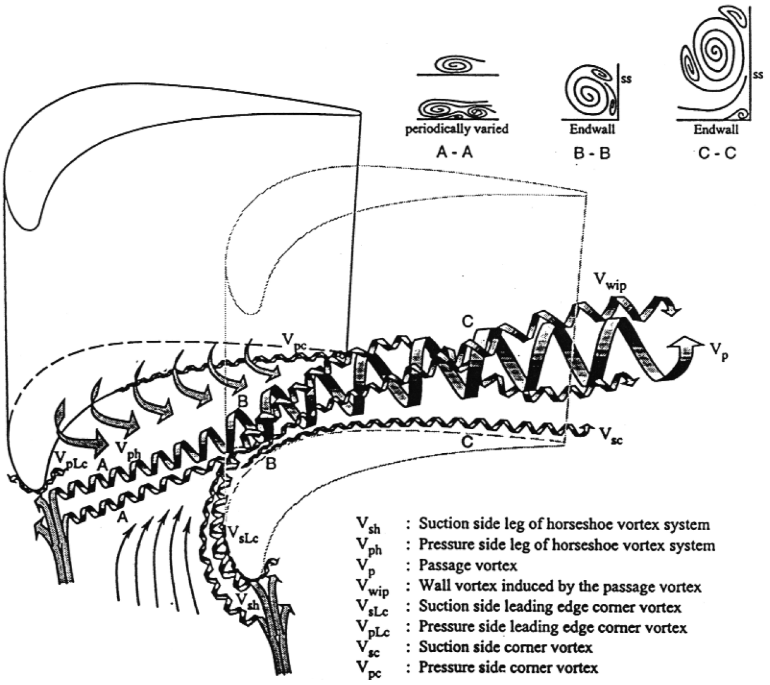

Figure 1.5: **The 3D separation of a boundary layer entering a turbine cascade (Wang et al. (1997))**

endwall of the cascade is devided at a saddle point to either side the blade and the pressure gradient in the flow direction causes the boundary layer to coil up forming vortices on both sides of the blade. This vortex structure is called the horseshoe vortex system. The pressure side leg of this vortex is drawn towards the suction side of the adjacent blade by the pressure difference which also affects the main flow and the boundary layer flow between the blades. But as the boundary layer flow travels with lower velocity it has a stronger inclination towards the adjacent blade. More fluid is transported from the pressure side to the suction side. The blade wall forms a barrier which pushes the flow upwards along the wall. Through this deflection the passage vortex is initiated. The passage vortex has the same sense of rotation as the pressure leg of the horseshoe vortex and they usually merge. The counter vortex shown in Fig. 1.4 represents the suction side leg of the horseshoe vortex which has a sense of rotation opposite to the passage vortex and is much smaller. It may also be dissipated by viscosity.

Another detailed study of a cascade flow using laser light and multiple smoke wires was presented by Wang et al. (1997). The complex multi-vortex pattern they proposed is shown in Fig. 1.5. Essentially the same secondary flow structures are observed but some differences and additional vortex structures are depicted. The pressure side leg of the horseshoe vortex is illustrated as a multi-vortex structure (V_{ph} at section A-A) that is gradually squeezed into a single vortex. A wall vortex V_{wip} is introduced that originates near the merging point of the

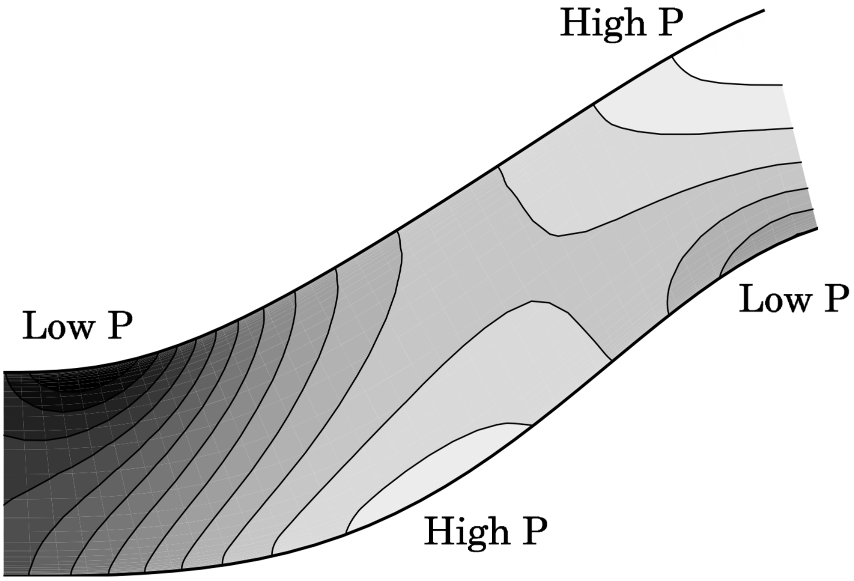

Figure 1.6: **Schematic pressure field distribution in an ITD (Wallin (2008))**

two legs of the horseshoe vortex system. It is defined as a small and very intense vortex. Wang et al. (1997) state that Jabbari et al. (1992) found the content of this vortex to come from the inlet boundary layer between the saddle points ahead of the cascade. Also four corner vortices V_{sLc},V_{pLc},V_{sc} and V_{pc} are shown based on the results of Jabbari et al. (1992) and Goldstein et al. (1995).

Another vortex structure common in turbine cascades is the trailing edge shed vortex (which is not depicted in either of the figures shown here). At the trailing edge of the blade shear stresses develop in the flow due to the different velocity direction and magnitude of the boundary flows from the suction side and pressure side. These shear stresses induce the trailing edge shed vortex.

Aside from these secondary flow structures that have predominantly been studied in linear cascades, in the ITD there is additionally the duct curvature that causes high streamwise pressure gradients. Fig. 1.6 shows the qualitative distribution of the pressure field in an aggressive vaneless ITD. After the first bend of the shroud the flow must overcome a strong adverse pressure gradient which causes it to slow down. The deceleration due to an adverse pressure gradient and the streamwise curvature result in the growth of the boundary layer and introduce the risk of separation. ITDs also commonly have load carrying structures in them. These struts can cause a considerable blockage due to their thickness which imposes additional pressure gradients on the walls. They cause the flow to accelerate in the vane passage up to the vane maximum thickness location and then decelerate. This superposed deceleration increases the risk of separation. In the case of the TMTF the struts also function as lifting vanes. Through

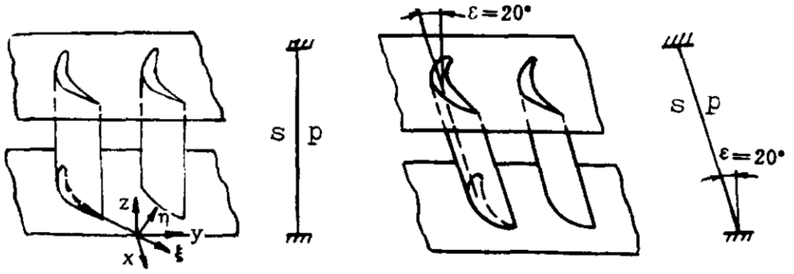

(a)Traditional Linear blade Cascade (b)Lean Linear blade Cascade

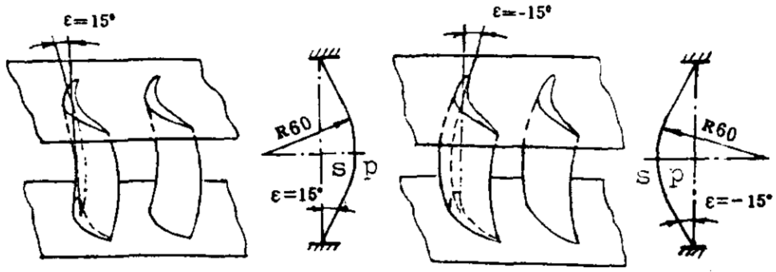

(c)Positively curved blade Cascade (d)Negatively Curved blade Cascade

Fig. 1 Tested Cascades and shapes of Profile stacked Lines

Figure 1.7: **Lean and bow blade configurations investigated by Wanjin et al. (1993)**

the turning the flow experiences a stronger retardation on the vane suction side. Hence the intersection of the vane suction side with the shroud endwall as well as the hub endwall become problematic regions with an imminent risk of separation.

1.2 Contour Modifications for Secondary Flow Reduction

In the past several methods have been investigated to reduce the loss generated by secondary flow. Sieverding (1975) and Biesinger (1993) provide an overview of such methods. In this work passive methods which generally refer to geometrical modification of the blades or endwalls are in focus. There are various alternatives for modifying the geometry of blades and endwalls.

Possible modifications for blades include radial stacking (lean, compound lean, twist), sweep, re-cambering or radial variations of the blade chord. By blade stacking the radial loading distribution can be improved. Lean airfoils were proposed by Deich et al. (1960). Harrison (1990) found out that lean and compound lean (similar to negatively curved blade cascade in Fig. 1.7) redistribute losses radially without any significant reduction. Wanjin et al. (1993) point out that in cascades with low-aspect ratio and high-turning angle, the secondary losses from horseshoe and passage vortices constitute the main part of the total losses. The

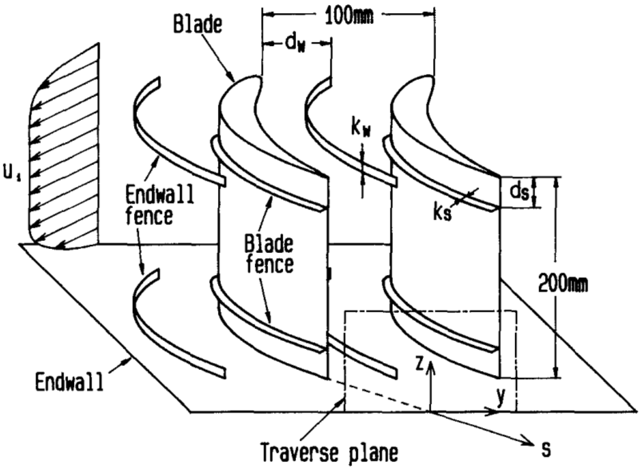

Figure 1.8: **Cascade and combined boundary layer fences investigated by Kawai (1994)**

leaning of the blade intensifies the passage vortices in the acute angle zones and moves them towards the obtuse angle zones, such that the aerodynamic performance is enhanced in the acute angle zone but degraded in the obtuse angle zone. A negatively curved blade creates acute angle zones at the hub and shroud and so confines the upper and lower passage vortices in their own corner, avoiding their meeting and preventing increased secondary flow losses through their mixing. The geometry of the test cascades used by Wanjin et al. (1993), which led to these conclusions, are shown in Fig. 1.7.

The application of boundary layer fences to reduce secondary flow have been investigated (amongst others) by Kawai et al. (1989); Prümper (1975) and Doerffler and Amecke (1994). Kawai et al. (1989) concluded that if the boundary layer fences are attached to the channel-confining endwalls of a linear turbine cascade in streamwise direction loss through secondary flow can effectively be reduced. The benefits of combined boundary layer fences (on blade and endwall) were discussed later by Kawai (1994). He was able to further reduce the loss generated by secondary flow. Doerffler and Amecke (1994) investigated two different fence configurations. In one case they applied streamwise fences (with respect to the main flow) and observed significant reduction of secondary flow with the oil visualization technique. In the second case, the transverse fences which were applied perpendicular to endwall boundary flow direction (cross flow), seemed to only displace the secondary flow cores.

The first references to axisymmetric endwall contour modification date back to Deich et al. (1960). They reported on an optimal contraction ratio as a function of the aspect ratio to reduce the cross-channel pressure gradient to suppress the secondary flow. Fig. 1.9 shows the contour they proposed and the efficiency that can be gained as a function of the contraction ratio for different aspect ratios. Dejc (1965) regarded tip endwall contouring to be one of the most effective methods to improve the performance of low aspect ratio turbine vanes.

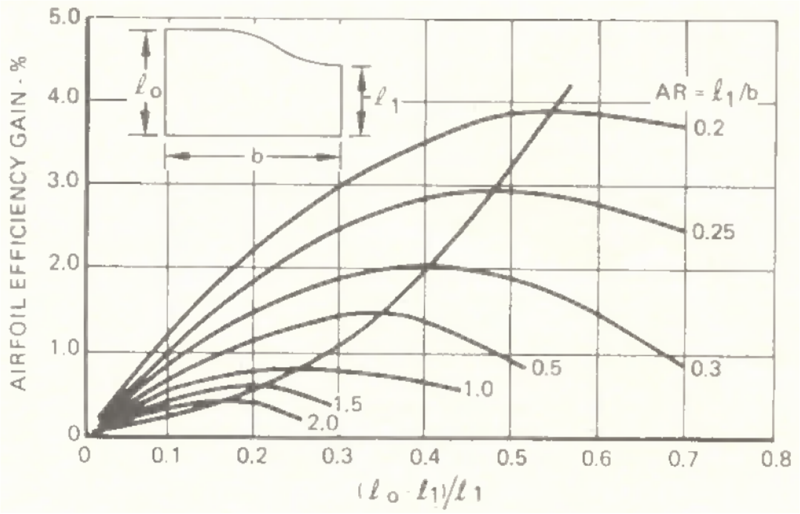

Figure 1.9: **Contoured vane endwall design criteria (Deich et al. (1960))**

The benefits of the method are stated to be due to the increase of the channel convergence, the decrease of the pitchwise pressure gradient at the front half of the blade passage, and the positive influence on the span-wise static pressure distribution at the blade trailing edge region. Ewen et al. (1973) reported on a 1.5 percent point improvement of efficiency through endwall contouring much of which he attributed to reduced blade row loss obtained from improved blade inlet flow conditions. Morris and Hoare (1975) showed reduction in the total pressure loss on the side of the flat endwall and no change close to the contouring side in their plane cascade. Besides a reduction in the secondary losses, Kopper et al. (1981) determined that the aerodynamic loading was reduced around the frontal part of the vane and the point of minimum pressure was moved towards the trailing edge. The adverse pressure gradient downstream of the point of minimum pressure was reduced for the flat wall but increased for the contoured side. Dossena et al. (1998) explained that the main mechanism resulting in the lower loss is the lower velocity inside the vane passage. In the contoured cascade, they also observed a stronger decrease of secondary loss at the flat side where the secondary flow structure is similar to a typical configuration of straight cascades, but with lower vortex intensity.

The first investigations of three dimensional endwall profiles were undertaken by Atkins (1987); Morris and Hoare (1975) and Rose (1994). Not all were successful. Morris and Hoare (1975) intended to move the velocity maximum nearer to the leading edge and to create a more rapid deceleration towards the trailing edge. Measurements of static pressure indicated that the position of the peak velocity was barely moved but the amount of deceleration increased. Adjacent to the profiled endwall a large region of high total pressure loss appeared, indicating that the wall boundary layer had been thickened and may have separated. Mass averaged total pressure measurements showed that near the flat wall the losses were unchanged, but adjacent

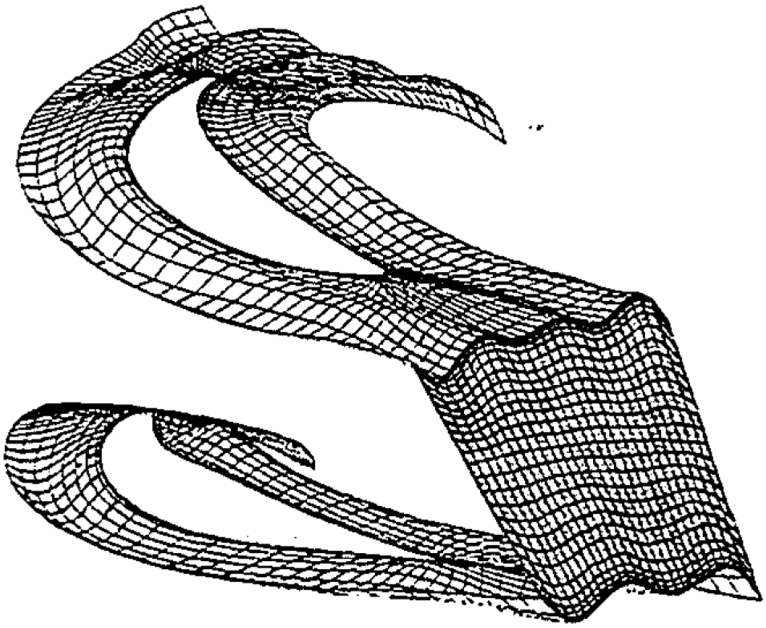

Figure 1.10: **Example of a perturbed endwall (Harvey et al. (1999))**

to the profiled wall the losses were increased. Atkins (1987) tested two non-axisymmetric contours. One profile was intended to reduce the cross-channel pressure gradient by lowering the pressure next to the pressure surface. The other profile intended to reduce the size of the suction peak on the suction surface of the blade without affecting the pressure surface. Both designs were based on a dent adjacent to one blade surface reducing to no profile near the opposite surface. The first profile was believed to have caused a small amount of separation on the contoured endwall. The second profile reduced the loading over most of the passage but this was offset by increased loading close to the trailing edge. Rose (1994) intended to smooth out the nozzle guide vanes pressure field. His main concern was not the reduction of secondary losses but to decrease disc coolant flow leakage. He proposed convexity to drop the pressure and concavity to increase the pressure resulting in a non-axisymmetric endwall contouring and he was able to achieve a 70 % reduction in the non-uniformity of the pressure distribution on the hub. He also pointed out that endwall profiling causes local modifications to the Mach number distribution around the airfoils which have the potential to remove any benefit the endwall profiling may offer.

Hartland et al. (1998) continued this effort on the linear cascade at the Durham University and successfully reduced the non-uniformity. The endwall profiling produced no significant change in secondary flow, although a slight increase in secondary loss is reported. Following this, Harvey et al. (1999) applied endwall profiling on the Durham linear cascade to decrease secondary losses by reducing the cross-passage pressure gradient which can be regarded as what gives rise to the secondary flow in turbomachinery blade rows. They adapted a systematic linear design method to achieve lower secondary losses and use it for the first time for the design of endwalls and achieved profiles that they had not contrived without a systematic design study. Fig. 1.10 shows an example of such an endwall design. Numerical evaluations predicted a 4 % reduction in the row loss which is within the accuracy of the CFD code. Reports of the experimental validation of this design are published by Hartland et al. (1999). Most of the results agreed well with their design predictions. The cross passage pressure difference was decreased as predicted and secondary flows were reduced, although a stronger corner counter vortex was observed. The experiments also revealed a significant reduction of the secondary loss; 30% at the downstream exit plane.

The complex nature of secondary flow and secondary loss as well as the results of these investigations, that have all contributed to our understanding of secondary flow phenomena but not always succeeded in effectively reducing secondary loss, emphasize the necessity of a systematic approach to endwall contour design. This has led to the application of optimization methods to obtain endwall contours with the desired reduction of loss and gain in efficiency. Such an approach requires the effective parametrization of the contour to describe various design modifications.

1.3 Geometry Parametrization

Geometry parametrization is one of the key elements of optimal shape design. It must allow a broad spectrum of modifications that hopefully includes the best solution, but also use as few parameters as possible to obtain results in an acceptable time span.

Despite the importance of the parametrization method, it is not in the focus of this thesis. In the following short discussion an overview of methods is persued to attain an understanding of the possibilities and role of parametrization techniques.

A good discussion of the topic has been presented by Anderson et al. (2012). Therein two types of geometry modeling are defined; constructive and deformation methods. In constructive modeling a geometry is defined with elements such as B-splines, Bernstein polynomials or NURBS surfaces. Anderson et al. (2012) state that the fundamental weakness of constructive modeling is the method used for the geometry definition itself, which dictates not only what a surface can do, but also what it cannot do and that poor geometry parametrization can cripple shape optimization by restricting design space. An alternative to improve the design space is to enhance constructive modeling with deformation techniques. These superimpose modifications to a baseline geometry and allow highly flexible reshaping enabling shape optimization tools to evaluate shapes that the original constructive parametrization could not reach.

Deformation methods can be classified as either surface-based or volumetric. As their names suggest, surface-based methods focus on the surface without consideration of the encompassing volume while volumetric methods do the opposite. Surface-based deformation techniques are conceptually straightforward. They allow for physically realistic deformations and make it easier to preserve geometric features. Further discussion on parametrization techniques can be found in Samareh (1999) and Mousavi et al. (2007).

The parametrization technique used in this thesis involves a surface-based deformation method utilizing non-rational B-spline surfaces. It will be introduced in chapter 3.

1.4 Optimization Methods

Traditionally design improvements have been based on experience gained through previous designs and simple correlations. A design process involved building and testing new designs until a design objective was achieved. The introduction of computational methods for fluid dynamics and structure mechanics has provided alternatives to time consuming and costly experiments. Initial analysis of designs can be performed within hours and significantly reduce the dependance on experiments. Still, the number of designs that can be tested within a certain time span, although increased, remains quite limited. Systematic approaches further increase the success of such endeavors. Optimization algorithms represent the automation of these systematic approaches. These algorithms maximize the performance of a design by modifying its parameters while requiring minimal intervention from the designer.

Optimization algorithms search for the minimum or maximum of one or more functions subject to constraints. If an optimization problem has only one objective function the problem is called a single-objective optimization. If more objective functions are involved the problem is referred to as a multi-objective optimization. And if more than one design point or off-design points are considered the problem is referred to as a multi-point optimization problem. This work does not involve multi-point multi-objective optimizations. Therefore, we will focus on the constrained single-objective optimization problem which can be mathematically formulated as:

$$\texttt{Minimize}: \quad f(\mathbf{x}) \tag{1.1}$$

$$\texttt{Subject to}: \quad g_i(\mathbf{x}) \leq 0, \qquad i = 1..p \tag{1.2}$$

$$h_j(\mathbf{x}) = 0, \qquad j = 1..q \tag{1.3}$$

$$x_k^l \leq x_k \leq x_{k,}^u \quad k = 1..r \tag{1.4}$$

$$\texttt{where}: \quad \mathbf{x} = \begin{Bmatrix} x_1 \\ x_2 \\ \vdots \\ x_r \end{Bmatrix} \tag{1.5}$$

The vector **x** is the vector of design variables and it contains the parameters of the design that can be modified. The function $f(\mathbf{x})$ is referred to as the objective function. In the optimization of a turbine vane row this can e.g. be the entropy, turbulent kinetic energy or total pressure drop. The inequality constraints given by Eq. (1.2) represent conditions that need to be satisfied and the equality constraints given by Eq. (1.3) usually represent relationships between design variables. Eq. (1.4) represents the range of the design variables.

Such a constrained optimization problem is difficult to solve due to the inequality constraints given by Eq. (1.2). Usually a pseudo-objective function $\tilde{f}(\mathbf{x})$ is introduced that translates the constrained formulation into an unconstrained optimization problem:

$$\tilde{f}(\mathbf{x}) = f(\mathbf{x}) + R \cdot \sum_{i=1}^{m} \delta_i \cdot (g_i(\mathbf{x}))^2 \tag{1.6}$$

$$\delta_i = 0, \textbf{ if } g_i(\mathbf{x}) \leq 0 \tag{1.7}$$

$$\delta_i = 1, \textbf{ if } g_i(\mathbf{x}) > 0 \tag{1.8}$$

This is however a weak formulation of the constraints. The value R, called the penalty multiplier, defines the weight given to satisfying the constraints. Large values of R ensure that the optimum of $\tilde{f}(\mathbf{x})$ will be closer to the constrained optimum of $f(\mathbf{x})$. However, Vanderplaats (1984) state that the problem becomes ill-conditioned. Thus the value of R is a trade off between numerical stability of the optimization and the degree of satisfaction of the constraints (Periaux and Verstraete (2012)).

Many approaches for the use of numerical methods in optimization have been developed. The methods are generally classified by the order of derivatives of the objective function used

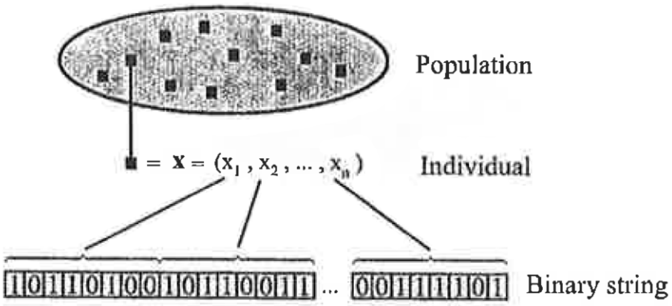

Figure 1.11: **Binary string representation of individuals in GAs (Verstraete (2012))**

in the algorithm. These are zero, first and second order methods. A very good introduction to optimization methods is given by Periaux and Verstraete (2012).

1.4.1 Zero Order Methods

For an optimization with zero order methods, which are also referred to as stochastic optimization methods, derivatives of the objective function are not used in the search algorithm. In the simplest approach a large number of random candidate vectors $\mathbf{x}$ are selected and the objective function is evaluated for each of them. The vector $\mathbf{x}$ which results in the smallest objective function satisfying all constraints is regarded as the optimum. This method is called the random search or random walk. It is evident that for a precise solution a very large number of candidate vectors have to be considered. For the evaluation of objective functions that require the iterative solution of complex partial differential equations, as is the case with CFD, the method is computationally very intensive. The slow convergence and consequently large computational effort is the major drawback of stochastic optimization methods, but they offer the advantage of the search for a global optimum and they are able tor solve noisy objective functions without information on their continuity. They also allow the direct specification of equality and inequality constraints.

Several approaches exist to increase the efficiency of zero order methods, e.g. simulated annealing and evolutionary algorithms (EA). Evolutionary algorithms have been introduced by Rechenberg (1973) and Holland (1975). They adapt the Darwinian evolution theory to the optimization problem; the design vector $\mathbf{x}$ is regarded as an individual and populations of individuals evolve over a search space to adapt to the environment by mutation, crossover or selection. The method requires the evaluation of an entire population per iteration.

Genetic algorithms (GA) (Goldberg (1989)) are one of the most popular evolutionary strategies. In this approach a population consists of a fixed number of individuals and each individual is represented by a binary string containing all values of the parameters as shown in

Fig. 1.11. The binary string can be considered analogous to chromosomes in lifeforms. Thus, reproduction mechanisms similar to those found in nature are defined; individuals mate and generate offsprings. This is represented by crossover operations between two individuals of a generation (parents) to create two individuals of the next generation (children).

A major disadvantage of EAs is the large number of evaluations of the objective function needed which is commonly more than a thousand and complex optimization problems may even require a drastically higher number of evaluations. This impediment lead to the development of acceleration techniques such as distributed EAs, hierarchical EAs and metamodel assisted EAs. Distributed EAs subdivide the entire population into islands which evolve in isolation. The most promising individuals of the islands are then regularly exchanged. The performance of distributed EAs have been studied by Mühlenbein et al. (1991) and recently by Giannakoglou and Karakasis (2006). Hierarchical EAs use less accurate evaluations of the objective function. In case of CFD accuracy and computational effort can be reduced by decreasing the resolution of the computational space (number of grid points) or by reducing the complexity of the analysis, e.g. by solving the Euler equations instead of the Navier-Stokes equations. As these models are less accurate, promising individuals still have to be reevaluated with the original model. The technique can be combined with distributed EAs (Giannakoglou and Karakasis (2006)). Metamodels, also known as surrogate models, are even less accurate as they are not based on physics but on artificial intelligence techniques such as neural networks. These models have to be trained first to reproduce accurate results for a range of variables. They can then be used to approximate the performance of designs close to the already evaluated ones. Designs significantly different than the initial set should be evaluated with the original model. Alternatively, the metamodel can be trained during the optimization as well with the reevaluation of promising individuals using the original model.

These algorithms can effectively be applied for the solution of multi-point multi-objective optimization problems. Recently, a multi-point and multi-objective optimization was published by Reutter et al. (2014). The successful optimization still comes with the price of high computational cost as the objective functions were evaluated over 4000 times.

1.4.2 First Order Methods

First order methods assume the continuity of the objective function and use gradient information. With the gradient information a more efficient convergence compared to zero order methods can be achieved, but the convergence is generally towards the local minimum. Their performance is also rather poor in the presence of noise or if the objective function has discontinous first derivatives.

In a gradient based approach a design is iteratively improved by adjusting the parameters based on the gradient information of the objective function:

$$\mathbf{x}_{n+1} = \mathbf{x}_n - \alpha_n \mathbf{S}_n. \tag{1.9}$$

$\mathbf{S}_n$ is the search direction of the current step n:

$$\mathbf{S}_n = \nabla f(\mathbf{x}_n) \tag{1.10}$$

The magnitude of change is set by the step size α_n which should be chosen small enough to prevent an overshoot of the objective function on the path towards the optimum. There are a number of methods to determine the amplitude α_n. A straightforward approach is the steepest descend method where the step size is chosen as large as possible to accelerate convergence, but as it also effects the stability of the optimization an estimation of its limit is pursued. Other methods also use the information of previous iterations to achieve fast convergence. An overview and introduction to these methods is given by Chong and Zak (2001)

The main challenge of first order methods though is computing the gradient which can be a computationally very intensive task, specifically if the number of design parameters is large and if a single evaluation is computationally expensive, as is usually the case with CFD based optimization. A simple approach to compute the gradient is by the evaluation of a small perturbation of each design variable (Hicks and Henne (1978)):

$$\frac{\partial f(\mathbf{x})}{\partial x_i} \approx \frac{f(\mathbf{x}+h.\mathbf{e}_i) - f(\mathbf{x})}{h}, \quad i = 1..r \tag{1.11}$$

where $\mathbf{e}_i$ is the i-th unit vector and h is a small scalar step size. This method, referred to as the *finite difference method*, requires an additional computation for the approximation of the derivative of each design variable, resulting in $r+1$ computations at each optimization iteration. The consequent large computational expense for optimization problems involving iterative partial differential equation solvers are usually the cause for finite difference methods to be deemed unsuitable for many optimization problems. Another similar approach is the *complex variable method* (Squire and Trapp (1998)), where instead of using a real perturbation h, an imaginary perturbation $i \cdot h$ is used. Finally, the *adjoint method* provides an efficient algorithm for the calculation of derivatives as the computational expense is, to a large extent, independent of the number of design variables. It has mainly been advocated by Pironneau (1973) and Jameson (1988) and has been widely used in the aerodynamic design optimization for airfoils, wings and wing-body configurations (Jameson (1995); Kim et al. (2004)). Recently its application has been extended to turbomachinery design optimization (Corral and Gisbert (2008); Frey et al. (2009a); Giles et al. (2001); Luo et al. (2011, 2014); Papadimitriou and Giannakoglou (2006); Wang and He (2010); Wu and Liu (2005); Yang et al. (2006)). As it is also used in an optimization described in this thesis and two related publications (Akin et al. (2014, 2015) a closer look at the adjoint method will be provided in the next chapter.

1.4.3 Second Order Methods

Second order methods use the Hessian matrix (second derivatives) to determine the step size. They need only one iteration to optimize a quadratic function. For non-quadratic functions several iterations are needed, but the convergence is faster than for first order methods. The computation of the second derivative is computationally expensive and eventually also noise-sensitive. Additionally, the Hessian matrix might be non-positive definite or even singular. As a result of their computationally expensive and numerically unstable nature second order methods are generally not used in shape optimization problems involving Navier-Stokes or stress computations (Verstraete (2012)).

1.4.4 A Quasi-First-Order Method

Main objective of this thesis is to introduce a new optimization method and demonstrate its applicability on the optimization of a TMTF. It is introduced as an alternative to gradient based methods. It is based on incomplete gradient information which is obtained through incomplete CFD calculations instead of less accurate evaluations of the objective function with hierarchical or surrogate models. The incomplete gradient information poses new challenges. A discussion on how to overcome these challenges will also be presented.

Chapter 2

Optimization Approach

2.1 Adjoint Method

The optimization problem previously defined in section 1.4 can simplified for a single-objective optimization problem with only one equality constraint to satisfy. Also, it is common to use a different notation for the mathematical formulation of the adjoint method.

$$\begin{aligned} \texttt{Minimize:} \quad & I(\mathbf{U},\mathbf{x}) && (2.1)\\ \texttt{Subject to:} \quad & R(\mathbf{U},\mathbf{x}) = 0 && (2.2)\\ & x_k^l \leq x_k \leq x_{k,}^u \quad k = 1..r && (2.3) \end{aligned}$$

In shape optimization problems with CFD the equality constraint in Eq. 2.2 represents the RANS equations that the state vector $\mathbf{U}$ and design variables $\mathbf{x}$ satisfy. This formulation of the general problem implies the possibility to modify both the state vector $\mathbf{U}$ as well as the shape geometry parameters $\mathbf{x}$. However, the state vector $\mathbf{U}$ contains the physical quantities which are determined to satisfy the equality constraint (Eq. 2.2). The gradient of the objective function is computed with respect to the geometrical design variables $\mathbf{x}$. Using the chain rule the derivative of the objective function can be expressed as:

$$\frac{dI}{d\mathbf{x}} = \frac{\partial I}{\partial \mathbf{U}} \frac{\partial \mathbf{U}}{\partial \mathbf{x}} + \frac{\partial I}{\partial \mathbf{x}}. \tag{2.4}$$

The computation of the first-order state derivatives $\frac{\partial \mathbf{U}}{\partial \mathbf{x}}$ is computationally expensive as the RANS equations would have to be evaluated for every design variable variation. The application of the chain rule on the equality constraint provides additional information:

$$\frac{\partial R}{\partial \mathbf{U}} \frac{\partial \mathbf{U}}{\partial \mathbf{x}} + \frac{\partial R}{\partial \mathbf{x}} = 0. \tag{2.5}$$

$\frac{\partial \mathbf{U}}{\partial \mathbf{x}}$, which is needed for Eq. 2.4, can be evaluated from Eq. 2.5. But it would still be very inefficient. Reformulating Eq. (2.5) for $\frac{\partial U}{\partial x}$ results in:

$$\frac{\partial \mathbf{U}}{\partial \mathbf{x}} = -\left(\frac{\partial R}{\partial \mathbf{U}}\right)^{-1} \frac{\partial R}{\partial \mathbf{x}} \tag{2.6}$$

After inserting Eq. (2.6) into Eq. (2.4) the sensitivities can be rewritten as:

$$\frac{dI}{d\mathbf{x}} = \Psi^T \frac{\partial R}{\partial \mathbf{x}} + \frac{\partial I}{\partial \mathbf{x}}, \tag{2.7}$$

where Ψ represents the vector of adjoint variables containing the adjoints of the state variables and is the solution of

$$(\frac{\partial R}{\partial \mathbf{U}})^T \Psi = -(\frac{\partial I}{\partial \mathbf{U}})^T. \tag{2.8}$$

For the evaluation of the sensitivities of the objective function with the adjoint method Eq. (2.8), which represents the adjoint equation, is solved first. The solution of the adjoint equation is approximately as expensive as the solution of the RANS equations, but it is not dependent on the design variables. So, for a single-objective optimization problem without additional constraints it has to be calculated only once for each design cycle.

This derivation of the adjoint formulation represents the discrete approach as the state equation $R(\mathbf{U},\mathbf{x}) = 0$ is considered to be in its discrete form. The alternative continuous adjoint formulation derives the adjoint equation based on the analytical formulation of the state equations, which is then discretized. The adjoint solver used in this project is based on the discrete approach, so the continuous adjoint will not be further discussed. An introduction to the continuous adjoint can be found in Giannakoglou et al. (2012) and further discussion on both approaches has been published by Giles et al. (2003) and Papadimitriou et al. (2005). The advantage of the discrete approach is that it prescribes a discretization of the adjoint partial differential equation so that the choice for appropriate discretization schemes becomes redundant and the sensitivities relate directly to the objective function as it is evaluated numerically. Consequently, if a local optimum is found by driving the discrete gradient to zero, it may be easily verified with re-evaluations of the objective function for small perturbations. When the continuous gradient is driven to zero, local perturbations of the discrete objective function may not verify that a local minimum has been obtained (Vassberg and Jameson (2012)).

The work presented in this thesis does not involve the implementation of an adjoint solver. The solver TRACE, which also includes an adjoint solver implemented by Frey et al. (2009b), is used for the CFD and sensitivity evaluations. The adjoint formulation has not been extended to any of the turbulence models available in the solver. It is based on the constant eddy viscosity assumption so that when computing sensitivities with respect to shape variations the eddy viscosity has the same values as in the solution for the current optimization step. This approach has the advantage of faster implementation and less computational cost in comparison to the adjoint equation corresponding to a full turbulence model. It results in mostly good agreement of the sensitivities with those calculated by finite differences as shown by Frey et al. (2009a,b, 2011). The adjoint equation is solved by a generalized minimal residual method (GMRES) . The solver provides the option to precondition the system with either incomplete lower-upper decomposition (ILU) or symmetric successive over-relaxation (SSOR). In this work the solver was set to precondition with ILU. More information can be found in Frey et al. (2009a,b).

After the adjoint Ψ is determined Eq. (2.7) can be evaluated for the sensitivities. Most turbomachinery specific cost functions depend only on the state at certain planes, typically the inlet and exit of blade rows. Therefore, the evaluation can be simplified with the assumption that the sensitivities depend only on the sensitivity of averaged states as long as hub or casing geometry are not varied at these planes. In this case $\frac{\partial I}{\partial x}$ in Eq. (2.7) can be set to 0. The term $\frac{\partial R}{\partial x}$ is approximated by forward finite differences by evaluating the residuals of the flow solution for a perturbation of each design variable (Frey et al., 2009b). This step is approximately as time consuming as one time step of the CFD solver. It is the only step for which the CPU time is proportional to the number of parameters. A new mesh has to be generated for each parameter and this can become computationally expensive if the number of parameters are high and the mesh is large.

After the sensitivities $S_n = \frac{dI}{d\mathbf{x}}$ are determined the parameters of the next step of the optimization procedure can be calculated with Eq. (1.9). For the convenience of the reader the equation is presented again:

$$\mathbf{x}_{n+1} = \mathbf{x}_n - \alpha_n \mathbf{S}_n. \tag{2.9}$$

A variety of search methods exist to determine the step size α_n, e.g. the steepest descent, modified steepest descent with smoothing, implicit descent, multigrid steepest descent, Krylov acceleration, and quasi-Newton methods. The optimizations that were performed within the framework of this thesis were either performed using the steepest descent method or the rank one (R1) quasi-Newton method. Quasi-Newton methods approximate the Hessian (second order derivatives) or its inverse from changes in the gradient during the search steps. They are widely regarded as the method of choice for general optimization problems (Periaux and Verstraete, 2012). The R1 method uses the following equation:

$$\alpha_{n+1} = \alpha_n + \frac{\mathbf{P}_n(\mathbf{P}_n)^T}{(\mathbf{P}_n)^T \Delta\mathbf{S}_n} \tag{2.10}$$

where

$$\mathbf{P}_n = \Delta\mathbf{x}_n - \alpha_n \Delta\mathbf{S}_n. \tag{2.11}$$

and Δ is the difference operator.

Finally, Fig. 2.1 shows the flow chart of the optimization routine. Starting with the initial geometry the CFD and the adjoint solution are calculated. Concurrently, a new grid is generated for each design variable of the current step after applying a small perturbation to the variable. These constitute the grid variants of the iteration which are generated with an in-house mesher developed by Pieringer (2012). The grid variants are used to evaluate $\frac{\partial R}{\partial x}$. Then the sensitivities are calculated using the adjoint solution and the grid variants according to Eq. 2.7 (with $\frac{\partial I}{\partial x} = 0$). For the calculation of the RANS and adjoint solution as well as the sensitivities TRACE is used. The optimization routine is controlled with Python scripts and the step size α_n is also calculated within a Python subroutine.

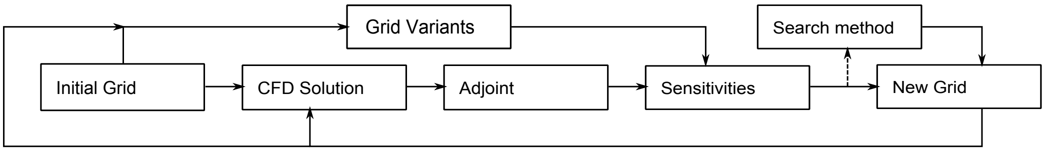

Figure 2.1: **Optimization flow chart**

2.2 Quasi-First-Order Method

The second optimization method used in this thesis is the quasi-first-order optimization method. It is developed as an alternative to the adjoint method which involves some challenges that are discussed as the results of the optimizations are presented. The proposed method is unrivaled in its simplicity, but naturally, it has its drawbacks as well.

The idea behind the method is not complicated, but it is still easier to grasp, if it is built up gradually. Therefore it will be demonstrated for the minimization of a simple, well-known quadratic function without additional constraints:

$$f(x) = x^2 \tag{2.12}$$

According to Eq. (2.9), besides an initial guess, which is set to $x_0 = 1$, we need a search direction S and a step size α. The search direction corresponds to the sign of the first derivative, so it is either 1 or -1. This parameter barely influences the optimization, as will be demonstrated.

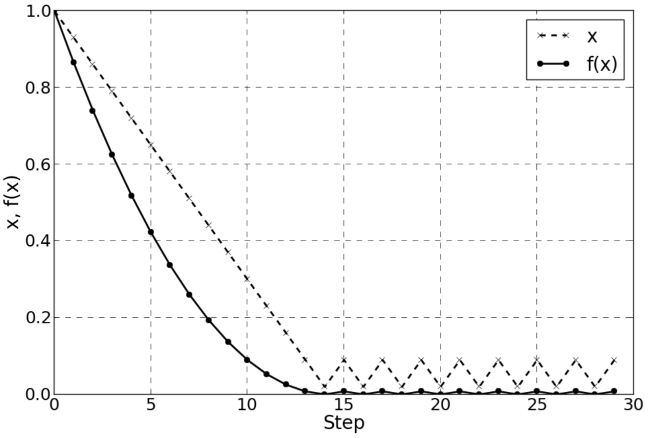

Figure 2.2: **First optimization of $f(x)$**

For the step size α initially a random magnitude is set. After setting the search direction $S = 1$ and the step size $\alpha = 0.07$, the function $f(x)$ is evaluated at $x_1 = 1 - 0.07 = 0.93$ and compared to the start value:

$$\begin{aligned} \texttt{Step 0}: \quad & x_0 = 1.00 \iff & f(x_0) = 1.0000 \\ \texttt{Step 1}: \quad & x_1 = 0.93 \iff & f(x_1) = 0.8649 \end{aligned}$$

As $f(x_1) < f(x_0)$, x_1 is closer to the optimum than x_0. In this case, this value will be excepted as the new solution of the objective function and the search direction is kept. Up to step 14 Fig. 2.2 shows the optimization in this form. The values at the iteration steps are marked with an x. The filled line represents the $f(x)$ values. At $n = 14$ x has a value of $x_{14} = 0.02$. For the next iteration (step 15) the evaluation of the cost function is:

$$\begin{aligned} \texttt{Step 14}: \quad & x_{14} = +0.02 \iff & f(x_{14}) = 0.0004 \\ \texttt{Step 15}: \quad & x_{15} = -0.05 \iff & f(x_{15}) = 0.0025 \end{aligned}$$

As $f(x_{15}) \not< f(x_{14})$, x_{15} is not accepted. In this case, the search direction for this step is reversed and $x_{15} = 0.02 + 0.07 = 0.09$ is assigned without evaluating the objective function again (even though the value of the objective function with $x_{15} = 0.09$ is inferior to both evaluations). If the optimization is continued in this manner the behavior shown in Fig. 2.2 results. The x value converges initially quite fast, and then it starts oscillating. This is an indication for the fact that the results are close to the optimum value.

So for the solution to converge to the optimum the step size must be gradually decreased

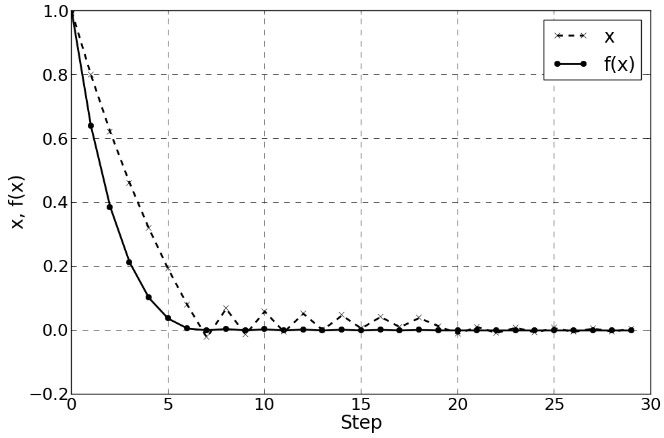

Figure 2.3: **Optimization of $f(x)$ with a scale factor**

close to the optimum. A scale factor Δ is introduced to Eq. (2.9) so that $\alpha_{eff} = \frac{\alpha}{\Delta^n}$ is the effective step size, where the iteration number n is the exponent of the scale factor.

$$x_{n+1} = x_n - \frac{\alpha}{\Delta^n} S. \tag{2.13}$$

The optimization of the function $f(x) = x^2$ with the step size $\alpha = 0.2$ and scale factor $\Delta = 1.12$ is shown in Fig. 2.3. It can be observed that the oscillations carry on, but with a steadily decreasing magnitude as the solution converges towards the optimum.

After a number of iterations the exponentiation of the scale factor Δ^n becomes so large that the change in the design variable is small. If the change in the design variable is too minor for it to influence the objective function, the optimization might be mistaken for converged. This can be prevented by introducing a limiter δ . Thus the final search/optimization method can be formulated as:

$$\mathbf{x}_{n+1}^{test} = \begin{cases} \mathbf{x}_n - \frac{\alpha}{\Delta^n}\mathbf{S}, & \frac{\alpha}{\Delta^n} \geq \delta \\ \mathbf{x}_n - \delta\mathbf{S}, & \frac{\alpha}{\Delta^n} < \delta \end{cases} \tag{2.14}$$

$$\texttt{if} \quad f(\mathbf{x}_{n+1}^{test}) < f(\mathbf{x}_n): \quad \mathbf{x}_{n+1} = \mathbf{x}_{n+1}^{test} \tag{2.15}$$

$$\texttt{elseif} \quad f(\mathbf{x}_{n+1}^{test}) > f(\mathbf{x}_n): \quad \mathbf{x}_{n+1} = \begin{cases} \mathbf{x}_n + \frac{\alpha}{\Delta^n}\mathbf{S}, & \frac{\alpha}{\Delta^n} \geq \delta \\ \mathbf{x}_n + \delta\mathbf{S}, & \frac{\alpha}{\Delta^n} < \delta \end{cases} \tag{2.16}$$

$$\texttt{else}: \quad \mathbf{x}_{n+1} = \mathbf{x}_n \tag{2.17}$$

This optimization method requires only 4 parameters to be determined: The first one is the

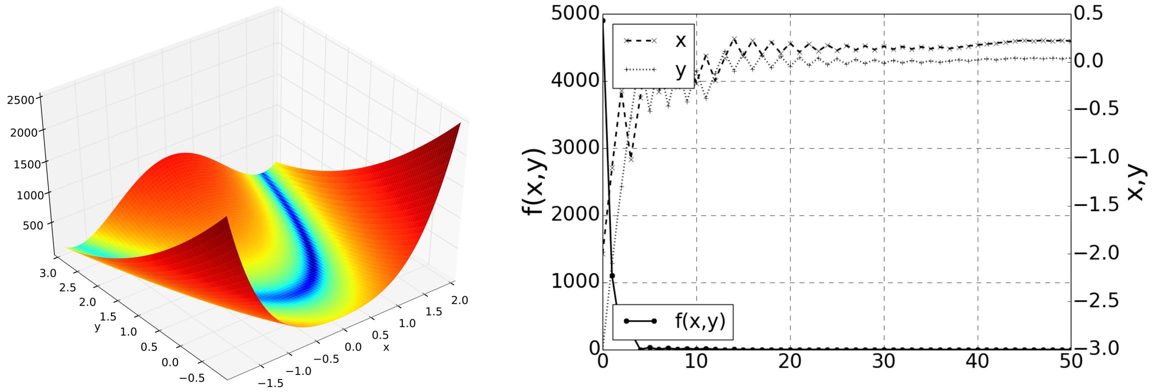

Figure 2.4: **Example of the development of the objective function during a CFD calculation**

search direction S. It is either -1 or 1, and the initial choice for its value doesn't have much influence on the optimization. The second parameter is the step size α. It should be chosen as large as possible; a bigger value will reduce the number of iterations necessary to approach the optimum. But it is advantageous to determine the step size together with the scale factor Δ which should be set to a value that reduces the effective step size to the value of the limiter δ within a convenient number of iterations. Finally, the limiter δ, should be set to a minimum value, which is given by either production tolerances or computational sensitivity.

One of the drawbacks of this method is that if the objective function has very small gradients around the optimum the routine may not find the optimum, but will converge to a value of the objective function very close to the optimum value. Such behavior can be observed with the Rosenbrock function. Fig. 2.4 (left) shows the Rosenbrock function

$$f(x,y) = (a-x)^2 + b\left(y-x^2\right)^2 \tag{2.18}$$

for $a = 1$ and $b = 100$ and the convergence of the optimization method on the right. The minimum function value is $f(x,y) = 0$ for $x = y = 1$. A position in the long and narrow valley, where the optimum is located, can be found effortlessly. But the optimization does not converge any further once it reaches the valley, as from any such position both search directions for each parameter individually do not improve the objective function value.

In optimal shape design using CFD there is generally more than one design variable and the cost function can't be evaluated as simply and fast as the function x^2. It involves computationally intensive methods to achieve a solution for $f(\mathbf{x}_{n+1}^{test})$. But the method described does *not really* require the exact value of $f(\mathbf{x}_{n+1}^{test})$. It is sufficient to determine if the value of the objective function is rising or falling with the new value of a design variable. This requires monitoring the development of the objective function during its numerical evaluation for a

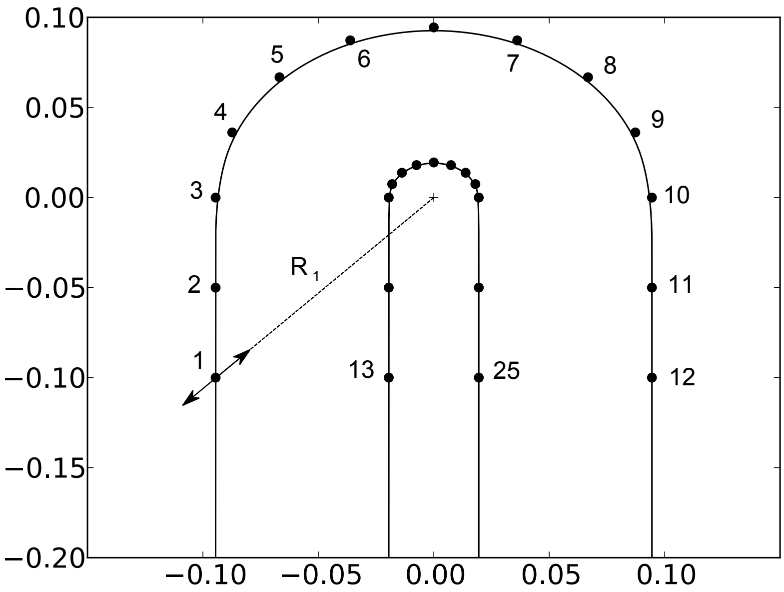

Figure 2.5: **Parametrization of the B-spline curves defining the U-bend**

design parameter, so that it can be discontinued as soon as the trend is visible. Developing criteria for the termination of the CFD evaluation for a parameter is the tricky part of the method.

The first test case that was studied is a U-bend which had been previously optimized by Verstraete et al. (2013). Its optimization with the quasi-first-order method has been reported on in Akin and Sanz (2015). The paper can be found in appendix A.5. The parametrization of the U-bend for one of the test cases presented in the paper is shown in Fig. 2.5. The U-bend is defined by two B-splines; an inner and an outer one. The control points on the U-bend constitute the design variables which are moved in the radial direction as implied in the figure. Figure 2.6 shows the development of the objective function after changing only one of these parameters in reference to its value in the last design . The second line (dotted line) is its summation over the iterations. The interpretation of the development of the objective function and its summation allows the development of a simple termination criterion. After a specified number of initial iterations has been performed (here 500 steps) the values of these two functions are compared in regular intervals. If they both have the same sign the solver run is terminated. Comparing these functions ensures that the value of the objective function has been constantly bigger or smaller than its previous value for a number of iterations. At the point where the criterion is met, the assumption is made that the influence of the parameter on the objective function can be correctly predicted. In Fig. 2.6 the calculations continues for a bit longer after the condition is met because after each time the criterion is evaluated a certain

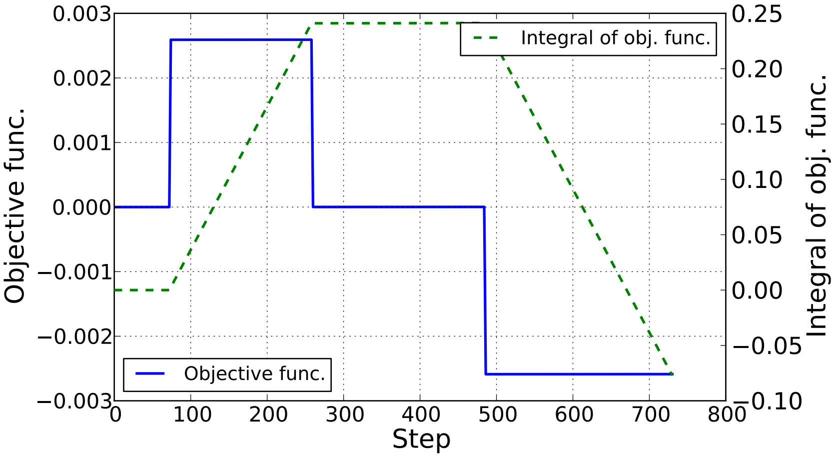

Figure 2.6: **Example of the development of the objective function during a CFD calculation**

time period is allowed to elapse. The criterion can be formulated as:

$$
\begin{aligned}
& \Delta f = f(\mathrm{x}_{n+1}^{test}) - f(\mathbf{x}_n): \\
\texttt{if} \quad & \mathrm{sign}(\Delta f) = \mathrm{sign}(\sum_i \Delta f): \quad i = 1..current\,iteration \\
& \quad \texttt{terminate CFD run} \\
\texttt{else}: & \\
& \quad \texttt{continue CFD run}
\end{aligned}
\tag{2.19}
$$

For the U-bend this proved sufficient to ensure that the influence of the parameters are correctly predicted. As the convergence behavior of CFD is generally case and solver dependent, it should be analyzed for every optimization to formulate a minimum number of initial iterations, or eventually also modify the termination criterion.

Chapter 3

Endwall Contour Parametrization

It is possible to modify the endwalls at the base and tip of the blade which are also referred to as hub and shroud endwall contours. Although the introduced methods can easily be used to modify both endwall contours, the optimizations discussed only optimize the hub endwall contour. It is initially defined with a meridional line creating an axisymmetric contour and the parametrization is realized by defining a cloud of points on the hub surface.

The definition of the contour using points on the hub is a very flexible method. In general, it allows the application of various parametrization methods such as using mathematical functions to define the contour, adding perturbations to a baseline contour using functions and also of course the method used in this thesis which will be explained in the following. These methods should only provide a sufficient number of points on the endwall contour for the subsequent generation of the surface with a B-spline.

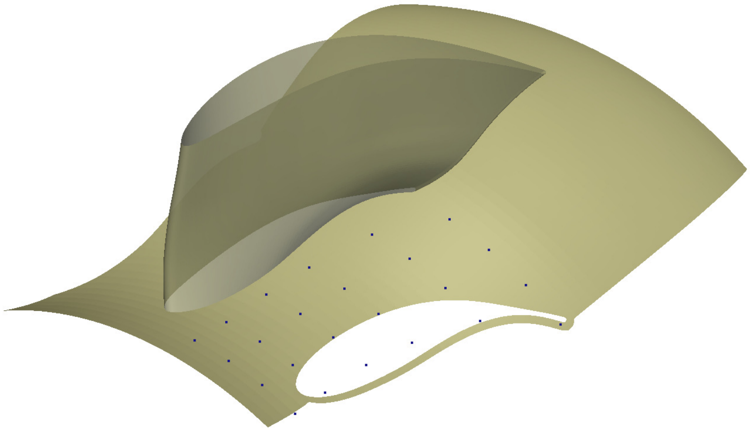

Figure 3.1: **Positions of the 24 points defining the hub contour**

In the optimizations performed the contour is manipulated by moving a number of points, which are initially placed on the axisymmetric contour, in the radial direction. In this manner, the surface can assume many shapes as well as form bumps and dents on the surface. In Fig. 3.1 the location of the points are shown for the 24 design variables which were also used in the presented optimizations. This is a simple yet effective method. An appropriate spacing and suitable surface fitting should ensure the smoothness of the contour.

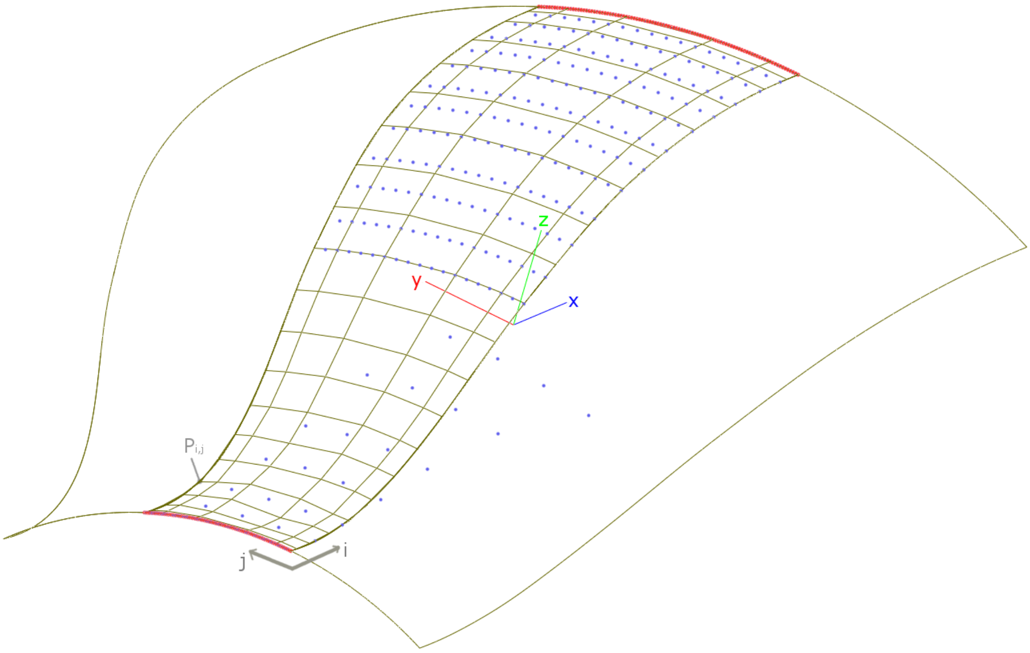

Figure 3.2: **Surface representation for contour fitting**

The points are fitted using a uniform B-spline surface which defines the geometry of the endwall contour:

$$r(x,y) = \sum_{i=0}^{m} \sum_{j=0}^{n} \mathbf{P}_{i,j} N_{i,k}(x) M_{j,l}(y) \tag{3.1}$$

with the basis functions N and M defined as

$$N_{i,0}(x) = \begin{cases} 1 & \text{if } x_i \leq x < x_{i+1} \\ 0 & \text{otherwise} \end{cases} \tag{3.2}$$

$$N_{i,k}(x) = \frac{x - x_i}{x_{i+k} - x_i} N_{i,k-1}(x) + \frac{x_{i+k+1} - x}{x_{i+k+1} - x_{i+1}} N_{i+1,k-1}(x) \tag{3.3}$$

$$M_{j,0}(y) = \begin{cases} 1 & \text{if } y_j \leq y < y_{j+1} \\ 0 & \text{otherwise} \end{cases} \tag{3.4}$$

$$M_{j,l}(y) = \frac{y - y_j}{y_{j+l} - y_j} M_{j,l-1}(y) + \frac{y_{j+l+1} - y}{y_{j+l+1} - y_{j+1}} M_{j+1,l-1}(y) \tag{3.5}$$

$\mathbf{P}_{i,j}$ is the input set of control parameters. The number of control parameters in the respective directions in space are defined by m and n. The value of m and n should be chosen to ensure approximately equal spacing in both directions on the surface. These parameters are not the design variables. Instead, they are the parameters that are adjusted for the best possible approximation to the design variables; ideally, the surface $r(x,y)$ includes the design variables. This fitting is fulfilled by minimizing the sum of squares of the deviation (least squares fitting).

The degree of the B-spline in the respective directions in space are defined by k and l and affects the smoothness of the surface. A higher order B-spline leads to smoother surfaces. But it may also cause a less accurate fitting. The smoothness of a third order B-spline was determined to be appropriate.

Figure 3.2 shows three sections of the TMTF. On the middle section the parametrization and definition of the hub endwall surface is demonstrated. The 24 blue points in the lower part of the picture are the design variables. The other blue points defined are not manipulated to ensure that the contour in this area is not changed, because this region does not actually belong to the TMTF. It is an extension to prevent a numerical problem that will be explained in Chapter 5. The red points at the inlet and outlet are defined to ensure that the inlet and outlet contours remain unchanged. The grid of B-spline points is defined by the number of control parameters of the B-spline which is set to 21 in the axial direction and 6 in the tangential direction.

The B-spline surface defines the hub endwall contour on which the boundary nodes of the grid should be placed. The grid is initially generated for an axisymmetric contour and consequently fitted on to this surface. These procedures have been implemented into the in-house mesher by Pieringer (2012).

Chapter 4

Computational Fluid Dynamics

Computational Fluid Dynamics is the analysis of physical processes involving fluid flow, heat transfer and associated phenomena by means of computer-based simulation. There are two main advantages of these simulations compared to physical experiments. They can elucidate details of a flow field in a way not achievable in a real laboratory experiment and they generally cost much less. It is also an essential part of the optimization chain as the evaluation of the objective function depends on the correct prediction and quantification of flow phenomena. These programs solve the Navier-Stokes equations which is the fundamental basis of CFD methods.

4.1 Navier-Stokes Equations

The Navier-Stokes equations are the mathematical statements of three fundamental physical principles. These principles are the conservations of mass, momentum and energy. The equations are derived by applying these principals to a suitable model of the flow. Different models of the flow lead to different formulations of the equations. Applying them to an infinitesimally small fluid element fixed in space leads to partial differential equations in conservation form. In the equations introduced belowρ is density, u_i are the velocity components, p is static pressure, T is temperature and e is the specific total inner energy.

The equation for the conservation of mass reads (using the Einstein notation):

$$\frac{\partial \rho}{\partial t} + \frac{\partial \left(\rho u_j\right)}{\partial x_j} = 0 \tag{4.1}$$

This equation is also referred to as the continuity equation. The first term represents the change of density over time and the second term represents the change of density due to the mass flow through the element boundaries.

The conservation of momentum is formulated as:

$$\frac{\partial\left(\rho u_i\right)}{\partial t}+\frac{\partial\left(\rho u_i u_j\right)}{\partial x_j}=-\frac{\partial p}{\partial x_i}+S_i^{vol}+\frac{\partial \tau_{ij}}{\partial x_j} \tag{4.2}$$

Similar to the continuity equation, the left-hand side accounts for the change of momentum over time and the change of momentum due to the momentum flow through the element boundaries. The first term on the right-hand side represents the effect of pressure forces on the surface, the second term accounts for external forces on the element such as gravitational forces which can be neglected in thermal turbomachinery. For Newtonian fluids the stress tensor τ of the third term is defined by the Stokes' law for viscous forces. This equation is then called the Navier-Stokes equation, which is a historically accurate notation, but modern CFD literature has extended this terminology to include the entire system of flow equations for the solution of a viscous flow, which includes the conservation of energy as well:

$$\frac{\partial\left(\rho e\right)}{\partial t}+\frac{\partial\left(u_i\rho e\right)}{\partial x_i}=\frac{\partial Q}{\partial t}+S_i^{vol}u_i-\frac{\partial q}{\partial x_i}-\frac{\partial\left(p u_i\right)}{\partial x_i}+\frac{\partial\left(\tau_{ij}u_j\right)}{\partial x_i} \tag{4.3}$$

The left-hand side accounts for the change of energy over time and energy flow through the volume boundaries. The first term on the right-hand side specifies the influence of internal heat sources and the second term defines the influence of volume forces. The third term accounts for the energy loss through heat conduction and is defined by Fourier's law:

$$q=-k\nabla T \tag{4.4}$$

The last two terms in Eq. 4.3 characterizes the rate of work done on an element due to surface forces, i.e. pressure and shear stress.

These equations represent 5 partial differential equations. The conservation of momentum represents three equations; one for each velocity component in 3 dimensional space. But there are 7 unknowns: ρ, u, v, w, p, T, e. Closing the system requires two more equations. The thermodynamic equation of state can be used to derive these additional relations and the assumption of an ideal gas mostly leads to results that are accurate enough for thermal turbomachinery, so that the following equations can be formulated with the gas constant R and the heat capacity ratio κ:

$$e=\frac{p}{\rho\left(\kappa-1\right)}+\frac{u_i^2}{2} \tag{4.5}$$

$$T=\left(e-\frac{u_i^2}{2}\right)\frac{\left(\kappa-1\right)}{R} \tag{4.6}$$

To solve this system of equations numerically a geometry is discretized in space using a mesh. The equations are then solved only at discrete points represented by the mesh. An accurate solution requires a very fine mesh and consequently a high computational expense which is not applicable in most cases. In academic research these methods called DNS (Direct Numerical Simulation) are being further developed. The necessity to reduce computational time leads to coarser girds which are not able to account for physical phenomena, such as turbulence, as the finer scales of the flow are not resolved. Turbulent velocity fluctuations can be considered by applying a time averaging to the Navier-Stokes equations and introducing turbulence models. This can be done by replacing the flow variables by their Reynolds decomposition which separates a variable into a mean value $\bar{x}$ (time averaged) and a fluctuating component x''. For a velocity component the relation is:

$$u_i = \bar{u}_i + u_i''$$

Applying Reynolds averaging to the conservation of mass leads to the following expression:

$$\frac{\partial \bar{\rho}}{\partial t} + \frac{\partial}{\partial x_j}\left(\bar{\rho}\bar{u}_j + \overline{\rho'' u_j''}\right) = 0 \tag{4.7}$$

The expression $\overline{\rho'' u_j''}$ disappears only for incompressible flow. The compressible flows it is an unknown that would have to be modeled.

As an alternative to Reynolds' method is the decomposition of the variables with mass weighted averaging. The most common one is the mass weighted averaging by Favre (1965). It decomposes the instantaneous value into a mass weighted mean value $\tilde{x}$ and a fluctuation component x'. For the velocity component the relation is:

$$u_i = \tilde{u}_i + u'_i, \;\; \tilde{u}_i = \frac{\overline{\rho u_i}}{\bar{\rho}}$$

Favre averaging is applied to the velocity and the thermal variables, whereas density and pressure are Reynolds averaged. In the case of incompressible flows Favre averaging and Reynolds averaging are identical. For compressible flows Favre averaging has the advantage that it leads to less additional unknowns in the equations. The equation for the conservation of mass after Favre averaging is:

$$\frac{\partial \bar{\rho}}{\partial t} + \frac{\partial}{\partial x_j}\left(\bar{\rho}\tilde{u}_j\right) = 0 \tag{4.8}$$

As this is the case for each conservation equation for compressible flows generally Favre averaging is applied to the Navier-Stokes equations which leads to the system of equations referred to as the Reynolds-averaged Navier-Stokes (RANS) equations. Considering only the momentum equation, the new form of this equation is:

$$\frac{\partial \rho u_i}{\partial t} + \frac{\partial \left(\rho u_i u_j\right)}{\partial x_j} = -\frac{\partial p}{\partial x_i} + S_i^{vol} + \frac{\partial \left(\tau_{ij} - \rho u_i' u_j'\right)}{\partial x_j} \tag{4.9}$$

The bar and tilde on the top of the time-averaged values has been ignored for ease of notation, so that the flow variables without the bar always refers to their time-averaged values in the following.

The Favre averaged equation for the conservation of momentum 4.9 includes the non-linear term $-\rho u_i' u_j'$ for the velocity fluctuations which is called the Reynolds stress tensor. The tensor in equation 4.10 is with $u_i' u_j' = u_j' u_i'$ symmetric. The diagonal elements represent the normal stresses and the rest the shear stresses.

$$-\rho u_i' u_j' = -\rho \begin{bmatrix} u'u' & u'v' & u'w' \\ v'u' & v'v' & v'w' \\ w'u' & w'v' & w'w' \end{bmatrix} \tag{4.10}$$

The computation of the Reynolds stresses introduces 6 additional non-linear partial differential equations to the RANS system of equations. The cost for such computations is still considered indefensible for most applications and analysis. An alternative is using linear or non-linear eddy viscosity models which assume isotropic turbulence in the free stream. Eddy viscosity models are based on an approach introduced by Boussinesq (1877) that correlates the Reynolds stresses to the averaged velocity profiles and a turbulent viscosity μ_t as shown in Eq. 4.11.

$$-\rho u_i' u_j' = \mu_t \left(\frac{\partial u_i'}{\partial x_j} + \frac{\partial u_j'}{\partial x_i} - \frac{\partial u_k'}{\partial x_k} \delta_{ij} \right) - \frac{1}{3} \delta_{ij} \rho u_k' u_k' \tag{4.11}$$

μ_t is the turbulent viscosity by analogy with the molecular viscosity μ, and requires additional equations to calculate. It is not a characteristic of the fluid but a parameter that depends on the flow condition.

Close to the wall the assumption of isotropic turbulence does not hold as the oscillations normal to the wall are damped causing the turbulent Reynolds number to sink and the molecular viscosity to become more significant. This results in a viscous sublayer where the transport equations for turbulence need to be adapted. The modifications introduced to encounter this requirement are called low-Reynolds number models.

4.2 Turbulence Model

Turbulence models make up one of the main uncertainties of numerical simulations. Broad trends can be captured by two equation eddy-viscosity models, but they are unable to predict the effect of streamline curvature on the turbulence structure (Wickerath (2009)). Consequently, secondary flows and flow separation further increases the uncertainty of CFD simulations. Still, due to their lower computational cost one-equation and two-equation models are employed widely in industrial applications. For the investigations performed in the context of this thesis the one-equation turbulence model by Spalart and Allmaras (1994) (SA) and the two-equation shear stress transport (SST) turbulence model by Menter et al. (2003) were used. As the final investigations presented in the thesis utilize the SST model it will be presented in following. It accounts separately for the free stream flow and near wall region by combining the advantages of the $k-\varepsilon$ and $k-\omega$ models which were introduced by Jones and Launder (1972) and Wilcox (1993), respectively. In the near wall region the $k-\omega$ model is used and for the rest of the flow the $k-\varepsilon$ model. To realize this a blending function F_1 is introduced which is equal to one near the solid surface and equal to zero for the flow domain away from the wall. Menter's formulation of the k and ω transport equations are derived through a transformation of the $k-\varepsilon$ model. The equations for the turbulent kinetic energy k and the turbulence frequency ω are as follows:

$$\frac{\partial(\rho k)}{\partial t}+\frac{\partial(\rho u_i k)}{\partial x_i}=P-\beta^*\rho\omega k+\frac{\partial}{\partial x_i}\left[(\mu+\sigma_k\mu_t)\frac{\partial k}{\partial x_i}\right] \tag{4.12}$$

$$\frac{\partial(\rho\omega)}{\partial t}+\frac{\partial(\rho u_i\omega)}{\partial x_i}=\alpha\frac{\omega}{k}P-\beta\rho\omega^2+\frac{\partial}{\partial x_i}\left[(\mu+\sigma_\omega\mu_t)\frac{\partial\omega}{\partial x_i}\right]+(1-F_1)CDT \tag{4.13}$$

$$\text{with}\quad CDT=2\rho\sigma_{\omega2}\frac{1}{\omega}\frac{\partial k}{\partial x_i}\frac{\partial\omega}{\partial x_i}. \tag{4.14}$$

and the isotropic production term:

$$P=\mu_t\frac{\partial u_i}{\partial x_j}\left(\frac{\partial u_i}{\partial x_j}+\frac{\partial u_j}{\partial x_i}\right)$$

The blending function F_1 is calculated from

$$F_1=\tanh\left(\left[\min\left(\max\left(\Gamma_1,\Gamma_3\right),\Gamma_2\right)\right]^4\right). \tag{4.15}$$

The arguments Γ_1, Γ_2 and Γ_3 are dependent on the wall distance y:

$$\Gamma_1 = \frac{500\mu}{\rho y^2 \omega}, \quad \Gamma_2 = \frac{4\rho\sigma_{\omega 2} k}{CD_{k\omega} y^2}, \quad \Gamma_3 = \frac{\sqrt{k}}{\beta^* \omega y} \tag{4.16}$$

$$\text{and} \quad CD_{kw} = \max(2\rho\sigma_{\omega 2}\frac{1}{\omega}\frac{\partial k}{\partial x_i}\frac{\partial \omega}{\partial x_i}, 1e^{-10}) \tag{4.17}$$

The equation for calculating the turbulent viscosity is

$$\mu_t = \min\left(\frac{\rho k}{\omega}, \frac{0.3\rho k}{SF_2}\right).$$

The blending function F_2 is obtained from

$$F_2 = \tanh\left(\max\left(2\Gamma_3, \Gamma_1\right)\right).$$

In addition to turning the term CDT on and off the model coefficients φ are also functions of the blending function F_1:

$$\varphi = F_1\varphi_1 + (1 - F_1)\varphi_2$$

φ_1 and φ_2 represent the coefficients of the $k - \omega$ and $k - \varepsilon$ models respectively:

$$\sigma_{k1} = 1.176,\ \sigma_{\omega 1} = 2.0,\ \ \kappa = 0.41,\ \alpha_1 = 0.5532,\ \beta_1 = 0.075,\ \beta^* = 0.09,\ c_1 = 10 \tag{4.18}$$

$$\sigma_{k2} = 1.000,\ \sigma_{\omega 2} = 1.168,\ \ \kappa = 0.41,\ \alpha_2 = 0.4403,\ \beta_2 = 0.0828,\ \beta^* = 0.09 \tag{4.19}$$

4.3 Transition Model

Transition phenomena can play an important role in turbomachinery. Yet the optimizations carried out have been performed without transition modeling. The influence of transition phenomena on the overall flow is investigated in two papers, given in the attachment. These investigations have not shown much influence of transition modeling on the agreement with experimental results or on the flow prediction other then in the boundary layer flow. For optimal shape design it may still play an important role. Finding a conclusion on its relevance for endwall contouring would require extensive investigations. Transition is not modeled in the optimizations to reduce computational effort and time. Still, as the investigations of the flow through the turbine in two papers include transition modeling the formulation of the required equations are presented here briefly.

The $\gamma - Re_\theta$ correlation-based transition model by Menter et al. (2004) with the modification introduced by Langtry and Menter (2005) is used for transition modeling. The model is based on two transport equations; one for the intermittency γ and one for the transition momentum thickness Reynolds number $\tilde{Re}_{\theta t}$. The transport equation for intermittency γ is defined as

$$\frac{\partial(\rho\gamma)}{\partial t}+\frac{\partial(\rho u_i\gamma)}{\partial x_i} = P_{\gamma 1}-E_{\gamma 1}+P_{\gamma 2}-E_{\gamma 2}+\frac{\partial}{\partial x_i}\left[\left(\mu+\frac{\mu_t}{\sigma_\gamma}\right)\frac{\partial\gamma}{\partial x_i}\right] \tag{4.20}$$

with the transition sources:

$$P_{\gamma 1}=F_{length}c_{a1}\rho S\left[\gamma F_{onset}\right]^{c_a};\; E_{\gamma 1}=c_{e1}P_{\gamma 1}\gamma \tag{4.21}$$

S is the strain rate magnitude and F_{length} is an empirical correlation that controls the length of the transition region. $P_{\gamma 2}$ and $E_{\gamma 2}$ are the destruction and re-laminarization sources:

$$P_{\gamma 2}=c_{a1}\rho|\Omega|\gamma F_{turb};\; E_{\gamma 2}=c_{e2}P_{\gamma 2}\gamma \tag{4.22}$$

where Ω is the vorticity and

$$F_{turb}=e^{-\left(\frac{R_T}{4}\right)^4}$$

The transition onset is controlled by the following equation:

$$F_{onset}=\max\left(F_{onset2}-F_{onset3},0\right)$$

with

$$\begin{aligned} F_{onset1} &= \frac{Re_v}{2.193Re_{\theta c}}; \\ F_{onset2} &= \min\left(\max\left(F_{onset1},F_{onset1}^4\right),2\right) \\ F_{onset3} &= \max\left(1-\left(\frac{R_T}{2.5}\right)^3,0\right); \end{aligned} \tag{4.23}$$

and

$$Re_v=\frac{\rho y^2 S}{\mu};\; R_T=\frac{\rho k}{\mu\omega} \tag{4.24}$$

$Re_{\theta c}$ is the critical momentum thickness Reynolds number where the intermittency starts to increase in the boundary layer.

The transport equation for the transition onset momentum thickness Reynolds number,

$\tilde{Re}_{\theta t}$, is:

$$\frac{\partial(\rho \tilde{Re}_{\theta t})}{\partial t}+\frac{\partial(\rho u_j \tilde{Re}_{\theta t})}{\partial x_j}=P_{\theta t}+\frac{\partial}{\partial x_j}\left[\sigma_{\theta t}\left(\mu+\mu_t\right)\frac{\partial \tilde{Re}_{\theta t}}{\partial x_j}\right], \tag{4.25}$$

where $P_{\theta t}$ is the source term designed to force the transported scalar $\tilde{Re}_{\theta t}$ to match the local value of $Re_{\theta t}$ calculated from an empirical correlation outside the boundary layer.

The model contains three empirical correlations; one for the transition onset momentum thickness Reynolds number $Re_{\theta t}$ (based on free stream conditions) as observed in experiments, one for F_{length}, which is a measure for the length of the transition zone and one for$Re_{\theta c}$, which defines the location where the model is activated. Two of these correlations were originally not published by Menter et al. for proprietary reasons. At ITTM empirical formulations of these correlations were found in extensive numerical studies and implemented into the LINARS code (Kelterer et al. (2011, 2010)). The correlations are:

$$\begin{aligned}
&\tilde{Re}_{\theta t} \leq 215 \Rightarrow \\
&Re_{\theta c} = 1.02\cdot\tilde{Re}_{\theta t}-35+\tanh\left(\frac{-\tilde{Re}_{\theta t}+138}{54}\right)\cdot 36 \\
&\tilde{Re}_{\theta t} > 215 \Rightarrow \\
&Re_{\theta c} = 155+\tanh\left(\frac{-\tilde{Re}_{\theta t}-215}{15}\right)\cdot 45
\end{aligned}$$

$$F_{length}=\min\left[250\cdot\exp\left(-\left(\frac{\tilde{Re}_{\theta t}}{130}\right)^{1.7}\right)+10,40\right] \tag{4.26}$$

After their publication, the correlations by Menter and Langtry (2009) were also implemented into the in-house solver. But the correlations used in this investigation are those developed at ITTM as these have shown better results with the in-house CFD-solver. Also, Kelterer et al. (2010) report on a strong code dependency of the correlations.

Finally the transition model interacts with the SST turbulence model by modification of the production and diffusion term of the k-equation

$$\frac{\partial(\rho k)}{\partial t}+\frac{\partial(\rho u_j k)}{\partial x_j}=\tilde{P}_k-\tilde{D}_k+\frac{\partial}{\partial x_j}\left(\left(\mu+\sigma_k\mu_t\right)\frac{\partial k}{\partial x_j}\right), \tag{4.27}$$

with

$$\tilde{P}_k=\gamma P_k;\ \tilde{D}_k=\min\left(\max\left(\gamma,0.1\right),1\right)D_k, \tag{4.28}$$

where P_k and D_k are the original production and destruction terms.

4.4 Flows Solvers

In the course of the investigations performed for the thesis two different flow solvers are used. One of them is the in-house solver LINARS. As it is an in-house code and the source code is available, necessary modifications can be implemented with ease. The other solver is TRACE which is developed by DLR's Institute of Propulsion Technology. TRACE is chosen for the optimizations with the adjoint method as an adjoint solver is already implemented.

The solvers use the same solution methods to a great extent. They both work with structured grids that are utilized in multiblock assignment. TRACE can also operate with unstructured grids. The solution method is based on the Reynolds-averaged Navier-Stokes equations in conservative form that are treated by a fully-implicit time-marching finite volume method. The non-linear set of equations is solved by a Newton procedure. The convective fluxes are discretized using Roe's total variation diminishing (TVD) upwind scheme, which is combined with van Leer's monotone upstream-centered scheme for conservation laws (MUSCL) to obtain second-order accuracy in space. The viscid flux vector at the cell interfaces is constructed in a central-differencing manner using Green's theorem. Convergence of steady-state simulations is improved by using a local time step based on a local stability criterion. LINARS also uses a multigrid V-cycle.

Detailed information on LINARS can be found in the references Gehrer (1998); Sanz et al. (1995) and Gehrer (2001) and for TRACE in Yang et al. (2006) and Simmendinger and Kügeler (2010).

Chapter 5

Test Turbine

The Institute of Thermal Turbomachinery and Machine Dynamics operates a unique transonic turbine test facility (TTTF) that allows the testing of transonic gas turbine stages in full scale. It is a continuously operating cold-flow open-circuit plant and is driven by an electrically powered compressor station with a power supply of 3 MW. TTTF allows testing of various configurations of turbines up to two stages and 800 mm diameter. Recently, a two-stage counter-rotating turbine has been investigated extensively on the test rig.

Fig. 5.1 shows the TTTF. It also comprises a three-stage radial brake compressor which is connected to the shaft of the high pressure turbine and delivers part of the overall flow for the test section. The main air flow driving the turbines is supplied from the compressor station. A total mass flow of up to $22\,\frac{\mathrm{kg}}{s}$ can be achieved. Inlet pressure is limited to 4.5 bar and inlet temperature can be regulated between 40°C and 185°C by cooling the air coming from the compressor station. Maximum rotational speed of the high pressure stage is limited to 11550 rpm. Depending on the operation mode and on the stage setup a maximum coupling power of 2.8 MW can be reached. The power output of the low pressure turbine is absorbed by a water brake and limited to 700 kW with a maximum rotational speed of 4500 rpm. Detailed information about the initial concept and construction of the test facility for single stage turbines can be found in Erhard and Gehrer (2000). Neumayer et al. (2001) describe its operational behavior. It was extended for testing two-stage two-shaft turbines by Hubinka et al. (2009, 2011).

The two-stage counter-rotating turbine was developed in the framework of the former European project DREAM (vali**D**ation of **R**adical **E**ngine **A**rchitecture syste**M**s) which was launched in 2008. Fig. 5.2 shows the two-stage turbine along with the meridional section of the TTTF. The air from the compressors is accumulated in the mixing chamber and then guided towards the inlet of the test section. The test section consists of a transonic high pressure stage, an S-shaped TMTF (turning mid turbine frame) and a counter-rotating shrouded

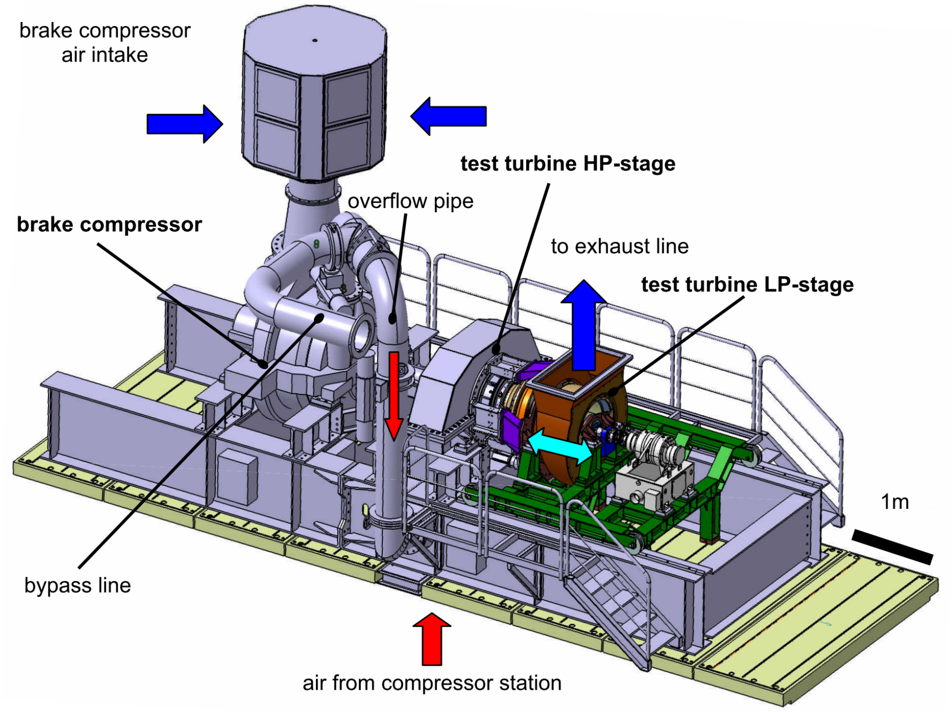

Figure 5.1: **Transonic test turbine facility (TTTF) (Hubinka et al. (2009))**

low pressure turbine. After the test section the flow passes by the support struts with a simple straight airfoil shape and a diffuser to recover pressure before entering the exhaust casing.

Two versions of the TMTF for this two-stage turbine were developed for testing in the DREAM project. The first one (C1) was designed by MTU Aero Engines. The other (C2) was designed by Volvo Aero (which was later acquired by GKN plc). The second one was designed to shorten the length of the TMTF, while still delivering the same inlet flow conditions to the low pressure rotor. C2 is 10 % shorter than C1. It also uses a different blade profile. And for the pressure loss to match that of the first design the hub of C2 was optimized (Wallin et al. (2011)) so that it has a non-axisymmetric contour.

The work accomplished in the course of this thesis involves mainly the configuration of the turbine utilizing the TMTF of the C2 design. Fig. 5.3 shows a closer look at the meridional section of this test turbine with the measurement planes for various investigations. The measurement plane A is at the inlet of the high pressure stage. Results from measurements at this location are used as inlet conditions for CFD calculations. Plane C is at the outlet of the high pressure rotor. Planes D and E are at the exit of the TMTF, where plane D is slightly inclined, due to sensor specific reasons. And finally plane F is at the exit of the low pressure rotor. The air flow is from left to right first going into the high pressure turbine where it is accelerated in circumferential direction by the vanes before entering the rotor. It leaves the rotor with a

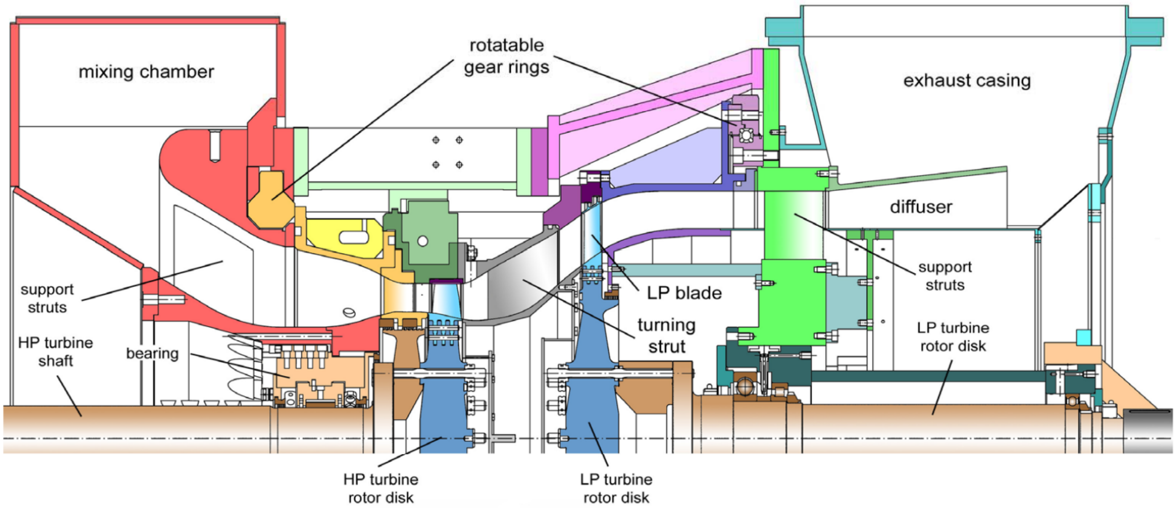

Figure 5.2: **Meridional section of the TTTF for the two-stage counter-rotating turbine**

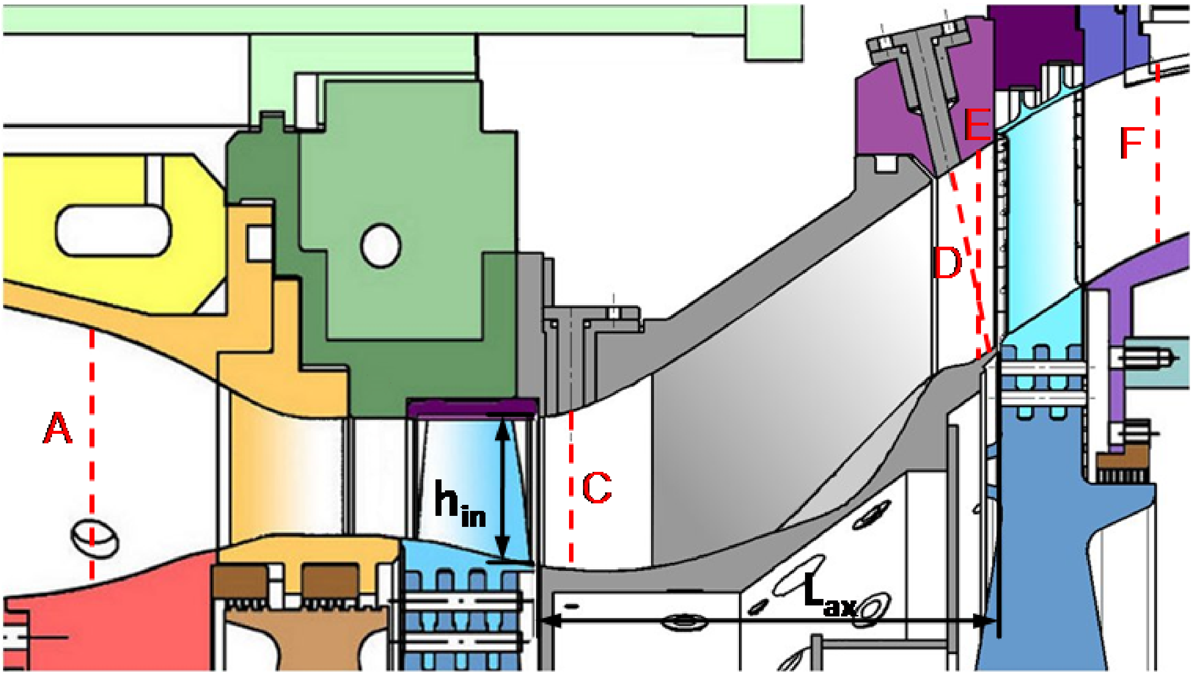

Figure 5.3: **Meridional section of C2 indicating the measurement planes**

		HPV	HPR	TMTF	LPR
Total pressure ratio		3		1.3	
Blade count		24	36	16	72
Reynolds number	10^6	2.38	1.1	1.86	0.46
Reduced rotational speed	$\frac{rpm}{\sqrt{K}}$		524.4		168.2

Table 5.1: **Operating conditions of the test rig**

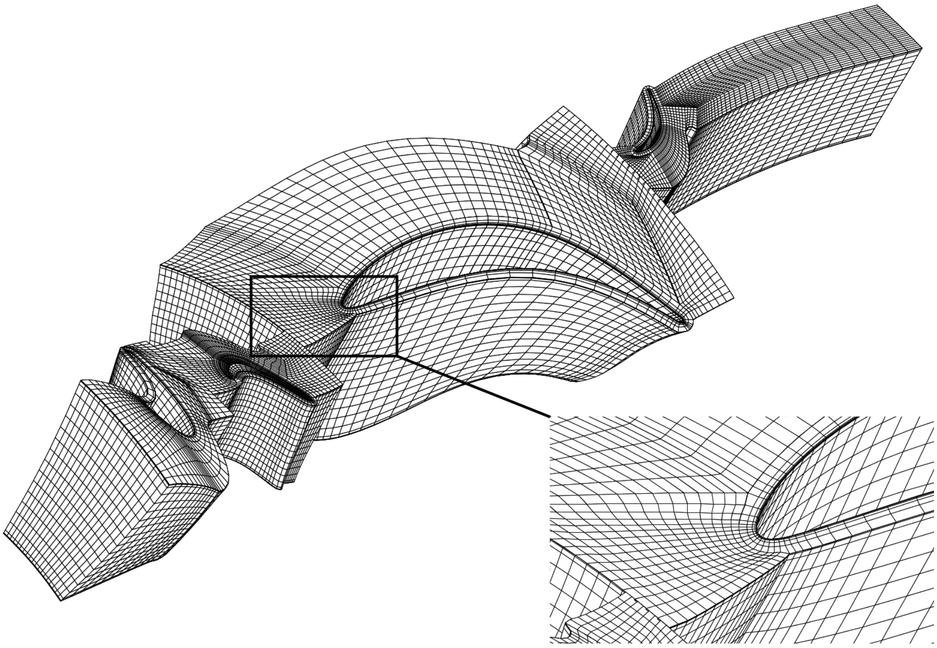

Figure 5.4: **Computational grid of the test turbine with every fourth node plotted**

negative swirl, which has a different intensity at the hub and shroud sections. Subsequently it is turned by the struts of the TMTF in the positive direction. The air then enters the low pressure rotor which rotates in the opposite direction of the high pressure rotor at about one third of its speed. Table 5.1 shows the main parameters of the test rig at design condition. The high pressure stage consists of 24 vanes and 36 blades and the low pressure stage consists of 16 struts and 72 blades. The entire setup with the high pressure turbine, TMTF and low pressure rotor has a periodicity of 90°.

Many publications from the institute can be found regarding various investigations on the test turbine. Detailed reports of investigations in the framework of the DREAM project were presented by Santner et al. (2011) and Santner (2013). In this thesis experimental investigations have not been performed. But the turbine has been investigated numerically and results have been compared with experimental results acquired in the course of the DREAM project at the institute.

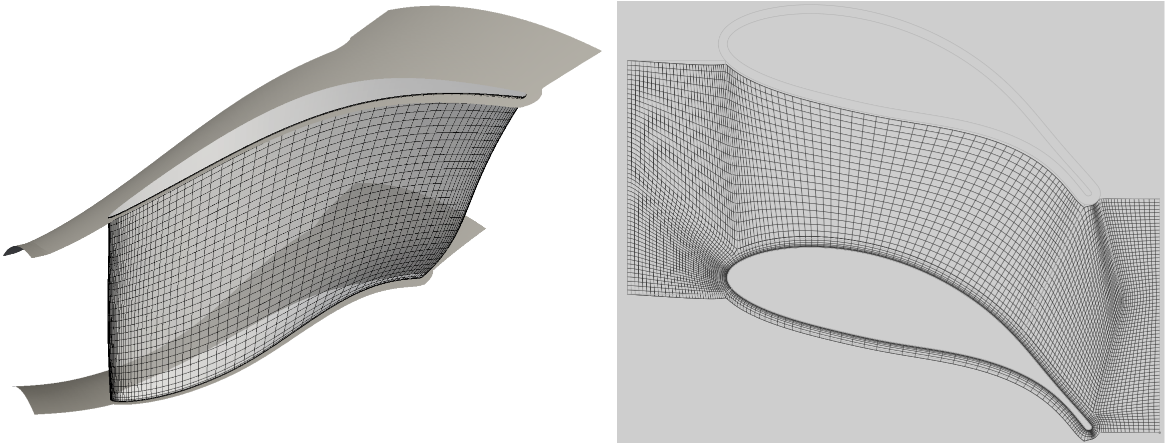

Figure 5.5: **Computational domain of the TMTF and the grid on the blade (left) and a 2D projection of the grid on the hub (right). Every 2nd node of the original grid is shown.**

5.1 Numerical Setup

The test turbine mesh is generated with the in-house mesher developed by Pieringer (2012). Fig. 5.4 displays one channel of the multiblock grid with the high pressure stator, high pressure rotor, TMTF and low pressure rotor. Each vane/blade row is comprised of 5 blocks and an O-type block encloses each blade. Only the high pressure rotor channel is meshed with 8 blocks as the tip leakage volume also has to be meshed. The high pressure stator is meshed with 1.05, the high pressure rotor with 2.15, the TMTF with 2.5 and the low pressure rotor with 2.2 million cells. The y^+ value at all walls is below 1. A quasi-3D mesh convergence study has been performed in the bachelor thesis of (Salzmann (2012)) to verify the mesh independence.

To improve the performance of the TMTF through contouring its hub endwall it is desirable to reduce computational cost by performing CFD simulations of only the TMTF. Fig. 5.5 shows this computational domain. On the picture to the left in Fig. 5.5 the meridional contour of the TMTF and the grid on the blade is shown. To the right a 2D grid is shown which is the conformal map of the grid at the hub onto a plane.

For the optimizations presented here the hub contour of the C2 TMTF design has been set to an axisymmetric hub (baseline) contour. The main loss mechanism in the TMTF with this axisymmetric baseline contour is flow separation at the trailing edge of the strut (which will be discussed in the results section). The back flow region extends till the TMTF exit. This proved to be a problem for the adjoint solver, so that the computational exit plane is placed further downstream to allow the separation region to reattach before reaching the exit plane. The resulting computational domain is shown in Fig. 5.6 in the upper picture. In the lower picture the conformal map of the grid at the hub onto a plane can be seen. The longer exit increases

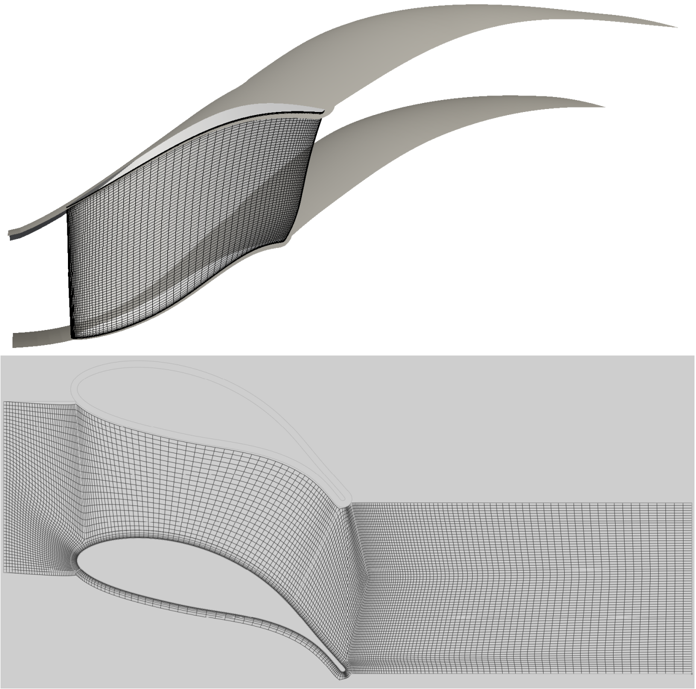

Figure 5.6: **Computational domain of the TMTF with elongated exit and the grid on the blade (upper) and a 2D projection of the grid on the hub (lower). Every 2nd node of the original grid is shown.**

the cell count by approximately 1.2 million resulting in a TMTF grid with 3.7 million cells. To increase computing speed by parallelization the block count has been increased to 18 by block splitting.

5.2 Boundary Conditions

Dirichlet boundary conditions are applied on the inlet and outlet boundaries. At the inlet a radial distribution of the total pressure, total temperature, and flow angles as well as of the turbulent kinetic energy and dissipation are specified. At the outlet the static pressure in the middle of the channel height is specified with a non-reflecting boundary and radial equilibrium. Periodic boundary conditions are used on the lateral boundaries of the computational domain.

The inlet and outlet boundary conditions are obtained from steady-state simulations of the two-stage turbine as shown in Fig. 5.4. Details of these simulations are presented by Akin and Sanz (2014b) (see Paper I in Appendix A). In this paper three simulations are compared which differ in their turbulence and transition modeling: One of the simulations uses the SA turbulence model, the second uses the SST turbulence model, and the third considers transition with the $\gamma - Re_\theta$ correlation-based transition model while using the SST turbulence model for turbulence modeling. The boundary conditions used for the analysis that are presented in the results section have been extracted from the second simulation using the SST turbulence model. Specifically, this means that the radial distribution specified at the inlet of the TMTF for the investigations in the thesis are the circumferentially averaged values at this location resulting from these previous investigations presented in the papers.

5.3 Computational Environment

The computations are performed on computer clusters of Graz University of Technology. Two different clusters are used mainly. The first one (called *I-Cluster*) is comprised of 15 nodes. 8 of these nodes have each access to 128 GB memory and 8 quad-core CPUs with a clock speed of 2.3 GHz and the other 7 nodes have each access to 256 GB memory and 8 octa-core CPUs also with 2.3 GHz clock speed. The second one (called *D-Cluster*) is comprised of 120 nodes, each one with access to 64 GB memory and 16 cores with a CPU clock speed of 2.0 GHz.

Chapter 6

Results

Before the optimization of the TMTF was performed, the two-stage counter-rotating turbine that was tested on the TTTF was analyzed first with steady-state CFD simulations (Akin and Sanz (2014b), see Paper I in Appendix A). Mainly, this analysis served to validate CFD modeling and turbulence modeling as well as to determine the necessity of transition modeling. Two simulations, one using the SA turbulence model and one using the SST turbulence model were performed. A third simulation considered transition modeling with the SST turbulence model. The investigations were able to determine good agreement of the CFD simulations with measurement results. The SST model marginally outperformed the SA model. Laminar to turbulent transition regions could be identified using transition modeling on the blade suction side surfaces. The flow structures and overall performance of the turbine was only minorly affected by transition modeling. The endwalls remained mostly turbulent, which is one of the most important results of the investigation with regard to the optimization problem. For a final statement to be made, optimizations with transition modeling would also have to be performed and analyzed, but these findings significantly reduce the importance of transition modeling for the optimization of the TMTF endwall.

The steady-state calculations were followed by time-accurate simulations with transition modeling (Akin and Sanz (2014a), see Paper II in Appendix A). The results were compared to the previously published steady-state analysis. The significance of time-accurate calculations or rather the inaccuracy of steady-state calculations using the mixing plane model was confirmed. The comparison to measurement results showed much better agreement for time-accurate simulations both in quantitative terms of flow variables and in secondary flow structures, which were inaccurate with steady-state calculations due to averaging at the mixing plane. Additionally, transition regions were significantly different in both simulations. The results show the importance of time-accurate simulations for accurate predictions of turbine flow. But as computational time is a major factor regarding modeling decisions for optimization, steady-state simulations without transition modeling were assumed to be sufficient initially.

The first optimization performed was essentially to demonstrate the correct application of the adjoint method with the TRACE solver (Akin et al. (2014), see A.3 in A). The TMTF total pressure losses were minimized using the steepest descent method with the major simplification of uniform inlet boundary conditions. The optimization successfully reduced the total pressure losses in 15 steps.

The second optimization eliminated the simplifications of the first optimization (Akin et al. (2015), see Paper IV in Appendix A). Radial distribution of total temperature, total pressure and flow direction were specified at the inlet. To ensure appropriate inflow at the LPR the optimization should be constrained with the yaw angle at the exit of the TMTF. But constrained optimization would require additional adjoint calculations. To avoid this, the TMTF was optimized with the low pressure rotor for isentropic efficiency. In this case, the outlet yaw angle of the TMTF doesn't have to be specified as a constraint, as an inconvenient inflow at the low pressure rotor would cause significant reduction of the efficiency. This optimization converged in 24 steps, improved the isentropic efficiency by 5.2 % and nearly fully eliminated flow separation at the trailing edge suction side. But a previously optimized hub endwall design of the same TMTF by Wallin et al. (2011) outperforms the newly optimized design by 1.1 %. It is then evident that a global optimum could not be reached. The previous optimization used a gradient-based method as well; the gradients were approximated by surrogate models. But also a different parametrization technique was used, which probably has a more significant effect on the result of the optimization than the different methodical approach. Although the optimization used by Akin et al. (2015) would also allow the same contour it does not converge to the same design, because the solution is trapped in a local optimum.

The optimization with the adjoint method was successful in that it improved the design by reaching a local optimum, as is generally the case with gradient-based optimization methods. The optimization technique has some flaws though that will be discussed in the following section as an optimization of the TMTF with an extended outlet section is analyzed in detail. These flaws significantly affect the reliability and stability of an adjoint-based optimization technique. Therefore it was desired to find an alternative method which is fast, efficient and easy to implement. This led to the development of the quasi-first-order optimization routine. A demonstration of the successful application of the method is presented in Akin and Sanz (2015) (see Paper V in Appendix A) which shows the optimization of a U-Bend initially optimized by Verstraete et al. (2013). Both optimizations achieve similar reduction of the total pressure loss in the channel with the U-bend.

The optimization of the U-Bend demonstrated that the proposed quasi-first-order optimization method works. But it does not compare directly to the optimization performed by Verstraete et al. (2013), because a different parametrization were used and because for the demonstration of the new method the calculations were performed two-dimensional. Direct comparisons with other optimization methods are necessarily to evaluate the performance of the new method.

In the following, the TMTF is first optimized with the adjoint method as well as the new method using the same grid, boundary conditions and parametrization technique. The grid and boundary conditions are presented in Chapter 5 and the grid is shown in Fig. 5.6. The parametrization technique with 24 parameters is introduced in Chapter 3 and shown in Fig. 3.1. The objective function of the following optimizations is the mass averaged total pressure ratio

$$I = \frac{(p_t)_{outlet}}{(p_t)_{inlet}} \tag{6.1}$$

which is maximized to ensure minimal pressure loss. In the following section (6.1) the optimization of the TMTF with the adjoint method is discussed and in the next section (6.2) the optimization of the same test case with the quasi-first-order method is discussed.

6.1 Optimization Using the Adjoint Method

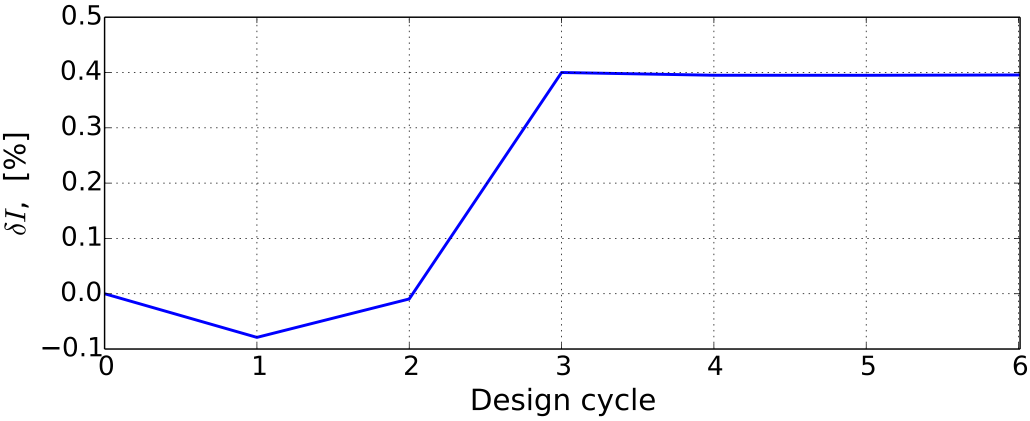

Figure 6.1: **Development of total pressure ratio in reference to its initial value**

The optimization using the adjoint method for gradient evaluation was performed using the TRACE solver. It required a conveniently small number of design cycles to reach the optimum of the configuration. The development of the total pressure ratio can be viewed in Fig. 6.1. The first design cycle results in a reduction of the total pressure ratio which could either emanate from an inaccurate prediction of sensitivities or an interdependency of the parameters. The subsequent two cycles improve the total pressure ratio resulting in a total increase of 0.4 %. After the third design cycle the optimization is already converged.

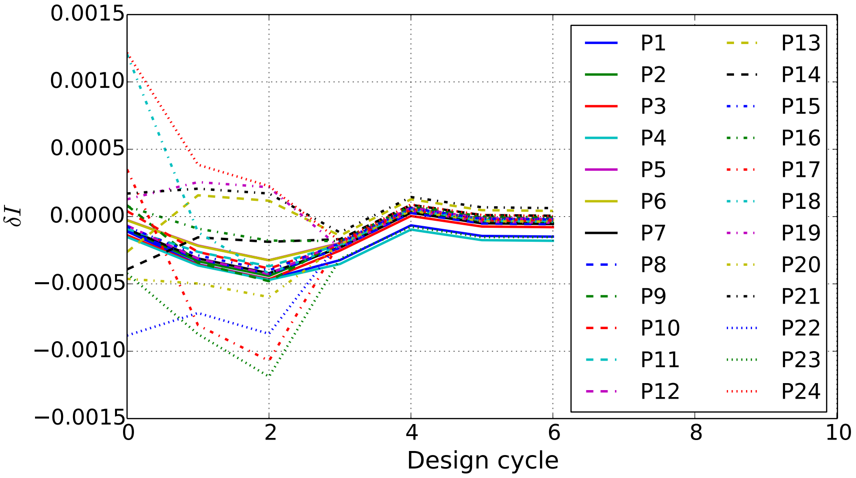

Figure 6.2: **Influence of each parameter change on the total pressure ratio**

Fig. 6.2 shows the influence of each parameter change on the mass averaged total pressure ratio during the optimization. The values are calculated with a constant deviation of 2 mm for a parameter at every design cycle, which is based on preliminary studies with the solver to achieve a reliable sensitivity analysis. The highest sensitivities are observed in the initial design cycle as expected and a consecutive decrease of the sensitivities occurs in the following cycles. Some parameters are an exception to this statement, displaying higher sensitivities at design cycle 1 and 2 (e.g. P14, P17, P19, P23) compared to the initial value of their sensitivity. But the general trend is consistent and very minor changes are observed after the third design cycle such that also the sensitivities plot confirm the achievement of an optimal solution.

It is interesting to take a closer look at the sensitivities and compare them with evaluations using the finite difference method (FDM), as it provides a more reliable sensitivity analysis. These values are calculated using forward finite differences using the same deviation of 2mm. Fig. 6.3 displays the sensitivities of all parameters calculated with the adjoint method and FDM for all the design cycles. For the initial condition (design cycle 0) it is evident that the agreement is quite poor. 9 parameters exhibit opposite signs and the others show a large deviation in magnitude. The same analysis for design cycle 1 reveals a slightly better agreement of the sensitivities. Now only 5 parameters have conflicting signs. The discrepancy in magnitude of most parameters is still significant. Design cycle 2 is not much better in this respect. But with the 3rd design cycle the sensitivities start matching much better. In design cycle 3 there is only a small offset between the sensitivities calculated with FDM and the adjoint method. The sensitivities are in general much smaller than in the previous steps; in fact,

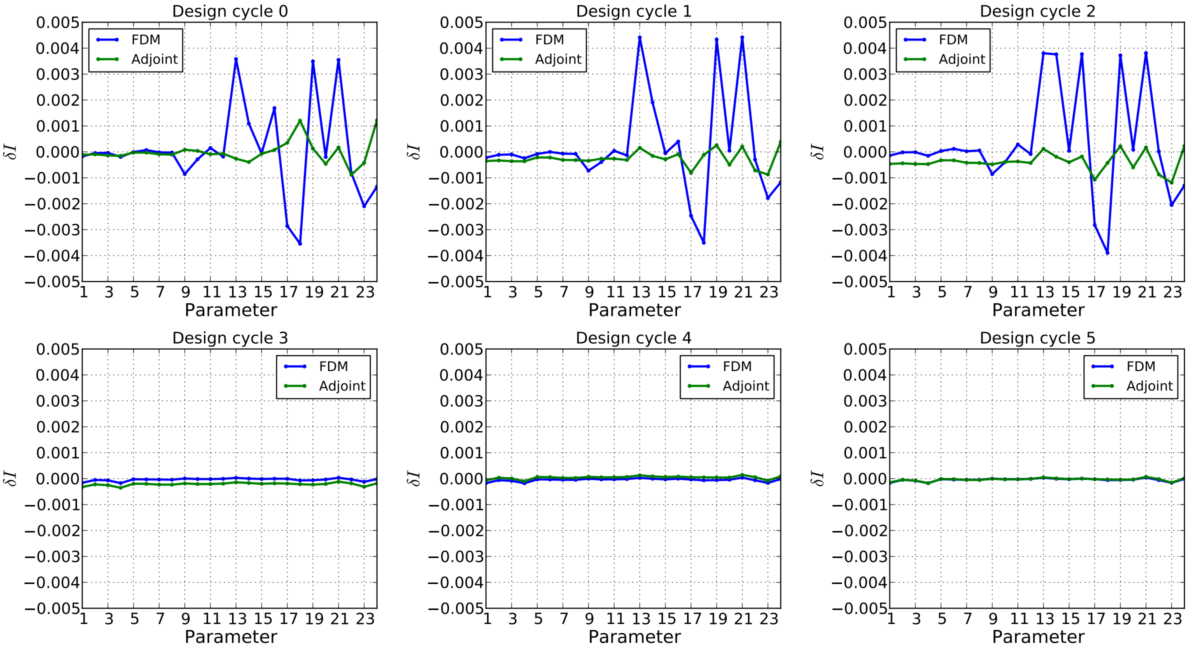

Figure 6.3: **Comparison of sensitivities calculated with FDM and adjoint method for the design cycles**

they are nearly zero. In the next two design cycles the agreement is improved with the offset becoming smaller. And at design cycle 5 there is nearly a perfect match.

Design cycle	0	1	2	3	4	5
Adoint residuals	6.1x10^{-2}	9.0x10^{-2}	9.9x10^{-2}	9.3x10^{-4}	9.6x10^{-4}	8.2x10^{-4}

Table 6.1: **Residuals of the adjoint solution for the design cycles**

The residuals of the adjoint solver explain the behaviour of the sensitivities. In Table 6.1 the attained residuals are listed. At design cycles 0, 1 and 2 the residuals are in the order of 10^{-2} and at design cycles 3, 4 and 5 they are in the order of 10^{-4}. It is then evident that residuals of the order of 10^{-4} have to be achieved for the sensitivities to be calculated correctly with the adjoint method. But it was not possible to reduce the residuals of the first three design cycles. As the settings of the solvers were unchanged for the different design cycles, the flow characteristics of the first three designs must be unfavorable for the adjoint solver. As will be discussed later, the initial design has a flow seperation region that is eliminated after the 3rd design cycle. Then, the adjoint solver is able to reduce the residuals to below 10^{-3}.

Fig. 6.4 shows the resulting contour after the 5th design cycle. The changes to the axisymmetric contour are rather small with a magnitude of around 1 mm. The contour representation shows the change in the radius with respect to the baseline design where the red colour indicates an increase in the radius (bump) and the blue colour a decrease in the radius (dent).

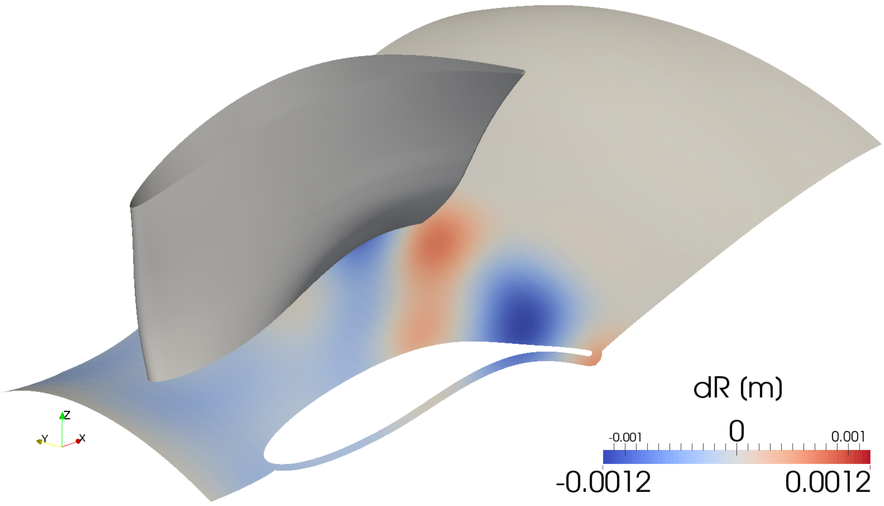

Figure 6.4: **New contour after the 5th design cycle**

Shortly after the inlet the radius is reduced nearly up to midchord leading to a larger flow area. On the pressure side two bumps are formed; one at mid chord and the other at the trailing edge. Similarly, on the suction side the reduction of the radius is followed by an increase and a subsequent decrease. Downstream of approximately mid chord, the bumps and dents on the suction and pressure sides are aligned perpendicularly to the streamline.

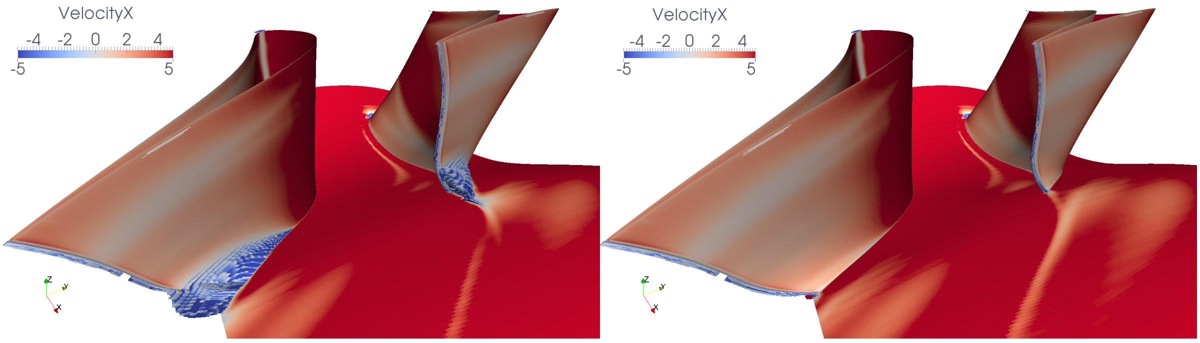

Figure 6.5: **Axial velocity component of the baseline (left) and new (right) design showing flow separation regions**

The main secondary flow structure that can be observed in the baseline design of the TMTF is flow separation on the suction side close to the trailing edge. This phenomenon is visualized in Fig. 6.5 on the left for the baseline design. The colouring represents the axial velocity and the scale is set between $-5\,\frac{\mathrm{m}}{\mathrm{s}}$ and $5\,\frac{\mathrm{m}}{\mathrm{s}}$ to better visualize positive and negative axial velocity values. As this is an axial machine negative axial velocity indicates backflow regions with flow separation. The negative velocities that are not adjacent to a contour are also visualized to give a sense of the volume of the backflow region. This flow separation is not only a source of energy loss through turbulence and entropy generation, it also causes significant deviations from the intended inlet flow yaw angle for the following low pressure rotor. On the right in Fig. 6.5 the same visualization is replicated for the new design: the flow separation region is fully eliminated.

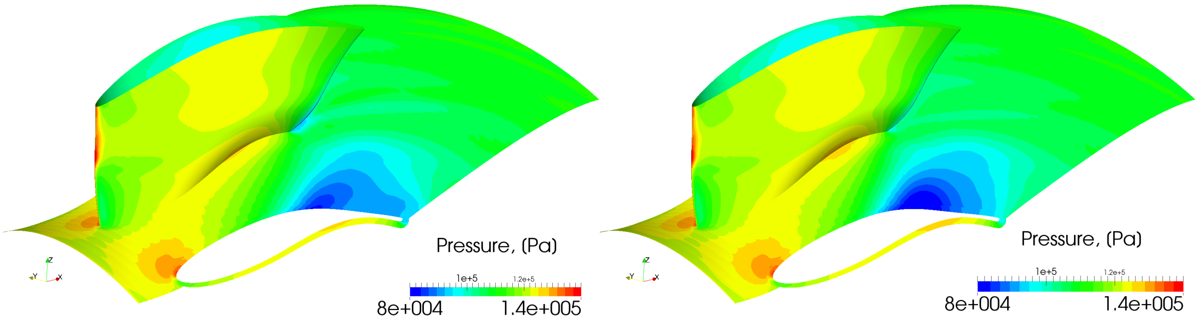

Figure 6.6: **Contour plots of pressure on the hub and blade walls for the baseline (left) and optimized (right) endwall contours**

The flow separation is caused by a positive pressure gradient. It is shown in Fig. 6.6. The aft loaded design of the blade has a sharp turning after mid chord which creates a low pressure region on the suction side. The lowest pressure value is shortly upstream of the trailing edge after which the pressure starts rising creating a positive pressure gradient. It can be observed in the figure on the left for the baseline design. The boundary flow can't overcome the pressure increase to follow the contour and separates. The same pressure contour plot is shown on the right for the new design which actually shows an increase in the pressure drop and the consequent adverse pressure gradient.

The Mach number distribution and flow propagation shown in Fig. 6.7 explain how the flow separation is subdued inspite of the increased pressure gradient. The vectors shown are velocity vectors which help clarify the flow profile and indicate clearly where the flow separation occurs. A comparison of the baseline and new design shows an increase of the Mach number just before the separation point; the momentum of the flow is increased to overcome the pressure increase without separating from the strut and hub contour walls.

The flow condition of the axisymmetric and new contours are shown in Fig. 6.8 downstream of the strut. This location is where the actual exit of the TMTF would be (slightly downstream of plane E in Fig. 5.3) if the computational domain had not been extended for numerical reasons. The viewing direction is from downstream of the flow. Visualized are the contour plots of the total pressure coefficient $c_{p_t} = \frac{2(p_t - p_{inlet})}{\rho_{inlet}|\mathbf{V}|^2_{inlet}}$, normalized yaw angle $\alpha_n = \frac{\alpha}{C}$ and entropy. The yaw angle is defined as the angle between the tangential velocity v_t and the

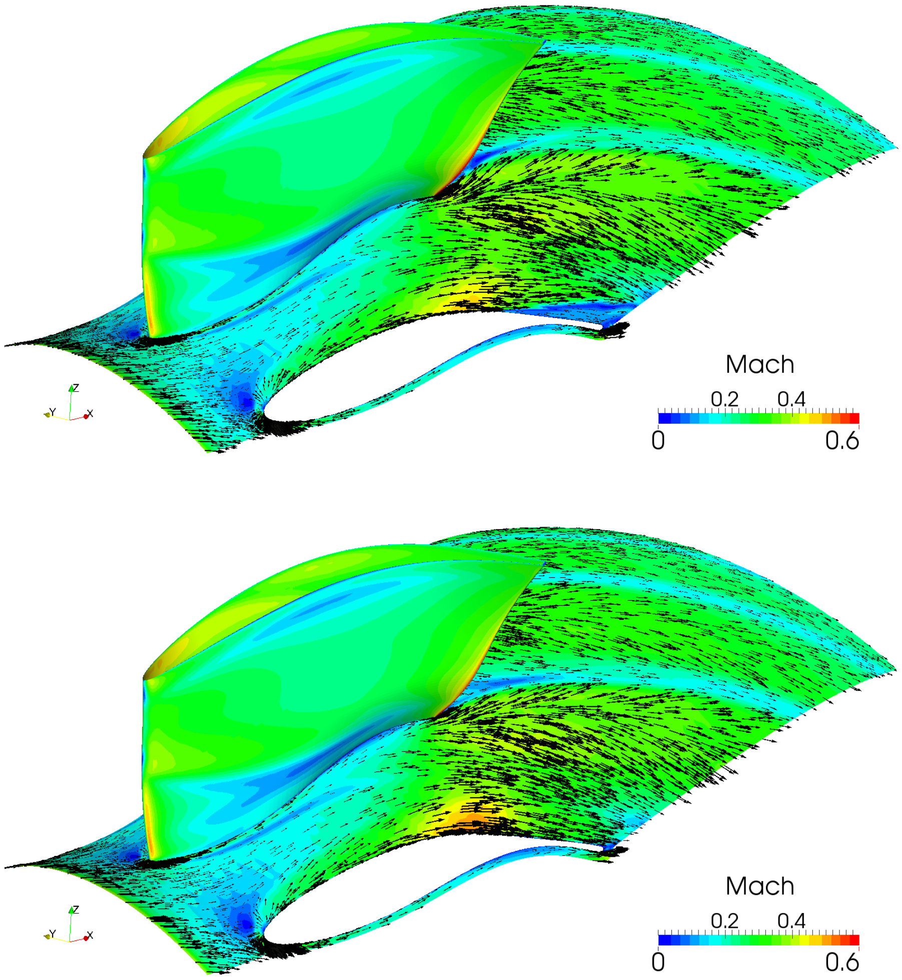

Figure 6.7: **Flow propagation on the hub contour of the baseline (above) and new (below) designs**

axial velocity component u:

$$\alpha = \arctan\left(\frac{v_t}{u}\right) \tag{6.2}$$

A positive turning is in the counter-clockwise direction when an observer is looking at the machine from the exit. Consequently, the TMTF creates a positive yaw angle.

In the plot of the total pressure coefficient of the axisymmetric contour (on the left in Fig. 6.8) a green region is noticable which is mainly because of the shed vortices from the trailing edge. Close to the shroud this region extends slightly due to the interaction with the upper passage vortex. Close to the hub endwall in this lower pressure region there is a zone with an even lower total pressure caused by the flow losses from the separation region. On the right the same contour plot is shown for the new contour. The low pressure region due to flow separation is eliminated. This trend is similar for the plots of the normalized yaw angle and entropy. Near

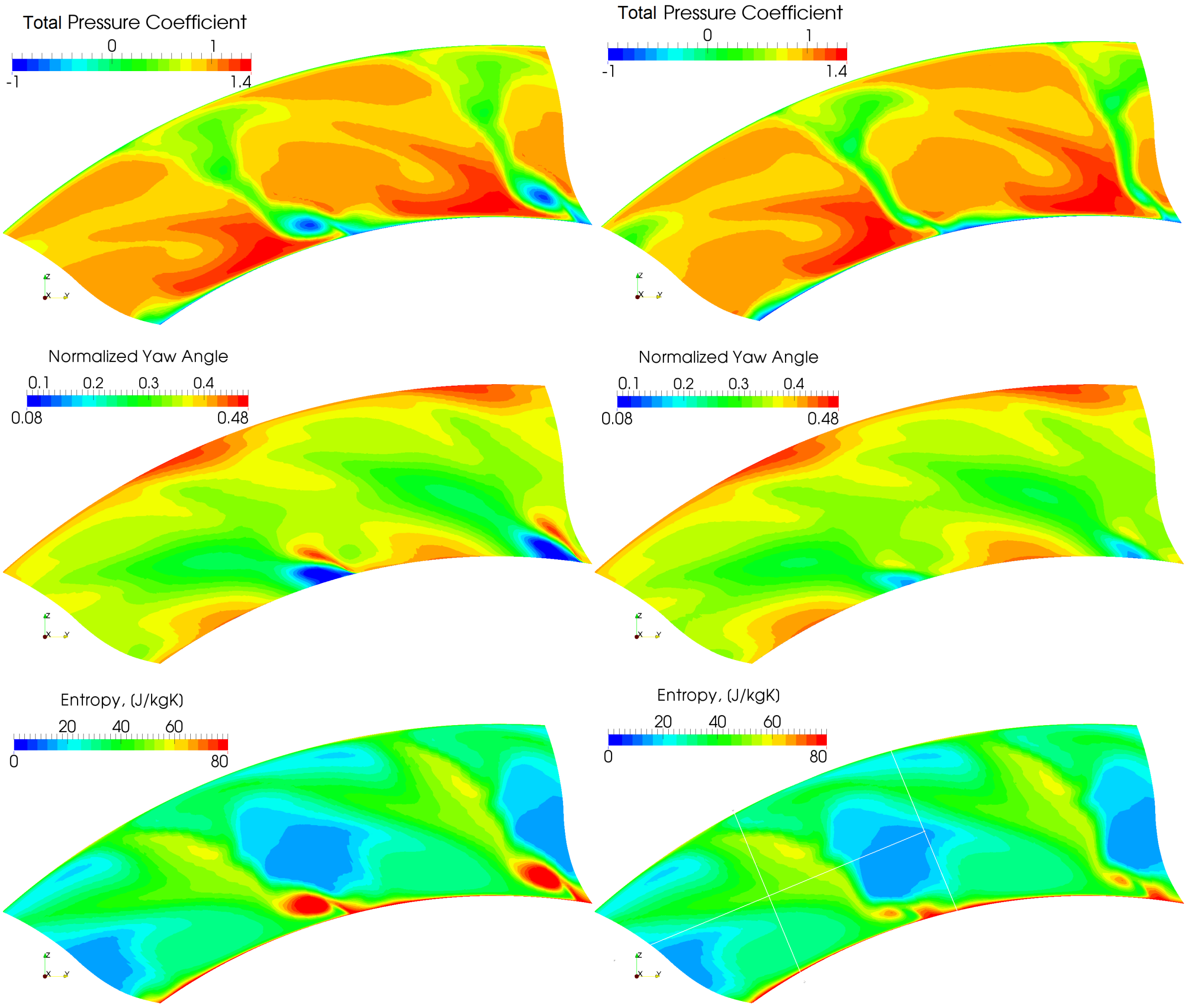

Figure 6.8: **Contours of the total pressure coefficient, normalized yaw angle and specific entropy at the exit of the TMTF (plane E) of the baseline (left) and optimized (right) designs**

the hub the flow separation creates a region with low turning as can be seen on the contour plot of the normalized yaw angle. It is again mostly eliminated by the new contour. The other irregularities in the yaw angle are partly caused by the inlet flow profile which is influenced by an unshrouded rotor with tip leakage, and other secondary flow phenomena in the TMTF. These were discussed in previous papers, e.g. Akin and Sanz (2014b); Spataro et al. (2012). Finally, the entropy contour plot enables us to gain an impression of the loss mechanisms and their magnitude. The strongest negative influence is caused by the flow separation, which is again eliminated with the new contour.

Fig. 6.9 presents the circumferentially averaged flow at the exit of the TMTF (plane E) for the optimized contour in comparison with the axisymmetric contour. The total pressure coefficient is increased below 0.35 span through the elimination of the separation region. The

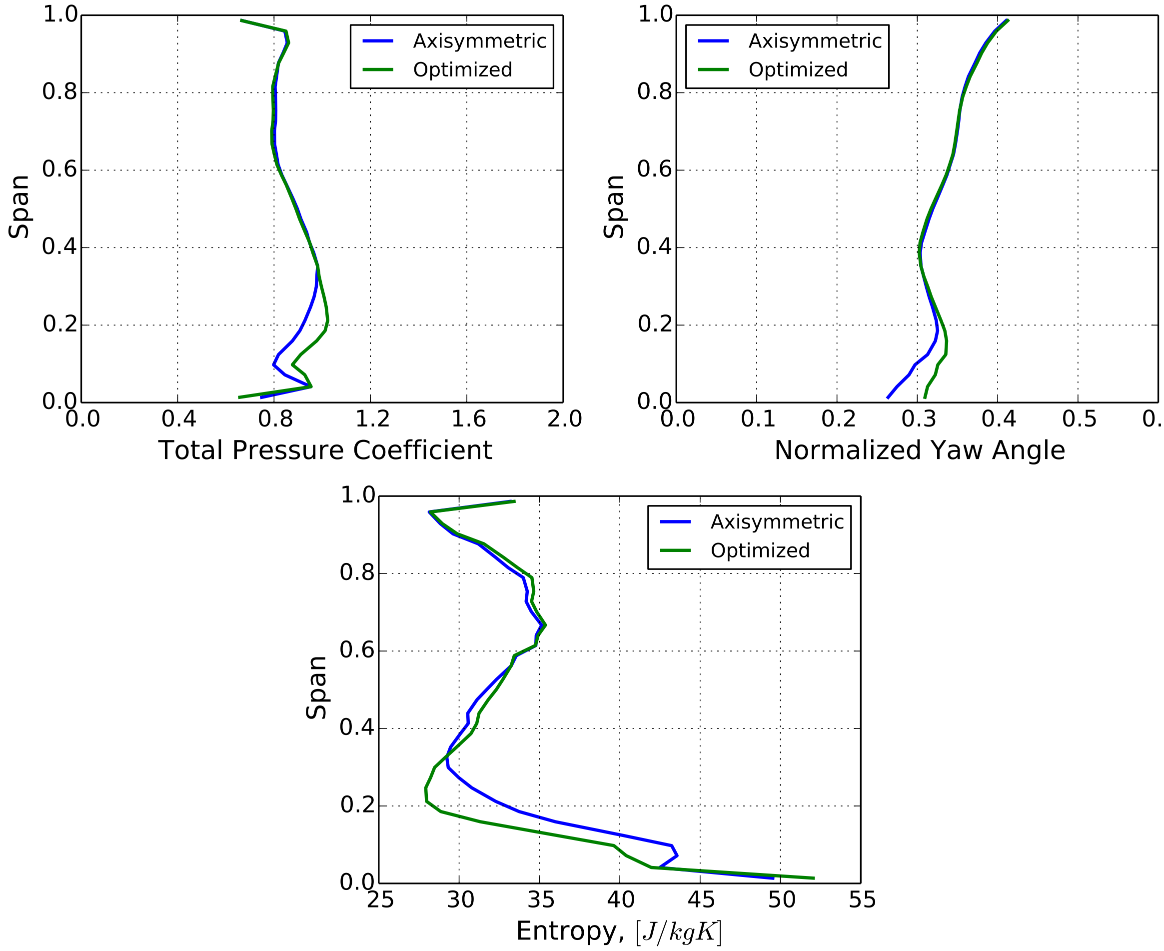

Figure 6.9: **Circumferentially averaged total pressure coefficient, normalized yaw angle and specific entropy at the exit of the TMTF**

break down of the yaw angle below 0.2 span is also reduced. And similarly, entropy production is reduced below 0.35 span. Between 0.35 and 0.9 span there is a slight increase in the entropy which reveals a slight increase in the pressure losses in this region.

The number of iterations required for convergence at each step of the optimization is shown in Table 6.2. On the D-Cluster using 10 processors the CFD solver required approximately 6.7 s wall time and the adjoint solver required 10.5 s wall time for one iteration. This results in a total wall time of 88 hours for the optimization with 5 design cycles. For example, one design cycle with 2000 iterations of the CFD solver and 5000 iterations of the adjoint solver would require 18.3 hours.

	S0	S1	S2	S3	S4	S5	Total iterations	Total wall time
CFD	3794	2294	1893	2430	1917	1440	13768	92245.6 s
Adjoint	5000	5000	5000	4969	1440	-	21409	2284794.5 s

Table 6.2: **Time requirement of the adjoint optimization**

6.1.1 Performance of the optimized contour with the low pressure rotor

The improvement of the flow with the suppression of separation highlights the success of the optimization routine. But to compare its performance with previous optimizations and the original Volvo contour, a CFD simulation of the TMTF with the contoured endwall and succeeding low pressure turbine is performed using mixing planes at the blade row interface.

Fig. 6.10 presents the circumferentially averaged values of the total pressure coefficient, normalized yaw angle and entropy at the exit of the TMTF. On the plots of the total pressure coefficient and normalized yaw angle in Fig. 6.10 experimental results of the Volvo contour are also incorporated. The good agreement of the simulation results with the measured values demonstrates the reliability of the CFD results.

The differences of these results in comparison to Fig. 6.9 are due to upstream effects caused by the low pressure rotor. The improvement achieved by the optimization can be observed more clearly. The increase of the total pressure is from the hub up to 0.7 span, with the exception at around 0.15 span. Similarly the yaw angle is increased between the hub and 0.7 span, creating a more homogeneous outflow angle. And the entropy is decreased between 0 and 0.7 span. But there is also an increase between 0.7 and 0.9 span.

Results from previous optimizations are also shown in this figure to demonstrate the quality of the optimization. Akin et al. (2015) (see Paper IV in Appendix A) performed an optimization of the TMTF in this configuration (with the low pressure rotor). The results from this optimization are also shown in Fig. 6.10. Both optimized contours perform very similarly. Careful observation reveals slight improvements of the current optimization in comparison to the previous one. These improvements can be observed for the the total pressure coefficient at about 0.2 span, for the yaw angle below 0.15 span and for the entropy below 0.25 span . But aslo, the contour optimized by Akin et al. (2015) shows a reduction of the entropy also at around 0.9 span which is not seen in the currently optimized contour. All in all, these minor changes result in a better performance of the low pressure stage with the newly optimized contour. The increase of the isentropic efficiency is by 0.6 % in comparison to the previously optimized contour (Akin et al. (2015)), which achieved an improvement of 5.2 % compared to the baseline design. So, the new contour presented here improves the baseline design by 5.8 %. Also Wallin et al. (2011) optimized the TMTF hub endwall contour using a gradient based optimization method and a different parametrization technique resulting in

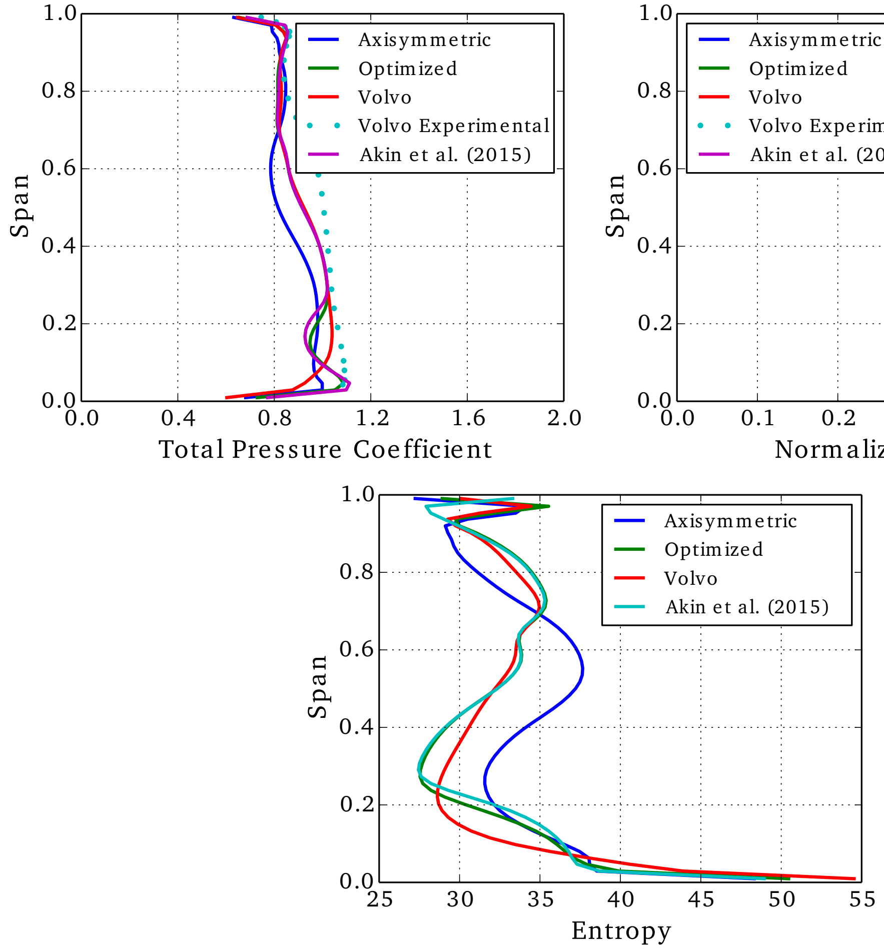

Figure 6.10: **Circumferentially averaged total pressure coefficient, normalized yaw angle and specific entropy at the exit of the TMTF**

the Volvo contour. They also applied a constraint on the objective function to achieve a more homegenous outflow, which is probably the main reason for the more uniform yaw angle and reduced total pressure loss between 0 and 0.2 span. Finally, this results in the higher isentropic efficiency of the Volvo contour which is 6.3 % better than that of the axisymmetric contour.

Achieving a better isentropic efficiency of the stage with the optimization method presented (a value closer to or exceeding the performance of the Volvo contour) might be possible by using a pseudo-objective function to constrain the yaw angle, so that it fits better to the LPR. Although using a constraint might seem counterproductive, it is not. The axisymmetric contour performs very poorly in terms of a uniform yaw angle. So an additional term yaw angle constraint in the objective function would help in achieving a better yaw angle distribution. And as the increase of the objective function, which is the total pressure ratio, also improves the yaw angle, the additional contraint could have less of a constrainig effect than a positive effect on the efficiency of the stage. As the adjoint method would require the implementation of the adjoint of this pseudo-objective function such an optimization is not performed.

6.2 Optimization Using the Quasi-First-Order Method

In a first step the optimization will be performed on a coarser grid to analyze the method. Then a finer grid (same grid as for the presented adjoint method) will be used to optimize and then analyze the flow changes. For these optimizations the LINARS solver is used.

6.2.1 Optimization with a coarser grid

As stated before, during the discription of the method, it suffices for the optimization to determine if a certain shape change has a positive or negative influence on the objective function. This requires an analysis of the response of the objective function to parameter changes. It must be determined when the evaluation of the sensitivity of a paramter can be stopped, such that the direction of the paramter's influence can be correctly predicted with the minimum number of CFD iterations.

Fig. 6.11 shows the convergence of three chosen parameters. In the plots the green line is produced by continuing the calculation of the converged, initial CFD solution without changing any parameters. A converged solution does not necessarily lead to a definite value of the objective function for a given test case such as the TMTF which has a complex 3D flow field with flow separation. The value of the objective function oscillates slightly. Assuming a constant value for the objective function (for the initial state or after a design cycle) can be misleading for parameters with very small influence not bigger than the fluctuation. In such a case the decision for a parameter would be based on the (in)accuracy of the solver or the unsteady effects in the flow field rather then the influence of the parameter. Calculating this *reference progress* helps prevent that in most cases. The blue line is the development of the objective function, similar to the green line but for a modification of the contour shape by changing one parameter. Which parameter a plot belongs to is shown on the top of each plot. The black line shows the difference between the blue line and the green line and the red line is the average difference which is constructed at a certain iteration by using the values of previous iterations. The calculations have been performed for 5000 iterations, based on experience for the convergence of the setup. The plots show that the solution can be regarded as converged after 5000 iterations.

The three parameteres (7, 13, 17) shown in Fig. 6.11 have been chosen so that all three possibilities of a sensitivity can be discussed. The sensitivity of parameter 7 is 0. The value

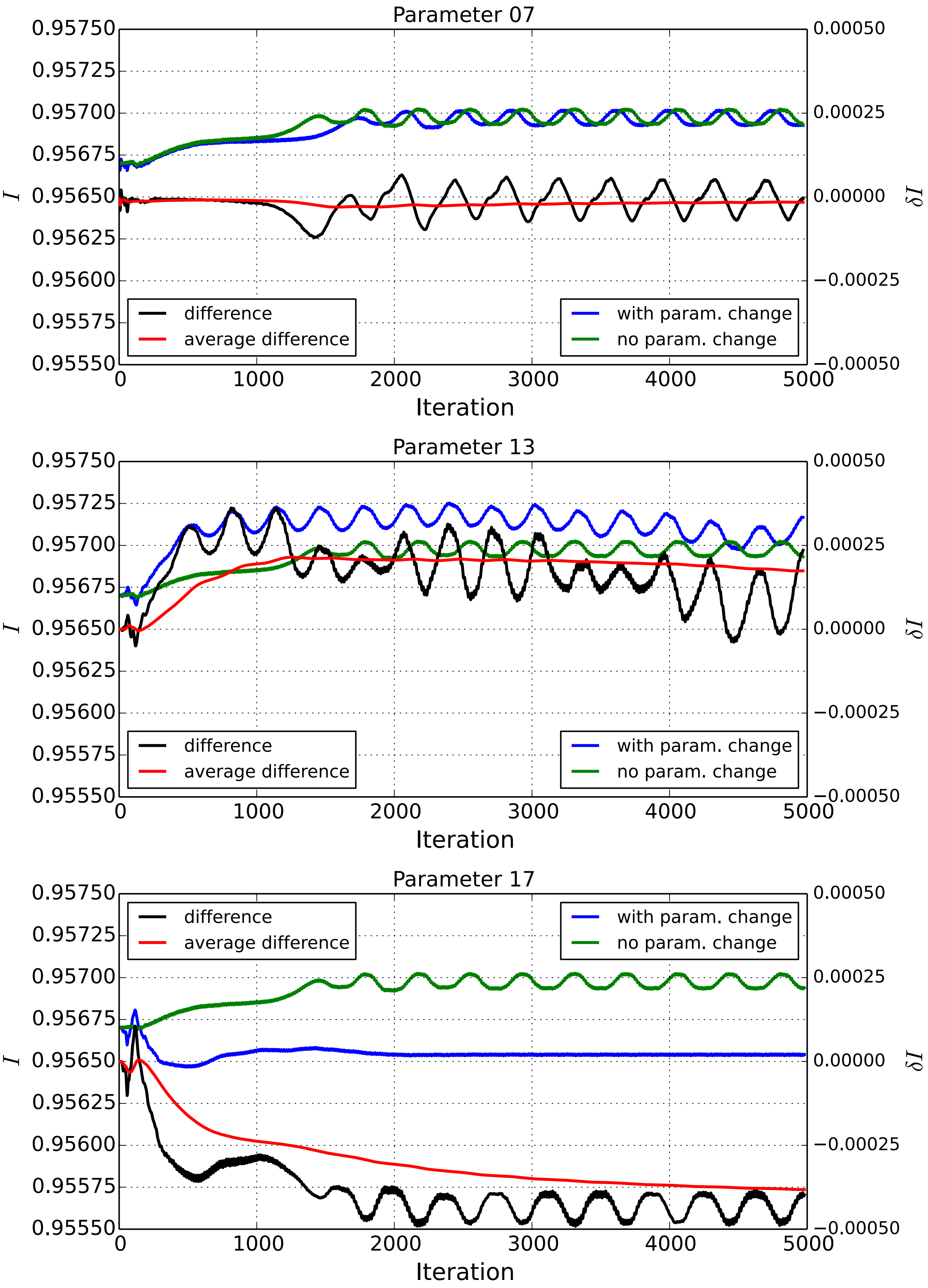

Figure 6.11: **Convergence of CFD calculation for changes in the parameters 7,13 and 17**

of the objective function barely differs from that of the objective function with no parameter change. Once both solutions are converged the result oscillates for both simulations within a small range. Due to a phase offset of the oscillations between the two CFD runs the evaluation of the sensitivity using finite differences can result in a very small positive or negative value. As the introduced method only requires a sign evaluation it can be positive or negative, both being equally right (or wrong). Theoretically this should not have a negative effect on the optimization and it could even have the added benefit of not being caught in the closest local optimum, thus increasing the probability of finding a global optimum.

The second parameter, parameter 13, has a positive influence on the objective function. After approximately 200 iterations the objective function of the simulation with the parameter change is constantly higher than the reference simulation. The evaluation of the sensitivity of such parameters can then be aborted after 200 iterations.

The third parameter shown in Fig. 6.11, paramter 17, has a negative influence on the objective function. And just as with parameter 13 the trend can be correctly predicted after 200 iterations.

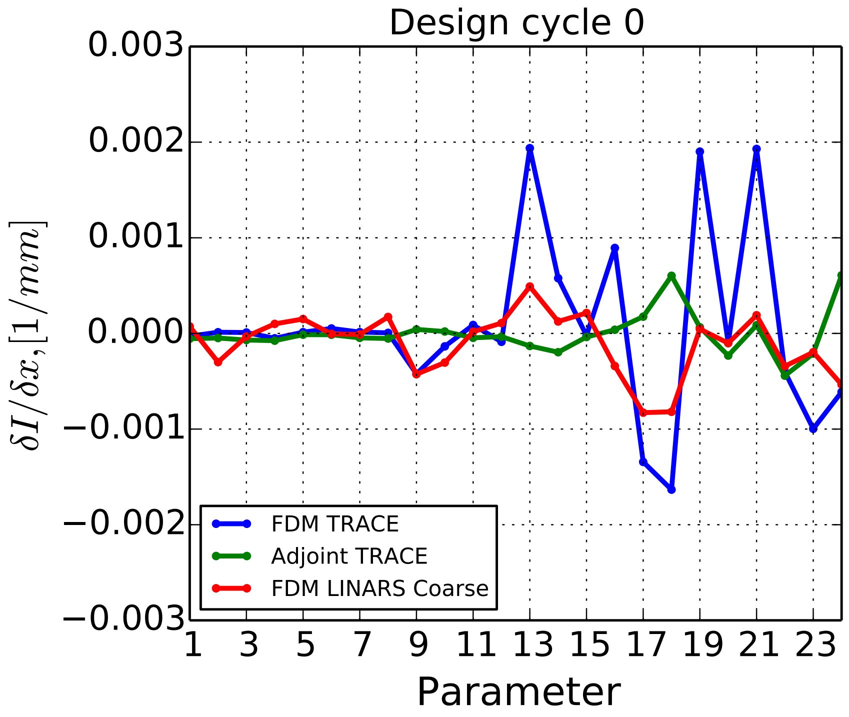

Figure 6.12: **Comparison of the sensitivities between the two solvers and methods**

The sensitivities calculated with the coarser grid using LINARS are compared with the sensitivities calculated using TRACE for the adjoint method and FDM in Fig. 6.12. We can assume that the sensitivities calculated applying the FDM method using TRACE to be correct for the flow simulated by TRACE. The sensitivities calculated using LINARS with the FDM method are in good agreement with the results achieved using TRACE in light of the fact that the magnitude of each parameter change is about a quarter of the value used for the calculations with TRACE. The parameter change δx has been set to 0.48 mm for the evaluation with forward finite differences using LINARS, as it is a good initial value for the optimization, if the maximum expected change of the contour is considered. Also, it should be remembered that a coarser grid is used. Although the magnitude of the sensitivities differ for many parameters their signs are mostly concordant.

Fig. 6.13 compares the flow in the TMTF for the simulations using TRACE and LINARS (coarser grid) with the main focus on the separation region at the trailing edge. Very good agreement of both solvers can be observed. There are only minor differences in the separation region even though the same grid was not used. The difference in the colouring of the backflow is caused by the visualization software due to different file formats of the TRACE and LINARS results. Other minor differences can be explained by the different grid resolution.

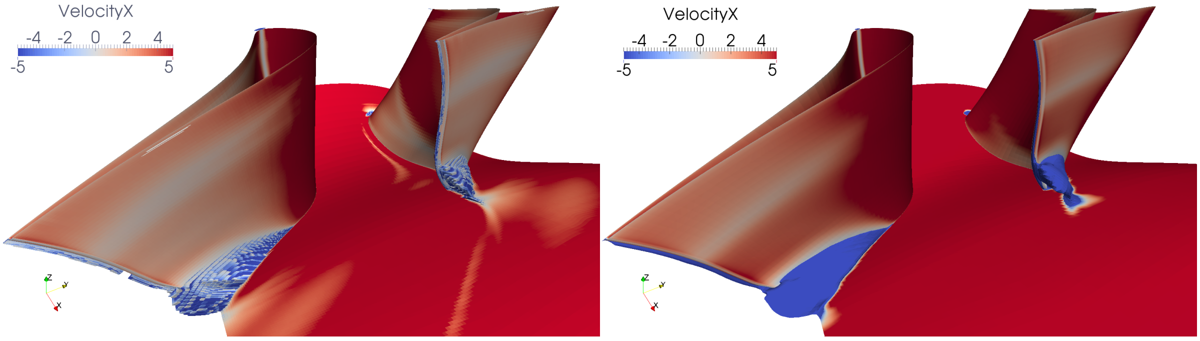

Figure 6.13: **Axial velocity component of the baseline design showing flow separation regions with TRACE (left) and with LINARS using a coarser grid (right)**

Fig. 6.12 shows that there are many parameters with a sensitivity very close to zero. But irrespective of their minor influence they will have a positive or a negative sign. These are parameters that don't necessarily have to be correctly predicted. Table 6.3 shows the sign of the sensitivities for each parameter. The parameters that have a significant sensitivity are highlighted with a bolder script.

Parameter	1	2	3	4	5	6	7	8	**9**	**10**	11	12
Sign	+	-	-	+	+	-	-	+	**-**	**-**	+	+
Parameter	**13**	14	15	**16**	**17**	**18**	**19**	**20**	21	**22**	**23**	**24**
Sign	**+**	+	+	**-**	**-**	**-**	**+**	**-**	+	**-**	**-**	**-**

Table 6.3: **Sign of the sensitivities calculated with FDM using LINARS and a coarse grid**

Two optimizations are performed in consideration of these aspects. The most significant settings for these optimizations are shown in Table 6.4. The first optimization is set to achieve a good converging and a stable optimization. The minimum number of iterations for the evaluation of each parameter is set to 250 as suggested by the preceding analysis. To avoid loosing too much time on a parameter the maximum number of iterations for evaluations is set to 500. 6000 iterations are specified to achieve a fully converged solution. The initial parameter change is set 0.48 mm. The scaling factor and minimum parameter change are specified with 1.12 and 0.1 mm, respectively. The value of 0.1 mm still has a measurable influence on the objective function of this test case. The settings for the second optimization are chosen to improve the speed of the optimization: The minimum number of iterations for each parameter is set to 50 and the maximum is limited with 250. The number of iterations for convergence is reduced by 1000 resulting in 5000 iterations. Also the scaling factor is adjusted to reduce the magnitude of the parameter changes faster and it is set to 1.25.

Optimization	1	2
Min. number of evaluation iterations	250	50
Max. number of evaluation iterations	500	250
Number of iterations for convergence	6000	5000
Initial parameter change	0.48 mm	0.48 mm
Scaling factor	1.12	1.25
Min. parameter change	0.1 mm	0.1 mm
Multi-grid levels of parameter eval.	2	2
Multi-grid levels for convergence	2	2

Table 6.4: **Solver control values for optimization evaluations**

Tables 6.5 and 6.6 show the predicted signs of the parameters for the first step of these two optimization runs which can be directly compared with the signs shown in Table. 6.3. Of the 10 highlighted parameters which have a significant sensitivity 9 are correctly predicted by the first optimization. By the second optimization 6 are correctly predicted.

Fig. 6.14 shows the development the objective function (total pressure ratio) in reference to its initial value for both optimizations. Both optimizations converge to a significantly better value. The first optimization improves the cost function by 0.55 % and the second by 0.45 %. The first optimization also converges significantly faster than the second. This is due the fact that the first optimization predicts the sign of the parameters more often correctly. Also the scale factor of the first optimization is perhaps more convenient for this test case, such that a smoother reduction of the magnitude of the parameter changes is better than a fast reduction.

Parameter	1	2	3	4	5	6	7	8	**9**	**10**	11	12
Sign	-	-	-	-	-	-	-	-	**-**	**-**	+	-
Parameter	**13**	14	15	**16**	**17**	**18**	**19**	**20**	21	**22**	**23**	**24**
Sign	**+**	+	+	**+**	**-**	**-**	**+**	**-**	-	**-**	**-**	**-**

Table 6.5: **Sign of sensitivities by incomplete calculations for the first step of optimization 1**

Parameter	1	2	3	4	5	6	7	8	**9**	**10**	11	12
Sign	-	-	-	-	-	-	-	-	**-**	**+**	-	-
Parameter	**13**	14	15	**16**	**17**	**18**	**19**	**20**	21	**22**	**23**	**24**
Sign	**-**	-	-	**-**	**-**	**-**	**-**	**+**	-	**-**	**-**	**-**

Table 6.6: **Sign of sensitivities by incomplete calculations for the first step of optimization 2**

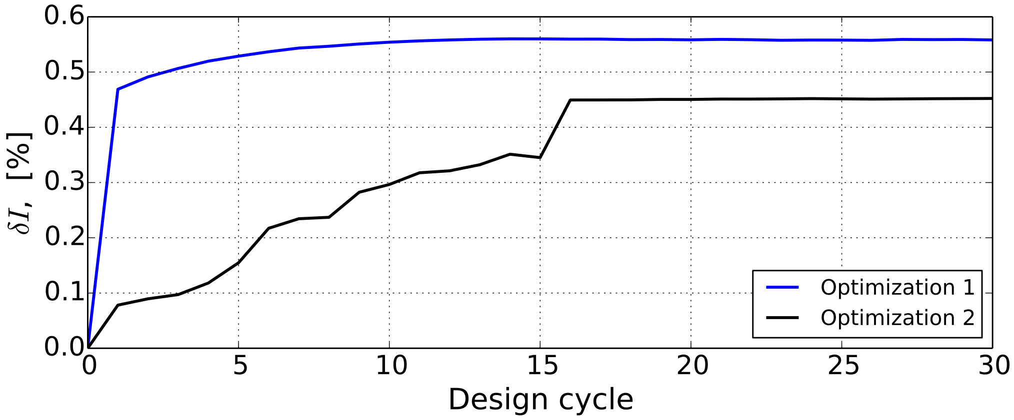

Figure 6.14: **Development of the total pressure ratio in reference to the initial value**

6.2.2 Optimization with the fine grid

The convergence behaviour of the CFD run with the fine grid is more advantageous, so that the number of iterations for parameter evaluations and to achieve converged results could be reduced. The reason for faster convergence is that the calculations are performed with 3 multi-grid levels. The reduced number of steps does not result in a reduced computational effort compared to the optimizations with the coarser grid. An iteration of the coarse grid required approximately 3.2 s wall time using 15 processors on the I-Cluster, whereas the finer grid required approximately 11.7 s wall time using 15 processors on the D-Cluster.

The setup of the solver is shown in Table 6.7. The minimum and maximum number of CFD iterations for a parameter sensitivity evaluation is set to 5 and 100, respectively. With the criterion introduced earlier this results in approximately 30 iterations for each parameter. Full convergence is achieved after 3000 iterations. The initial parameter change is 0.48 mm as with the optimization using the coarser grid. The scaling factor λ is set to 1.18.

Optimization	Fine grid
Min. number of evaluation iterations	5
Max. number of evaluation iterations	100
Number of iterations for convergence	3000
Initial parameter change	0.48 mm
Scaling factor	1.18
Min. parameter change	0.02 mm
Multi-grid levels of parameter eval.	3
Multi-grid levels for convergence	3

Table 6.7: **Solver control values for optimization evaluations**

Parameter	1	2	3	4	5	6	7	8	**9**	**10**	11	12
Sign after complete evaluations	-	-	-	-	+	+	-	-	**-**	**-**	+	-
Sign after incomplete evaluations	-	-	-	-	-	-	-	-	**+**	**-**	-	-
Parameter	**13**	14	15	**16**	**17**	**18**	**19**	**20**	21	**22**	**23**	**24**
Sign after complete evaluations	**+**	+	-	**-**	**-**	**-**	**+**	**+**	-	**-**	**-**	**-**
Sign after incomplete evaluations	**+**	-	+	**+**	**-**	**-**	**-**	**-**	-	**-**	**-**	**-**

Table 6.8: **Comparison of sensitivities by complete (3000 CFD iterations) and incomplete (~30 CFD iterations) calculations for the first step**

Reducing the number of iterations for the parameter sensitivity evaluation has an influence on the number of correctly predicted parameter sensitivities. Table 6.8 compares the predictions of the complete and incomplete calculations. For the first step 15 of 24 parameters are predicted correctly. Previously we discussed that some parameters have a much smaller sensitivity. Only 11 parameters have a significant effect on the cost function during the first iteration step. 7 of them are correctly predicted.

Fig. 6.15 shows the development of the cost function during the optimization. The optimization run is stable and converges quite rapidly. The best result is obtained already after the second optimization cycle, which results in an improvement of the cost function by 0.5 %. This is 0.1 %-points more than the improvement achieved using the adjoint method for the optimization (see Fig. 6.1).

Fig. 6.16 shows the resulting contour after the 2nd design cycle. The changes are, with a magnitude of around 1.5 mm, slightly larger than in the previous optimization. The contour representation shows the change in the radius with respect to the baseline design where the red colour indicates an increase in the radius (bump) and the blue colour a decrease in the radius (dent). Shortly after the inlet the radius is reduced nearly up to midchord. On the pressure side a small bump is formed, as with the adjoint optimization. Unlike the contour optimization with the adjoint method the structures are not formed along the streamline.

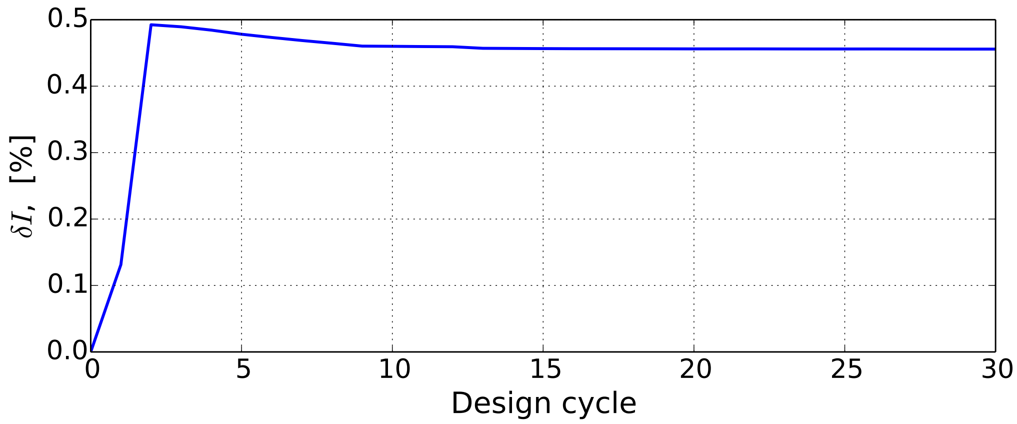

Figure 6.15: **Development of total pressure in reference to the initial value**

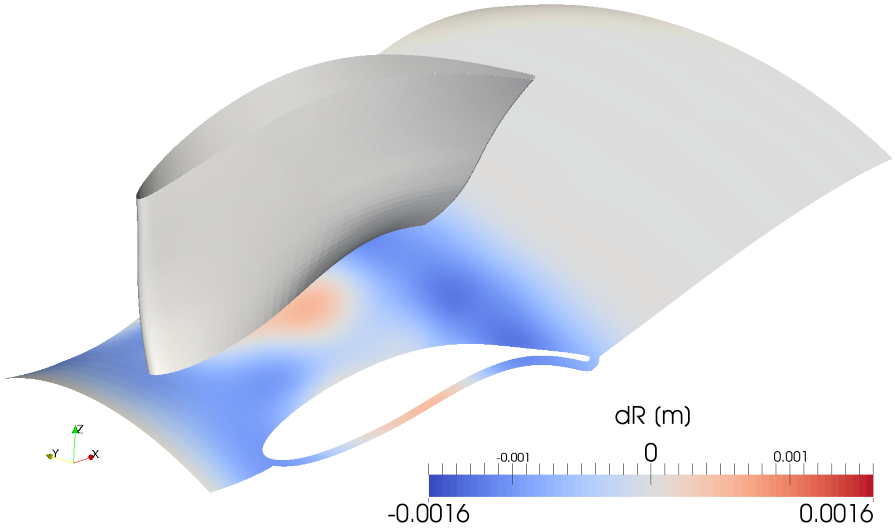

Figure 6.16: **New contour after the 2nd cycle**

The separation regions before and after the optimization are visualized in Fig. 6.17 on the left for the baseline design and on the right for the optimized design. The colouring represents the axial velocity and the scale is set between $-5\,\frac{\mathrm{m}}{\mathrm{s}}$ and $5\,\frac{\mathrm{m}}{\mathrm{s}}$ to better visualize positive and negative axial velocity values. As this is an axial machine negative axial velocity indicates backflow regions and apart from the region of the stagnation point on the leading edge, backflow mostly indicates flow separation. The extent of the negative velocity regions are also displayed in the figure. On the contour plot of the optimized design the flow separation region is almost fully eliminated. A minimal backflow region at the corner of the blade suction side and the hub endwall contour close to the trailing edge can be observed.

The positive pressure gradient that causes the flow separation is shown in Fig. 6.18. The

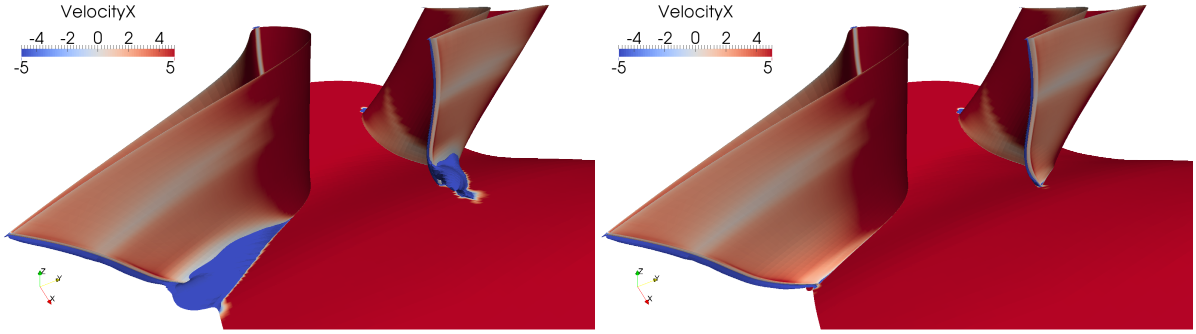

Figure 6.17: **Axial velocity component of the baseline (left) and optimized (right) design showing flow separation regions**

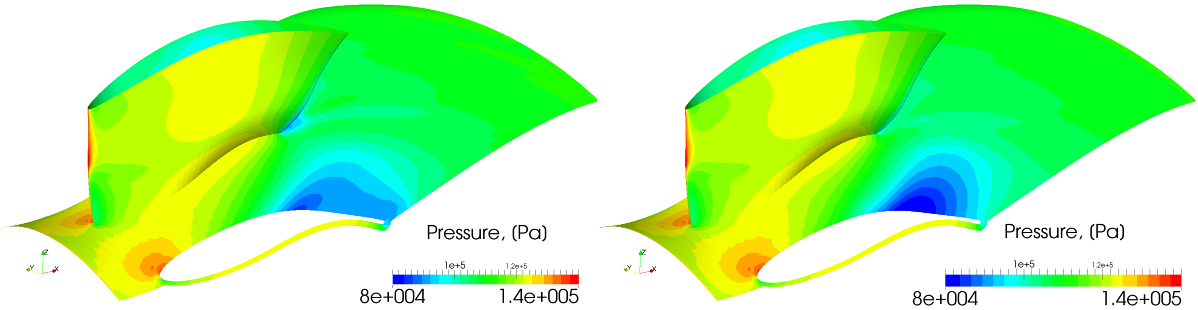

Figure 6.18: **Contour plots of pressure on the hub and blade walls for the baseline (left) and optimized (right) endwall contours**

aft loaded design of the blade has a sharp turning after mid chord which creates a low pressure region on the suction side. The lowest pressure value is shortly upstream of the trailing edge after which the pressure starts rising creating a positive pressure gradient. It can be observed in the figure on the left for the baseline design. The boundary flow is not able to overcome the pressure increase to follow the contour and separates. The same pressure contour plot is shown on the right for the new design. As with the adjoint optimization, the pressure drop and the resulting adverse pressure gradient are actually increased.

The Mach number distribution and flow propagation is shown in Fig. 6.19. The velocity vectors help clarify the flow profile and indicate clearly where the flow separation occurs. Although the resulting contours achieved with the two optimizations are not the same, it is the same mechanism with which the adverse pressure gradient is overcome without flow separation; the velocity and therefore the momentum is increased just before the separation point by decreasing the cross section.

The contour plots of the axisymmetric and new hub contours downstream of the strut are shown in Fig. 6.20. This location is where the actual exit of the TMTF would be (slightly

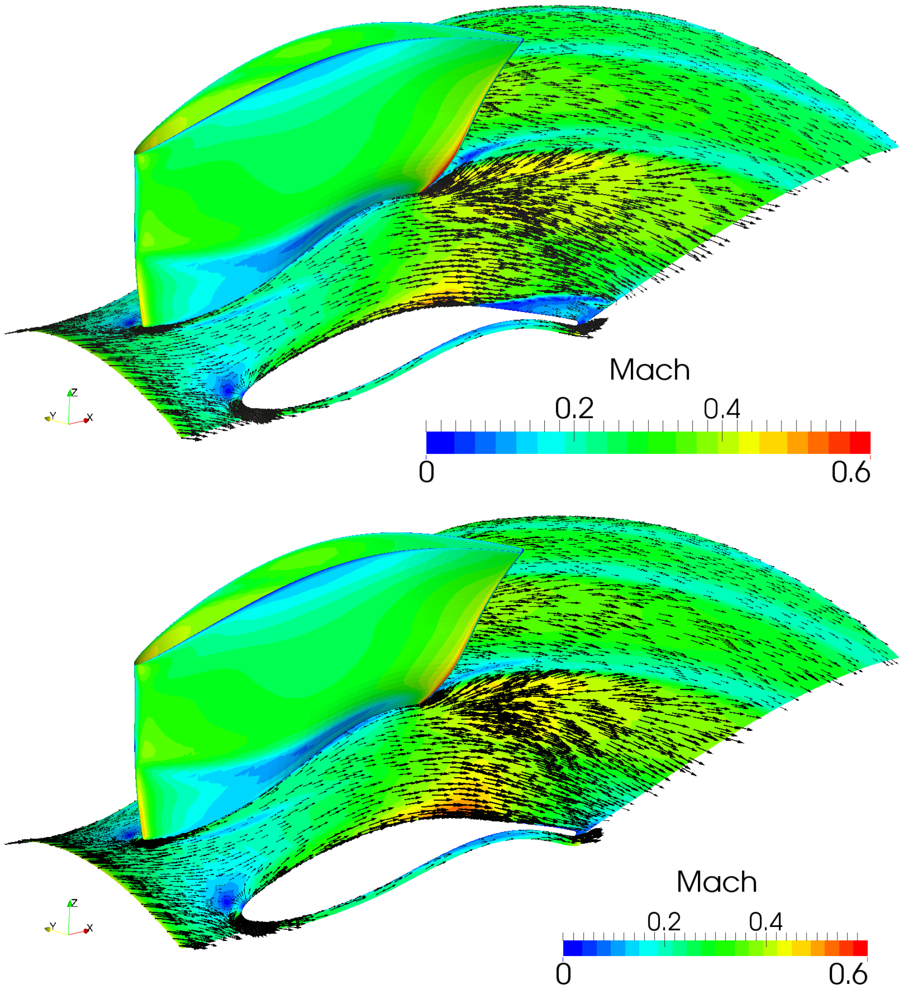

Figure 6.19: **Flow propagation on the hub contour of the baseline (above) and optimized (below) designs**

downstream of plane E in Fig. 5.3) if the computational domain had not been extended for numerical reasons. The viewing direction is from downstream of the flow. Visualized are the contour plots of the total pressure coefficient, normalized yaw angle and specific entropy. Aside from small differences in the contour plots, the comparison yields the same results as with the adjoint optimization. In the plot of the total pressure coefficient of the axisymmetric contour (left) a green region is noticable which is mainly because of the shed vortices from the trailing edge. Close to the shroud this region extends slightly due to the interaction with the upper passage vortex. Close to the hub endwall in this lower pressure region there is a zone with an even lower total pressure caused by the flow losses from the separation region. On the right the same contour plot is shown for the new contour. The low pressure region due to flow separation is eliminated. This trend is similar for the plots of the normalized yaw angle

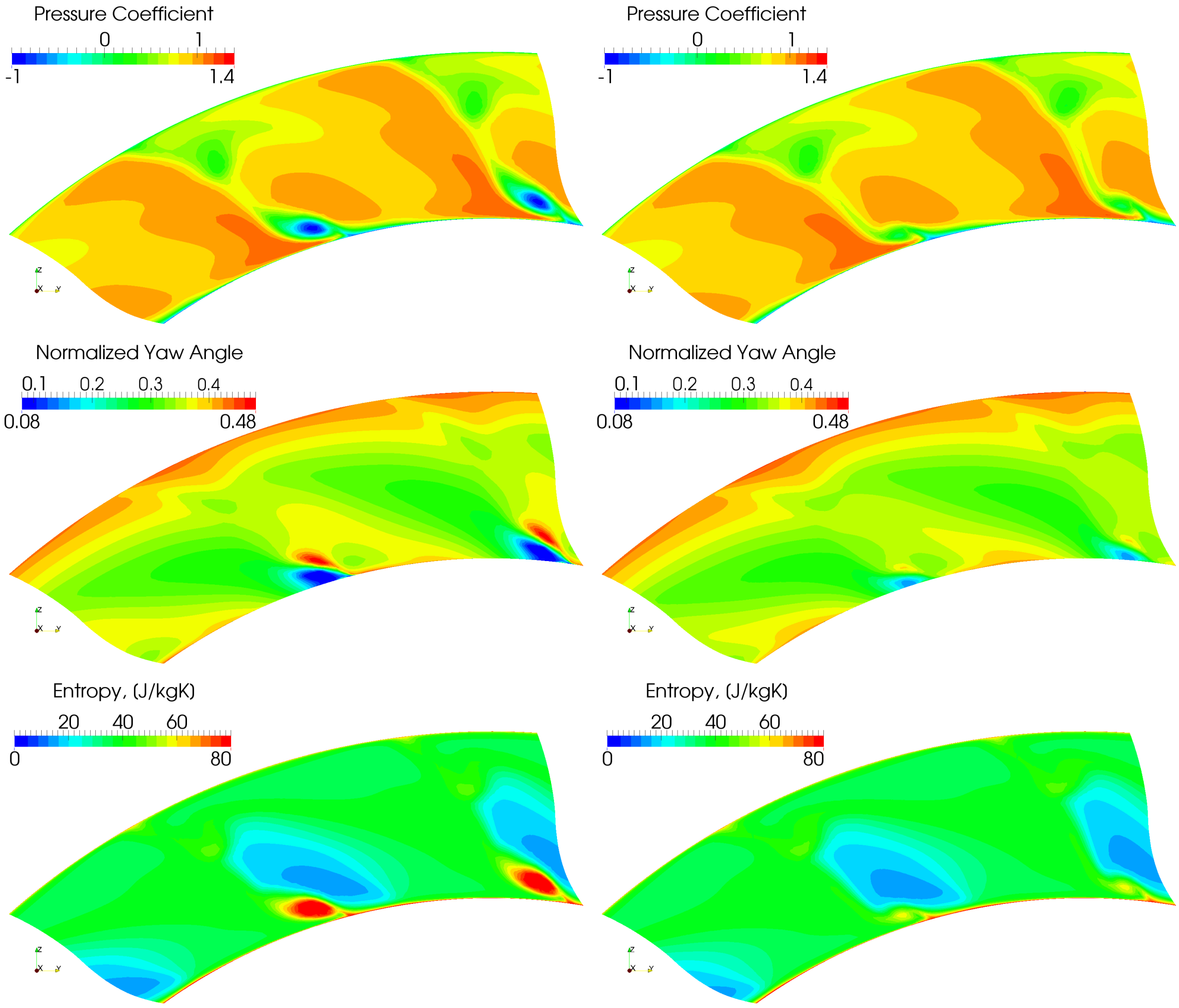

Figure 6.20: **Contours of the total pressure coefficient, normalized yaw angle and specific entropy downstream of the trailing edge for the baseline (left) and optimized (right) designs**

and entropy. Near the hub the flow separation creates a region with low turning as can be seen on the contour plot of the normalized yaw angle. It is again mostly eliminated by the new contour. Finally, on the entropy contour plot the strongest negative influence is caused by the flow separation, which is again eliminated with the new contour.

Fig. 6.21 presents the circumferentially averaged flow at the exit of the TMTF for the optimized contour in comparison with the axisymmetric contour. The total pressure coefficient is increased below 0.3 span through the elimination of the separation region. The break down of the yaw angle below 0.2 span is also reduced. And similarly, entropy production is reduced below 0.35 span. Between 0.35 and 0.9 span there is a slight increase in the entropy.

The required 3000 steps for a converged CFD solution and approximately 30 iterations for each parameter results in 3720 iterations for each design cycle with 24 parameters. Each iter-

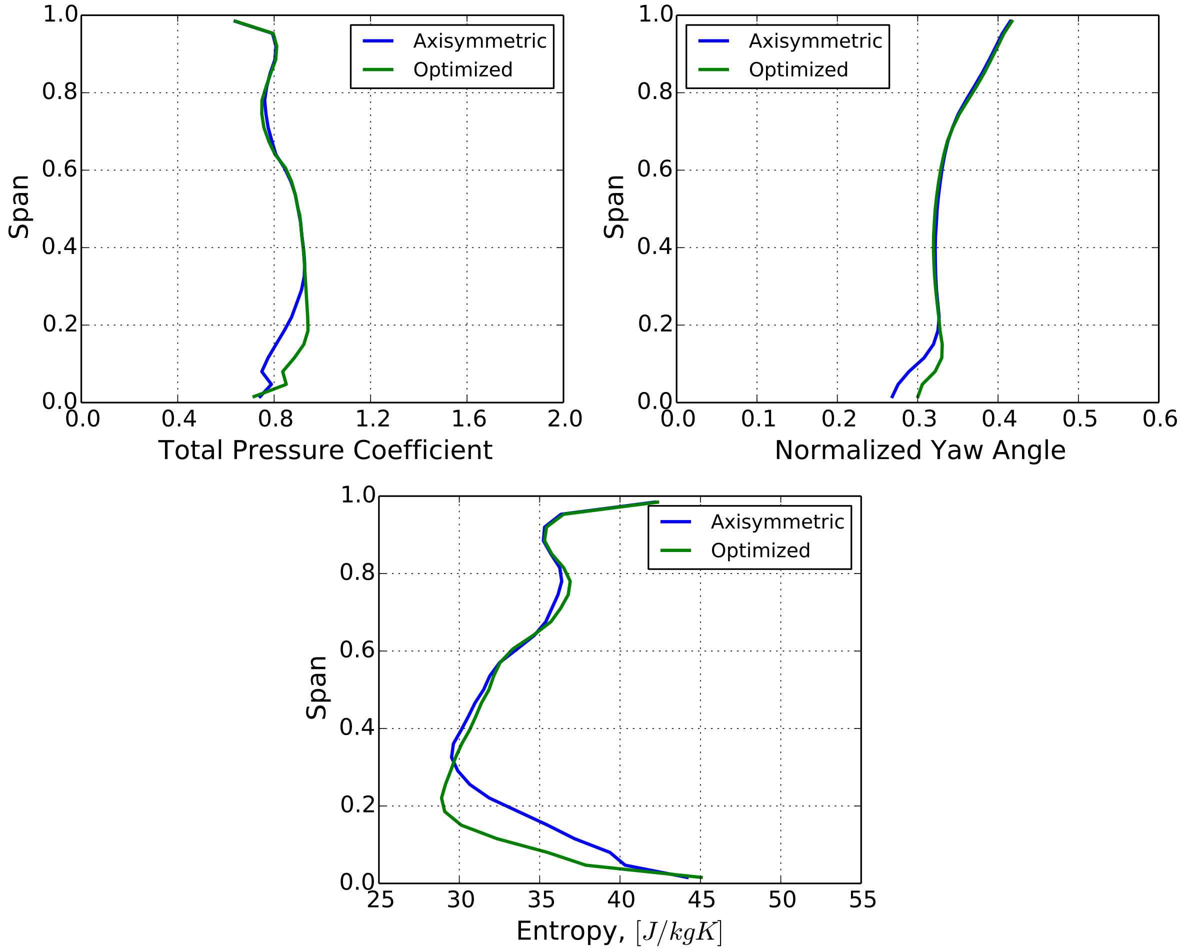

Figure 6.21: **Circumferentially averaged total pressure coefficient, normalized yaw angle and specific entropy at the exit of the TMTF**

ation of the LINARS CFD solver requires approximately 11.7 s wall time with 15 processors on the I-Cluster. One design cycle requires about 12 hours of wall time. This results in 70.2 hours for an optimization with 5 design cycles, compared to 88 hours for the adjoint method using TRACE.

6.3 Discussion of the Methods

Before the comparison of the optimization methods and their results, it is important to note that the optimizations have been performed with different solvers. Therefore without further investigation it is not possible to conclude directly which of the two contours would achieve a better performance of the stage in terms of isentropic efficiency. Furthermore, a comparison of the isentropic efficiency might also be misleading for comparing the methods as the contours were not directly optimized for the isentropic efficiency of the stage. The quasi-first-order method achieves a greater improvement relative to the axisymmetric design in terms of the objective function, but this could be due to small quantitative differences in the flow fields predicted by the different solvers. To be able to directly compare which method yields better results the same CFD solver should have been used. But it was not possible to use the same solver, as for the adjoint method an adjoint solver is needed and therefore TRACE was used. And implementing the quasi-first-order method required access to the source code of the solver and therefore LINARS had to be used. The discussion will concentrate on the aspects of efficiency and stability, while accepting that the solutions obtained are of the same (or similar) quality.

During the optimizations performed in the course of this thesis, the adjoint solver exhibited two main deficits. The first problem that most optimizations encountered is the lacking robustness of the adjoint solver; a successfull CFD run did not guarantee a successfull adjoint evaluation. As the source code was not available, it was not possible to determine the cause of the failed adjoint evaluations. Comparison of successful and failed adjoint runs indicated a strong sensitivity of the adjoint solver to surface smoothness. But a direct coherence could not be clearly asserted. The second problem is the inaccuracy of sensitivities as demonstrated in Fig. 6.3. As the residuals of the adjoint solution were still relatively high this can also be regarded as a stability issue of the adjoint solver due to failed convergence. It could be determined that the convergence issue is due to the flow separation; adjoint calculations of flows without separation achieved much lower residuals. The resulting sensitivities of flows with separation show a large discrepency compared to the FDM results. In most literature regarding discrete adjoint solver implementation it is stated that the adjoint solver adapts the convergence behaviour of the CFD solver. This assumption does not seem to hold entirely. Furthermore, the adjoint method requires an additional adjoint solver for each objective function as well as constraints. In short, the adjoint method is a very powerful and effective tool for optimal shape design with CFD, but its application is demanding. Its main advantage is that it saves computional time for optimization problems with many parameters, as its computational effort is independant of the number of design parameters.

The newly introduced quasi-first-order method avoids the challenges of the adjoint method. There are no additional stability issues apart from that of CFD calculations. But of course, the method has challenges of its own. The convergence behaviour of CFD solvers gains more importance and the initial convergence behaviour becomes the main focus due to the limited number of calculation steps. Every solver will probably have its own convergence behaviour and a different one for each objective function. So for a successful optimization the behaviour has to analyzed to be able to formulate appropriate criteria for the decisions regarding sensitivities.

The fact that rough gradient information is being used poses some challenges to more complicated problems such as the constrained optimization problem. As discussed previously and expressed in Eq. 1.6, fomulating a pseudo-objective function $\tilde{f}(\mathbf{x})$ that translates the constrained formulation into an unconstrained optimization problem is a promising strategy that can be pursued with the quasi-first-order method as well. For a constrained, multi-point, multi-objective optimization other stategies may need to be adapted.

The optimization of the TMTF using 24 parameters is faster with the proposed method than with the optimization using the adjoint method. Increasing the number of parameters would reduce the speed of the optimization, so that it will remain faster only up to a certain number of parameters (approximately 100). Further potential to increase the speed of the new method exists. Ideally, the fastest parameter evaluation can be achieved if only one CFD iteration per parameter evaluation would suffice.

Finally, the proposed method can offer a fast, effective and stable method for single-objective (constrained) optimization problems.

Chapter 7

Conclusions and Perspectives

Optimal shape design of a turning mid turbine frame is discussed. The optimizations focused on an unconstrained, single-objective problem.

The first optimization approach is based on the R1 quasi-Newton optimization method. Gradient information is obtained using the adjoint method, which provides a possibility for calculating gradient information of a vast number of parameters without significantly increasing computational expense. But a constrained multi-objective optimization requires the evaluation of additional adjoints, thus increasing computational expense. Aside from these well known aspects of adjoint methods, it poses two challenges for the test cases considered within the framework of this thesis. The optimization routine was unstable, as some design cycles failed to achieve an adjoint solution, although a CFD solution of the geometry converged to plausible results. Furthermore, the gradient information proved to be unreliable for the flow through the vane row if separation occurred. These challenges have successfully been overcome for the work presented here. But they limit the usability of adjoint methods. Thus an alternative optimization method is additionally introduced.

The second optimization approach is a new method which is referred to as a quasi-first-order optimization method. It is based on a very simple approach to optimization and eliminates the difficulties of the adjoint method. Its computational expense is not independent of the number of parameters, but the expense for the evaluation of each parameter is significantly low. In the test case analyzed in the thesis 24 design variables were evaluated with a lower computational effort than with the adjoint method, and up to 100 design variables could have been introduced, before the computational expense of the method would exceed that of the adjoint method. The speed of the method is one of its major advantages, besides its simplicity and ease of application. It is based on the utilization of incomplete gradient information; only the sign of the gradient is required. But this rough gradient information is also the cause for its major drawback; it poses a challenge while considering constraints or multiple-objective functions. Strategies for optimizing such problems have not been evaluated in the thesis, but considering constraints should be possible by reducing a constrained, multi-objective optimization problem to a single-objective optimization problem using a pseudo-objective function, as often practiced with deterministic methods.

Future work regarding this method should first concentrate on this aspect of optimization and determine the performance of the method for constrained and multi-objective optimization problems. Perhaps alternative strategies should be developed, if using pseudo-objective functions should yield unsatisfactory results.

Following up on this, a number of test cases should be evaluated for benchmarking. This thesis only introduces a new method that is desirable because of its simplicity and ease of use, and demonstrates that it actually works. But where this new method will be placed amongst current optimization methods is not clear. Perhaps it will only be a tool for fast, preliminary studies or it will truly become an alternative to gradient based optimization methods.

References

IPCC Fourth Assessment Report: Climate Change. Intergovernmental Panel on Climate Change, 2007.

CO_2 emissions from fuel combustion highlights. IEA Statistics, 2014.

Akin, M. B. and Sanz, W. Numerical investigation of a two-stage counter-rotating turbine with transition modeling and prediction improvement with time-accurate calculations. ETMM 10, Marbella, Spain, 2014a.

Akin, M. B. and Sanz, W. A quasi first order optimization method and its demonstration on the optimization of a U-bend. ASME Turbo Expo, Montreal, Canada, GT2015-42640, 2015.

Akin, M. B., Sanz, W., and Pieringer, P. Endwall contour optimization of a turning mid turbine frame using an adjoint method. ASME Turbo Expo, Düsseldorf, Germany, GT2014-26038, 2014.

Akin, M. B., Sanz, W., and Pieringer, P. Optimization of a low pressure turbine stage by hub endwall contouring of the turning mid turbine frame using an adjoint method. International Symposium on Experimental and Computational Aerothermodynamics of Internal Flows, Lerici, Italy, 2015.

Akin, M. B. and Sanz, W. Influence of transition on CFD calculations of a two-stage counter-rotating turbine. ASME Turbo Expo, Düsseldorf, Germany, GT2014-26044, 2014b.

Anderson, G. R., Aftosmis, M. J., and Nemec, M. Parametric deformation of discrete geometry for aerodynamic shape design. 50th AIAA Aerospace Sciences Meeting, Nashville, Tennessee, 2012.

Atkins, M. J. Secondary losses and endwall profiling in a turbine cascade. Proceedings of the IMechE, C255/87, pages 29–42, 1987.

Biesinger, T. E. Secondary Flow Reduction Techniques in Linear Turbine Cascades. PhD thesis, University of Durham, 1993.

Boussinesq, J. Theorie de l'ecoulement tourbillant. Memoire Presente par Divers Savants en Sciences Mathematiques et Physiques, 23, 1877.

Chong, E. K. and Zak, S. H. An Introduction to Optimization. John Wiley & Sons, Inc., 2001.

Corral, R. and Gisbert, F. Profiled end wall design using an adjoint Navier-Stokes solver. Journal of Turbomachinery, 130(2), 2008.

Deich, M., Zaryankin, A. E., Filippov, G. A., and Zatsepin, M. F. Method of increasing the efficiency of turbine stages with short blades. Teploenergetica, 2(Translation No. 2816), 1960.

Dejc, E. Atlas of axial turbine blade characteristics. Machinostroenie Publishing House, Moscow, C. E. Trans. 4563. CEGB Inf. Services, 1965.

Doerffler, P. P. and Amecke, J. Secondary flow control and streamwise vortices formation. ASME Turbo Expo, Hague, Netherlands, 94-GT-376, 1994.

Dossena, V., Perdichizzi, A., and Savini, M. The influence of endwall contouring on the performance of a turbine nozzle guide vane. ASME Turbo Expo, Stockholm, Sweden, 98-GT-71, 1998.

Erhard, J. and Gehrer, A. Design and construction of a transonic test turbine facility. ASME Turbo Expo 2000, Munich, Germany, GT2000-0480, 2000.

Ewen, J. S., Huber, F. W., and Mitchell, J. P. Investigation of the aerodynamic performance of small axial turbines. ASME International Gas Turbine and Products Show, Washington, DC, USA, 73-GT-3, April 1973.

Frey, C., Nuernberger, D., and Kersken, H. P. Development and application of an adjoint RANS solver for turbomachinery. 8th European Turbomachinery Conference, Graz, Austria, 2009a.

Frey, C., Kersken, H.-P., and Nuernberger, D. The discrete adjoint of a turbomachinery RANS solver. ASME Turbo Expo, Orlando, USA, GT2009-59062, 2009b.

Frey, C., Ashcroft, G., Backhaus, J., Kügeler, E., and Wellner, J. Adjoint-based flow sensitivity analysis using arbitrary control surfaces. ASME Turbo Expo, Vancouver, British Columbia, Canada, GT2011-45041, 2011.

Gehrer, A. Entwicklung eines 3D-Navier-Stokes Codes zur numerischen Berechnung der Turbomaschinenströmung. PhD thesis, Graz University of Technology, Oktober 1998.

Gehrer, A. Simulation of secondary flow development downstream of transonic turbine cascade using an implicit tvd upwind scheme. 4th European Conference on Turbomachinery, Firenze, Italy, ATI-CST-057/01, March 2001.

Giannakoglou, K. C. and Karakasis, M. K. . Hierarchical and distributed metamodel-assisted evolutionary algorithms. VKI Lecture Series on Introduction to Optimization and Multidiscipinary Design, Brussels, 2006.

Giannakoglou, K., Papadimitriou, D. I., and Papoutsis-Kiachagias, E. M. The continous adjoint method: Theory and industrial applications. Introduction to Optimization and Multidisciplinary Design in Aeronautics and Turbomachinery. Lecture Series of the von Karman Institue for Fluid Dynamics, 2012.

Giles, M. B., Duta, M. C., and Mueller, J.-D. Adjoint code developments using the exact discrete approach. 15th Computational Dynamics Conference, AIAA 2001-2596, 2001. doi: 10.2514/6.2001-2596.

Giles, M. B., Duta, M. C., Mueller, J.-D., and Pierce, N. A. Algorithm developments for discrete adjoint methods. AIAA Journal, 41(2), February 2003.

Goldberg, D. E. Genetic Algorithms in Search, Optimization, and Machine Learning. Addison-Wesley Publishing Company, Inc., 1989.

Goldstein, R. J., Wang, H. P., and Jabbari, M. Y. The influence of secondary flows near the endwall and boundary layer disturbance on convective transport from a turbine blade. ASME J. Turbomach., 117:657–665, 1995.

Harrison, S. The influence of blade lean on turbine losses. ASME Turbo Expo, Brussels, Belgium, 90-GT-55, June 1990.

Hartland, J. C., Gregory-Smith, D. G., and Rose, M. G. Non-axisymmetric endwall profiling in a turbine rotor blade. ASME Turbo Expo, Stockholm, Sweden, 98-GT-525, June 1998.

Hartland, J. C., Gregory-Smith, D. G., Harvey, N. W., and Rose, M. G. Non-axisymmetric turbine end wall design: Part II Experimental validation. ASME Turbo Expo, Indianapolis, Indiana, 99-GT-338, June 1999.

Harvey, N. W., Rose, M. G., Taylor, M. D., Shahpar, S., Hartland, J., and Gregory-Smith, D. G. Non-axisymmetric turbine end wall design: Part I Three-dimensional linear design system. ASME Turbo Expo, Indianapolis, Indiana, 99-GT-337, June 1999.

Hicks, R. M. and Henne, P. A. Wing design by numerical optimization. Journal of Aircraft, 15:407–412, 1978.

Holland, J. J. Adaption in Natural and Artificial Systems. University of Michigan Press, 1975.

Hubinka, J., Santner, C., Paradiso, B., Malzacher, F., and Göttlich, E. Design and construction of a two shaft test turbine for investigation of mid turbine flows. International Society of Air Breathing Engines, ISABE-2009-1293, 2009.

Hubinka, J., Paradiso, B., Santner, C., Pirker, H., and Göttlich, E. Design and operation of a two spool high pressure test turbine facility. 9th European Turbomachinery Conference, Istanbul, Turkey, March 2011.

Jabbari, M. Y., Goldstein, R. J., Marston, K. C., and Eckert, R. R. G. Three dimensional flow within large scale turbine cascades. Wärme- und Stoffübertragung, 27:51–59, 1992.

Jameson, A. Optimum aerodynamic design using CFD and control theory. AIAA 12th Computational Fluid Dynamics Conference, AIAA 95-1729, San Diego, June 1995.

Jameson, A. Aerodynamic design via control theory. Journal of Scientific Computing, 3: 233–260, 1988.

Jones, W. P. and Launder, B. E. The prediction of laminarization with a two-equation model of turbulence. Int. J. Heat Mass Transfer, 15:301–314, 1972.

Kawai, T. Effect of combined boundary layer fences on turbine secondary flow and losses. JSME International Journal, 37(2), 1994.

Kawai, T., Shinoki, S., and Adachi, T. Secondary flow control and loss reduction in a turbine cascade using endwall fences. JSME International Journal, 32(3), 1989.

Kelterer, M. E., Burgstaller, R., and Sanz, W. Application of the gamma-Re_theta transition model to transitional flow. International Symposium on Experimental and Computational Aerothermodynamics of Internal Flows, Brussels, Belgium, ISAIF10-091, 2011.

Kelterer, M., Pecnik, R., and Sanz, W. Computation of laminar-turbulent transition in turbomachinery using the correlation based γ-Re_θ transition model. ASME Turbo Expo 2010, Glasgow, UK, GT2010-22207, Glasgow, Scotland, June 2010.

Kim, S., Alonso, J., and Jameson, A. Multi-element high-lift configuration design optimization using viscous continous adjoint method. Journal of Aircraft, 41:1082–1097, 2004.

Kopper, F. C., Milano, R., and Vanco, M. An experimental investigation of endwall profiling in a turbine blade cascade. AIAA Journal, 19(8):1033–1040, 1981.

Langston, L. S. Crossflows in a turbine cascade passage. ASME Turbo Expo, New Orleans, Louisiana, USA, 80-GT-5, March 1980.

Langston, L. S. Secondary flows in axial turbines - A review. Annals of the New York Academy of Sciences, 934:11–26, 2001.

Langtry, R. B. and Menter, F. R. Transition modeling for general CFD applications in aeronautics. 43rd AIAA Aerospace Sciences Meeting and Exhibit, AIAA 2005-522, January 2005.

Luo, J., Liu, F., and McBean, I. Optimization of endwall contours of a turbine blade row using an adjoint method. ASME Turbo Expo, Vancouver, Canada, GT2011-46163, 2011.

Luo, J., Zhou, C., and Liu, F. Multipoint design optimization of a transonic compressor blade by using and adjoint method. Jounal of Turbomachinery, 136, 2014.

Menter, F. R. and Langtry, R. B. Correlation-based transition modeling for unstructured parallelized computational fluid dynamics codes. AIAA Journal, 47(12):2894–2906, 2009.

Menter, F. R., Ferreira, J. C., Esch, T., and Konno, B. The SST turbulence model with improved wall treatment for heat transfer predictions in gas turbines. International Gas Turbine Congress, Tokyo, Japan, 2003.

Menter, F. R., Langtry, R. B., Liki, S. R., Suzen, Y. B., Huang, P. G., and Voelker, S. A correlation-based transition model usind local variables Part 1 - Model formulation. ASME Turbo Expo 2004, Vienna, Austria, GT2004-53452, 2004.

Morris, A. W. H. and Hoare, R. G. Secondary loss measurements in a cascade of turbine blades with meridional wall profiling. ASME, 75-WA/GT-13, 1975.

Mousavi, A., Castonguay, P., and Nadarajah, S. K. Survey of shape parameterization techniques and its effect on three-dimensional aerodynamic shape optimization. 18th AIAA Computational Fluid Dynamics Conference, AIAA 2007-3837, June 2007.

Mühlenbein, H., Schomisch, M., and Born, J. The parallel genetic algorithm as function optimizer. Parallel Computing, 17:619–632, 1991.

Neumayer, F., Kulhanek, G., Pirker, H.-P., Jericha, H., Seyr, A., and Sanz, W. Operational behavior of a complex transonic test turbine facility. ASME Turbo Expo 2001, New Orleans, Luisiana, GT2000-0480, 2001.

Papadimitriou, D. I. and Giannakoglou, K. C. A continous adjoint method for the minimization of losses in cascade viscous flows. 44th AIAA Aerospace Sciences Meeting and Exhibit, AIAA 2006-49, Reno, Nevada, January 2006.

Papadimitriou, D. I., Zymaris, A. S., and Giannokoglou, K. C. Discrete and continous adjoint formulations for turbomachinery applications. Evolutionary and Deterministic Methods for Desing, Optimization and Control with Applications to Industrial and Societal Problems, EUROGEN, 2005.

Periaux, J. and Verstraete, T., editors. Introduction to optimization and multidisciplinary design in aeronautics and turbomachinery. Lecture Series of the von Karman Institue for Fluid Dynamics, 2012.

Pieringer, P. Springer und Pieringer EDV Dienstleistungen OEG, 2012.

Pironneau, O. On optimal profiles for stokes flow. J. Fluid Mech., 59:117–128, 1973.

Prümper, H. Verbesserung des Wirkungsgrades axialer Turbinenstufen durch Reduzierung der Sekundärverluste. PhD thesis, RWTH Aachen, 1975.

Rechenberg, I. Evolutionsstrategie - Optimierung technischer Systeme nach Prinzipien der biologischen Evolution. Fomann-Holzboog, Stuttgart, 1973.

Reutter, O., Hemmert-Pottman, S., Hergt, A., and Nicke, E. Endwall contouring and fillet design for reducing losses and homogenizing the outflow of a compressor cascade. ASME Turbo Expo, Düsseldorf, Germany, GT2014-25277, 2014.

Rose, M. G. Non-axisymmetric endwall profiling in the HP NGV's of an axial flow gas turbine. ASME Turbo Expo, The Hague, Netherlands, 94-GT-249, 1994.

Salzmann, M. Gitterunabhängigkeitsstudie einer zweistufigen Axialturbine. Bachelor thesis, TU Graz, 2012.

Samareh, J. A. A survey of shape parameterization techniques. CEAS/AIAA/ICASE/NASA Langley International Forum on Aeroelasticity and Structural Dynamics, Williamsburg, VA, June 1999.

Santner, C., Paradiso, B., Malzacher, F., Hoeger, M., Hubinka, J., and Goettlich, E. Evolution of the flow through a turning mid turbine frame applied between a transonic HP-turbine stage and a counter-rotation LP-turbine. 9th European Turbomachinery Conference, Istanbul, Turkey, March 2011.

Santner, C. Experimental investigation of turning mid turbine frame designs. PhD thesis, TU Graz, 2013.

Sanz, W., Gehrer, A., and Paßrucker, H. An implicit TVD upwind relaxation scheme for the unsteady 2d-euler-equations. ASME Cogen Turbo Power Conference, Vienna, Austria, August 1995.

Sieverding, C. H. Reduction of secondary losses in turbines. VKI course note 95, 1975.

Sieverding, C. H. Recent progress in the understanding of basic aspects of secondary flows in turbine blade passages. ASME Turbo Expo, Amsterdam, Netherlands, 84-GT-78, June 1984.

Simmendinger, C. and Kügeler, E. Hybrid parallelization of a turbomachinery CFD code: Performance enhancements on multicore architectures. V European Conference on Computational Fluid Dynamics, 2010.

Spalart, P. R. and Allmaras, S. R. A one-equation turbulence model for aerodynamic flows. Recherche Aerospatiale, 1:5–21, 1994.

Spataro, R., Santner, C., Lengani, D., and Goettlich, E. On the flow evolution through a LP turbine with wide-chord vanes in an S-shaped channel. ASME Turbo Expo, Copenhagen, Denmark, GT2012-68178, 2012.

Squire, W. and Trapp, G. Using complex variables to estimate derivatives of real functions. SIAM Review, 40(1):110–112, 1998.

Vanderplaats, G. N. Numerical Optimization Techniques for Engineering Design. McGraw-Hill, New York, 1984.

Vassberg, J. C. and Jameson, A. Theoretical background for aerodynamic shape optimization. Introduction to Optimization and Multidisciplinary Design in Aeronautics and Turbomachinery. Lecture Series of the von Karman Institue for Fluid Dynamics, 2012.

Verstraete, T. Introduction to optimization and multidisciplinary design. Introduction to Optimization and Multidisciplinary Design in Aeronautics and Turbomachinery. Lecture Series of the von Karman Institue for Fluid Dynamics, 2012.

Verstraete, T., Coletti, F., Bulle, J., Vanderwielen, T., and Arts, T. Optimization of a U-bend for minimal pressure loss in internal cooling channels - Part I: Numerical method. Journal of Turbomachinery, 135, September 2013.

Wallin, F. Flow Control and Shape Optimization of Intermediate Turbine Ducts for Turbofan Engines. PhD thesis, Chalmers University of Technology, 2008.

Wallin, F., Ore, S., Göttlich, E., and Santner, C. Aero-design and validation of a turning mid turbine frame. 20th ISABE Conference, Gothenburg, Sweden, ISABE-2011-1713, March 2011.

Wang, D. and He, L. Adjoint aerodynamic design optimization for blades in multi-stage turbomachines: Part I - Methodology and verification. Journal of Turbomachinery, 132(2), 2010.

Wang, H. P., Olson, S. J., Goldstein, R. J., and Eckert, E. R. G. Flow visualization in a linear turbine cascade of high performance turbine blades. Journal of Turbomachinery, 119, 1997.

Wanjin, H., Chunqing, T., Hong, S., Mochun, Z., and Zhongqi, W. Effects of leaning and curving of blades with high turning angles on the aerodynamic characteristics of turbine rectangular cascades. ASME Turbo Expo, Cincinnati, Ohio, United States, 93-GT-296, May 24-27 1993.

Wickerath, B. Untersuchung nichtlinearer Wirbelviskositätsmodelle zur Berechnung turbulenter Strömungen in Turbomaschinen. PhD thesis, Rheinisch-Westfälische Technische Hochschule Aachen, 2009.

Wilcox, D. C. Turbulence Modeling for CFD. DCW Industries, Inc., 1993.

Wu, H. and Liu, F. Aerodynamic design of turbine blades using an adjoint equation method. 43rd AIAA Aerospace Sciences Meeting and Exhibit, AIAA 2005-1006, Reno, Nevada, January 2005.

Yang, H., Nuernberger, D., and Kersken, H.-P. Towards excellence in turbomachinery computational fluid dynamics: A hybrid structured-unstructured Reynolds-averaged Navier-Stokes solver. Journal of Turbomachinery, 128:390–402, 2006.

Appendix A

Related Publications

This appendix contains papers that are related to this project in the order that they contribute to the work presented in this thesis. This is also roughly the order in which they have been published.

A short introduction to each paper is included to indicate how it relates to the main text.

A.1 Paper I

Akin, M. B. and Sanz, W. Influence of transition on CFD calculations of a two-stage counter-rotating turbine. ASME Turbo Expo, Düsseldorf, Germany, GT2014-26044, 2014.

This paper reports on the steady-state CFD simulations of the two-stage counter-rotating turbine that was tested on the TTTF. This investigation mainly served to validate CFD modeling and turbulence modeling as well as to determine the necessity of transition modeling. Two simulations, one using the SA turbulence model and one using the SST turbulence model were performed. A third simulation considered transition modeling with the SST turbulence model. The investigations were able to determine good agreement of the CFD simulaions with measurement results. The SST model marginally outperformed the SA model. Laminar to turbulent transiton regions could be identified using transition modeling on the blade suction side surfaces. The flow structures and overall performance of the turbine was only minorly affected by transition modeling. The endwalls remained mostly turbulent, which is one of the most important results of the investigation with regard to the optimization problem. For a final statement to be made, optimizations with transition modeling would also have to be performed and analysed, but these findings significantly reduce the importance of transition modeling for the optimization of the TMTF endwall.

THE INFLUENCE OF TRANSITION ON CFD CALCULATIONS OF A TWO-STAGE COUNTER-ROTATING TURBINE

M. Bugra Akin, Wolfgang Sanz
Institute for Thermal Turbomachinery and Machine Dynamics
Graz University of Technology
Graz, Austria, A-8010
Email: bugra.akin@tugraz.at

ABSTRACT

Accurate numerical simulations depend on the correct prediction of all relevant flow phenomena. For many aeronautical devices such as turbomachinery the behaviour of boundary layers, wall shear stress and wall heat transfer are significant for the performance. Turbulence and transition may influence such flow characteristics. Onset and the extent of transition can therefore be of high importance for the design process.

In this paper three-dimensional steady-state simulations of a two-stage turbine with and without modeling of transition are performed. The configuration consists of a transonic high pressure turbine stage followed by an S-shaped turning mid turbine frame and a counter-rotating low pressure turbine rotor. The in-house Reynolds-averaged Navier-Stokes solver has been applied to this configuration with the correlation based $\gamma - Re_\theta$ *transition model developed by Menter et al. which has been added to the SST turbulence model. Also, calculations without transition with the SST and the Spalart-Allmaras turbulence model have been performed. This configuration is also the subject of experimental investigations at the Institute for Thermal Turbomachinery and Machine Dynamics at Graz University of Technology, so that measurement data at two planes are used for the verification of the simulations. After verification and flow analysis, the results are also discussed to evaluate the effect of modeling transition phenomena. An analysis of the overall efficiency of the turbine and the efficiency losses in the blade and vane rows are finally presented.*

NOMENCLATURE

c_p	specific heat at constant pressure
c_a, c_e	constants
k	turbulent kinetic energy
Re	Reynolds number
R_T	viscosity ratio
s	specific entropy
T	temperature
t	time
U, v	velocity
y	wall distance
Ω	vorticity magnitude
γ	intermittency
δ	boundary layer thickness
η	efficiency
μ	dynamic viscosity
ρ	density
ω	turbulent specific dissipation, vorticity
MD	measurement data
HPV	high pressure vane
HPB	high pressure blade
LPB	low pressure blade
SA	Spalart and Allmaras turbulence model
SST	Shear stress transport model
$SSTTR$	SST with transition modeling
TKE	turbulent kinetic energy
$TMTF$	turning mid turbine frame

1 Introduction

Accurate solutions for aerodynamic analysis are one of the fundamental objectives of CFD. It constitutes a groundwork for various aerodynamic designs and improvements. Design proposals achieved with CFD can only be as good as the flow solution acquired, which depends on the correct prediction of all relevant flow phenomena. Turbulence and transition play an important role in turbomachinery applications and influence other flow characteristics such as separation behaviour of boundary layers, wall shear stress and wall heat transfer.

An overview of the transition phenomena in turbomachinery was presented by Mayle [1]. In his work three different modes of transition in boundary layers are introduced; natural, bypass and separated-flow transition.

Currently prediction of these transition phenomena is based mainly on two approaches. The first one makes use of low-Re number turbulence models, where the wall damping functions of the underlying turbulence model trigger the transition onset. The second one is based on models using experimental correlations. Menter *et al.* [2] argue that there is no inherent reason, why damping functions, which have been optimized to damp the turbulence in the viscous sublayer, should reliably predict an entirely different and complex physical process. On the other hand models based on experimental correlations do not attempt to model the physical process, but the physics are contained in the experimental correlations. Thus they can be used for all transition modes, provided that appropriate correlations are available.

The objective of this work is to investigate the influence of transition and turbulence modeling on the design process of turbomachinery. The correlation based $\gamma - Re_\theta$ transition model developed by Menter *et al.* [2], which has been implemented into the in-house CFD-code LINARS by Kelterer *et al.* [3], will be used to investigate the effects of transition.

Three steady-state simulations have been performed which differ only in the turbulence and transition modeling. One simulation has been performed with transition modeling (SSTTR). In this simulation turbulence was modeled with the SST turbulence model (SST) [4]. In the other two simulations the Spalart-Allmaras turbulence model (SA) [5] and the SST turbulence model have been used. The test case is a two-stage turbine which consists of a high pressure turbine stage followed by an S-shaped turning mid turbine frame and a counter-rotating low-pressure turbine rotor. The simulations have been performed steady-state with the mixing-plane approach for the interfaces between the blades and vanes as it is usually done in industry for blade design.

2 NUMERICAL METHOD

The computations were performed with the Navier-Stokes code LINARS developed at the Institute for Thermal Turbomachinery and Machine Dynamics (ITTM) by Pecnik *et al.* [6], which has been successfully utilized for the solution of numerous applications. The code solves the compressible Reynolds averaged Navier-Stokes equations in conservative form by means of a fully-implicit time-marching finite-volume method. Structured grids are utilized in multi-block assignment.

The inviscid fluxes are discretized with the upwind flux-difference splitting method by Roe [7]. A higher order of spatial accuracy for the convective fluxes is achieved through monotone upstream-centered schemes (MUSCL). To avoid numerical instabilities the total variation diminishing scheme (TVD) is applied, which switches to first order accuracy in regions of high state vector gradients. The viscid flux vector at the cell interfaces is constructed in a central-differencing manner using Green's theorem.

A linear set of algebraic equations is obtained by discretization in time with the Newton-Raphson procedure. The linearization of the inviscid fluxes is spatially of first order. The viscid fluxes are linearized with the thin layer approximation to obtain a block tridiagonal matrix of the implicit side for each grid index line. The linear equation set is solved by the alternating direction implicit scheme. Convergence of steady state simulations is improved by using a local time step based on a local stability criterion and a 3-level multigrid V-cycle. The main flow equations, the turbulence equations, and the transition equations are solved sequentially.

2.1 Turbulence Modeling

For the computations two different turbulence models have been used: The one-equation turbulence model by Spalart and Allmaras [5] (SA) and the two-equation shear stress transport (SST) model by Menter [4]. The reader is referred to the cited references for details about the models.

2.2 Transition Modeling

Transition modeling has been realized using the $\gamma - Re_\theta$ correlation-based transition model by Menter *et al.* [2] with the modification introduced by Langtry and Menter [8]. Detailed model formulation can be found in these references. Here the main equations and the interaction with the turbulence model will be introduced.

The model is based on two transport equations; one for the intermittency γ and one for the transition momentum thickness Reynolds number $\tilde{Re}_{\theta t}$. The transport equation for intermittency γ is defined as

$$\frac{\partial(\rho\gamma)}{\partial t} + \frac{\partial(\rho U_j \gamma)}{\partial x_j} = P_{\gamma 1} - E_{\gamma 1} + P_{\gamma 2} - E_{\gamma 2} + \frac{\partial}{\partial x_j}\left[\left(\mu + \frac{\mu_t}{\sigma_\gamma}\right)\frac{\partial \gamma}{\partial x_j}\right] \quad (1)$$

with the transition sources:

$$P_{\gamma 1} = F_{length} c_{a1} \rho S \left[\gamma F_{onset}\right]^{c_a}; \; E_{\gamma 1} = c_{e1} P_{\gamma 1} \gamma \qquad (2)$$

S is the strain rate magnitude and F_{length} is an empirical correlation that controls the length of the transition region. $P_{\gamma 2}$ and $E_{\gamma 2}$ are the destruction and relaminarization sources:

$$P_{\gamma 2} = c_{a1} \rho \Omega \gamma F_{turb}; \; E_{\gamma 2} = c_{e2} P_{\gamma 2} \gamma \qquad (3)$$

where Ω is the vorticity magnitude and

$$F_{turb} = e^{-\left(\frac{R_T}{4}\right)^4}. \qquad (4)$$

The transition onset is controlled by the following equation:

$$F_{onset} = max\left(F_{onset2} - F_{onset3}, 0\right) \qquad (5)$$

with

$$\begin{aligned} F_{onset1} &= \frac{Re_v}{2.193 Re_{\theta c}}; \\ F_{onset2} &= min\left(max\left(F_{onset1}, F_{onset1}^4\right), 2\right) \\ F_{onset3} &= max\left(1 - \left(\frac{R_T}{2.5}\right)^3, 0\right); \end{aligned} \qquad (6)$$

and

$$Re_v = \frac{\rho y^2 S}{\mu}; \; R_T = \frac{\rho k}{\mu \omega} \qquad (7)$$

$Re_{\theta c}$ is the critical momentum thickness Reynolds number where the intermittency starts to increase in the boundary layer.

The transport equation for the transition onset momentum thickness Reynolds number, $\tilde{Re}_{\theta t}$, is:

$$\frac{\partial(\rho \tilde{Re}_{\theta t})}{\partial t} + \frac{\partial(\rho U_j \tilde{Re}_{\theta t})}{\partial x_j} = P_{\theta t} + \frac{\partial}{\partial x_j}\left[\sigma_{\theta t}\left(\mu + \mu_t\right)\frac{\partial \tilde{Re}_{\theta t}}{\partial x_j}\right], \qquad (8)$$

where $P_{\theta t}$ is the source term depending on the transition momentum thickness Reynolds number $\tilde{Re}_{\theta t}$ and transition onset momentum thickness Reynolds number $Re_{\theta t}$.

The model contains three empirical correlations; one for the transition onset momentum thickness Reynolds number $Re_{\theta t}$ (based on freestream conditions) as observed in experiments, one for F_{length}, which is a measure for the length of the transition zone and one for $Re_{\theta c}$, which defines the location where the model is activated. These empirical correlations had originally not been published by Menter *et al.* for proprietary reasons. At ITTM empirical formulations of these correlations were based on extensive experimental and numerical studies and implemented into the LINARS code. The formulation of these corretions have been presented by Kelterer *et al* [3], [9]:

$$\begin{aligned} &\tilde{Re}_{\theta t} \leq 215 \Rightarrow \\ &Re_{\theta c} = 1.02 \cdot \tilde{Re}_{\theta t} - 35 + tanh\left(\frac{-\tilde{Re}_{\theta t} + 138}{54}\right) \cdot 36 \\ &\tilde{Re}_{\theta t} > 215 \Rightarrow \\ &Re_{\theta c} = 155 + tanh\left(\frac{\tilde{Re}_{\theta t} - 215}{15}\right) \cdot 45 \end{aligned} \qquad (9)$$

$$F_{length} = min\left[250 \cdot exp\left(-\left(\frac{\tilde{Re}_{\theta t}}{130}\right)^{1.7}\right) + 10; 40\right] \qquad (10)$$

Later after the publication of the correlations by Menter and Langtry [10] they were also implemented into the solver LINARS. The correlations used in this investigation are those developed at ITTM. Also simulations with the correlations by Menter and Langtry have been performed. They have shown similar results and will not be presented in this paper.

Finally the transition model interacts with the SST turbulence model by modification of the production and diffusion term of the k-equation

$$\frac{\partial(\rho k)}{\partial t} + \frac{\partial(\rho U_j k)}{\partial x_j} = \tilde{P}_k - \tilde{D}_k + \frac{\partial}{\partial x_j}\left(\left(\mu + \sigma_k \mu_t\right)\frac{\partial k}{\partial x_j}\right), \qquad (11)$$

with

$$\tilde{P}_k = \gamma P_k; \; \tilde{D}_k = min\left(max\left(\gamma, 0.1\right), 1\right) D_k, \qquad (12)$$

where P_k and D_k are the original production and destruction terms.

TABLE 1. OPERATING CONDITIONS OF THE TEST RIG

		HPV	HPB	TMTF	LPB
Total pressure ratio	-	3		1.3	
Blade count		24	36	16	72
Reynolds number	10^6	2.38	1.1	1.86	0.46
Reduced rot. speed	$\frac{rpm}{\sqrt{K}}$		524.4		168.2

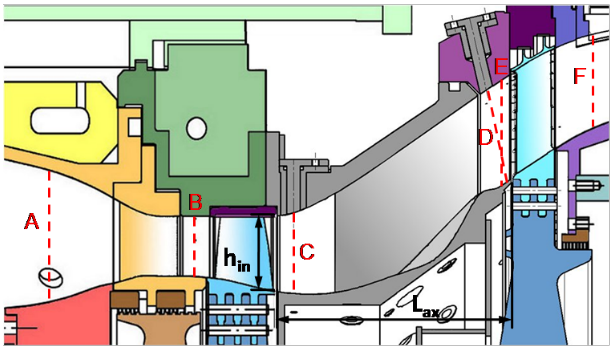

FIGURE 1. MERIDIONAL SECTION OF THE TEST SETUP SHOWING THE MEASUREMENT PLANES

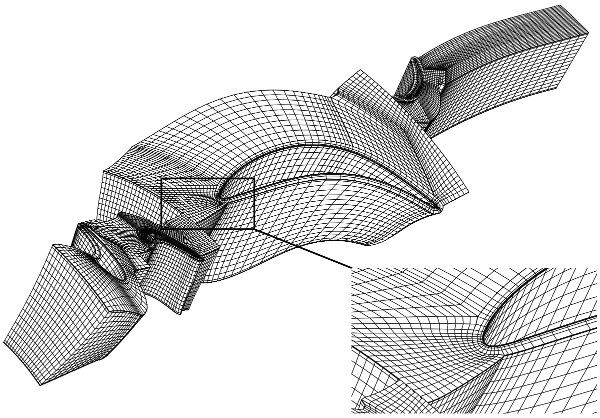

FIGURE 2. COMPUTATIONAL GRID OF 8.8 MILLION CELLS WITH EVERY FOURTH NODE PLOTTED

TEST CASE

Geometry and Experimental Setup

The test case for this study is a setup used for various experimental investigations which were conducted on the transonic test turbine facility (TTTF) of ITTM. The TTTF is a continously operating two-stage cold-flow open-circuit plant.

The test setup consists of a single-stage unshrouded transonic HP turbine, an S-shaped turning mid turbine frame (TMTF) followed by a shrouded counter-rotationg LP turbine. The turbine has been designed by MTU Aero Engines. The TMTF design used in this test case was developed by Volvo Aero (recently acquired by GKN plc.). These designs have both been developed within the framework of the EU Project DREAM. In Fig. 1 the meridional section of the test setup with the TMTF is shown, as well as the measurement planes A - F. The air flowing into the HP turbine is accelerated in circumferential direction by the vanes before entering the rotor. It leaves the rotor with a negative swirl which differs between hub and shroud section. Afterwards it is turned by the struts of the TMTF opposite to the direction of rotation of the HP rotor. The air then enters the LP rotor which rotates in the opposite direction of the HP rotor at about one third of its speed.

Table 1 shows the main parameters of the test rig at design conditions. The HP stage consists of 24 vanes and 36 blades and the LP stage consists of 16 struts and 72 blades. The entire setup with the HPT, TMTF and LP rotor has a periodicity of 90°.

The TMTF by Volvo Aero was designed with endwall contouring to reduce secondary flow losses. Fig. 3 shows the three dimensional contoured endwall profile of the hub. The contouring is illustrated with the contour plot of the deviation of the radius. Red indicates an increase and blue a decrease in respect to the axisymmetric contour. The design intent and benefits of this design have been discussed by Wallin *et al.* [11].

Detailed reports of the experimental investigations of the turbine are presented by Santner *et al.* [12] and Spataro *et al.* [13]. The measurements were conducted with five-hole probes, which were traversed radially over 95% of the blade height and over one HP vane pitch on plane C and over one TMTF strut pitch on plane E. The results obtained in these experimental campaigns are used for the validation of the simulations.

Grid Topology

Fig. 2 displays the multi-block grid consisting of 5 blocks for each vane/blade channel except for the HP blade, which is meshed with 8 blocks due to the tip leakage flow. An O-type block encloses each blade. The grid consists of a total of 8.8 million cells. The HP stator, HP rotor, TMTF and LP rotor are meshed with 1.05, 2.15,

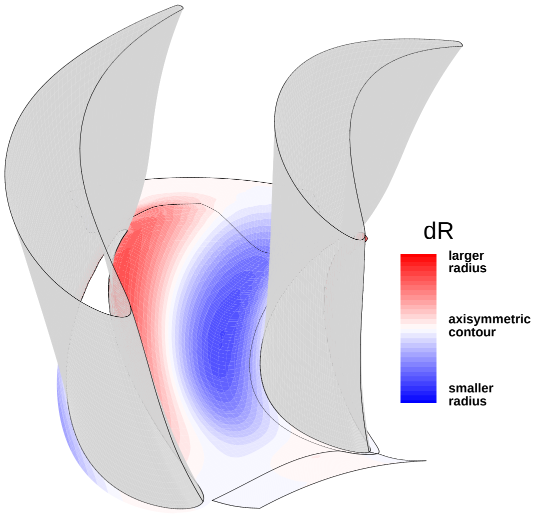

FIGURE 3. TMTF BLADES WITH A CONTOURED HUB ENDWALL

3.4 and 2.2 million cells, respectively. The y^+ value at all walls is mostly below 1. The mesh has been generated with an in-house mesher developed by Pieringer [14].

Boundary Conditions

Dirichlet boundary conditions have been applied. At the inlet total pressure, total temperature and flow direction have been specified and at the outlet the static pressure. The turbulence intensity has been set to 11% for the calculations with the SST model in accordance with measurement results. The mixing length is set to $1mm$. For the SST and SSTTR models the specified boundary conditions led to an average ratio of turbulent to laminar viscosity of 300 at the inlet. Consequently, for the SA model the ratio of turbulent to laminar viscosity is set to 300 at the inlet.

COMPUTATIONAL RESULTS AND DISCUSSION

Validation and Flow Analysis

As the flow in the TMTF is of special interest for recent and ongoing investigations in the institute, experimental results at the inlet (plane C) and outlet (plane E) of the TMTF are available. These planes are adequate for the validation of CFD results. Also plane B at the exit of the HP vane is of high importance for validation purposes and understanding the differences between measurements and CFD results. Unfortunately five-hole probes have not been applied to this plane as accessing it is not possible due to construction. In the following a comparison of the circumferentially averaged values of static pressure, total pressure and yaw angle of CFD and measurement results in Plane C and Plane E will be presented and analysed. Measurement uncertainties are $\pm 5.4\,mbar$ for the static pressure, $\pm 3\,mbar$ for the total pressure and $\pm 0.3^\circ$ for the yaw angle, so that they are not visible in the diagrams.

Plane C Fig. 4 shows the circumferentially averaged results of the measurements and simulations in plane C. Static pressure, total pressure and yaw angle have been evaluated. The static pressure distribution shows a drop of pressure from the hub to the casing. This trend is also predicted by CFD. In the measurement results the effect of the tip leakage flow can be seen close to the shroud, as a static pressure drop at 90% span can be observed. This trend is also reproduced by the CFD results. But the local minimum arising due to the tip leackage flow is at 80% span. Close to the mid section there is a region of faster pressure drop. This behaviour is less distinctive in the CFD results. The calculated values are about 0.015 to 0.025 bar higher than the measured values. The reason for this difference is not yet clearly understood and will be discussed at the end of the section.

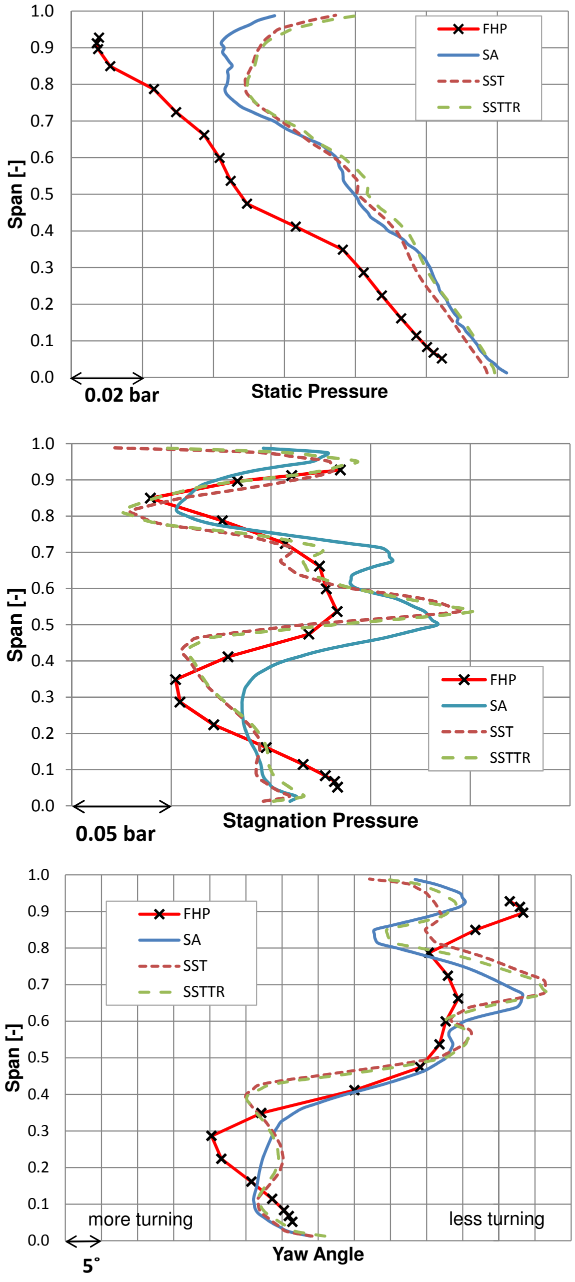

FIGURE 4. CIRCUMFERENTIALLY AVERAGED FIVE-HOLE-PROBE AND SIMULATION RESULTS ON PLANE C

In the plot of the total pressure the effect of the tip leakage can be seen. Less energy being extracted in this region close to the casing leads to an unloading of the rotor and an increased total pressure. The SST and SSTTR models predict this effect well, the SA predicts the region of higher total pressure closer to the wall. The steep fall below is better predicted by the SST and SSTTR models.

The SST and SSTTR models achieve a better agreement in the midspan region than the SA model, which overpredicts the total pressure, also showing a local minimum in the midspan region which is barely visible in the measurement results. In the region below 0.4 relative height the SA model predicts the position of the local minimum more accurately. But in regard of the value of the minimum pressure the SST and SSTTR models perform better.

The yaw angle distribution over the channel height shows that the flow is less turned close to the shroud (yaw angle is negative), because of the tip leakage flow and unloading of the rotor. The trend of the curve is captured relatively well. But the positions of the local minimum and maximum differ from measurement results. The SST and SSTTR models yield mostly concordant results except in the region close to the shroud.

To achieve a better understanding of the flow and the variations in the results as compared with the measurements the vortical structures in plane C have been analysed. The vortices that emerge as the flow passes through the HP blades in respect to the tip leakage flow have been discussed in detail by Sanz *et al.* [15]. Likewise, to work out the details of the vortical structures the streamwise vorticity has been inspected;

$$\omega_{SW} = \frac{\omega \cdot U}{\rho |U|^2} \tag{13}$$

Fig. 5 shows the contour plots of the streamwise vorticity for the three models. The viewing direction is from downstream of the flow. Red indicates an anti-clockwise rotation and blue a clockwise rotation of a vortex structure. The same vortices can be found on the plots of all models, but with varying intensity. The stationary shroud, which in respect to the fluid motion is turning in an anticlockwise direction, pulls the fluid along. The fluid which is pushed through the tip leakage works against this motion and the scraping vortex (A) and the tip leakage vortex B are formed. The tip leakage vortex rotates in the clockwise direction and the scraping vortex rotates in the anticlockwise. C is the upper passage vortex and D is the lower passage vortex. The development of these structures has been analyzed in detail by Wang *et al.* [16]. E and F are a result of the trailing edge shed vortex. The effects of these vortical structures can be seen on the total pressure distribution in Fig. 4. The high-energetic leakage flow causes the peak in the total pressure close to the shroud. The steep fall below is caused by the strong passage vortex. The fluctuations in the midspan region are caused by the vortices C and F. The loss in total pressure below midspan is due to the lower passage vortex carrying flow with less energy from the boundary regions into the middle of the channel.

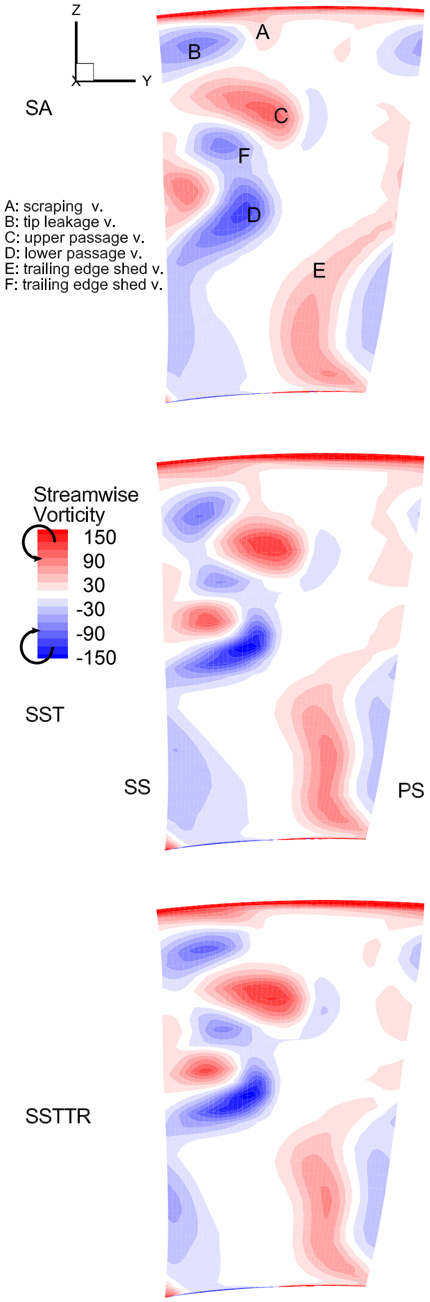

FIGURE 5. CONTOUR PLOTS OF THE STREAMWISE VORTICITY IN PLANE C FOR THE THREE MODELS

There is very little diffference in the solutions with the three models. They yield the same vortex structures with varying intensity and slight changes in their exact positions, which is reflected in the circumferentially averaged results as shown in Fig. 4.

Plane E The measurements in plane E (Fig. 6) show a more uniform distribution of the circumferentially averaged values. The radial distribution of the static pressure is a result of the S-shaped contour of the intermediate duct. The radius of the second bend before exit, which is smaller at the hub, leads to higher velocities and lower static pressure. Also the decrease of total pressure very close to the hub (5% span) indicates the presence of a thick boundary layer. The CFD results of static pressure show good agreement with measurement results. The SST model is in excellent accordance above 30% span, whereas the SSTTR model slightly overpredicts the static pressure, especially in the lower half of the passage. The SA model yields results similar to those with the SSTTR model. Below 30% all models underpredict the static pressure.

Contrary to the static pressure the SST and SSTTR models are in very good agreement with the total pressure measurement results in the lower region below 40% span. It can be seen that the CFD results for these cases are nearly the same as measurement results. All models underpredict the total pressure between 44% and 82% span. Above this region the calculated values are higher than the measured results except for the results of the SA model. Apart from these deviations the trends of the curves are the same. There are differences in position and magnitude of local minima and maxima.

The yaw angle is predicted with relatively good accuracy above 60% span with all three models. There is no significant advantage of one model over the other. Below 60% span there is a drop in the turning of more than 10° which is not confirmed by the measurement results (the yaw angle is negative). The reason for this lies in the modeling of interfaces with the mixing-plane approach, and will be explained with the help of the next figure (Fig. 7).

Fig. 7 shows contour plots of the streamwise vorticity for plane E. Again, the viewing direction is from downstream of the flow. The development of the vortex structures that can be observed in a similar TMTF has been discussed in detail by Spataro *et al.* [13]. The main structures that are expected to be seen after the trailing edge are the upper and lower passage vortices, as discussed by Wallin *et al.* [11]. The upper channel vortex A and the counter-rotating trailing edge shed vortex B can be identified in the contour plot. C can be interpreted as the trailing edge shed vortex, which rotates in the opposite direction of the lower passage vortex. Yet the lower passage vortex cannot be observed. Other vortex structures that can be seen in Fig. 7, that have been denoted with D and E (or not denoted at all) stem from the high pressure rotor. They are already existent at the mixing-plane inlet and are transported downstream with a slight distortion. This distortion is a twisting motion in the clock-wise direction. It has been identified by Spataro *et al.* [13] as the vane passage vortex.

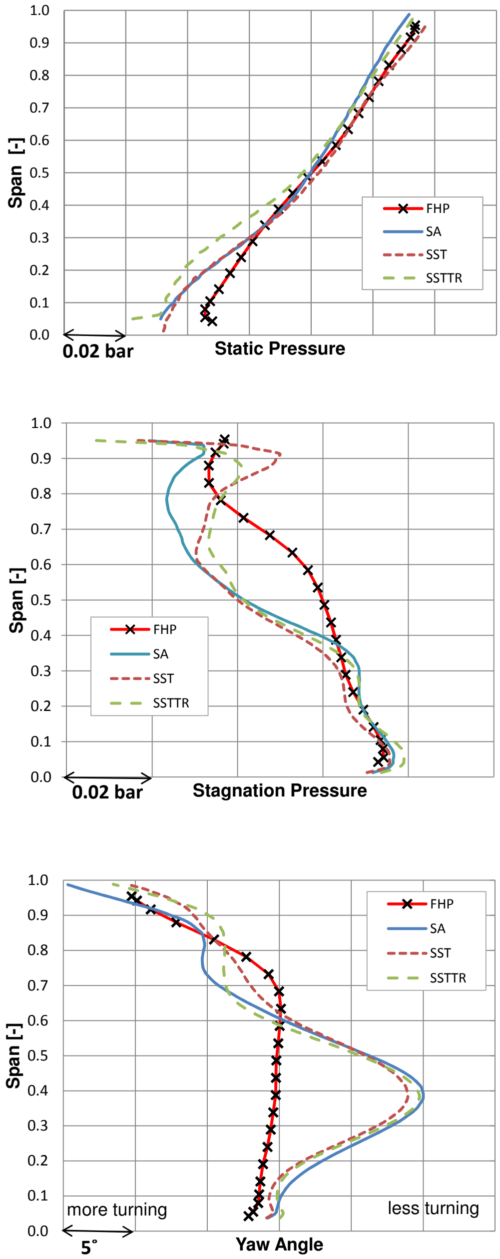

FIGURE 6. CIRCUMFERENTIALLY AVERAGED FIVE-HOLE-PROBE AND SIMULATION RESULTS ON PLANE E

The vortices D and E are responsible for the prediction of less turning in the lower half of the passage which can be seen in the plot of the yaw angle in Fig. 6. The rotation direction of these vortices has been drawn on the results from the SST model in Fig. 7. The turning induced upon the flow by the blades is from the viewing

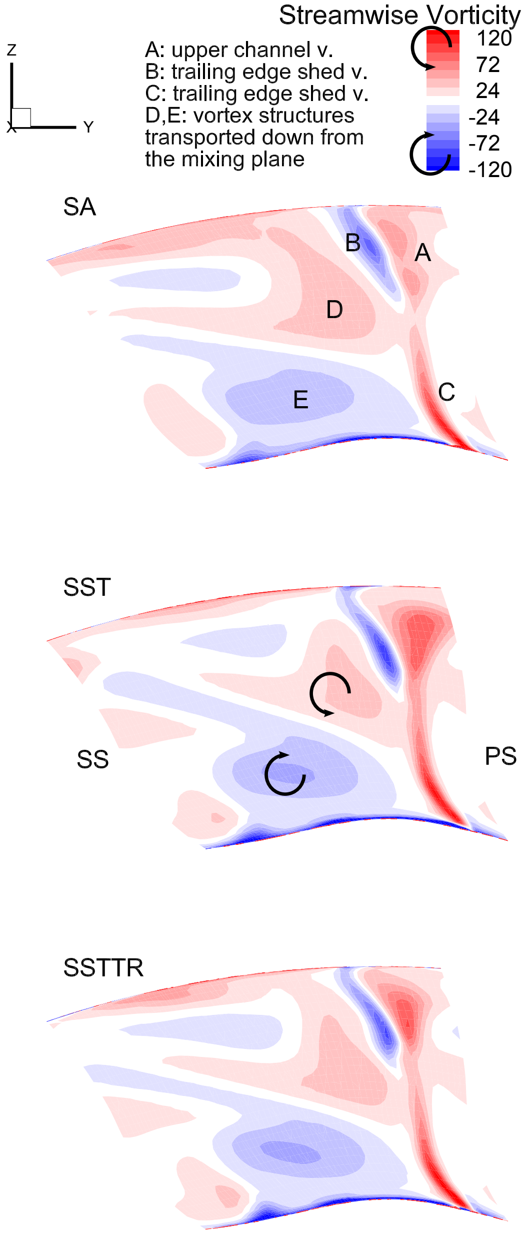

FIGURE 7. CONTOUR PLOTS OF THE STREAMWISE VORTICITY IN PLANE E FOR THE THREE MODELS

direction to the left. The vortices D and E both push the flow to the right at approximately 40% span due to their vorticity, hence causing less flow turning at this region of the flow.

The individual vortices differ in their strength between the different solutions. This explains the differences of the CFD results seen in the radial distributions in Fig. 6. The simulations are in good agreement with the measurements, but partly with significant local deviations. The SST and SSTTR solutions differ only slightly from each other, whereas the differences to the SA solution are more distinctive.

Efficiency

Amongst the most important analysis performed with CFD is the calculation of the efficiency and mass flow rate for development and improvement studies of designs. Here we will discuss these values for this setup and compare them with measurement results. Fig. 8 (above) shows the total-to-static efficiency and the mass flow rate of the turbine in reference to the experimental results.

The SSTTR models approximates the mass flow rate best, with only a slight overprediction of 0.09%, whereas the SA and SST models underpredict it with a slightly higher deviation of 0.25% and 0.16%, respectively.

The efficiency is overestimated by all three models. But in contrast to the mass flow rate the efficiency is best approximated with the SA model. The difference of the efficiency to the reference value is about 3.5% for the SA, 4% for the SST and 4.25% for the SSTTR model.

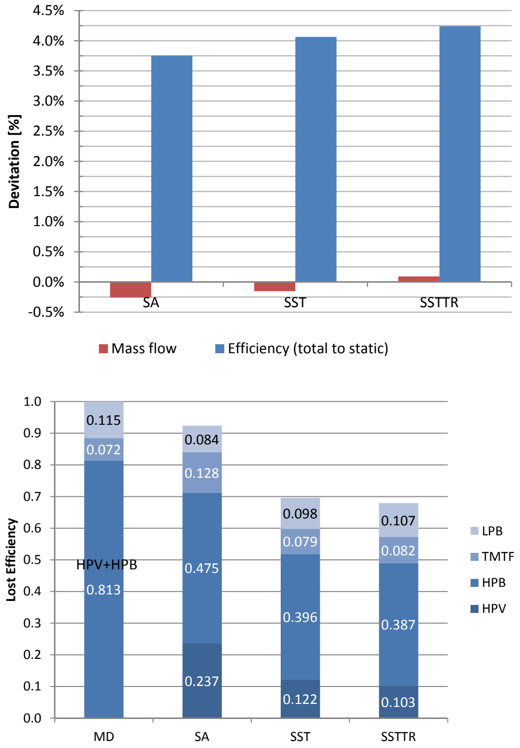

FIGURE 8. EFFICIENCY AND MASS FLOW PREDICTED BY THE DIFFERENT MODELS AND THE LOSS DISTRIBUTION OF THE BLADE AND VANE ROWS

TABLE 2. TURBULENT KINETIC ENERGY AT ROW EXITS

TKE	HPV	HPB	TMTF	LPB
SST	109.6	437.2	157.6	68.0
SSTTR	100.2	419.1	169.0	73.1

According to Pullan *et al.* [17] the loss of the individual blade rows can be approximated by

$$\Delta\eta = \frac{\Delta s_{blade} T_{t_F}}{c_p \left(T_{t_A} - T_{t_F}\right) + \Delta s_{turbine} T_{t_F}} \tag{14}$$

where T_{t_A} is the total temperature at turbine inlet (plane A) and T_{t_F} is the total temperature at turbine outlet (plane F). $\Delta s_{turbine}$ refers to the entropy difference from the turbine inlet to the turbine outlet and Δs_{blade} refers to the entropy production in a specific blade row. All values are mass averaged. The first term in the denominator in Eq. 14 is the work output of the turbine. The second term is the energy loss due to entropy generation. The sum of both the terms is the potential of work output of the isentropic process. The numerator is the energy loss in a specific blade row due to entropy generation.

In Fig. 8 (below) the results of this evaluation are represented. The lost efficiency is plotted in reference to measurement results, which has been scaled to a hundred percent. As there are no measurement results in plane B the loss generated in HPV and HPB has been merged in the plot. There is a big difference in the amount of loss generated in the HP stage between measurements and simulations. This is due to an underprediction of the total temperature which will be discussed in the next section.

The influence of transition modeling can be observed by comparing the losses in the HPV and HPB where transition is predicted. The lowest losses in these blade rows are calculated with the SSTTR model which explains the higher efficiency calculated with this model. These lower losses are due to a laminar or transitional region with smaller turbulent viscosity causing less frictional losses.

The TMTF and the LPR flows are predicted to be mostly turbulent by the SSTTR model. The losses predicted in these rows are higher than those predicted with the SA and SST models. This is unexpected and might be caused by other loss mechanisms. Higher turbulence can be determined in the passage flow by comparing the TKE at blade row outlets as shown in Table 2. It can be seen that the TKE predicted by SSTTR is higher for these two rows.

Discussion of measurement and CFD results

The calculations with CFD have shown two important deviations from measurement results. These are the overprediction of static pressure and the underprediction of total temperature at the HP stage exit. The temperature deviation has not been shown explicitly. But they are reflected in Fig. 8. The loss evaluated for the HP stage with Eq. 14 is lower because of the lower temperature predicted with CFD which affects the calculated entropie generation in the vane/blade rows. The reason for these discrepancies is not completely clear. It could be due to a possible overprediction of the flow turning at plane B, possibly caused by slight deviations in the geometry. For this test case it can be demonstrated with Euler's turbine equation that a difference of 1° in the yaw angle at plane B would cause a temperature deviation of around $5\,K$, which is the amount of the deviation between measurement and CFD results. Also, the difference in geometry would affect the static pressure as the mass flow through the turbine is determined by the HP stator throat area. Such geometry deviations could exist because of production inaccuracy or fillets at the blade-endwall intersection which are not modelled in the CFD. Unfortunately experimental data at plane B does not exist. Further research will follow regarding this topic.

Effects of transition modeling

The comparison with measurement results, analysis of flow structures or the calculation of the efficiency show that with transition modeling better agreement with measurement data couldn't be achieved. Yet the boundary layer flow is clearly influenced by transitional effects. Fig. 9 shows the intermittency on the hub and blades through the turbine channel. The values have been plotted a few cells away from the boundary layer. It has to be noted that with increasing boundary layer thickness the cell layer can remain within the laminar sublayer so that the representation has to be seen qualitatively. Transition regions along the channel walls can be observed. On the suction side of the HP vane transition of the flow to fully turbulent can be seen, also on the hub a laminar region can be observed. The boundary layer flow downstream of this region is nearly fully turbulent on the hub. There is also a transition region on the suction side of the HP blade, which is shown on Fig. 12. The boundary layer around the TMTF blade and LP blade is mainly turbulent. Additionally on the endwall contours the flow is mostly turbulent.

Fig. 10 shows a 3D plot of the skin friction coefficient along the suction surface of the HP vane and line plots at 25%, 50% and 75% span. Both turbulence models without transition show similar results. Transition is assumed to be completed when the SSTTR values of skin friction coincide with the SST values. At 75% span

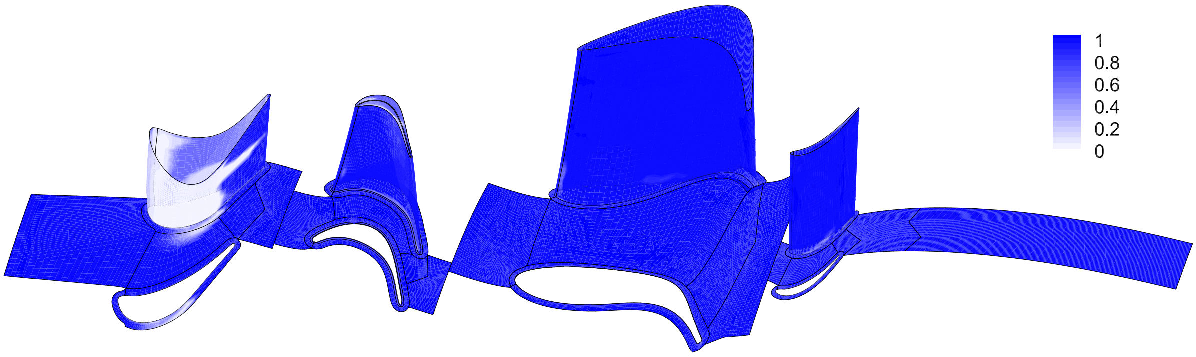

FIGURE 9. INTERMITTENCY ON THE WALLS THROUGH THE CHANNEL

the transitional boundary layer becomes fully turbulent at about 0.7 axial chord and shows then slightly higher values than the SST model. At midspan the boundary layer remains transitional up to the trailing edge. At 25% span the skin friction coefficient of the SA and SST solutions increases rapidly to 0.75 axial chord then decreases suddenly. This sudden change is the influence of a shock which triggers transition to fully turbulent flow for the SSTTR solution. On the pressure side the SSTTR solution predicts lower skin friction in the aft section of the blade.

To see the influence of transition on the passage flow at the HPV exit the stagnation pressure results from the SST and SSTTR solutions are compared at plane B. Less stagnation pressure loss is predicted by the SSTTR model. The trend of this result is similar to those in the planes C and E, and is due to the fact that the same secondary flow structures can be seen in both the solutions, but with varying magnitude of the vortices.

A transitional region is located on the suction side of the HP blade which can be seen in Fig. 12. The SSTTR solution predicts transitional flow in the front section of the blade suction side. Overlap with the SST solution and thus full transition can be observed at 0.45, 0.6 and 0.4 axial chord at 75%, 50% and 25% spans, respectively. It is interesting to observe that transition at mid-section occurs, as with the HPV, at the furthest downstream position. At all locations the SA model predicts a higher skin friction. Again, on the pressure side the SSTTR solution predicts lower skin friction only in the aft section of the blade.

In the TMTF (Fig. 13), there is very little difference between the SST and SSTTR solutions. Only at 75% and 25% span slight deviations can be seen in the front section. At 75% span the SSTTR solution predicts the drop in the value of the skin friction later than the SST model. At 25% span there seems to be relaminarization at 0.1 axial chord and transition back to turbulent at 0.4 axial chord (this can also be seen in intermittency plots). The SA model shows values in the same range apart from higher values on the pressure side at 75% span.

Fig. 14 shows the skin friction values for the last blade row. All models predict a similar distribution; the SA model predicts the highest values. The SSTTR model predicts transitional flow for the most part of the blade suction side. Fully turbulent flow occurs at the aft section of the blade. On the pressure side the results are nearly identical.

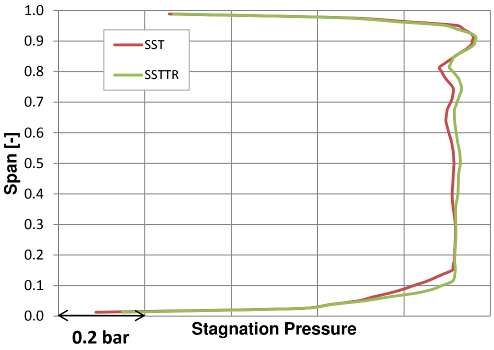

FIGURE 11. CIRCUMFERENTIALLY AVERAGED STAGNATION PRESSURE ON PLANE B CALCULATED WITH THE SST AND SSTTR MODELS

TABLE 3. SKIN FRICTION FORCE ON THE BLADE WALLS

F_s $[N]$	HPV	HPB	TMTF	LPB
SA	2.527	2.025	2.284	0.539
SST	2.392	1.496	2.185	0.499
SSTTR	1.756	1.344	2.205	0.473

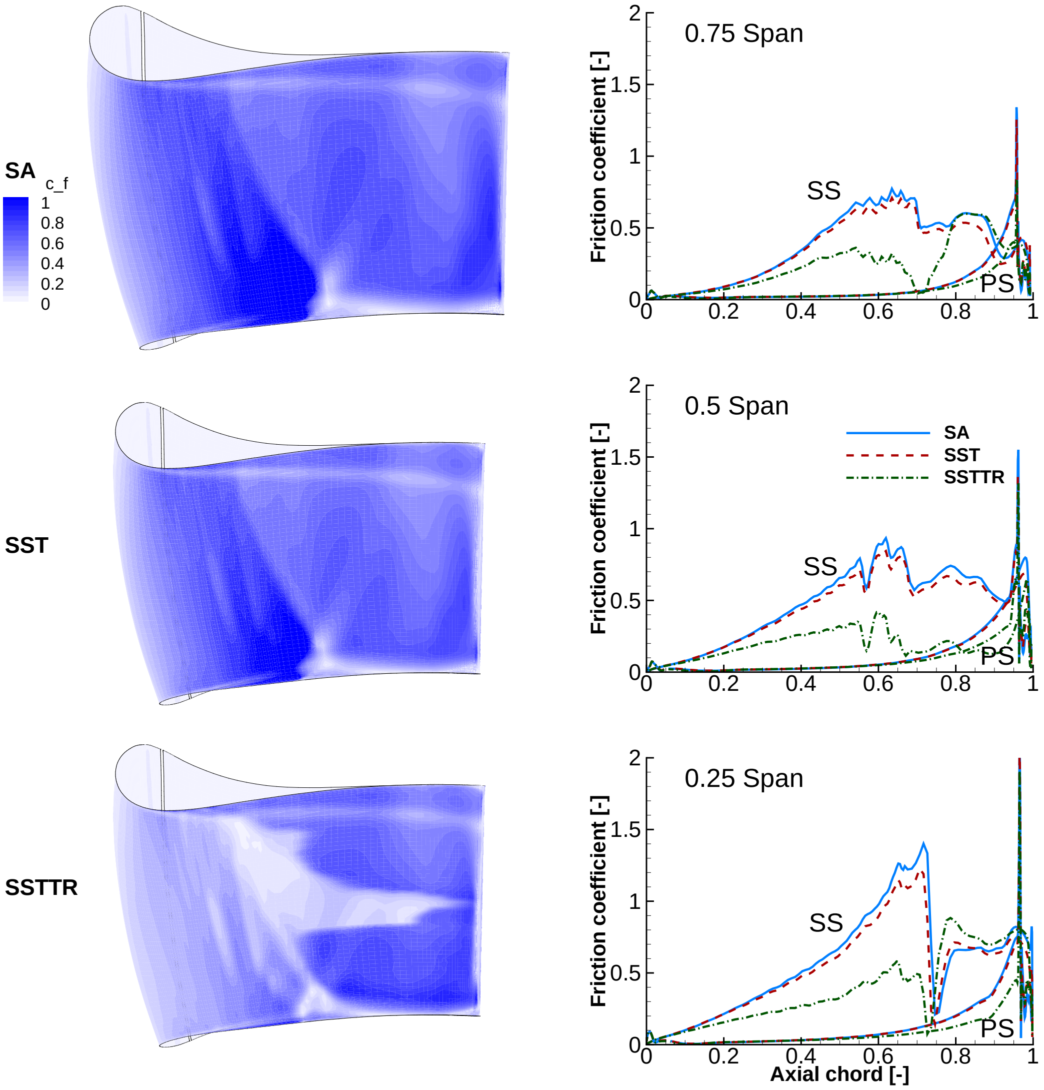

FIGURE 10. SKIN FRICTION COEFFICIENT ON THE SUCTION SIDE OF THE HP VANE AND AT 25%, 50% AND 75% SPAN

In Table 3 the frictional forces induced upon the flow by the blades are printed. They explain the differences in the lost efficiencies plotted in Fig. 8, as a lower frictional force results in lower losses in the blade rows. For example, for the HP vane rows the frictional force calculated with the SSTTR model is lowest. Also the lost efficiency calculated with this model for this blade row is lowest. This correlation is also present for for the next blade rows, except for the LP rotor.

Loss in the LP rotor, as shown in Fig. 8, cannot be explained by the frictional force induced by the blades. The loss is predicted highest with the SSTTR model, whereas the frictional force induced by the blades is lower than of the calculations without transition. Therefore the turbulent kinetic energy was analyzed at the exit planes of each blade row (Table 2). Although in the high pressure stage the SST model predicts higher turbulence, in both blade rows of the low pressure stage the turbulence is higher for the SSTTR model. This indicates higher losses by turbulent fluctuations, which may cause the higher total losses in the LP blade predicted by the SSTTR model, despite lower friction losses an the blade walls.

CONCLUSIONS

Three-dimensional steady-state simulations with mixing-plane interfaces of a two stage turbine have been performed using two different turbulence models, Spalart-Allmaras and SST. A third simulation using the transition model by Menter *et al.* has also been done.

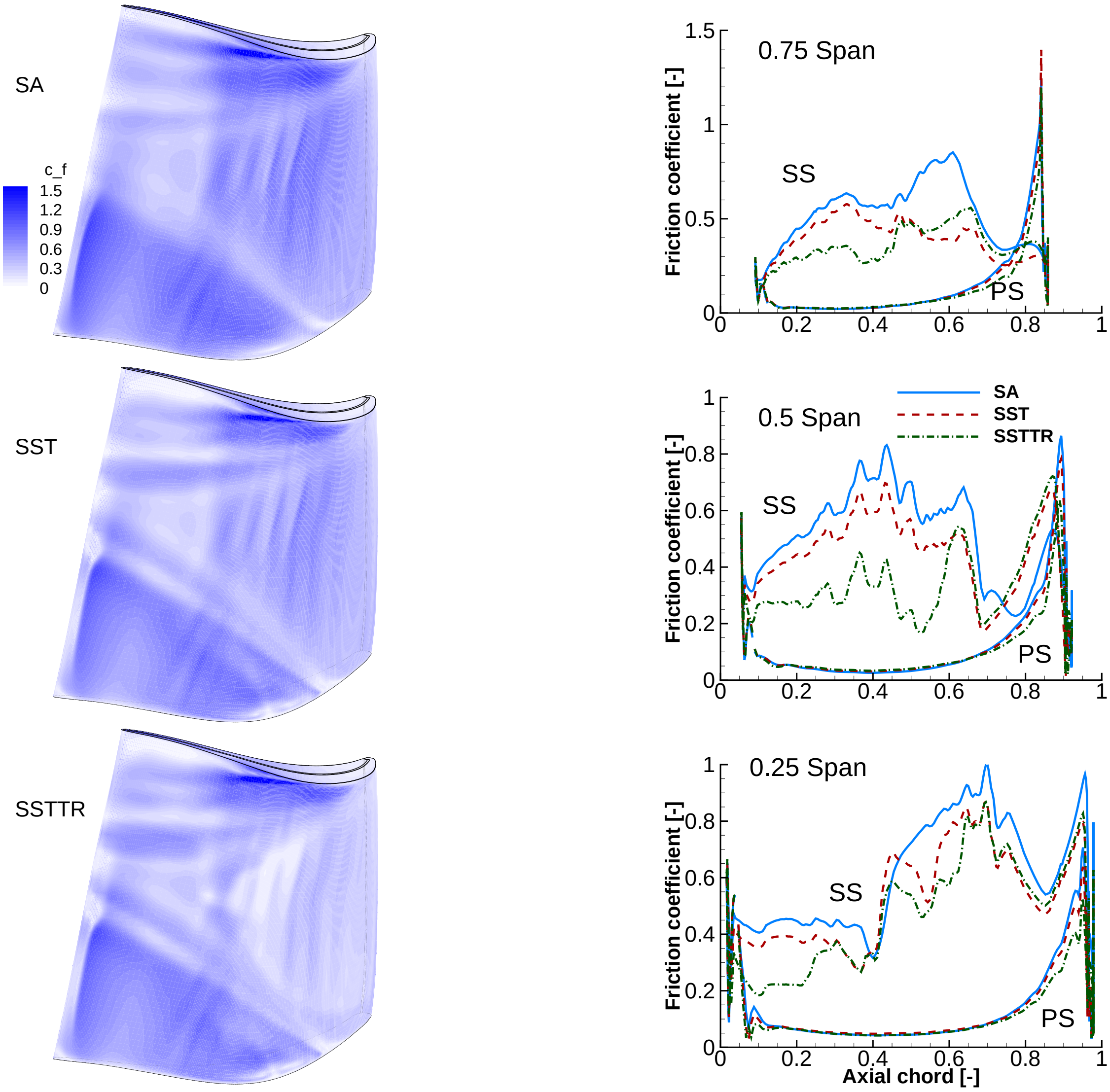

FIGURE 12. SKIN FRICTION COEFFICIENT ON THE SUCTION SIDE OF THE HP BLADE AND AT 25%, 50% AND 75% SPAN

The calculations have been validated with measurement results, and the secondary flow effects have been analysed.

The SST model yields slightly better results than the SA model in comparison to the measurement values in the planes C and E, in front of and behind the TMTF. There is generally good agreement, especially in the comparison of the static pressure (above 0.5 span) and of the total pressure (below 0.5 span) in plane E. But there are also some considerable discrepancies. For example, the flow turning in plane E at the exit of the turning mid turbine frame is partly underpredicted. It has been explained that the mixing-plane approach causes this difference. Another disagreement was observed in the results of the the static pressure and total temperature. The reason is not completely clear. It is assumed to lie in geometry differences such as blade-endwall fillets which are not modeled. This will be further investigated.

The effect of transition on the flow has also been investigated in detail. The evolution of transition has been visualised on the blade surfaces with contour plots and line plots. It has been seen that the flow is mostly transitional on the suction side of all blades, and distinct transition takes place on the suction side of the HP vanes and blades. The skin friction force induced upon the blades is less, if transition is taken into account. Additionally, it has been pointed out that transition on wall surfaces can affect the turbulence level of the passage flow through the turbine.

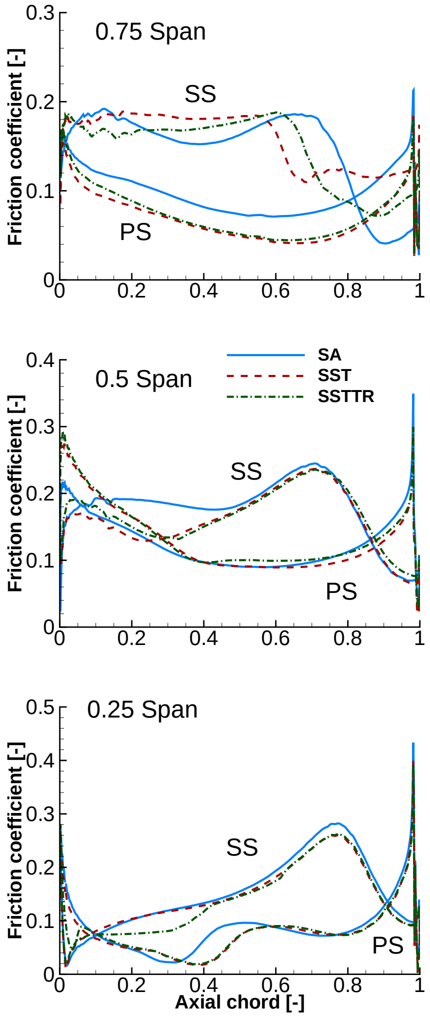

FIGURE 13. SKIN FRICTION COEFFICIENT AT 25%, 50% AND 75% SPAN OF THE TMTF

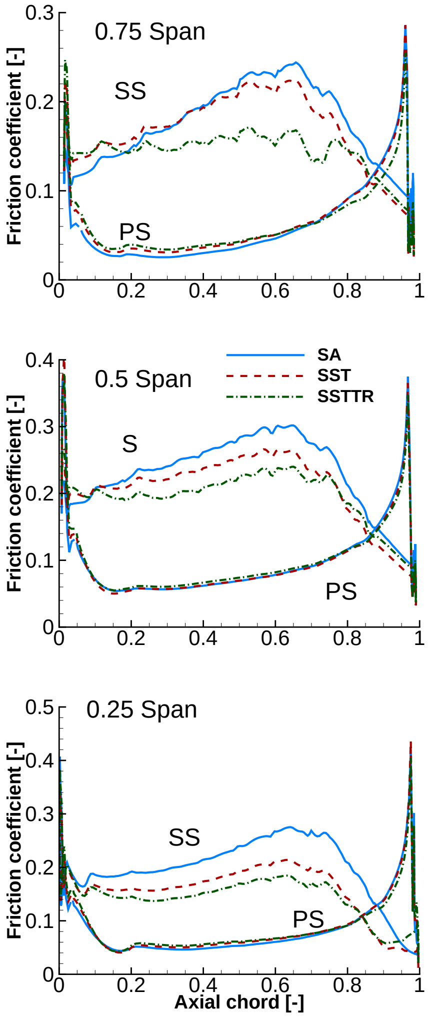

FIGURE 14. SKIN FRICTION COEFFICIENT AT 25%, 50% AND 75% SPAN OF THE LPB

ACKNOWLEDGMENT

The authors would like to thank the Austrian Federal Ministry for Transport, Innovation and Technology who funded the project SEIKON3D within the Austrian Aeronautics Program TAKE OFF. The research leading to some of these results has been partially funded by the European Union within the EU-project DREAM (contract No. ACP7-GA-2008-211861), as well as from the Austrian Federal Ministry for Finance.

REFERENCES

[1] Mayle, R. E., 1991. "The 1991 IGTI scholar lecture: The role of laminar-turbulent transition in gas turbine engines". *Journal of Turbomachinery,* **113**(4), pp. 509–536.

[2] Menter, F. R., Langtry, R. B., Liki, S. R., Suzen, Y. B., Huang, P. G., and Voelker, S., 2004. "A correlation-based transition model usind local variables Part 1 - Model formulation". ASME Turbo Expo 2004, Vienna, Austria, no. GT2004-53452.

[3] Kelterer, M., Pecnik, R., and Sanz, W., 2010. "Computation of laminar-turbulent transition in turbomachinery using the correlation based γ-Re$_\theta$ transition model". ASME Turbo Expo 2010: Power for Land, Sea and Air, Glasgow, UK, no. GT2010-22207.

[4] Menter, F. R., 1994. "Two-equation eddy-viscosity turbulence models for engineering applications". *AIAA Jounal,* **32**, pp. 1598–1605.

[5] Spalart, P. R., and Allmaras, S. R., 1994. "A one-equation turbulence model for aerodynamic flows". *Recherche Aerospatiale,* **1**, pp. 5–21.

[6] Pecnik, R., Pieringer, P., and Sanz, W., 2005. "Numerical investigation of the secondary flow of a tran-

sonic turbine stage using various turbulence closures". ASME Turbo Expo 2005, Nevada, USA, no. GT2005-68754.

[7] Roe, P. L., 1981. "Approximate riemann solvers, parameter vectors and differencing scheme". *Journal of Computational Physics,* **43**, pp. 357–372.

[8] Langtry, R. B., and Menter, F. R., 2005. "Transition modeling for general CFD applications in aeronautics". 43rd AIAA Aerospace Sciences Meeting and Exhibit, no. AIAA 2005-522.

[9] Kelterer, M. E., Burgstaller, R., and Sanz, W., 2011. "Application of the gamma-Re_theta transition model to transitional flow". International Symposium on Experimental and Computational Aerothermodynamics of Internal Flows, Brussels, Belgium, no. ISAIF10-091.

[10] Menter, F. R., and Langtry, R. B., 2009. "Correlation-based transition modeling for unstructured parallelized computational fluid dynamics codes". *AIAA Journal,* **47**(12), pp. 2894–2906.

[11] Wallin, F., Ore, S., Goettlich, E., and Santner, C., 2011. "Aero-design and validation of a turning mid turbine frame". 20th ISABE Conference, Gothenburg, Sweden, no. ISABE-2011-1713.

[12] Santner, C., Paradiso, B., Malzacher, F., Hoeger, M., Hubinka, J., and Goettlich, E., 2011. "Evolution of the flow through a turning mid turbine frame applied between a transonic HP-turbine stage and a counter-rotation LP-turbine". 9th European Turbomachinery Conference, Istanbul, Tuerkei.

[13] Spataro, R., Santner, C., Lengani, D., and Goettlich, E., 2012. "On the flow evolution through a LP turbine with wide-chord vanes in an S-shaped channel". ASME Turbo Expo 2012, Copenhagen, Denmark, no. GT2012-68178.

[14] Pieringer, P., 2012. AIGRID3D. Springer und Pieringer EDV Dienstleistungen OEG.

[15] Sanz, W., Kelterer, M., Pecnik, R., Marn, A., and Goettlich, E., 2009. "Numerical investigation of the effect of tip leakage flow on an s-shaped intermediate turbine duct". ASME Turbo Expo 2009, Florida, USA.

[16] Wang, H. P., Olson, S. J., Goldstein, R. J., and Eckert, E. R. G., 1997. "Flow visualization in a linear turbine cascade of high performance turbine blades". *Journal of Turbomachinery,* **119**.

[17] Pullan, G., Denton, J., and Curtis, E., 2006. "Improving the performance of a turbine with low aspect ratio stators by aft-loading". *Journal of Turbomachinery,* **128**(3), pp. 492–499.

A.2 Paper II

Akin, M. B. and Sanz, W. Numerical investigation of a two-stage counter-rotating turbine with transition modeling and prediction improvement with time-accurate calculations. ETMM 10, Marbella, Spain, 2014.

This paper reports on the time-accurate simulations with transition modeling. The results are compared to previously published steady-state analysis. The significance of time-accurate calculations or rather the inaccuracy of steady-state calculations using mixing-planes is confirmed. The comparison to measurement results showed much better agreement for time-accurate simulations both in quantitive terms of flow variables and in secondary flow structures, which were inaccurate with steady-state calculations due to averaging at the mixing-plane. Additionally, transition regions are significantly different in both simulations. The results show the importance of time-accurate simulations for accurate predictions of turbine flow.

NUMERICAL INVESTIGATION OF A TWO-STAGE COUNTER-ROTATING TURBINE WITH TRANSITION MODELING AND PREDICTION IMPROVEMENT WITH TIME-ACCURATE CALCULATIONS

M. Bugra Akin, Wolfgang Sanz

Institute for Thermal Turbomachinery and Machine Dynamics
Graz University of Technology
Graz, Austria, A-8010

bugra.akin@tugraz.at

Abstract

Accurate numerical simulations depend on the correct prediction of all relevant flow phenomena. For many aeronautical devices such as turbomachinery the behavior of boundary layers, wall-shear-stress and wall heat transfer are significant for the performance. Turbulence and transition influence such flow characteristics. Onset and extent of transition can therefore be of high importance for the design process.

Three-dimensional steady-state and time-accurate simulations of a two-stage turbine with transition modeling have been performed. The configuration consists of a transonic high pressure turbine stage followed by an S-shaped turning mid turbine frame and a counter-rotating low pressure turbine rotor. The inhouse Reynolds-averaged Navier-Stokes solver has been applied to this configuration with the correlation based $\gamma - Re_\theta$ transition model developed by Menter et al. which was added to the SST turbulence model. The results are discussed to evaluate the accuracy gain through time-accurate simulations and its effect on transition phenomena. An analysis of the overall efficiency of the turbine and the efficiency losses in the blade and vane rows are also presented.

1 Introduction

Accurate predictions for aerodynamic analysis are one of the fundamental objectives of CFD. It constitutes a groundwork for various aerodynamic designs and improvements. Design proposals achieved with CFD can only be as good as the flow solution acquired, which depends on the correct prediction of all relevant flow phenomena. Turbulence and transition play an important role in turbomachinery applications and influence other flow characteristics such as separation behavior of boundary layers, wall shear stress and wall heat transfer. An overview of the transition phenomena in turbomachinery was presented by Mayle (1991).

Previous work of our group on the influence of transition and turbulence modeling on the design process of turbomachinery has been published by Akin and Sanz (2014). The correlation based $\gamma - Re_\theta$ transition model developed by Menter et al. (2004), which has been implemented into the in-house CFD-code LINARS by Kelterer et al. (2010), was used to investigate the effects of transition on a steady-state test case.

This work extends these investigations with a time-accurate simulation to clarify the relevance of details lost in the steady-state calculation with the mixing-plane approach.

2 Numerical Method

The computations were performed with the Navier-Stokes code LINARS developed at the institute by Pecnik et al. (2005), which has been successfully utilized for the solution of numerous applications. The code solves the compressible Reynolds-averaged Navier-Stokes equations in conservative form by means of a fully-implicit time-marching finite-volume method. Structured grids are utilized in multiblock assignment.

The inviscid fluxes are discretized with the upwind flux-difference splitting method by Roe (1981). A higher order of spatial accuracy for the convective fluxes is achieved through monotone upstream-centered schemes (MUSCL). To avoid numerical instabilities the total variation diminishing scheme (TVD) is applied, which switches to first order accuracy in regions of high state vector gradients. The viscid flux vector at the cell interfaces is constructed in a central-differencing manner using Green's theorem.

A linear set of algebraic equations is obtained by discretization in time with the Newton-Raphson procedure. The linearization of the inviscid fluxes is spatially of first order. The viscid fluxes are linearized with the thin layer approximation to obtain a block tridiagonal matrix of the implicit side for each grid index line. The linear equation set is solved by the alternating direction implicit scheme. Convergence of steady-state simulations is improved by using a local time step based on a local stability criterion and a 3-level multigrid V-cycle. The main flow equations, the turbulence equations, and the transition equations are solved sequentially.

To gain periodic solutions in time and space for arbitrary stator and rotor blade numbers, phase-lag boundary conditions at geometrical periodic boundaries and at the interface between stator and rotor domain were applied. This has been implemented into the code by Pieringer et al. (2005).

Turbulence and Transition Modeling

The calculations have been performed with the two-equation shear stress transport turbulence model by Menter (1994).

Transition modeling has been realized using the $\gamma - Re_\theta$ correlation-based transition model by Menter et al. (2004) with the modification introduced by Langtry and Menter (2005). The model is based on two transport equations: one for the intermittency γ, which is the fraction over time the flow is turbulent at a certain location; and one for the transition momentum thickness Reynolds number $\tilde{Re}_{\theta t}$. Detailed model formulation can be found in Menter et al. (2004) and Menter and Langtry (2009). The model contains two empirical correlations which were initially not published: one for F_{length}, which is a measure for the length of the transition zone; and one for $Re_{\theta c}$, which defines the location where the model is activated. Therefore in-house correlations were developed by Kelterer et al. (2010, 2011):

$$\tilde{Re}_{\theta t} \leq 215 \Rightarrow \tag{1}$$

$$Re_{\theta c} = 1.02 \cdot \tilde{Re}_{\theta t} - 35 + \tanh\left(\frac{-\tilde{Re}_{\theta t} + 138}{54}\right) \cdot 36 \tag{2}$$

$$\tilde{Re}_{\theta t} > 215 \Rightarrow \tag{3}$$

$$Re_{\theta c} = 155 + \tanh\left(\frac{-\tilde{Re}_{\theta t} - 215}{15}\right) \cdot 45 \tag{4}$$

$$F_{length} = \min\left[250 \cdot \exp\left(\left(\frac{-\tilde{Re}_{\theta t}}{130}\right)^{1.7}\right) + 10, 40\right], \tag{5}$$

where $\tilde{Re}_{\theta t}$ is the transition onset momentum thickness Reynolds number (based on free stream conditions) as observed in experiments.

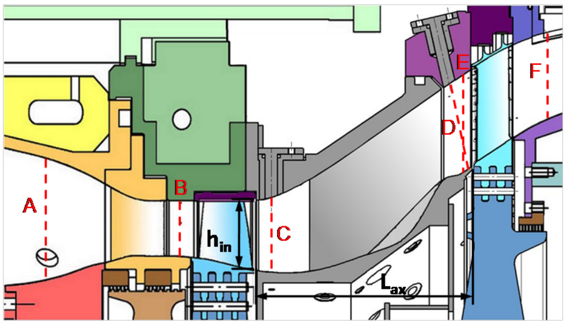

Figure 1: Meridional section of the test setup showing the measurement planes

Table 1: Operating conditions of the test rig

		HPV	HPR	TMTF	LPR
Tot. press. ratio		3		1.3	
Blade count		24	36	16	72
Reynolds number	10^6	2.38	1.1	1.86	0.46
Reduced rot. speed	$\frac{rpm}{\sqrt{K}}$		524.4		168.2

3 Test Case

Geometry and Experimental Setup

The test case used in this study is a setup designed for various experimental investigations which were conducted on the transonic test turbine facility (TTTF) of the Institute for Thermal Turbomachinery and Machine Dynamics. The TTTF is a continuously operating two-stage cold-flow open-circuit plant.

The test setup consists of a single-stage unshrouded transonic high pressure (HP) turbine, an S-shaped turning mid turbine frame (TMTF) followed by a shrouded counter-rotating low pressure (LP) rotor. The TMTF design used in this test case was developed by Volvo Aero (recently acquired by GKN plc.) with endwall contouring (Wallin et al. (2011)) within the framework of the EU Project DREAM. In Fig. 1 the meridional section of the test setup with the TMTF as well as the measurement planes A, C-F are shown. The air flowing into the HP turbine (HPT) is accelerated in the circumferential direction by the vanes (HPV) before entering the rotor. It leaves the rotor (HPR) with a negative swirl which differs between hub and shroud section, because of the tip leakage of the unshrouded rotor. Afterwards it is turned by the struts of the TMTF in the positive direction. The air then enters the LP rotor (LPR) which rotates in the opposite direction of the HP rotor at about one third of its speed.

Table 1 shows the main parameters of the test rig at design conditions. The HP stage consists of 24 vanes and 36 blades and the LP stage consists of 16 struts and 72 blades. The entire setup with the HPT, TMTF and LPR has a periodicity of 90°.

Detailed reports of the experimental investigations of the turbine are presented by Santner et al. (2011) and

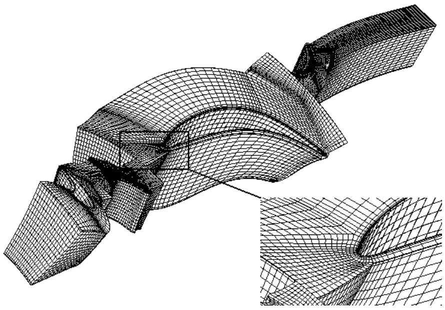

Figure 2: One channel of the computational grid with every fourth node plotted

Spataro et al. (2012). The measurements were conducted with five-hole probes, which were traversed radially over 90% of the blade height and over one HP vane pitch on plane C and over one TMTF strut pitch on plane E. The results obtained in these experimental campaigns are used for the validation of the simulations.

Grid Topology

Fig. 2 displays one channel of the multiblock grid consisting of 5 blocks for each vane/blade except for the HP blade, which is meshed with 8 blocks due to the tip leakage. An O-type block encloses each blade. The HP stator, HP rotor, TMTF and LP rotor are meshed with 1.05, 2.15, 3.4 and 2.2 million cells, respectively. The y^+ value at all walls is mostly below 1. For the time-accurate calculation with phase-lag boundary conditions the first and second blade rows were extended to three channels and the last two blade rows were extended to two channels. The resulting grid consists of a total of nearly 21 million cells.The mesh was generated with an in-house mesher developed by Pieringer (2012).

Boundary Conditions

Dirichlet boundary conditions were applied. At the inlet total pressure, total temperature and flow direction were specified and at the outlet the static pressure. The inlet turbulence intensity was set to 11% for the calculations with the SST model in accordance with measurement results. The mixing length was set to $1mm$.

Additionally, in order to be able to calculate with phase-lag boundary conditions the rotation speed of the low pressure turbine were adapted. It was set to exactly a third of the rotation speed of the high pressure turbine. This results in an approximately 4% higher rotational speed.

4 Computational Results and Discussion

A comparison of the circumferentially averaged values of static pressure, total pressure and total temperature of CFD simulations and measurement results in plane E is presented in Fig. 3. Measurement uncertainties are $\pm 5.4 mbar$ for the static pressure, $\pm 3 mbar$ for the total pressure, and $\pm 0.6 K$ for the total temperature, as stated by Santner (2013).

In the diagrams measurement results, results of the steady-state calculation (Mixing Planes) and results of the unsteady simulation are plotted. From the unsteady simulation three results are displayed. *Time Step* 0° and *Time Step* 12° are selected time instances during the calculation. The phase difference of the HPR between these two solutions is 12°. For the LPR the difference is 4°. These instances have been chosen as they constitute two different time steps that might have remarkably differing solutions. Also time averaged results are plotted. As these three solutions from the unsteady calculation differ unnoticeaby they will not be further discussed in the following.

The radial distribution of the static pressure is caused by the S-shaped contour of the intermediate duct. The radius of the second bend before exit leads to higher velocities closer to the hub and lower static pressure.The CFD results of static pressure show generally good

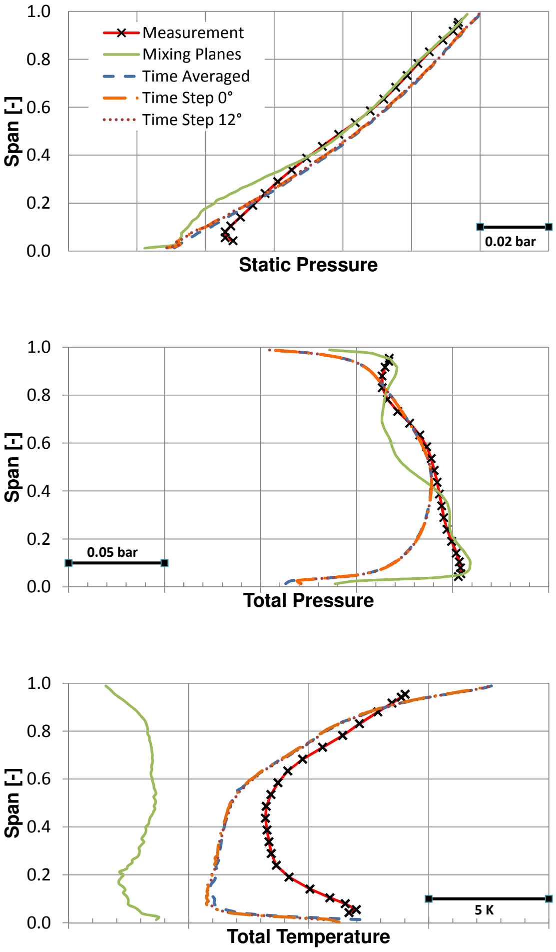

Figure 3: Circumferentially averaged measurement and simulation results on plane E

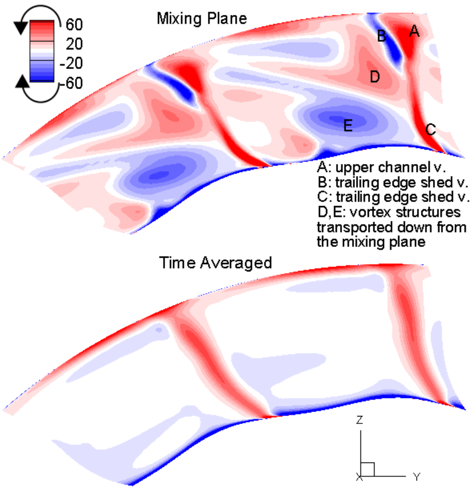

Figure 4: Contour plots of the streamwise vorticity in plane E

agreement with measurement results. The steady-state solution with mixing planes is in very good agreement above 40 % span, but below 40 % span the static pressure is underpredicted. The time-accurate calculation achieves a better overall prediction. The discrepancy with measurement results in the lower half starts below 20 % span and is less distinctive.

Looking at the total pressure plot it can be observed that all calculations are mostly in good accordance with measurement results. The steady-state calculation is in better agreement below 40 % span, whereas the time-accurate solution differs remarkably. In contrast the time-accurate calculation performs better between 40 % and 90 % span. Above this region the result of the steady-state calculation is closer to the measurement results.

The results of total temperature show a more distinctive difference between the steady-state calculation and the time-accurate simulation. The steady-state calculation underpredicts the total temperature by 5 K to 10 K. Although the unsteady calculation also underpredicts the total temperature the difference is much less with a maximum of 5 K. Also the trend of the curve is reflected more accurately. The steady-state calculation predicts a rise in the total temperature above 80 % span. This contradicts the measurements.

Fig. 4 shows the contour plots of the streamwise vorticity. The viewing direction is from downstream of the flow. Red indicates an anti-clockwise rotation and blue a clockwise rotation of a vortex structure. The development of the vortex structures that can be observed in a similar TMTF has been discussed in detail by Spataro et al. (2012). The main structures that are expected to be seen after the trailing edge are the upper and lower passage vortices, as discussed by Wang et al. (1997). The upper channel vortex A and the counter-rotating trailing edge shed vortex B can be identified in the contour plot. C can be interpreted as the trailing edge shed vortex, which rotates in the opposite direction of the lower passage vortex. Other vortex structures that can be seen in Fig. 7 denoted with D and E (or not denoted at all) stem from the high pressure rotor. They are visible at the mixing plane inlet as banded structures and are transported downstream with a slight distortion. This distortion is a twisting motion in the clock-wise direction. It has been identified by Spataro et al. (2012) as the vane passage vortex. The vortex structures due to the mixing planes do not occur in the contour plot of the time averaged results, as expected. But also the channel vortex A and the trailing edge shed vortices that can be observed in both plots have different intensities. The time-accurate calculation predicts less intensive vortices.

Summing up the comparison with the measurements, a considerable improvement of the prediction accuracy of CFD are achieved with the time-accurate simulation. Two major differences to the steady-state calculation are in the values of the total temperature and the predicted secondary flow structures. These are both essential for the correct analysis of turbomachinery. With the correct prediction of total temperature efficiency can also be predicted much more accurately. Fig. 5 shows the total to static isentropic efficiency calculated with the results of the different simulations in comparison to the

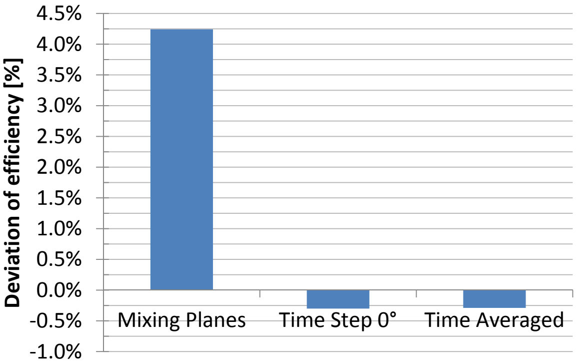

Figure 5: Total to static efficiency compared to measurement data

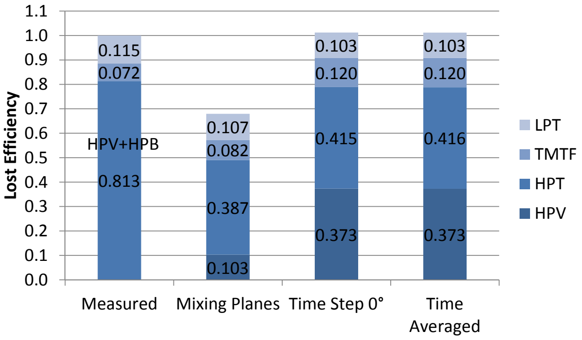

Figure 6: Loss distribution of the blade and vane rows

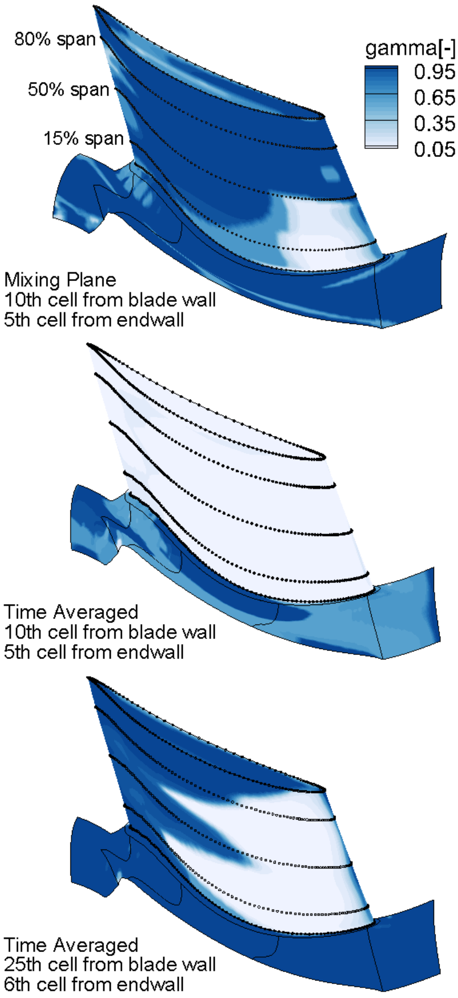

Figure 7: Intermittency on the suction side of the TMTF vane

efficiency calculated with the results of the measurements. The steady-state calculation with mixing planes overestimates the efficiency of the turbine by 4.25 %, whereas with the unsteady calculation, both a time instance and the time averaged data, result in an efficiency only 0.25 % less than that derived from measurement data.

According to Pullan et al. (2006) the loss of the individual blade rows can be approximated by

$$\Delta\eta = \frac{\Delta s_{blade} T_{tF}}{c_p(T_{tA} - T_{tF}) + \Delta s_{turbine} T_{tF}} \tag{6}$$

where T_{tA} is the total temperature at turbine inlet (plane A) and T_{tF} is the total temperature at turbine outlet (plane F). $\Delta s_{turbine}$ refers to the entropy difference from the turbine inlet to the turbine outlet and Δs_{blade} refers to the entropy production in a specific blade row. c_p is the specific heat at constant pressure. All values are mass averaged. The first term in the denominator in Eq. (6) is the work output of the turbine. The second term is the energy loss due to entropy generation. The sum of both terms is the potential of work output of the isentropic process. The numerator is the energy loss in a specific blade row due to entropy generation.

In Fig. 6 the results of this evaluation are presented. The lost efficiency is plotted in reference to measurement results, which has been scaled to hundred percent. As there are no measurement results in plane B the losses generated in HPV and HPR have been merged in the plot. There is a big difference in the amount of loss generated in the HP stage between measurements and the steady-state simulation. This is due to the underprediction of the total temperature which has been shown in Fig. 3. Both the loss distributions calculated with data from unsteady results are very close to each other and the agreement with measurement data is very good.

The transition behavior along the wall of the TMTF vanes is very different for the calculation with mixing-plane interfaces and the time-accurate simulation. Fig. 7 shows contour plots of the intermittency close to the walls of the TMTF vane on the suction side and on the inner endwalls. On the first plot (above) the contours on the 10th cell from the blade wall and 5th cell from the endwall for the calculation with mixing planes are plotted. It can be observed that the intermittency values are high suggesting a mostly turbulent flow. The endwall shows no clear region of transition, but small areas with lower intermittency. Close to the leading edge on the lower half of the vane the flow is laminar. It quickly becomes turbulent at 50 % span. At lower span regions this happens further downstream. The next contour plot shows the values on the same cells from the time averaged data (middle). The flow around the blade is clearly laminar and the endwall has more distinctive regions of turbulent and transitional flow. Also cells further away

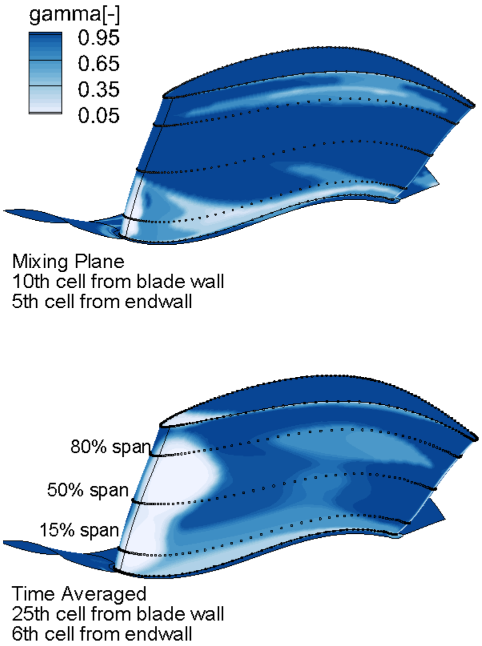

Figure 8: Intermittency on the pressure side of the TMTF vane

from the walls are plotted (below). At the 25th cell away from the blade wall the plots display a laminar flow at the leading edge and a distinctive transition to turbulent at about mid chord, depending on the span location. These results indicate a thicker laminar sublayer in the unsteady simulation.

The same difference in the thickness of the laminar sublayer can be observed on the pressure side of the TMTF vane. Fig. 8 shows the intermittency on the 10th cell away from the wall for the steady-state calculation and on the 25th cell for the unsteady calculation. The calculation with mixing-plane interfaces predicts a laminar region at the leading edge close to the hub, whereas the time-accurate calculation predicts a laminar region along the whole span and transition shortly downstream.

These intermittency values are consistent with the skin friction coefficient values shown in Fig. 9. The skin friction coefficient has been plotted at 15 %, 50 % and 80 % span for the calculation with mixing planes and the time-accurate simulation. As stated before, the transient calculation with phase-lag boundary conditions has been performed with two blade rows of the TMTF, so the values on both blades are plotted (Transient Blade 1 and 2). At 80 % span the steady-state solution predicts a friction coefficient of nearly 0.2 that stays constant until a steep fall at 0.7 axial chord. With the unsteady calculation the frictions coefficient falls along the blade wall till it reaches 0.3 axial chord, after which it starts increasing indicating transition. The decrease of the friction coefficient after 0.6 axial chord is similar to the steady-state calculation. The flow here is still turbulent as can be seen in Fig. 7. On the pressure side the friction coefficient from the steady-state calculation shows no transition, whereas the unsteady results indicate transition at 0.15 axial chord length. At 50 % span transition on the suction side begins shortly before 0.4 axial chord length for both calculations. The skin friction coefficient rises from 0.1 (for the time-accurate result) and 0.15 (for the steady-state result) to 0.25 at about 0.75 axial chord. On the pressure side transition can be seen at 0.1 to 0.3 axial chord only with the unsteady calculation. At 15 % span transition can be observed on the suction side. At 0.3 axial chord the friction coefficient starts rising from below 0.1 to approximately 0.25 at nearly 0.8 axial chord. On the pressure side the time-accurate calculation predicts transition starting at 0.1 axial chord, which completes nearly at the trailing edge. The steady-state solution indicates a similar development of the boundary layer starting at 0.4 axial chord.

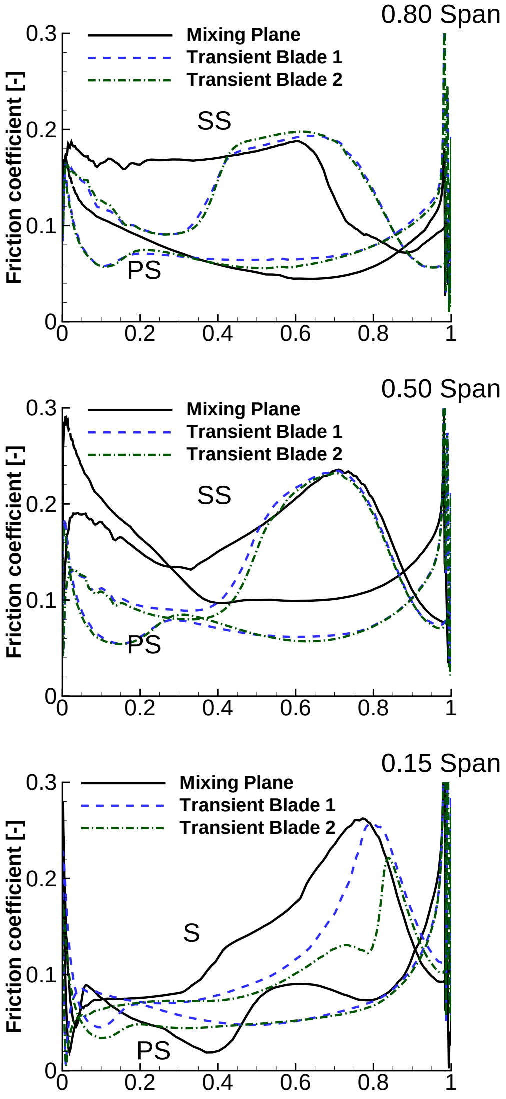

Figure 9: Skin friction coefficient at 15 %, 50 % and 80 % span

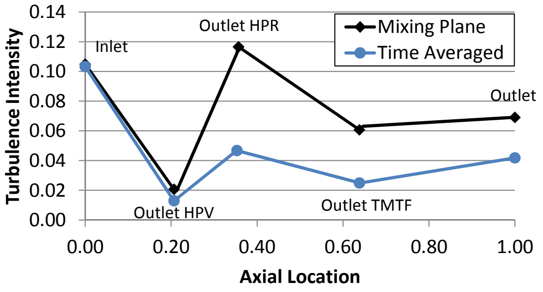

Figure 10: Turbulence intensity along the flow path

The differences in the results between steady-state and unsteady simulations can be explained by the development of the turbulence intensity along the channels. Fig. 10 shows the turbulence intensity at the inlet and outlet of each blade row. Plane E is at the outlet of the TMTF at approximately 0.6 axial location. The turbulence intensity calculated with time averaged results is approximately 0.02, whereas the steady-state calculation predicts about 0.06. This is mainly due to much higher turbulence generation in the high pressure rotor. Mayle (1991) has shown that the free-stream turbulence level increases the production rate of turbulent spots, so that it can be expected that this considerable difference will affect the thicknesses of the laminar sublayer and transition regions as well as the strength of the vortices.

5 Conclusions

CFD analysis of a two-stage counter-rotating turbine with transition modeling have been presented. Two calculations were performed: a steady-state calculation with mixing plane interfaces and an unsteady calculation with phase-lag boundary conditions. Very good agreement with measurement results have been achieved with the unsteady calculation, which has given considerably better results for the total temperature. Efficiency estimation with results from the time-accurate simulation is 0.25 % off from measurement results, whereas steady-state results differ by 4.25 %. Also vortices that are caused by mixing-plane interfaces are not seen in the unsteady calculation, allowing a much more reliable prediction of the secondary flow.

Transition phenomena on the TMTF walls have been investigated. There are distinctive discrepancies between steady and unsteady calculations regarding transition regions and boundary layer thickness. The laminar layer is much thicker in the unsteady simulation. Also laminar to turbulent transition regions differ clearly. The boundary layer flow at the leading edge of the TMTF is predicted to be laminar along the whole span by the the unsteady calculation. The steady-state calculation predicts only the region below 50 % span to be laminar.

There have not yet been reliable experimental investigations of transition on the blades for this setup. But based on the comparisons with measurement results, it can be expected that the boundary layer behavior predicted by the unsteady calculation is correct.

To find a reason for these differences the turbulence intensity at the inlets and outlets of the vane/blade rows have been analyzed. The turbulence levels are considerably higher after the first mixing-plane interface between the HP vane and blade rows. These higher turbulence levels can affect the strength of the vortices and transition phenomena.

Acknowledgements

The authors would like to thank the Austrian Federal Ministry for Transport, Innovation and Technology who funded the project SEIKON3D within the Austrian Aeronautics Program TAKE OFF. The research leading to some of these results has been partially funded by the European Union within the EU-project DREAM (contract No. ACP7-GA-2008-211861), as well as from the Austrian Federal Ministry for Finance.

References

Akin, M. Bugra and Sanz, Wolfgang. Influence of transition on CFD calculations of a two-stage counter-rotating turbine. In *ASME Turbo Expo 2014, Duesseldorf, Germany*, GT2014-26044, 2014.

Kelterer, M. E., Burgstaller, R., and Sanz, W. Application of the gamma-Re_theta transition model to transitional flow. In *International Symposium on Experimental and Computational Aerothermodynamics of Internal Flows, Brussels, Belgium*, ISAIF10-091, 2011.

Kelterer, M.E., Pecnik, R., and Sanz, W. Computation of laminar-turbulent transition in turbomachinery using the correlation based γ-Re_θ transition model. In *ASME Turbo Expo 2010: Power for Land, Sea and Air, Glasgow, UK*, GT2010-22207, Glasgow, Scotland, June 2010.

Langtry, R. B. and Menter, F. R. Transition modeling for general CFD applications in aeronautics. In *43rd AIAA Aerospace Sciences Meeting and Exhibit*, AIAA 2005-522, January 2005.

Mayle, Robert Edward. The 1991 IGTI scholar lecture: The role of laminar-turbulent transition in gas turbine engines. *Journal of Turbomachinery*, 113(4): 509–536, 1991.

Menter, F. R. Two-equation eddy-viscosity turbulence models for engineering applications. *AIAA Jounal*, 32:1598–1605, 1994.

Menter, F. R. and Langtry, R. B. Correlation-based transition modeling for unstructured parallelized computational fluid dynamics codes. *AIAA Journal*, 47(12): 2894–2906, 2009.

Menter, F. R., Langtry, R. B., Liki, S. R., Suzen, Y. B., Huang, P. G., and Voelker, S. A correlation-based transition model usind local variables Part 1 - Model formulation. In *ASME Turbo Expo 2004, Vienna, Austria*, GT2004-53452, 2004.

Pecnik, R., Pieringer, P., and Sanz, W. Numerical investigation of the secondary flow of a transonic turbine stage using various turbulence closures. In *ASME Turbo Expo 2005, Nevada, USA*, GT2005-68754, Nevada, USA, 2005.

Pieringer, P. AIGRID3D. Springer und Pieringer EDV Dienstleistungen OEG, 2012.

Pieringer, P., Goettlich, E., Woisetschlaeger, J., Sanz, W., and Heitmeir, F. Numerical investigation of the unsteady flow through a transonic turbine stage using an innovative flow solver. In *6th European Conference on Turbomachinery*, 032-04/164, Lille, France, March 2005.

Pullan, Graham, Denton, John, and Curtis, Eric. Improving the performance of a turbine with low aspect ratio stators by aft-loading. *Journal of Turbomachinery*, 128(3):492–499, 2006.

Roe, P. L. Approximate riemann solvers, parameter vectors and differencing scheme. *Journal of Computational Physics*, 43:357–372, 1981.

Santner, C., Paradiso, B., Malzacher, F., Hoeger, M., Hubinka, J., and Goettlich, E. Evolution of the flow through a turning mid turbine frame applied between a transonic HP-turbine stage and a counter-rotation LP-turbine. In *9th European Turbomachinery Conference, Istanbul, Tuerkei*, March 2011.

Santner, Cornelia. *Experimental Investigation of Turning Mid Turbine Frame Designs*. PhD thesis, TU Graz, 2013.

Spataro, R., Santner, C., Lengani, D., and Goettlich, E. On the flow evolution through a LP turbine with wide-chord vanes in an S-shaped channel. In *ASME Turbo Expo 2012, Copenhagen, Denmark*, GT2012-68178, 2012.

Wallin, Fredrik, Ore, Sofia, Goettlich, Emil, and Santner, Cornelia. Aero-design and validation of a turning mid turbine frame. In *20th ISABE Conference, Gothenburg, Sweden*, ISABE-2011-1713, March 2011.

Wang, H. P., Olson, S. J., Goldstein, R. J., and Eckert, E. R. G. Flow visualization in a linear turbine cascade of high performance turbine blades. *Journal of Turbomachinery*, 119, 1997.

A.3 Paper III

Akin, M. B., Sanz, W., and Pieringer, P. Endwall contour optimization of a turning mid turbine frame using an adjoint method. ASME Turbo Expo, Düsseldorf, Germany, GT2014-26038, 2014.

This paper reports on the first optimization performed which was essentially to demonstrate the application of the adjoint method with the TRACE solver. The TMTF total pressure losses are minimized using the steepest descent method with the major simplification of uniform inlet boundary conditions. The optimization successfully reduced the total pressure loss in 15 steps.

ENDWALL CONTOUR OPTIMIZATION OF A TURNING MID TURBINE FRAME USING AN ADJOINT METHOD

M. Bugra Akin[*], **Wolfgang Sanz**
Institute for
Thermal Turbomachinery and Machine Dynamics
Graz University of Technology
Graz, Austria, A-8010
Email: bugra.akin@tugraz.at

Paul Pieringer
Springer und Pieringer
EDV-Dienstleistungen OG
Haydngasse 7
Graz, Austria, A-8010
Email: pieringer@acoustic-interfaces.at

ABSTRACT

This paper presents the application of a viscous adjoint method in the optimization of the endwall contour of a turning mid turbine frame (TMTF). The adjoint method is a gradient based optimization method that allows for the computation of the complete gradient information by solving the governing flow equations and their corresponding adjoint equations only once per function of interest (objective and constraints), so that the computation time of the optimization is nearly independent of the number of parameters. With the use of a greater number of parameters a more detailed definition of endwall contours is possible, so that an optimum can be approached more precisely. A Navier-Stokes flow solver coupled with Menter's SST $k-\omega$ *turbulence model is utilized for the CFD simulations, whereas the adjoint formulation is based on the constant eddy viscosity approximation for turbulence. The total pressure ratio is used as the objective function in the optimization. The effect of contouring on the secondary flows is evaluated and the performance of the axisymmetric TMTF is calculated and compared with the optimized design.*

NOMENCLATURE

G	gradients
I	cost function
R	state equation
$\mathbf{U}$	state vector
V	velocity vector
ρ	density
$\mathbf{x}$	vector of design variables
λ	step-size parameter
Ψ	adjoint
Ω_s	streamwise vorticity
ω	vorticity

INTRODUCTION

The improvement of the performance of engineering products is in the center of its development, whether to achieve greater technical objectives, increase reliability, reduce costs or preserve natural resources. One of the main focuses in the improvement of turbomachinery is to increase the thermal efficiency. Even very slight achievements in this respect have a big impact on the overall fuel consumption, which significantly affects economy, consumption of natural resources and pollution.

Computational Fluid Dynamics in conjunction with optimization algorithms provide an effective method for

---

[*] Corresponding author

such improvements. The rapid increase in computing capacity and advances in numerical methods allow for the application of these methods more generally and in a cost-effective manner. Many approaches for the use of numerical methods in optimization have been developed and some are widely used today. The methods are generally classified by the order of derivatives of the objective function used. These are zero, first and second order methods, which, as their names imply, use only the function values, first and second order derivatives, respectively. Examples for zero order methods are *evolutionary algorithms* such as *genetic algorithm*s [1] and *differential evolution* [2] and for first order methods *finite difference methods* [3] and *adjoint methods*. The adjoint method, which is the method of choice for this study, has been advocated amongst others mainly by Pironneau [4] and Jameson [5].

The adjoint method provides a highly efficient alternative for the calculation of the gradient in cases where many parameters are involved. It has been widely used in the aerodynamic design optimization for airfoils, wings and wing-body configurations [6, 7]. Recently its application has been extended to turbomachinery design optimization [8–15].

The main advantage of the adjoint method is that for each optimization cycle the computational cost required to obtain the derivatives is nearly independent of the number of parameters. Only an extra inexpensive calculation in addition to the computation of the Navier-Stokes equations and their viscous adjoint equations has to be performed for each parameter. This will be discussed in the following section. The adjoint of the Navier-Stokes equations can be derived either with a continuous adjoint approach or a discrete adjoint approach. In this paper a discrete adjoint method has been applied.

An essential component of the optimization is the flow solver. The solutions provided by the solver must be physically accurate or at least representative of the actual flow. But one of the greatest weaknesses of CFD is the turbulence and transition modeling. But models which can accurately capture these phenomena in all situations still have not been achieved. An overview of turbulence models has been presented by Wilcox [16], also arguing that models based on the ω-equation can support satisfactory solutions for most of the flows. Therefor, in this work, Menter's SST $k-\omega$ turbulence model [17] is used.

The test case presented in this study is optimized with respect to the total pressure ratio through the channel. The solver TRACE has been utilized, which has been developed at the DLR for internal flows, specifically for turbomachinery [8]. More information on the methods used and procedure will be presented in the following.

ADJOINT METHOD

The adjoint method will be described briefly for the sake of completeness. For a more detailed introduction the reader is referred to other sources such as Jameson *et al.* [18] and Périaux and Verstraete [19]. A description specifically for the solver TRACE, which is utilized in this work, can be found in Frey *et al.* [20].

For the derivation of the adjoint equation we will define a single-objective optimization problem as commonly defined with

$$I(\mathbf{U},\mathbf{x}) \tag{1}$$

as the cost function to be minimized (or maximized) subject to the state equation

$$R(\mathbf{U},\mathbf{x}) = 0, \tag{2}$$

which in this case are the RANS equations. $\mathbf{U}$ is the state vector and $\mathbf{x}$ the vector of design variables.

With the chain rule the sensitivities of the cost function can be written as:

$$\frac{dI(\mathbf{U},\mathbf{x})}{d\mathbf{x}} = \frac{\delta I}{\delta \mathbf{U}}\frac{\delta \mathbf{U}}{\delta \mathbf{x}} + \frac{\delta I}{\delta \mathbf{x}}. \tag{3}$$

The terms $\frac{\delta I}{\delta \mathbf{U}}$ and $\frac{\delta I}{\delta \mathbf{x}}$ are relatively easy to compute as the cost function I is expressed as an explicit function of the state variable $\mathbf{U}$ and the control variables $\mathbf{x}$. The computation of $\frac{\delta \mathbf{U}}{\delta \mathbf{x}}$ is rather more complicated and can be derived from the differentiation of the state equation:

$$\frac{\delta R}{\delta \mathbf{U}}\frac{\delta \mathbf{U}}{\delta \mathbf{x}} + \frac{\delta R}{\delta \mathbf{x}} = 0. \tag{4}$$

After reformulating Eq. 4 for $\frac{\delta U}{\delta x}$, Eq. 3 can be rewritten as:

$$\frac{dI}{d\mathbf{x}} = \Psi^T \frac{\delta R}{\delta \mathbf{x}} + \frac{\delta I}{\delta \mathbf{x}}, \tag{5}$$

where Ψ represents the adjoint and is the solution of

$$(\frac{\delta R}{\delta \mathbf{U}})^T \Psi = -(\frac{\delta I}{\delta \mathbf{U}})^T. \tag{6}$$

This means that for the evaluation of the sensitivities, first Eq. 6 has to be solved, which is a linear set

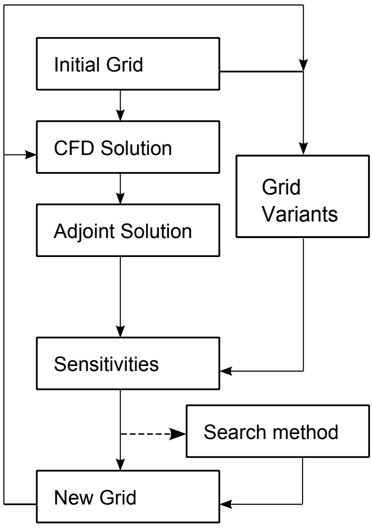

FIGURE 1. **OPTIMIZATION FLOW CHART**

of equations called the adjoint equation. The solution of the adjoint equation is as expensive as the solution of the RANS equations. The advantage is that it is not dependent on the design variables, so for a single-objective optimization problem without additional constraints, it has to be calculated only once for each design cycle. After the adjoint Ψ has been calculated Eq. 5, which is computationally much more inexpensive, can be evaluated for the sensitivities.

NUMERICAL METHOD

The tools utilized in this paper include a CFD solver, an adjoint solver and Python as a scripting language to control the solver. In Fig. 1 the flow chart of the optimization routine is shown. Starting with the initial grid the CFD solution and the adjoint are calculated. In the meantime also the grid variants are generated. The number of grid variants is equal to the number of parameters, as each grid variant is the grid at the current optimization step with one of the parameters manipulated. Grid generation is carried out with an in-house mesher developed by Pieringer [21]. Then the sensitivities are calculated with the adjoint solution and grid variants. The search method provides a step size with which the parameters are updated and a new grid is generated. Depending on the search method used the step size can be calculated from the sensitivities. In this study the step size is independent from the sensitivities.

Flow Solver

The Reynolds-averaged Navier Stokes (RANS) solver TRACE has been used for the calculation of the flow solution and the adjoint as well as sensitivities. The governing equations are integrated in time by a fully implicit formulation of the first or second-order accurate scheme. The convective fluxes are discretized using Roe's total variation diminishing (TVD) upwind scheme which is combined with van Leer's monotone upstream-centered scheme for conservation laws (MUSCL) to obtain second-order accuracy in space. The derivatives of the viscous fluxes are approximated by central differences. At inlet and outlet boundaries the non-reflecting formulation according to Giles is applied. Additionally the solver is parallelized. More detailed information on TRACE can be found in Yang *et al.* [8] and Simmendinger and Kügeler [22].

Adjoint Solution

In TRACE the discrete adjoint of the RANS equations has been implemented, which is based on the already discretized form of the Navier-Stokes equations. The advantage of this approach is that it prescribes a discretization of the adjoint PDE, so that the choice for appropriate discretization schemes becomes redundant, and sensitivities are naturally consistent with the flow solver. Further discussion on the discrete and continuous approaches can be found in Giles *et al.* [23] and Papadimitriou *et al.* [24].

The adjoint formulation has not been extended to any of the turbulence models available in the solver. It is based on the constant eddy viscosity assumption, so that when computing sensitivities with respect to shape variations the eddy viscosity assumes the same values as for the solution calculated for the current optimization step. This approach has the advantage of faster implementation and less computational cost, in comparison to an implementation of the adjoint equation corresponding to the full turbulence models. The validity of this simplification has been shown by Marta and Shankaran [25].

The adjoint equation is solved by a generalized minimal residual method (GMRES). The solver provides the option to precondition the system with either incomplete lower-upper decomposition (ILU) or symmetric successive over-relaxation (SSOR). In this work ILU was used. For more detail on the numerical method the reader is referred to Frey *et al.* [20, 26] .

Sensitivities

The sensitivities are calculated using Eq. 5 with the adjoint solution Ψ from Eq. 6 for a specific cost function. Most turbomachinery specific cost functions depend only on the state at certain planes, typically the inlet and exit of blade rows. Therefore, the evaluation can be simplified with the assumption that the sensitivities depend only on the sensitivity of averaged states, as long as hub or casing geometry are not varied at these planes [20]. In this case

$\frac{\delta I}{\delta x}$ in Eq. 5 can be set to 0 .

The term $\frac{\delta R}{\delta x}$ is approximated by finite differences, for which the residuals are evaluated for the grid variants [20]. The perturbation factor for the grid variants has been set to $0.001\,m$ in the radial direction for each point.

This step is approximately as time consuming as one time step of the CFD solver. It is the only step for which the CPU time remains proportional to the number of parameters. A new mesh has to be generated for each parameter, and this can become computationally expensive if the number of parameters are high and the mesh is large. Still, mesh generation can be performed parallel to the calculation of the CFD solution and adjoint equation to avoid losing time.

Search Method

After the sensitivities have been evaluated the parameters for the next step can be calculated with

$$x_{n+1} = x_n - \lambda G. \tag{7}$$

λ is the step-size parameter. In the case of a maximization problem λ is negative. It can be evaluated with a variety of search methods like the steepest descent, modified steepest descent with smoothing, implicit descent, multigrid steepest descent, Krylov acceleration, and quasi-Newton methods. For the optimization presented here the steepest descent method is used. This is a simple method as λ is chosen to be a constant factor, but poses the problem of finding a good value, as a value which is too big can cause the optimization to be unstable and a value which is too small would necessitate more iteration steps to reach the optimum. The magnitude of λ was set to -0.005, which led to very good results after 15 design cycles.

As this is an initial test case, the choice for the steepest descent method lies mainly in the simplicity of implementation. Solutions have also recently been achieved with a quasi-Newton method, that has proven the robustness expected from this method. The results of these investigations will be presented in future publications.

TEST CASE

The Institute for Thermal Turbomachinery and Machine Dynamics at Graz University of Technology operates a unique transonic test turbine facility (TTTF). On the test rig of the institute a two-stage counter-rotating turbine, which has been designed by MTU Aero Engines and Volvo Aero (recently acquired by GKN plc.), is the subject of various investigations. The configuration consists of a single-stage unshrouded transonic HP turbine, an S-shaped turning mid turbine frame (TMTF) followed by a shrouded counter-rotating LP turbine. Two different TMTFs have been designed in the framework of the former EU project DREAM. Information about the related investigations has been published by Santner [27]. The TMTF, which is the subject of this report, was already designed with endwall contouring to reduce secondary losses. For the initial condition of this optimization study this TMTF is extracted and the endwall contour replaced with an axisymmetric endwall. Additionally the outlet is moved further downstream to avoid backflow at the boundary. More information regarding the rig configuration and measurement campaigns is reported amongst others by Santner *et al. [28]* and Wallin *et al.* [29]. The flow in the TMTF of this setup has been investigated by Akin and Sanz [30]. Spataro et al. [31] have reported on the flow evolution through the other TMTF design.

Fig. 2 shows the TMTF and the computational domain. Steady-state calculations of the flow through 1

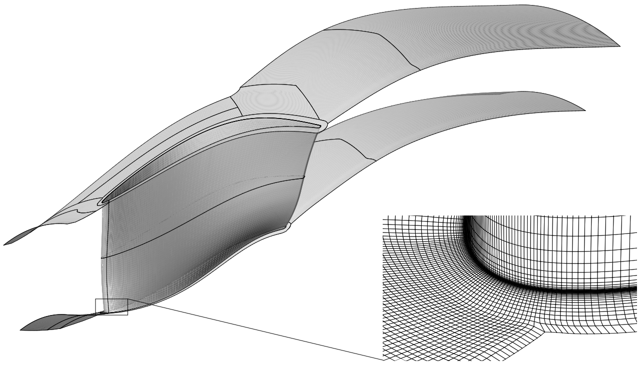

FIGURE 2. TMTF WITH AXISYMMETRIC ENDWALL CONTOUR AND CUTOUT OF THE COMPUTATIONAL GRID

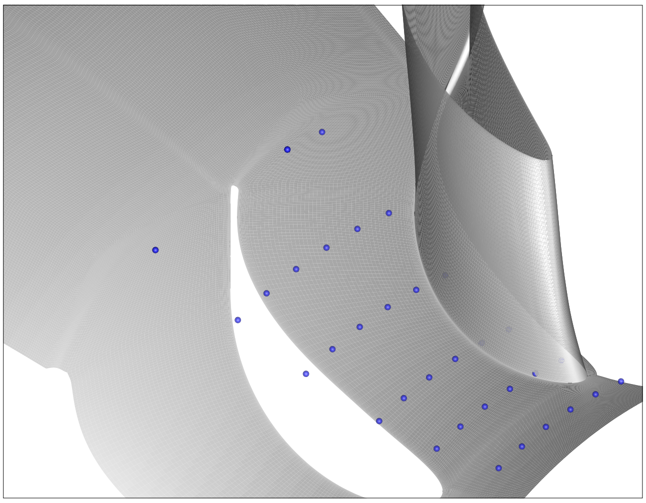

FIGURE 3. POSITIONS OF THE 33 POINTS ON THE HUB

TABLE 1. FLOW SOLUTIONS FOR THE AXISYMMETRIC AND OPTIMIZED TMTF

Solution	$p_{t_{out}}/p_{t_{in}}$	$\dot{m}[\%]$	$\Delta s[J/K]$	$\alpha_z[°]$
Axisymmetric	0.9724	100	4.55275	35.882
Optimized	0.9729	102.95	4.47059	36.946

of 16 channels have been performed. The meshing has been carried out with the in-house mesher developed by Pieringer [21]. The grid is a multi-block grid consisting of 18 blocks for the convenience of parallelization. An O-type block encloses the blade. The grid consists of approximately 3.7 million cells. The y+ value at all walls is below 1.

Dirichlet boundary conditions have been applied. At the inlet total pressure, total temperature and flow direction have been specified, and at the outlet static pressure. The inlet flow is specified as axial flow at the inlet. Turbulence has been modeled with the SST turbulence model with improved wall treatment by Menter *et al.* [17, 32]. Turbulence intensity has been set to 11% and the mixing length has been set to $0.1mm$. The flow in the TMTF has a Reynolds number of approximately $1.86x10^6$.

The optimization has been carried out with respect to the total pressure loss. The ratio of the outlet total pressure to the inlet total pressure is the cost function for which the adjoint was calculated. With this, the optimization problem at hand is a maximization problem. A significant rise in the pressure ratio is achieved after 15 steps.

The computations were performed on the high performance computing platform of the Graz University of Technology utilizing 10 processor cores with 2.27 GHz. For the adjoint solution each processor allocated about 2 GB of memory.

Depending on how much a new contour varies from the previous setup the CFD solution can take from 4 to 8 hours to achieve a precision of 0.001 % deviation in mass flow rate and the adjoint solution can take up to 10 hours to achieve a residual drop by 10^{-3}. The fastest step needed a little more than 5 hours for both solutions.

ENDWALL CONTOURING

For the parametrization of the endwall contour 36 equally spaced points were defined on the hub surface of the initial axisymmetric contour. In Fig. 3 the positions of 33 of these points are shown. Three points at the trailing edge have been removed as the flow in this region tends to separate. In preceding investigations the sensitivities of parameters in this region of the hub showed much higher values than in the other regions, resulting in greater deformations of that region and causing grid generation to fail. Future investigations will also concentrate on handling of such problems. There are also points that are at the location of the struts. Although there is no endwall there, these points will still affect the contour as one point has a larger influence area due to the spline fitting.

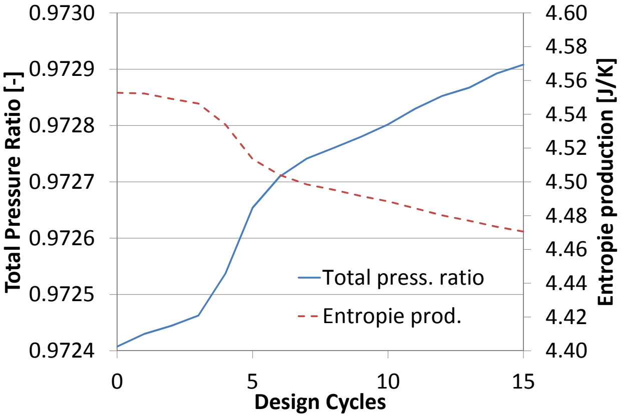

FIGURE 4. PROGRESS OF THE PRESSURE RATIO AND ENTROPY PRODUCTION DURING THE OPTIMIZATION

The points defined on the hub are moved only in the radial direction, so that each point has one degree of freedom. Consequently the test case has 33 design variables.

For the grid generation a B-Spline surface is defined and fitted on these 33 points, which is then used by the mesher to fit the grid on the contour. This procedure has been implemented into the mesher by Pieringer [21].

Similarly, B-Splines have been utilized for the parametrization of surfaces in the field of external aerodynamics. A survey of parametrization techniques in aerodynamic shape optimization is given by Mousavi *et al.* [33].

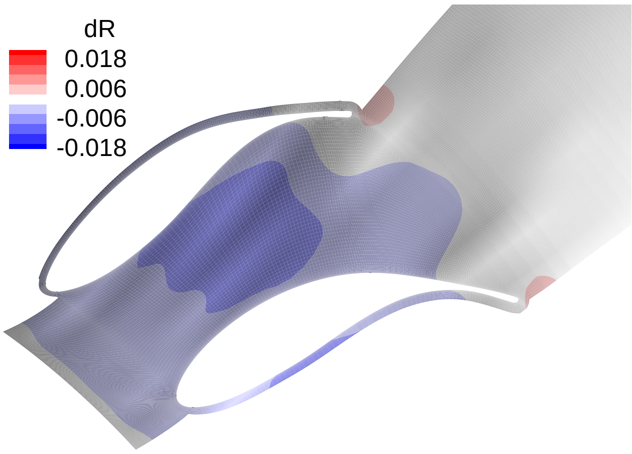

FIGURE 5. OPTIMIZED HUB CONTOUR

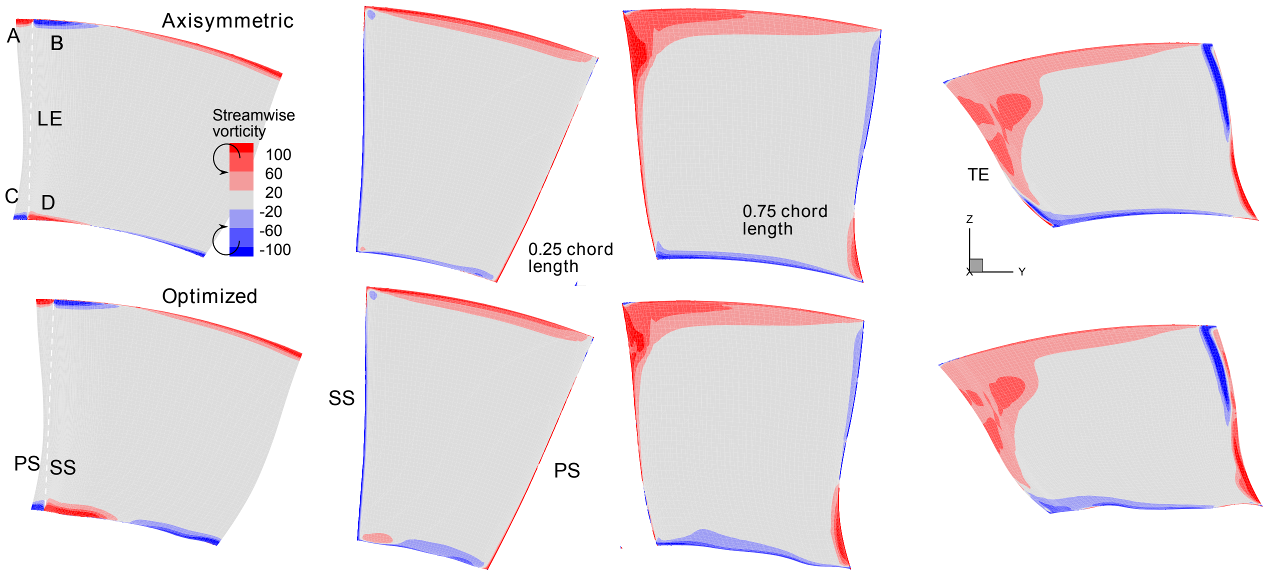

FIGURE 6. **STREAMWISE VORTICITY OF THE AXISYMMETRIC AND OPTIMIZED DESIGN AT LE, 25% AND 75% AXIAL CHORD LENGTH AND TRAILING EDGE**

RESULTS AND DISCUSSION

After 15 design cycles the optimization led to an endwall contour with less pressure loss. In the following this endwall contour is presented and the performance of the axisymmetric and optimized design will be compared. Besides the improvement of the performance it is important to understand the effect of the contouring on the flow through the channel. Thus the secondary flow and the changes therein are studied.

Table 1 summarizes the achievements of the optimization. The total pressure ratio is improved by 0.05%. There is a corresponding decrease in the entropy production by about $0.08J/K$. Besides the increase of the pressure ratio and decrease in the entropy generation the mass flow rate increases by nearly 3% mainly as a consequence of the reduced flow loss. The turning of the flow is also increased by slightly more than $1°$. Although this might not be a desired effect, as the outlet yaw angle is designed for the next blade row, no constraints were implemented for this test case to keep the turning constant. But it is also an added benefit as it creates potential for further design improvements. The struts can be designed with less curvature to achieve the desired turning of the flow, hence causing less flow loss.

In comparison to the original design of the TMTF with the contoured hub endwall, the pressure ratio achieved is nearly the same. This original design has a total pressure ratio of 0.9730 with the same boundary conditions.

Changes in the total pressure ratio with the optimization cycles is shown in Fig. 4. During the 15 cycles there is a constant progression of the pressure ratio towards a higher value. A corresponding decrease in the entropy production is present, which can also be seen in the diagram.

The contoured endwall after 15 design cycles is shown in Fig. 5. The deviation of the radius with respect to the initial axisymmetric endwall is illustrated by a contour plot. The blue region indicates a decrease in the radius, whereas the red region indicates an increase. A big blue zone emerges between the struts so that the cross sectional area along the blade cord is enlarged. The radius directly at the trailing edge of the struts is slightly increased. Also the surface develops a wavy structure in the circumferential direction. This fairly complicated contour design is possible with the flexible definition of the surface with points which can be manipulated independently.

Fig. 6 shows the secondary flow structures in the channel along the flow path for the axisymmetric and optimized design. Contour plots of the streamwise vorticity are visualized at the leading edge, at 25% and 75% axial chord length and at the trailing edge, with the streamwise vorticity Ω_s defined as

$$\Omega_s = \frac{\omega \cdot V}{\rho \cdot |V|^2}. \tag{8}$$

The viewing direction is from downstream of the flow so that the suction side (SS) is on the left, and the pressure side (PS) is on the right. Red indicates an anti-clockwise rotation and blue a clockwise rotation of a vortex. On the first plot the beginning of the horse shoe vortex can be identified at the shroud and hub corners of the blade. A identifies the PS leg of the horse-shoe vortex and B identifies the SS leg at the shroud. C and D denote the PS leg and SS leg of the horse-shoe vortex at the hub. At 25% chord length the SS leg of the horse-shoe vortex at the shroud is weakened. Similarly to the description of the development of the vortices in a cascade presented by Wang *et al.* [34], the PS leg of the horse-shoe vortex at the shroud is transported to the SS by the pressure gradient between the PS and SS. At 75% chord length the flow at the upper channel is dominated by the passage vortex. The same vortical structures can be observed at the hub with reversed rotation direction of the horse-shoe vortices. As in the upper channel the SS leg of the horse-shoe vortex starts diminishing and it is only a small structure at 25% chord length. The PS leg is transported to the SS. Further downstream the lower passage vortex and trailing edge shed vortices can be observed.

There is very little difference in the secondary flow between the two designs that can be visualized with the streamwise vorticity. The vortex D at the leading edge is stronger in the optimized design, so that it can also be clearly identified at 25% chord length. With careful study a slight decrease in the intensity of the upper passage vortex can be determined. A clearer reduction in the intensity of the streamwise vorticity is present at the SS corner of the hub at the trailing edge. This indicates that the main loss reduction of the flow is achieved in the corner flow on the SS.

Fig. 7 clarifies the influence of endwall contouring on the flow near the trailing edge on the SS. It shows a contour plot of the axial velocity in this section of the blade. The values in the neighboring cells adjacent to the cells on the walls are illustrated. The green regions indicate a positive axial velocity component, whereas the blue regions indicate a negative axial velocity component. A thin but long area can be identified where the axial velocity component of the flow is negative. This indicates backflow and consequently flow separation. The second blue area directly in the trailing edge corner indicates the vortices (Kàrmàn vortex street) induced by the trailing edge. A comparison of the axisymmetric and optimized contours shows that the slightly wavy contour which is generated close to the trailing edge causes the flow to separate further downstream, hence decreasing the backflow region. The streamlines further clarify the fluid flow and clearly identify the separation region and the vortex at the trailing edge.

The improvement of the flow condition influences the entropy production. Fig. 8 shows the contour plot of the entropy production at the trailing edge. High entropy production is observed due to the upper passage vortex and separation region as boundary layer flow is mixed into the passage flow. The optimized design influences mainly the entropy level in the region where separation occurs by lessening it. The area of higher entropy production is smaller resulting in the decreased pressure loss achieved by the optimization.

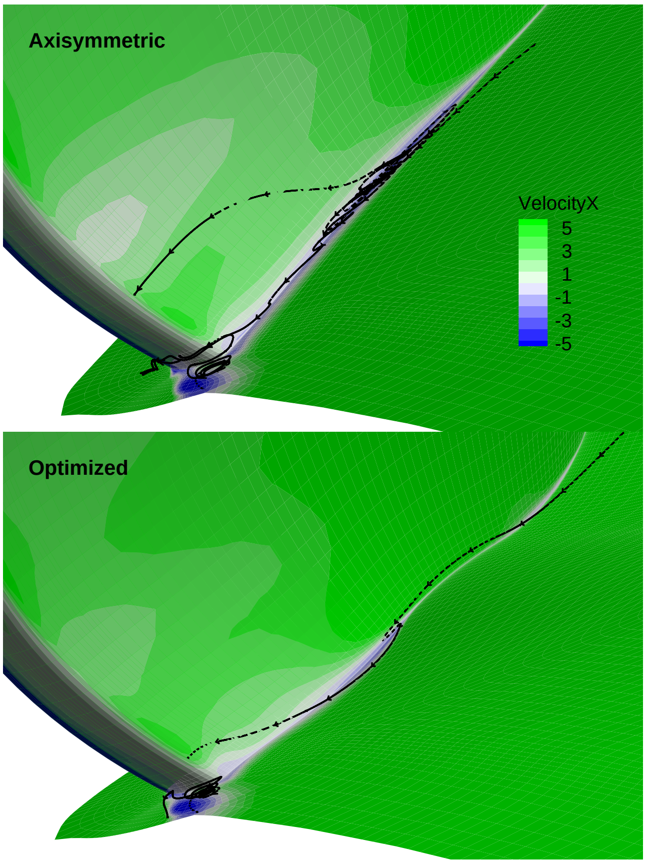

FIGURE 7. TRAILING EDGE SEPARATION REGION OF THE AXISYMMETRIC AND OPTIMIZED DESIGN

SUMMARY AND CONCLUSIONS

An application of the discrete adjoint method based on the RANS equations has been presented for the aerodynamic design optimization of the endwall contour of a turning mid-turbine frame. Gradients of the cost function in respect to the design variables are obtained by the adjoint method in which the adjoint of the RANS equations are solved only once at each design cycle irrespective of the number of design variables.

A design optimization case has been performed with the objective of minimizing pressure loss in a turning mid turbine frame. Additional constraints were not applied. The geometry of the optimized contoured endwall has been presented and the effect of the contoured endwall on the secondary flow and entropy production has been studied. Pressure loss and entropy production due to flow separation and boundary layer mixing is reduced signifi-

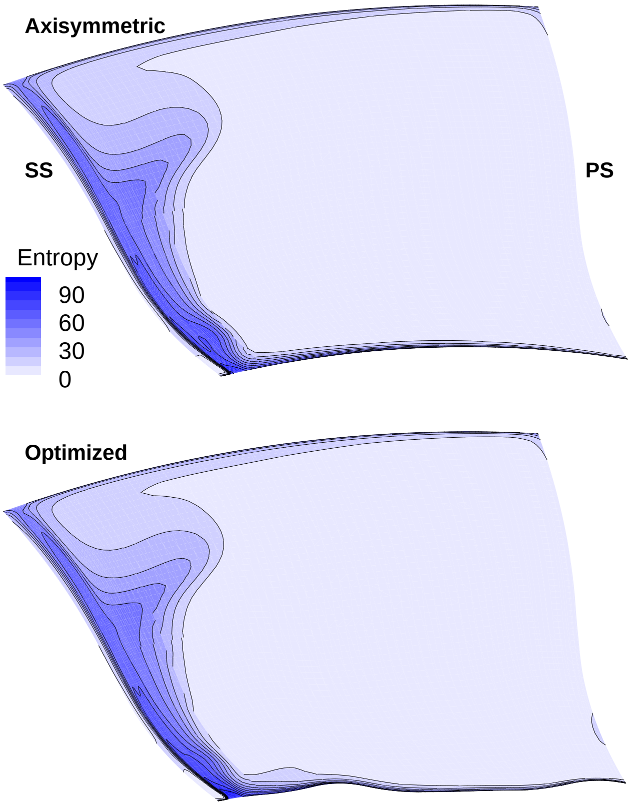

FIGURE 8. ENTROPY LEVELS OF THE AXISYMMETRIC AND OPTIMIZED DESIGN AT THE TRAILING EDGE

cantly with only 15 design cycles.

Additional benefits of the optimization are the increase in the mass flow rate and the increase of the turning of the flow which would allow for the design of struts with less curvature.

ACKNOWLEDGEMENT

The authors would like to thank the Austrian Federal Ministry for Transport, Innovation and Technology who funded the project SEIKON3D within the Austrian Aeronautics Program TAKE OFF as well as the German Aerospace Center (DLR) for the permission to make use of the CFD Solver TRACE and their extensive support. The research leading to some of the results used in this study has been partially funded by the European Union within the EU-project DREAM (contract No. ACP7-GA-2008-211861) as well as from the Austrian Federal Ministry for Finance.

REFERENCES

[1] Goldberg, D. E., 1989. *Genetic Algorithms in Search, Optimization, and Machine Learning*. Addison-Wesley Publishing Company, Inc.

[2] Price, K., and Storn, N., 1997. "Differencial evolution". *Dr. Dobb's Journal*.

[3] Hicks, R. M., and Henne, P. A., 1978. "Wing design by numerical optimization". *Journal of Aircraft,* ***15***, pp. 407–412.

[4] Pironneau, O., 1973. "On optimal profiles for stokes flow". *J. Fluid Mech.,* ***59***, pp. 117–128.

[5] Jameson, A., 1988. "Aerodynamic design via control theory". *Journal of Scientific Computing,* ***3***, pp. 233–260.

[6] Jameson, A., 1995. "Optimum aerodynamic design using CFD and control theory". AIAA 12th Computational Fluid Dynamics Conference, no. AIAA 95-1729.

[7] Kim, S., Alonso, J., and Jameson, A., 2004. "Multi-element high-lift configuration design optimization using viscous continous adjoint method". *Journal of Aircraft,* ***41***, pp. 1082–1097.

[8] Yang, H., Nuernberger, D., and Kersken, H.-P., 2006. "Towards excellence in turbomachinery computational fluid dynamics: A hybrid structured-unstructured Reynolds-averaged Navier-Stokes solver". *Journal of Turbomachinery,* ***128***, pp. 390–402.

[9] Wu, H., and Liu, F., 2005. "Aerodynamic design of turbine blades using an adjoint equation method". 43rd AIAA Aerospace Sciences Meeting and Exhibit, no. AIAA 2005-1006.

[10] Papadimitriou, D. I., and Giannakoglou, K. C., 2006. "A continous adjoint method for the minimization of losses in cascade viscous flows". 44th AIAA Aerospace Sciences Meeting and Exhibit, no. AIAA 2006-49.

[11] Corral, R., and Gisbert, F., 2008. "Profiled end wall design using an adjoint Navier-Stokes solver.". *Journal of Turbomachinery,* ***130(2)***.

[12] Wang, D., and He, L., 2010. "Adjoint aerodynamic design optimization for blades in multi-stage turbomachines: Part I - Methodology and verification". *Journal of Turbomachinery,* ***132(2)***.

[13] Wang, D., He, L., Li, Y. S., and Wells, R. G., 2010. "Adjoint aerodynamic design optimization for blades in multi-stage turbomachines: Part II - Methodology and verification". *Journal of Turbomachinery,* ***132(2)***.

[14] Luo, J., Xiong, J., Liu, F., and McBean, I., 2011. "Three-dimensional aerodynamic design optimization of a turbine blade by using an adjoint method". *Journal of Turbomachinery,* ***133***, January.

[15] Luo, J., Liu, F., and McBean, I., 2011. "Optimiza-

tion of endwall contours of a turbine blade row using an adjoint method". ASME Turbo Expo, Vancouver, Canada, no. GT2011-46163.

[16] Wilcox, D. C., 2001. "Turbulence modeling: An overview". *AIAA Paper 2001-0724*.

[17] Menter, F. R., Ferreira, J. C., Esch, T., and Konno, B., 2003. "The SST turbulence model with improved wall treatment for heat transfer predictions in gas turbines". International Gas Turbine Congress, Tokyo, Japan.

[18] Jameson, A., Alonso, J. J., Reuther, J. J., Martinelli, L., and Vassberg, J. C., 1998. "Aerodynamic shape optimization techniques based on control theory". *American Institute of Aeronautics and Astronautics, Inc.*

[19] Periaux, J., and Verstraete, T., eds., 2012. *Introduction to optimization and multidisciplinary design in aeronautics and turbomachinery*. Lecture Series of the von Karman Institue for Fluid Dynamics.

[20] Frey, C., Kersken, H.-P., and Nuernberger, D., 2009. "The discrete adjoint of a turbomachinery RANS solver". ASME Turbo Expo, Orlando, USA, no. GT2009-59062.

[21] Pieringer, P., 2012. Springer und Pieringer EDV Dienstleistungen OEG.

[22] Simmendinger, C., and Kügeler, E., 2010. "Hybrid parallelization of a turbomachinery CFD code: Performance enhancements on multicore architectures". V European Conference on Computational Fluid Dynamics.

[23] Giles, M. B., Duta, M. C., Mueller, J.-D., and Pierce, N. A., 2003. "Algorithm developments for discrete adjoint methods". *AIAA Journal,* ***41***(2), February.

[24] Papadimitriou, D. I., Zymaris, A. S., and Giannokoglou, K. C., 2005. "Discrete and continous adjoint formulations for turbomachinery applications". Evolutionary and Deterministic Methods for Desing, Optimization and Control with Applications to Industrial and Societal Problems, EUROGEN.

[25] Marta, A. C., and Shankaran, S., 2013. "On the handling of turbulence equations in rans adjoint solvers". *Computers and Fluids,* ***74***, pp. 102–113.

[26] Frey, C., Nuernberger, D., and Kersken, H. P., 2009. "Development and application of an adjoint RANS solver for turbomachinery". 8th European Turbomachinery Conference, Graz, Austria.

[27] Santner, C., 2013. "Experimental investigation of turning mid turbine frame designs". PhD thesis, TU Graz.

[28] Santner, C., Paradiso, B., Malzacher, F., Hoeger, M., Hubinka, J., and Goettlich, E., 2011. "Evolution of the flow through a turning mid turbine frame applied between a transonic HP-turbine stage and a counter-rotation LP-turbine". 9th European Turbomachinery Conference, Istanbul, Turkey.

[29] Wallin, F., Ore, S., Göttlich, E., and Santner, C., 2011. "Aero-design and validation of a turning mid turbine frame". 20th ISABE Conference, Gothenburg, Sweden, no. ISABE-2011-1713.

[30] Akin, M. B., and Sanz, W., 2014. "Influence of transition on CFD calculations of a two-stage counter-rotating turbine". ASME Turbo Expo, Düsseldorf, Germany, no. GT2014-26044.

[31] Spataro, R., Santner, C., Lengani, D., and Goettlich, E., 2012. "On the flow evolution through a LP turbine with wide-chord vanes in an S-shaped channel". ASME Turbo Expo, Copenhagen, Denmark, no. GT2012-68178.

[32] Menter, F. R., Kuntz, M., and Langtry, R., 2003. "Ten years of industrial experience with the sst turbulence model". Fourth International Symposium on Turbulence, Heat and Mass Transfer, Antalya, Turkey.

[33] Mousavi, A., Castonguay, P., and Nadarajah, S. K., 2007. "Survey of shape parameterization techniques and its effect on three-dimensional aerodynamic shape optimization". 18th AIAA Computational Fluid Dynamics Conference, no. AIAA 2007-3837.

[34] Wang, H. P., Olson, S. J., Goldstein, R. J., and Eckert, E. R. G., 1997. "Flow visualization in a linear turbine cascade of high performance turbine blades". *Journal of Turbomachinery,* ***119***.

A.4 Paper IV

Akin, M. B., Sanz, W., and Pieringer, P. Optimization of a low pressure turbine stage by hub endwall contouring of the turning mid turbine frame using an adjoint method. International Symposium on Experimental and Computational Aerothermodynamics of Internal Flows, Lerici, Italy, 2015.

This paper reports on the second optimization that eliminated the simplifications of the first opimization. Radial distribution of total temperatur, total pressure and flow direction were specified at the inlet. To ensure appropriate inflow at the LPR the optimization should be constrained with the yaw angle at the exit of the TMTF. But constrained optimization would require additional adjoint calculations. To avoid this, the TMTF was optimized with the low pressure rotor for isentropic efficiency. In this case, the outlet yaw angle of the TMTF doesn't have to be specified as a constraint, as an inconvenient inflow at the low pressure rotor would cause significant reduction of the efficiency. This optimization converged in 24 steps, improved the isentropic efficiency by 5.2 % and nearly fully eliminated flow separation at the trailing edge suction side.

Optimization of a Low Pressure Turbine Stage by Hub Endwall Contouring of the Turning Mid Turbine Frame Using an Adjoint Method

M. Bugra Akin[1], Paul Pieringer[2], Wolfgang Sanz[1]

1 Institute for Thermal Turbomachinery and Machine Dynamics
Graz University of Technology
Inffeldgasse 25A, Graz, Austria
Email: bugra.akin@tugraz.at

2 Springer und Pieringer
EDV-Dienstleistungen OG
Haydngasse 7, Graz, Austria

Abstract

This paper presents the application of a viscous adjoint method in the optimization of the endwall contour of a turning mid turbine frame (TMTF). The configuration consists of the TMTF and a succeeding low pressure turbine rotor. The adjoint method is a gradient based optimization method that allows for the computation of the complete gradient information by solving the governing flow equations and their corresponding adjoint equations only once per function of interest, so that the computation time of the optimization is nearly independent of the number of parameters.

A Navier-Stokes flow solver coupled with Menter's SST $k - \omega$ turbulence model is utilized for the CFD simulations, whereas the adjoint formulation is based on the constant eddy viscosity approximation for turbulence. The interface between the blade rows is calculated using the mixing-plane approach. The isentropic efficiency is the objective function of the optimization.

The optimization of the TMTF is performed including a downstream rotor row in order to capture the influence of the contoured endwall on the inflow to the rotor and to avoid adverse rotor inlet flow angle. Afterwards, the effect of contouring on the secondary flows is discussed and the performance of the axisymmetric TMTF is compared with the new design. The results are also compared with a former optimization of the TMTF using a different optimization strategy.

Keywords: CFD, optimization, endwall, hub, adjoint, turbine, turning mid turbine frame, TMTF

Nomenclature

$\mathbf{U}$	state vector
$\mathbf{V}$	velocity vector
$\mathbf{x}$	vector of design variables
C	constant
G	gradient
I	cost function
p	pressure
T	temperature
α	yaw angle
λ	step-size parameter
Ψ	adoint
ρ	density

Subscripts

t	total

Introduction

The improvement of the performance of engineering products is a major objective in their development; trying to achieve greater technical objectives such as increased reliability and reduced costs or to preserve natural resources. One of the main focuses in the improvement of turbomachinery is to increase thermal efficiency. Even very small achievements in this respect have a big impact on the overall fuel consumption which significantly affects economy, consumption of natural resources and emissions.

Computational Fluid Dynamics in conjunction with optimization algorithms provide an effective method to enable such improvements. The rapid increase in computing capacity and advances in numerical methods allow application of these methods more generally and in a cost-effective manner. Many approaches for the use of numerical optimization methods have been developed and some are widely used today. The methods are generally classified by the order of derivatives of the objective function used. These are zero, first and second order methods, which, as their names imply, use only the function values, first and second order derivatives, respectively. Examples for zero order methods are *evolutionary algorithms* such as *genetic algorithm*s [1] and *differential evolution* [2] and for first order methods *fi-*

nite difference methods [3] and *adjoint methods*. The adjoint method, which is the method of choice for this study, has been advocated amongst others mainly by Pironneau [4] and Jameson [5].

The adjoint method provides an efficient alternative for the calculation of the gradient in cases where many parameters are involved. It has been widely used in the aerodynamic design optimization for airfoils, wings and wing-body configurations [6, 7]. Recently, its application has been extended to turbomachinery design optimization [8, 9, 10, 11, 12, 13, 14, 15].

The main advantage of the adjoint method is that for each optimization cycle the computational cost required to obtain the derivatives is nearly independent of the number of parameters. Only one extra inexpensive calculation in addition to the computation of the Navier-Stokes equations and their viscous adjoint equations has to be performed for each parameter. The adjoint of the Navier-Stokes equations can be derived either with a continuous adjoint approach or a discrete adjoint approach. The solver applied in the current study utilizes the discrete adjoint method.

An essential component of the optimization is the flow solver. The solutions provided by the solver must be physically accurate or at least representative of the actual flow. But one of the greatest weaknesses of CFD is turbulence and transition modeling. Models which can accurately capture these phenomena under any conditions still have not been achieved. An overview of turbulence models has been presented by Wilcox [16], also arguing that models based on the ω-equation can support satisfactory solutions for most of the flows. Therefore, in this work Menter's SST $k-\omega$ turbulence model (Menter et al. [17]) is used.

The test case presented in this study is optimized with respect to the isentropic efficiency of the turbine stage. The solver TRACE has been utilized, which has been developed at DLR for internal flows, specifically for turbomachinery [8].

Adjoint Method

The adjoint method will be introduced briefly for the sake of completeness. For a more detailed description the reader is referred to other sources such as Jameson et al. [18] and Periaux and Verstraete [19]. A description specifically for the solver TRACE is published by Frey et al. [20].

For the derivation of the adjoint equation we will define a single-objective optimization problem as commonly defined with

$$I(\mathbf{U},\mathbf{x}) \qquad (1)$$

as the cost function to be minimized (or maximized) subject to the state equation

$$R(\mathbf{U},\mathbf{x}) = 0, \qquad (2)$$

which for optimal shape design with CFD are the RANS equations. $\mathbf{U}$ is the state vector and $\mathbf{x}$ the vector of design variables.

With the chain rule the sensitivities of the cost function can be written as:

$$\frac{dI(\mathbf{U},\mathbf{x})}{d\mathbf{x}} = \frac{\delta I}{\delta \mathbf{U}}\frac{\delta \mathbf{U}}{\delta \mathbf{x}} + \frac{\delta I}{\delta \mathbf{x}}. \qquad (3)$$

The terms $\frac{\delta I}{\delta \mathbf{U}}$ and $\frac{\delta I}{\delta \mathbf{x}}$ are relatively easy to compute as the cost function I is expressed as an explicit function of the state variable $\mathbf{U}$ and the control variables $\mathbf{x}$. The computation of $\frac{\delta \mathbf{U}}{\delta \mathbf{x}}$ is rather more complicated and requires a different strategy for efficient computation. The application of the chain rule on the state equation results in:

$$\frac{\delta R}{\delta \mathbf{U}}\frac{\delta \mathbf{U}}{\delta \mathbf{x}} + \frac{\delta R}{\delta \mathbf{x}} = 0. \qquad (4)$$

After reformulating Eq. (4) for $\frac{\delta U}{\delta x}$ and inserting into Eq. (3) the sensitivities can be rewritten as:

$$\frac{dI}{d\mathbf{x}} = \Psi^T \frac{\delta R}{\delta \mathbf{x}} + \frac{\delta I}{\delta \mathbf{x}}, \qquad (5)$$

where Ψ represents the adjoint and is the solution of

$$(\frac{\delta R}{\delta \mathbf{U}})^T \Psi = -(\frac{\delta I}{\delta \mathbf{U}})^T. \qquad (6)$$

This means that for the evaluation of the sensitivities, Eq. (6) has to be solved first, which is a set of equations called the adjoint equation. The solution of the adjoint equation is approximately as expensive as the solution of the RANS equations. The advantage is that it is not dependent on the design variables. So for a single-objective optimization problem without additional constraints it has to be calculated only once for each design cycle. After the adjoint Ψ has been calculated Eq. (5), which is computationally much more inexpensive, can be evaluated for the sensitivities.

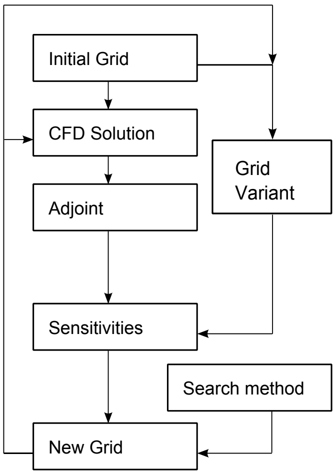

Figure 1: **Optimization flow chart**

Numerical Method

The tools utilized in this paper include a CFD solver, an adjoint solver, a mesher and Python as a scripting language to control them. In Fig. 1 the flow chart of the optimization routine is shown. Starting with the initial grid the CFD solution and the adjoint are calculated. In the meantime also the grid variants are generated. The number of grid variants is equal to the number of parameters, as each grid variant is the grid at the current optimization step with one of the parameters shifted. Grid generation is carried out with an in-house mesher developed by Pieringer [21]. Then the sensitivities are calculated using the adjoint solution and grid variants. The search method provides a step size with which the parameters are updated and a new geometry is generated and meshed. Depending on the search method used the step size can be calculated from the sensitivities as is the case with quasi-Newton methods.

Flow Solver

The Reynolds-averaged Navier Stokes (RANS) solver TRACE has been used for the calculation of the flow solution and the adjoint as well as sensitivities. The governing equations are integrated in time by a fully implicit formulation of the first-order accurate scheme. The convective fluxes are discretized using Roe's total variation diminishing (TVD) upwind scheme, which is combined with van Leer's monotone upstream-centered scheme for conservation laws (MUSCL) to obtain second-order accuracy in space. The derivatives of the viscous fluxes are approximated by central differences. At inlet and outlet boundaries the non-reflecting formulation according to Giles is applied. Additionally the solver is parallelized. Detailed information on TRACE can be found in the references [8], [22].

Adjoint Solution

In TRACE the discrete adjoint of the RANS equations has been implemented by Frey et al. [20], which is based on the already discretized form of the Navier-Stokes equations. The advantage of this approach is that it prescribes a discretization of the adjoint partial differential equation so that the choice for appropriate discretization schemes becomes redundant, and sensitivities are naturally consistent with the flow solver. Further discussion on the discrete and continuous approaches has been published by Giles et al. [23] and Papadimitriou et al. [24].

The adjoint formulation has not been extended to any of the turbulence models available in the solver. It is based on the constant eddy viscosity assumption so that when computing sensitivities with respect to shape variations the eddy viscosity assumes the same values as for the solution calculated for the current optimization step. This approach has the advantage of faster implementation and less computational cost in comparison to an implementation of the adjoint equation corresponding to the full turbulence models. It results in mostly good agreement of sensitivities with those calculated by finite differences as shown by Frey et al. [20, 25, 26].

The adjoint equation is solved by a generalized minimal residual method (GMRES). The solver provides the option to precondition the system with either incomplete lower-upper decomposition (ILU) or symmetric successive over-relaxation (SSOR). In this work ILU was used. For more details on the numerical method the reader is referred to Frey et al. [20, 25].

Sensitivities

The sensitivities are calculated using Eq. (5) with the adjoint solution Ψ from Eq. (6) for a specific cost function. Most turbomachinery specific cost functions depend only on the state at certain planes, typically the inlet and exit of blade rows. Therefore, the evaluation can be simplified with the assumption that the sensitivities depend only on the sensitivity of averaged states as long as hub or casing geometry are not varied at these planes [20]. In this case $\frac{\delta I}{\delta x}$ in Eq. (5) can be set to 0 .

The term $\frac{\delta R}{\delta x}$ is approximated by finite differences for which the residuals of the flow solution are evaluated for the grid variants [20]. The perturbation factor for the grid variants has been set to $1\ mm$ in the radial direction for each point.

This step is approximately as time consuming as one time step of the CFD solver. It is the only step for which the CPU time remains proportional to the number of parameters. A new mesh has to be generated for each parameter and this can become computationally expensive if the number of parameters are high and the mesh is large. Still, mesh generation can be performed parallel to the calculation of the CFD and adjoint solution to avoid losing time.

Search Method

After the sensitivities G_n have been evaluated the parameters of the next step for an optimization problem can be calculated with

$$x_{n+1} = x_n - \lambda G_n. \tag{7}$$

λ is the step-size parameter. A variety of search methods exist to determine the step size, e.g. the steepest descent, modified steepest descent with smoothing, implicit descent, multigrid steepest descent, Krylov acceleration, and quasi-Newton methods. For the optimization presented here the rank one (R1) quasi-Newton method is used. Quasi-Newton methods approximate the Hessian (second order derivatives) or its inverse from changes in the gradient during the search steps. They are widely regarded as the method of choice for general optimization problems [19]. The R1 method uses the following equation:

$$\lambda_{n+1} = \lambda_n + \frac{P_n(P_n)^T}{(P_n)^T \delta G_n} \tag{8}$$

where

$$P_n = \delta x_n - \lambda_n \delta G_n. \tag{9}$$

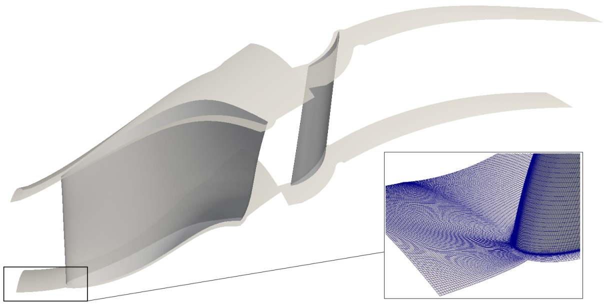

Figure 2: **Computational domain with the TMTF and LPR and mesh resolution at the leading edge of the TMTF**

Test Case

The Institute for Thermal Turbomachinery and Machine Dynamics at Graz University of Technology operates a unique transonic test turbine facility (TTTF). On the test rig of the institute a two-stage counter-rotating turbine, which has been designed by MTU Aero Engines and Volvo Aero (acquired by GKN plc.), is the subject of various investigations. The configuration consists of a single-stage unshrouded transonic high pressure (HP) turbine, an S-shaped turning mid turbine frame (TMTF) followed by a shrouded counter-rotating low pressure (LP) turbine. Two different TMTFs have been designed in the framework of the former EU project DREAM. Information about the related investigations has been published by Santner [27]. The design by Volvo Aero already uses a contoured hub endwall to reduce secondary losses. More information regarding the rig configuration and measurement campaigns is reported amongst others by Santner et al. [28] and Wallin et al. [29]. The flow in the TMTF with the Volvo design was investigated numerically by Akin and Sanz [30]. Spataro et al. [31] reported on the flow evolution through the other TMTF design.

The configuration in this study consists of the TMTF designed by Volvo and the low pressure rotor (LPR). Only the TMTF hub endwall is optimized. For the initial condition the contoured endwall is replaced by an axisymmetric mean contour.

Fig. 2 shows the computational domain and the mesh resolution at the leading edge of the TMTF. Steady-state calculations have been performed. The meshing has been carried out with the in-house mesher developed by Pieringer [21]. The grid is a multi-block grid consisting of 33 blocks for the convenience of parallelization and consists of 4.7 million cells. An O-type block encloses the blade. The y^+ value at all walls is below 1.

Dirichlet boundary conditions have been applied. At the inlet radial distribution of the total pressure, total temperature, and flow angles as well as turbulent kinetic energy and dissipation have been specified. These inlet conditions are the result of previous CFD investigations and were reported on by Akin and Sanz [30]. At the outlet the static pressure in the middle of the channel height and radial equilibrium was specified. Turbulence has been modeled with the SST turbulence model with improved wall treatment by Menter et al. [17, 32]. The optimization has been carried out with respect to isentropic efficiency, naturally trying to maximize its value.

The computations were performed on the high performance computing platform of Graz University of Technology utilizing 18 processor cores with 2.27 GHz. For the adjoint solution each processor allocated between 2.0 GB and 2.6 GB of memory.

Depending on how much a new contour differs from the previous setup the CFD solution can take from 13 to 20 hours to achieve a precision of $0.001\ \%$ deviation in mass flow rate and the adjoint solution can take up to 10 hours to achieve a residual drop by 10^{-1}.

Endwall Contouring

For the parametrization of the endwall contour 36 equally spaced points were defined on the hub surface of the initial axisymmetric contour. In Fig. 3 the positions of these points are shown. Some points are at the location of the struts. Although there is no endwall present there, these points will still affect the contour as each point has a larger influence area.

The points defined on the hub are moved only in the radial direction such that each point has one degree of freedom. Consequently the test case has 36 design variables.

The points are fitted using a B-spline surface which defines the geometry between them. A higher order B-spline leads to smoother surfaces and the smoothness of a third order B-spline was determined to be appropriate. This surface defines the hub contour and is used by the mesher to fit the nodes of the grid. The procedure has been implemented into the mesher by Pieringer [21].

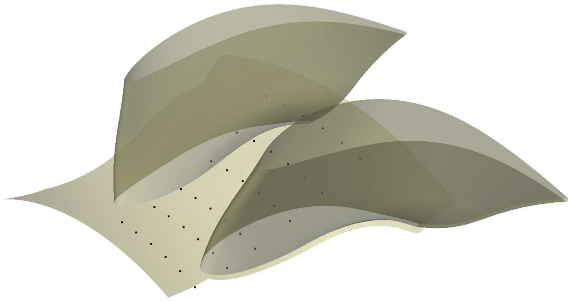

Figure 3: **Positions of the 36 points defining the hub contour**

Results and Discussion

A significant increase in the thermal efficiency of the turbine stage is achieved after 24 design cycles. Fig. 4 shows the development of the polytropic efficiency during the optimization, which is defined with

$$\eta_p = \frac{\ln\left(\frac{T_{t,outlet}}{T_{t,inlet}}\right)}{\ln\left(\frac{p_{t,outlet}}{p_{t,inlet}}\right)^{\frac{\gamma-1}{\gamma}}}. \tag{10}$$

The polytropic efficiency provides a measure for the performance of the stage which does not vary with pressure ratio. It is better to use polytropic efficiency instead of isentropic efficiency for comparison of the designs as the total pressure ratio of the stage changes due to the contour manipulation, even though the cost function is the isentropic efficiency. The change in the pressure ratio is so small though, that the plot in Fig. 4 is nearly identical for the isentropic efficiency. It can be observed that an optimum is achieved after 24 design cycles and the efficiency is increased by $5.2\,\%$.

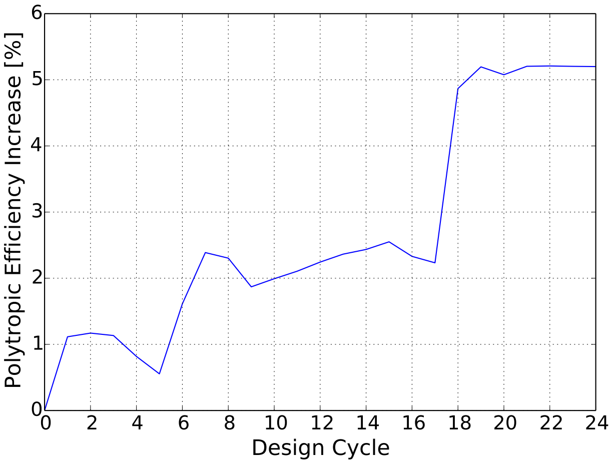

Figure 4: **Increase of polytropic efficiency during the optimization**

The contoured endwall after 24 design cycles is shown in Fig. 5. The deviation of the radius with respect to the initial axisymmetric endwall is illustrated by a contour plot. The blue region indicates a decrease in the radius whereas the red region indicates an increase. Up to approximately mid axial chord length the contour is mostly unchanged. Then it starts forming a wavy structure along the blade contour at the suction side. The local minima and maxima are greater closer to the blades. The highest deformation is at the suction side of the trailing edge and is about $1.52\,\mathrm{mm}$. On the pressure side trailing edge the contour radius is slightly increased.

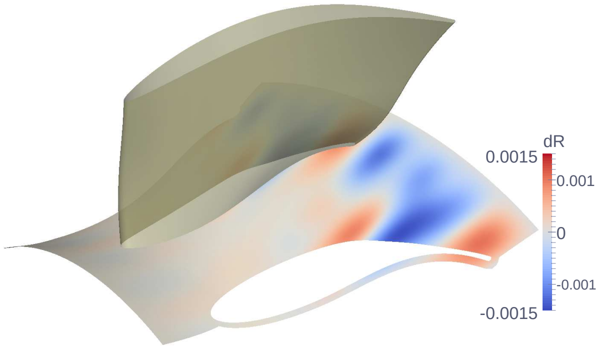

Figure 5: **Optimized hub contour**

Fig. 6 shows the flow in the TMTF close to the hub for the axisymmetric contour. The contour plot shows the axial velocity at a small distance from the wall (2^{nd} cell for the endwall, 8^{th} cell for the blades). The scale is between -10 and 10. The main objective is to visualize flow separation. As this is an axial machine negative axial velocity indicates flow separation. Regions with negative values of axial velocity are coloured with blue which can be seen on the suction side of the blade at the trailing edge. To display the volume of the separation regions isovolumes of negative velocity are also visualized. Two regions of flow separation can clearly be observed. A relatively large separation zone develops on the suction side of the blade. A second, smaller zone can be observed on the shroud just before the exit plane. It can be seen in Fig. 6 downstream of the tailing edge of the blade on the right above the aforementioned separation zone. Aside from other secondary flow phenomena (horse shoe vortex, passage vortex, etc.) this flow separation is one of the strongest causes of entropy generation in the TMTF. It can be expected that hub endwall contouring influences the flow separation region on the blade as this region can be directly influenced by this method.

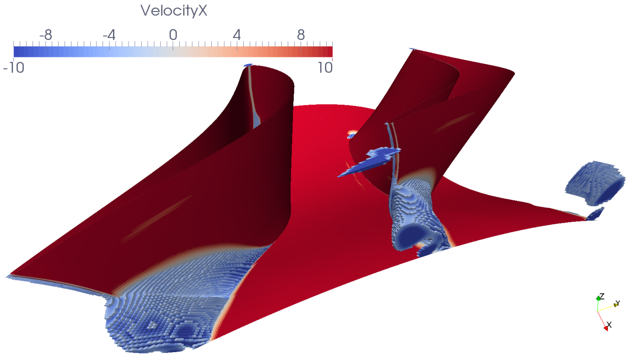

Figure 6: **Flow at the trailing edge of the TMTF with the axisymmetric contour**

Fig. 7 shows the flow in the TMTF with the hub contour after 24 optimization cycles (referred to as the new contour). Flow separation can still be observed but it is significantly reduced; the region which covered half the span at the trailing edge for the axisymmetric contour now covers only a very small area on the corner of the trailing edge. Consequently the volume of separated flow has become confined to a much smaller region so that the fluid can better follow the blade contour. Also the hub contouring has a positive affect on the flow close to the shroud. The separation which can be observed in Fig. 6 is eliminated by the new contour. The polytropic efficiency of the LP stage achieved by this design is 5.2 % better than that of the axisymmetric contour.

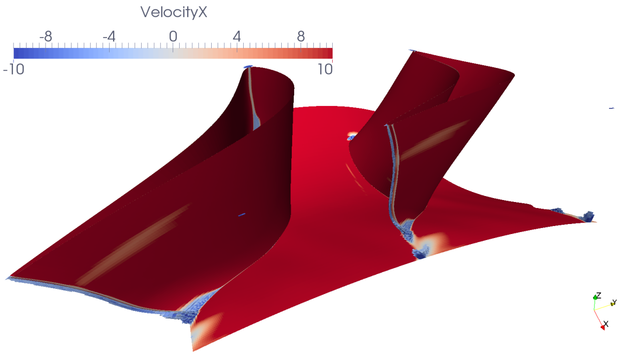

Figure 7: **Flow at the trailing edge of the TMTF with the new contour**

Fig. 8 shows the flow in the TMTF with the original Volvo hub contour. It was optimized using a constrained gradient-based method with surrogate models. The principles of the optimization strategy used for this design are described by Wallin [33] (although this design was also optimized it is referred to as the Volvo contour). The design fully eliminates the flow separation at the trailing edge such that the boundary layer flow is completely attached. But this contour seems to influence the separation region on the shroud minorly. Only a very careful comparison reveals that the volume of this zone is also slightly reduced.The polytropic efficiency of the LP stage achieved by this design is 6.3 % better than that of the axisymmetric contour shown in Fig. 6.

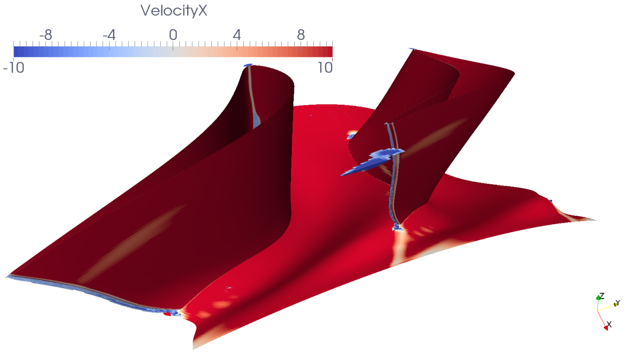

Figure 8: **Flow at the trailing edge of the TMTF with the Volvo contour**

The increase of efficiency by 5.2 % and 6.3 % are huge improvements which can be achieved because the design with the axisymmetric contour is not a mature design, but instead it emanates from a previous TMTF design. The intention of the design procedure was to make the new TMTF more aggressive while keeping the performance of the low pressure rotor unchanged and to avoid increased total pressure loss. The Volvo TMTF is therefore 10 % shorter than the original state-of-the-art TMTF design. Validation of the Volvo design is presented by Wallin et al. (2011).

Fig. 9 illustrates the influence of the optimization on the overall flow at the exit of the TMTF. The plots show the circumferentially averaged values of the total pressure coefficient $c_{p_t} = \frac{2(p_t - p_{inlet})}{\rho_{inlet}|\mathbf{V}|^2_{inlet}}$, normalized yaw angle $\alpha_n = \frac{\alpha}{C}$ and entropy over the span. The total pressure coefficient is increased specifically in the region below 0.7 span. The TMTF with the Volvo contour outperforms the contour optimized with the adjoint method. Clearly due to the fact that flow separation on the hub is fully prevented by this design. Although both contours improve the total pressure coefficient very similarly a lower total pressure coefficient can be observed at around 0.2 span with the new design, which is probably due to the influence of the small separation region. But closer to the hub this relation is reversed such that the design optimized with the adjoint method has a higher total pressure. Close to the shroud the total pressure coefficient is improved for both solutions, but only the new design fully eliminates the flow separation here. Although in the Volvo design this back flow region can still be observed its negative effect on the total pressure seems to be significantly reduced. The yaw angle has also become more homogeneous over the span. Due to the smaller separation region that is still present in the new design the region below 0.1 span experiences a lower turning than the Volvo design. There is very good agreement between the Volvo results and the optimized contour results from 0.1 span almost up to the shroud. At the shroud the unfavorable influence of the small separation region on the yaw angle is mostly eliminated by the new design.

On the plots of the total pressure coefficient and normalized yaw angle in Fig. 9 experimental results of the Volvo contour are also incorporated. The good agreement of the simulation results with the measured values demonstrates the reliability of the CFD results qualitatively. Nevertheless, there is flow separation and it increases the uncertainty of the solution. Broad trends can generally be captured with CFD simulations but the region and volume of separation zones may vary with different turbulence models. The flow separation on the shroud of the TMTF with the Volvo contour has not been noticed in measurements (for more information on the measurement campaigns please refer to Santner [27]). In the design verification published by Wallin et al. [29] the CFD simulations do not indicate such a flow separation on the shroud. But, this evaluation plane and the measurement plane are 1 cm upstream of the exit and before this small separation region on the shroud.

Finally the entropy plot in Fig. 9 shows the reduction of entropy generation. Close to the hub the new contour performs better as well as between 0.25 and 0.5 span and also close to the hub. Otherwise the Volvo contour shows less entropy especially in the lower span region, which in the new design is still influenced by a small separation region.

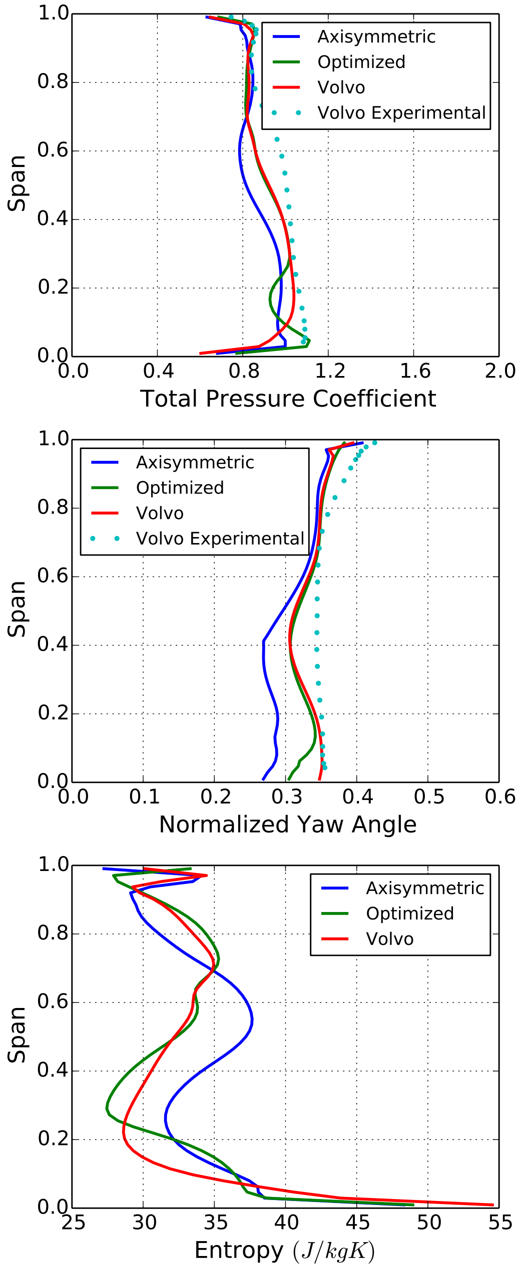

Figure 9: **Radially averaged total pressure coefficient, normalized yaw angle and specific entropy at the exit of the TMTF**

The adjoint method does not converge towards the Volvo contour. The contour that can be achieved by an optimization depends considerably on the parametrization. The method that led to the Volvo contour uses a procedure based on adding perturbations to a baseline design to change the meridional contour. These perturbations are linear combinations of orthogonal polynomials. Circumferential perturbations are realized by introducing circumferential cosine and sine functions. Details on this procedure are published by Wallin [33]. To achieve the same contour with the presented parametrization method is not possible. For that the number of parameters would have to be increased considerably. But simply using the same parametrization method would be a more convenient approach for such an endeavour. Also, the new contour that resulted from the optimization procedure with the adjoint method is clearly not the global optimum. At least an additional $1.1\,\%$ increase in the efficiency of the new contour can be achieved through endwall contouring. Arranging the parameters shown in Fig. 3 on the intended streamline might help achieve this goal. The expectation in this case is that the bumps and dents introduced on the hub contour might be on a more convenient path to have a stronger positive influence on the flow. Another idea is to reduce the number of parameters used which would help in creating a smoother contour.

Summary and Conclusions

An application of the discrete adjoint method based on the RANS equations is presented for the aerodynamic design optimization of the hub endwall contour of a turning mid-turbine frame with a parametrization based on perturbing a B-spline surface causing small bumps and dents. A design optimization case is performed with the objective of maximizing the isentropic efficiency of a turbine low pressure stage. The geometry of the optimized endwall and the affect of contouring on the secondary flow is presented. Flow separation regions, consequent pressure loss and entropy production are reduced significantly with 24 design cycles, radial yaw angle distribution is improved and an increase of polytropic efficiency by $5.2\,\%$ is achieved. These results are compared to the optimization of the same geometry with an optimization method based on gradient information achieved with polynomial response surfaces as surrogate models and a parametrization technique that adds perturbations to a baseline design using orthogonal polynomials as well as sine and cosine functions. This design fully eliminates the flow separation at the intersection of the hub and suction side of the strut trailing edge and achieves a better radial distribution of the outlet yaw angle. The efficiency of this design is $6.3\,\%$ better than the initial axisymmetric geometry.

This presented optimization has improved the efficiency of the low pressure turbine significantly. Yet comparison with the former optimization demonstrates that it is possible to improve the design further. This can be achieved with the parametrization. A simple improvement of this aspect would be to reorder the control points in the intended stream path and reconsider the number of parameters used. The idea will be tested in future work.

Acknowledgments

The authors would like to thank the Austrian Federal Ministry for Transport, Innovation and Technology who funded the project SEIKON3D within the Austrian Aeronautics Program TAKE OFF as well as the German Aerospace Center (DLR) for the permission to make use of the CFD Solver TRACE and their support. The research leading to some of the results used in this study has been partially funded by the European Union within the EU-project DREAM (contract No. ACP7-GA-2008-211861) as well as from the Austrian Federal Ministry for Finance.

[1] Goldberg, D. E. Genetic Algorithms in Search, Optimization, and Machine Learning. Addison-Wesley Publishing Company, Inc., 1989.

[2] Price, K. and Storn, N. Differencial evolution. Dr. Dobb's Journal, 1997.

[3] Hicks, R. M. and Henne, P. A. Wing design by numerical optimization. Journal of Aircraft, 15:407–412, 1978.

[4] Pironneau, O. On optimal profiles for stokes flow. J. Fluid Mech., 59:117–128, 1973.

[5] Jameson, A. Aerodynamic design via control theory. Journal of Scientific Computing, 3:233–260, 1988.

[6] Jameson, A. Optimum aerodynamic design using CFD and control theory. Proceedings of AIAA 12th Computational Fluid Dynamics Conference, AIAA 95-1729, San Diego, June 1995.

[7] Kim, S., Alonso, J., and Jameson, A. Multi-element high-lift configuration design optimization using viscous continous adjoint method. Journal of Aircraft, 41: 1082–1097, 2004.

[8] Yang, H., Nuernberger, D., and Kersken, H.-P. Towards excellence in turbomachinery computational fluid dynamics: A hybrid structured-unstructured Reynolds-averaged Navier-Stokes solver. Journal of Turbomachinery, 128:390–402, 2006.

[9] Wu, H. and Liu, F. Aerodynamic design of turbine blades using an adjoint equation method. Proceedings of 43rd AIAA Aerospace Sciences Meeting and Exhibit, AIAA 2005-1006, Reno, Nevada, January 2005.

[10] Papadimitriou, D. I. and Giannakoglou, K. C. A continous adjoint method for the minimization of losses in cascade viscous flows. Proceedings of 44th AIAA Aerospace Sciences Meeting and Exhibit, AIAA 2006-49, Reno, Nevada, January 2006.

[11] Corral, R. and Gisbert, F. Profiled end wall design using an adjoint Navier-Stokes solver. Journal of Turbomachinery, 130(2), 2008.

[12] Wang, D. and He, L. Adjoint aerodynamic design optimization for blades in multi-stage turbomachines: Part I - Methodology and verification. Journal of Turbomachinery, 132(2), 2010.

[13] Wang, D., He, L., Li, Y. S., and Wells, R. G. Adjoint aerodynamic design optimization for blades in multi-stage turbomachines: Part II - Methodology and verification. Journal of Turbomachinery, 132(2), 2010.

[14] Luo, J., Xiong, J., Liu, F., and McBean, I. Three-dimensional aerodynamic design optimization of a turbine blade by using an adjoint method. Journal of Turbomachinery, 133, January 2011.

[15] Luo, J., Liu, F., and McBean, I. Optimization of end-wall contours of a turbine blade row using an adjoint method. Proceedings of ASME Turbo Expo, Vancouver, Canada, GT2011-46163, 2011.

[16] Wilcox, D. C. Turbulence modeling: An overview. AIAA Paper 2001-0724, 2001.

[17] Menter, F. R., Ferreira, J. C., Esch, T., and Konno, B. The SST turbulence model with improved wall treatment for heat transfer predictions in gas turbines. Proceedings of International Gas Turbine Congress, Tokyo, Japan, 2003.

[18] Jameson, A., Alonso, J. J., Reuther, J. J., Martinelli, L., and Vassberg, J. C. Aerodynamic shape optimization techniques based on control theory. American Institute of Aeronautics and Astronautics, Inc., 1998.

[19] Periaux, J. and Verstraete, T., editors. Introduction to optimization and multidisciplinary design in aeronautics and turbomachinery. Lecture Series of the von Karman Institue for Fluid Dynamics, 2012.

[20] Frey, C., Kersken, H.-P., and Nuernberger, D. The discrete adjoint of a turbomachinery RANS solver. Proceedings of ASME Turbo Expo, Orlando, USA, GT2009-59062, 2009.

[21] Pieringer, P. Springer und Pieringer EDV Dienstleistungen OEG, 2012.

[22] Simmendinger, C. and Kuegeler, E. Hiybrid parallelization of a turbomachinery CFD code: Performance enhancements on multicore architectures. Proceedings of V European Conference on Computational Fluid Dynamics, 2010.

[23] Giles, M. B., Duta, M. C., Mueller, J.-D., and Pierce, N. A. Algorithm developments for discrete adjoint methods. AIAA Journal, 41(2), February 2003.

[24] Papadimitriou, D. I., Zymaris, A. S., and Giannokoglou, K. C. Discrete and continous adjoint formulations for turbomachinery applications. Proceedings of Evolutionary and Deterministic Methods for Desing, Optimization and Control with Applications to Industrial and Societal Problems, EUROGEN, 2005.

[25] Frey, C., Nuernberger, D., and Kersken, H. P. Development and application of an adjoint RANS solver for turbomachinery. Proceedings of 8th European Turbomachinery Conference, Graz, Austria, 2009.

[26] Frey, C., Ashcroft, G., Backhaus, J., Kügeler, E., and Wellner, J. Adjoint-based flow sensitivity analysis using arbitrary control surfaces. Proceedings of ASME Turbo Expo, Vancouver, British Columbia, Canada, GT2011-45041, 2011.

[27] Santner, C. Experimental investigation of turning mid turbine frame designs. PhD thesis, TU Graz, 2013.

[28] Santner, C., Paradiso, B., Malzacher, F., Hoeger, M., Hubinka, J., and Goettlich, E. Evolution of the flow through a turning mid turbine frame applied between a transonic HP-turbine stage and a counter-rotation LP-turbine. Proceedings of 9th European Turbomachinery Conference, Istanbul, Turkey, March 2011.

[29] Wallin, F., Ore, S., Göttlich, E., and Santner, C. Aerodesign and validation of a turning mid turbine frame. Proceedings of 20th ISABE Conference, Gothenburg, Sweden, ISABE-2011-1713, March 2011.

[30] Akin, M. B. and Sanz, W. Influence of transition on CFD calculations of a two-stage counter-rotating turbine. Proceedings of ASME Turbo Expo, Düsseldorf, Germany, GT2014-26044, 2014.

[31] Spataro, R., Santner, C., Lengani, D., and Goettlich, E. On the flow evolution through a LP turbine with wide-chord vanes in an S-shaped channel. Proceedings of ASME Turbo Expo, Copenhagen, Denmark, GT2012-68178, 2012.

[32] Menter, F. R., Kuntz, M., and Langtry, R. Ten years of industrial experience with the sst turbulence model. Proceedings of Fourth International Symposium on Turbulence, Heat and Mass Transfer, Antalya, Turkey, 2003.

[33] Wallin, F. Flow Control and Shape Optimization of Intermediate Turbine Ducts for Turbofan Engines. PhD thesis, Chalmers University of Technology, 2008.

A.5 Paper V

Akin, M. B. and Sanz, W. A quasi first order optimization method and its demonstration on the optimization of a U-bend. ASME Turbo Expo, Montreal, Canada, GT2015-42640, 2015.

This paper reports on the first test case that demonstrates the successful application of the new optimization method on a U-bend. It is an alternative optimization method which is fast, efficient and easy to implement and it is referred to as a quasi-first-order optimization method.

A QUASI-FIRST ORDER OPTIMIZATION METHOD AND ITS DEMONSTRATION ON THE OPTIMIZATION OF A U-BEND

M. Bugra Akin[*], **Wolfgang Sanz**
Institute for
Thermal Turbomachinery and Machine Dynamics
Graz University of Technology
Graz, Austria, A-8010
Email: bugra.akin@tugraz.at

ABSTRACT

Optimal shape design is widely used today to improve a variety of designs. It is a challenging task and several methods have been developed. These methods are generally classified by the order of derivatives used. They are zero, first and second order methods, which, as their names imply, use only the function values, first and second order derivatives, respectively. There are two common approaches to first order methods. These are the finite difference method and the adjoint method. The finite difference method requires an additional CFD calculation for each parameter, which quickly becomes computationally very expensive as the number of parameters rise. The adjoint method provides a computationally efficient alternative in such cases. But the computational cost of the adjoint method also becomes expensive if additional constraints are introduced or when multi-objective optimizations are considered.

This paper presents a novel optimization strategy which can be classified as a quasi-gradient based optimization method. As with the finite differences method an additional CFD calculation is performed for each parameter. But in order to save computational time the simulations are not performed to full convergence so that the derivatives are not calculated accurately. The only information that can be obtained in this way is whether the chosen contour manipulation leads to an improvement. A line search method is introduced that can find an optimum using this incomplete gradient information. The optimization method is demonstrated by the quasi-3d optimization of a U-bend.

NOMENCLATURE

f	cost/objective function
g	inequality constraint
h	equality constraint
k	turbulent kinetic energy
$k*$	normalized turbulent kinetic energy
n	step number
p	pressure
S	search direction
$\mathbf{S}$	vector of search directions
U_0	bulk velocity at the inlet
u	velocity in x-direction
u'	velocity fluctuation in x-direction
$\mathbf{V}$	velocity vector
v	velocity in y-direction
v'	velocity fluctuation in y-direction
x	design variable
$\mathbf{x}$	vector of design variables
α	step size
Δ	scale factor
ρ	density

INTRODUCTION

Optimization methods in conjunction with computational fluid dynamics (CFD) provide sophisticated tools for optimal shape design (OSD) for fluids. These methods are widely used today in several industries such as turbomachinery and airplane for the design of various components such as turbine/compressor blades, blade endwalls

---

[*] Corresponding author

and cooling channels. Despite its widespread use OSD is still a challenging and computationally intensive task.

A single-objective optimization problem in the form of a minimization problem can be formulated mathematically as:

$$\texttt{Minimize:} \quad f(\mathbf{x}) \tag{1}$$

$$\texttt{Subject to:} \quad g_i(\mathbf{x}) \leq 0, \quad i = 1..p \tag{2}$$

$$h_j(\mathbf{x}) = 0, \quad j = 1..q \tag{3}$$

$$x_k^l \leq x_k \leq x_{k,}^u \ k = 1..r \tag{4}$$

The vector $\mathbf{x}$ is the vector of design variables and it contains the parameters of the design that can be modified. The function $f(\mathbf{x})$ is referred to as the objective function. This can e.g. be the cost of a part or the efficiency of a process. The inequality constraints given by Eq. (2) represent conditions that need to be satisfied and the equality constraints given by Eq. (3) usually represent relationships between design variables. For the optimization for fluid flows the equality constraints are generally the RANS equations, as common cost functions like pressure drop or entropy production depend on fluid properties that also have to satisfy the RANS equations. Eq. (4) represents the range of the design variables. In an optimization a new design is usually based on the previous one:

$$\mathbf{x}_{n+1} = \mathbf{x}_n - \alpha_n \mathbf{S}_n. \tag{5}$$

$\mathbf{S}_n$ is the search direction of iteration step n and α_n is a scalar that sets the amplitude of the change.

Many approaches for the use of numerical methods in optimization have been developed. The methods are generally classified by the order of derivatives of the objective function used to find a minimum or maximum. These are zero, first and second order methods.

Zero order methods are technically the simplest approach to optimization. A large number of random candidate vectors $\mathbf{x}$ are selected and the objective function is evaluated for each of them. The vector $\mathbf{x}$ which results in the smallest objective function satisfying all constraints is regarded as the optimum. For a precise solution a very large number of candidate vectors have to be considered and for the evaluation of objective functions that require the iterative solution of complex partial differential equations the method is computationally very intensive [1]. Several approaches exist to increase the efficiency of zero order methods such as *genetic algorithms* [2] and *differential evolution* [3].

For first order methods the derivatives are usually calculated with the *finite difference methods* [4] or *adjoint methods* [5]. The finite difference method requires an additional evaluation of the objective function $f(\mathbf{x})$ for each element of the design vector $\mathbf{x}$. Therefore the method is computationally expensive for a design vector with many elements. The adjoint method provides a more efficient alternative for the calculation of the derivatives in such cases. The computational cost required to obtain the derivatives is nearly independent of the number of parameters. It has been widely used in the aerodynamic design optimization for airfoils, wings and wing-body configurations [6, 7]. Recently its application has been extended to turbomachinery design optimization [8–15]. The computational intensity and complexity of the adjoint method rises as additional constraints are introduced or a multi-objective optimization is considered.

The step size for first order methods are usually determined with the help of line search algorithms. There are a variety of line search algorithms developed for this purpose. An overview and introduction is given by Chong and Zak [16]. Two examples of line search algorithms are *steepest descent* and *quasi-Newton methods*. The method of steepest descent is an algorithm to determine a step size to achieve the maximum amount of decrease of the objective function at each individual step [16]. Quasi-Newton methods approximate the inverse Hessian (second derivatives) to achieve faster convergence.

Second order methods use the Hessian matrix to determine the step size. They need only one iteration to optimize a quadratic function. For non-quadratic functions several iterations are needed, but the convergence is faster than first order methods. The computation of the second derivative is computationally expensive and eventually also noise-sensitive. Additionally, the Hessian matrix (second derivatives) might be non positive definite or even singular. As a result of their computationally expensive and numerically unstable nature second order methods are generally not used in shape optimization problems involving Navier-Stokes or stress computations [1].

Zero and first order methods are computationally expensive for shape optimization problems involving CFD. Evolutionary algorithms such as genetic algorithms may require thousands of evaluations of the objective function. One of the methods that can be used to reduce the CPU cost of an optimization problem is to replace the expensive evaluations of the cost function by a surrogate evaluation model (or metamodel) which is computationally cheaper. These models must be trained to increase their accuracy. This training is essentially a comparison of the prediction of the metamodel and the result of a CFD evaluation. This technique in combination with differential evolution has been used by Verstraete *et al.* [17] to optimize a U-bend in internal cooling channels for minimum pressure loss. The optimization was performed with two different metamodels, artificial neural network and kriging. The best performing geometry was obtained with the use of the kriging metamodel after 20 optimization steps. As the metamodel was trained after each step this results in 20 CFD evaluations. Additionally, 65 CFD simulations were used for the initial training of the metamodel.

In this study, in order to reduce CPU costs and to allow the engineer to shift the focus back to the design rather than the relatively complex optimization methods, a simple, practical and straightforward optimization strategy is introduced. It adapts the strategy of finite difference methods. But to reduce computational time the first-order derivatives are calculated approximately. The CFD simulation is terminated as soon as it is clear whether a certain change in a design variable results in an improvement of the objective function. In the following, the method is explained in detail and its feasibility is demonstrated on the quasi-3d optimization of a U-bend. The results are compared with the results by Verstraete *et al.* [17].

THE OPTIMIZATION STRATEGY

The idea behind the method is not complicated, but it is still easier to grasp, if it is built up gradually. Therefore we will demonstrate it for the optimization of a simple, well-known quadratic function without additional constraints:

$$f(x) = x^2 \tag{6}$$

According to Eq. (5), besides an initial guess, which is set to $x_0 = 1$, we need a search direction S and a step size α. The search direction corresponds to the sign of the first derivative, so it is either 1 or -1. This parameter barely influences the optimization, as will be demonstrated. For the step size α we will firstly choose a random magnitude.

1. Initial Guess

After setting the search direction $S = 1$ and the step size $\alpha = 0.07$, we evaluate the function $f(x)$ at $x_1 = 1 - 0.07 = 0.93$ and compare the results:

$$\texttt{Step 0}: x_0 = 1.00 \iff f(x_0) = 1.0000$$
$$\texttt{Step 1}: x_1 = 0.93 \iff f(x_1) = 0.8649$$

Clearly $f(x_1) < f(x_0)$, and consequently x_1 is better than x_0. In this case, this value will be excepted as a new solution of the objective function. Up to step 14 Fig. 1 shows the optimization in this form. The values at time steps are marked with an x. The filled line represents the $f(x)$ values.

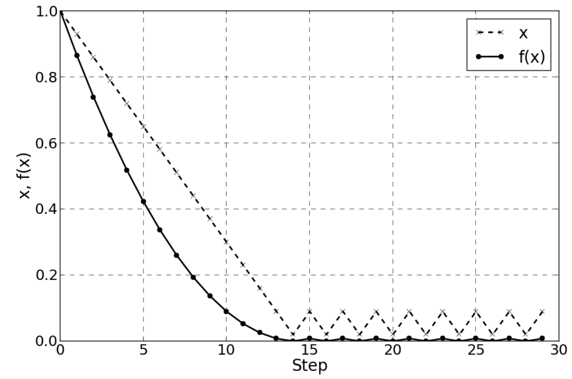

FIGURE 1. **FIRST OPTIMIZATION OF $f(x)$**

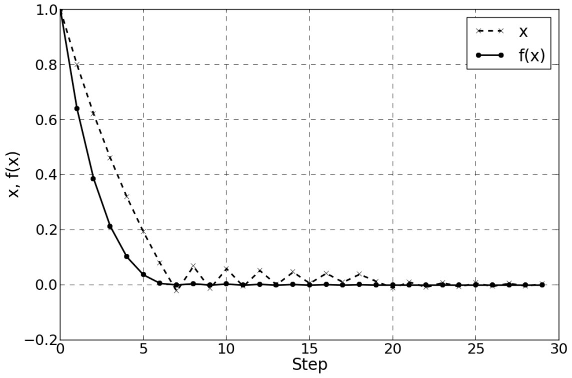

FIGURE 2. **OPTIMIZATION OF $f(x)$ WITH A SCALE FACTOR**

2. Direction Change

At $n = 14$ x has a value of $x_{14} = 0.02$. We continue with one more optimization step:

$$\texttt{Step 14}: x_{14} = +0.02 \iff f(x_{14}) = 0.0004$$
$$\texttt{Step 15}: x_{15} = -0.05 \iff f(x_{15}) = 0.0025$$

Clearly $f(x_{15}) \not< f(x_{14})$, and accordingly x_{15} is not better than x_{14} so that this value should not be accepted. In this case, we reverse the search direction for this step and set $x_{15} = 0.02 + 0.07 = 0.09$ without evaluating the function again (even thought the solution with 0.09 is inferior to both evaluations).

3. Oscillation Around the Optimum

If the optimization is progressed in this manner we get the behavior shown in Fig. 1. We can observe that the x values converge initially quite fast, but it starts oscillating close to the optimum. The reason is clear, as case 1 and 2 described above occur alternately. This is an indication for the fact that the optimum x value is somewhere between these alternating values. For the solution to converge to the optimum the step size must be decreased close to the optimum. This can be realized with a scale factor Δ. We modify Eq. (5) so that $\alpha_{eff} = \frac{\alpha}{\Delta^n}$ is the effective step size, where the iteration number n is the exponent of the scale factor.

$$x_{n+1} = x_n - \frac{\alpha}{\Delta^n} S. \tag{7}$$

The optimization of the function $f(x) = x^2$ with the step size $\alpha = 0.2$ and scale factor $\Delta = 1.12$ is shown in Fig. 2. It can be observed that the oscillations carry on, but with a continuously decreasing magnitude.

4. Sensitivity of the solution

After a number of iterations the exponentiation of the scale factor Δ^n becomes too large so that the change in the design variable is too small. In this case the value of the objective function might not change, and the optimization might be mistaken for converged. This can be prevented by introducing a limiter δ. The final search/optimization method can be formulated as:

$$\mathbf{x}_{n+1}^{test} = \begin{cases} \mathbf{x}_n - \frac{\alpha}{\Delta^n}\mathbf{S}, & \frac{\alpha}{\Delta^n} \geq \delta \\ \mathbf{x}_n - \delta\mathbf{S}, & \frac{\alpha}{\Delta^n} < \delta \end{cases} \tag{8}$$

$$\texttt{if} \quad f(\mathbf{x}_{n+1}^{test}) < f(\mathbf{x}_n): \quad \mathbf{x}_{n+1} = \mathbf{x}_{n+1}^{test} \tag{9}$$

$$\texttt{elseif} \quad f(\mathbf{x}_{n+1}^{test}) > f(\mathbf{x}_n): \quad \mathbf{x}_{n+1} = \begin{cases} \mathbf{x}_n + \frac{\alpha}{\Delta^n}\mathbf{S}, & \frac{\alpha}{\Delta^n} \geq \delta \\ \mathbf{x}_n + \delta\mathbf{S}, & \frac{\alpha}{\Delta^n} < \delta \end{cases} \tag{10}$$

$$\texttt{else}: \quad \mathbf{x}_{n+1} = \mathbf{x}_n \tag{11}$$

This optimization method requires only 4 parameters to be determined: The first one is the search direction S. This is either -1 or 1, and doesn't have much influence on the optimization. The convergence behavior close to the optimum may be improved by the right choice, but the influence is in most cases neglectable. The second parameter is the step size α. It should be chosen as large as possible as a bigger value will reduce the number of iterations necessary to get closer to the optimum. But it is advantageous to determine this parameter in dependance with the scale factor Δ. This factor should be set to a value that reduces the effective step size to the value of the limiter δ in the number of iterations expected (or desired) to reach the optimum. Finally, the limiter δ, should be set to a minimum value, which is given by either production tolerances or computational sensitivity.

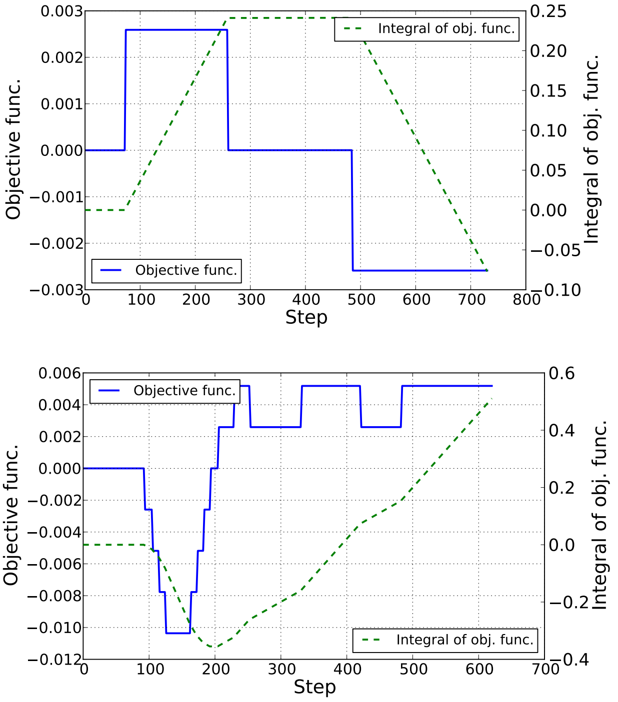

FIGURE 3. EXAMPLES OF THE DEVELOPMENT OF THE OBJECTIVE FUNCTION DURING A CFD CALCULATION

5. Optimization of more complex functions

Similar to most gradient-based methods the introduced optimization method converges towards a local minimum. In case of multimodal problems the minimum that will be found is strongly dependent on the start solution. Also if the objective function has very small gradients around the optimum the routine may not converge fully to the optimum, but find a value of the objective function very close to the optimum value. Such behavior can be observed by testing the routine on the Rosenbrock function. A position in the long and narrow valley, where the optimum is located, can be found effortlessly. But the optimization does not converge any further once it reaches the valley, as from any such position both search directions for each parameter individually do not improve the objective function value.

6. Complication due to convergence of CFD

In optimal shape design using CFD there is generally more than one design variable and the evaluation of the cost function is not so simple and fast. It involves computationally intensive methods to achieve a solution for $f(\mathbf{x}_{n+1}^{test})$. But the method described above does *not really* require the exact value of $f(\mathbf{x}_{n+1}^{test})$. It is sufficient to determine if the value of the objective function is rising or falling with the new value of a design variable. Consequently, we will require to monitor the development of the objective function during its numerical evaluation for a design parameter and discontinue it as soon as the trend can be determined.

Developing criteria for the termination of the CFD evaluation for the parameters is expected to be the tricky part of the method. The flow in a U-bend is the first test case. For the U-bend a simple criterion has been devised. Fig. 3 includes two diagrams, each showing the development of the objective function in reference to its value in the last design after changing one parameter. The second line (dotted line) is its summation over the iterations. After a specified number of initial iterations has been performed (here 500 steps) the values of these two functions are compared in regular intervals. If they are both positive or negative the solver run is terminated. Comparing these functions ensures that the value of the objective function has been constantly bigger or smaller than its previous value for a number of iterations. This allows us to assume that the tendency of the influence of the parameter on the objective function can at this point be correctly predicted.

```
         $\Delta f = f(x^{test}_{n+1}) - f(\mathbf{x}_n)$ :                    (12)
if       $\mathrm{sign}(\Delta f) = \mathrm{sign}(\sum_i \Delta f)$ : $i = 1..current\ iteration$
             terminate CFD run
else :
             continue CFD run
```

For the U-bend this proved sufficient to ensure that the influence of the parameters are correctly predicted. As the convergence behavior of CFD is generally case and solver dependent, it should be analyzed for every optimization to formulate a minimum number of initial iterations, or eventually also modify the termination criterion.

TEST CASE

At the von Karman Institute (VKI) for Fluid Dynamics Verstraete *et. al.* [17] have optimized a U-bend for minimum total pressure loss without additional constraints using evolutionary algorithms and metamodels. The results have been analyzed numerically and experimentally [18]. In the second half of the U-bend the flow on the inner curve separates, which is the main loss mechanism. An optimization will therefore attempt to reduce the loss due to separation. As the details of the geometry and parametrization have also been published, this optimization constitutes a very good test case for the presented optimization method.

Geometry and Boundary Conditions

The baseline geometry published by Verstraete *et. al.* [17] is presented in Fig. 4. It consists of a circular U-bend with a hydraulic diameter $D_h = 0.075\,m$. The channel has a rectangular cross section with an aspect ratio of 1. The radius of the inner curve is $0.26D_h$ and the radius of the outer curve is $1.26D_h$. Full 3d simulations as by Verstraete *et al.* have not been performed. Instead, the test case has been considered quasi-3d to save computational time. These quasi-3d simulations can be considered equivalent to 2d simulations, as the cells have a constant extension in the third dimension. It is assumed that the

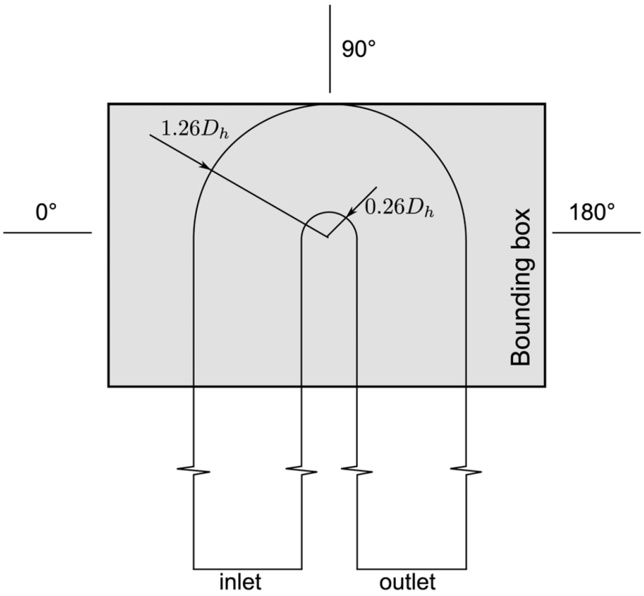

FIGURE 4. **BASELINE GEOMETRY AND DESIGN LIMITS [17]**

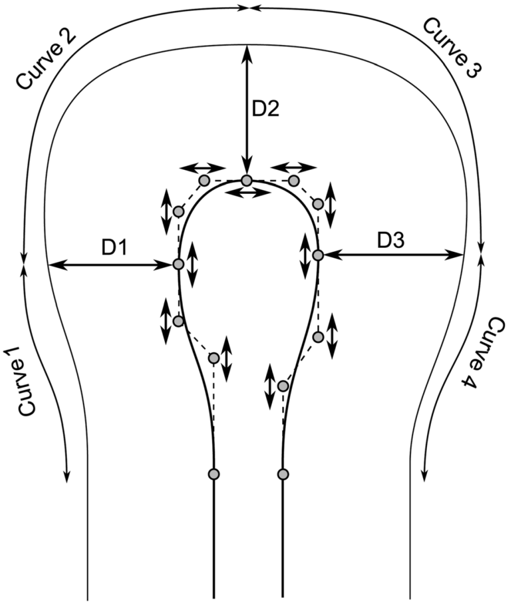

FIGURE 5. **PARAMETRIZATION OF THE INNER CURVE BY VERSTRAETE ET AL. [17]**

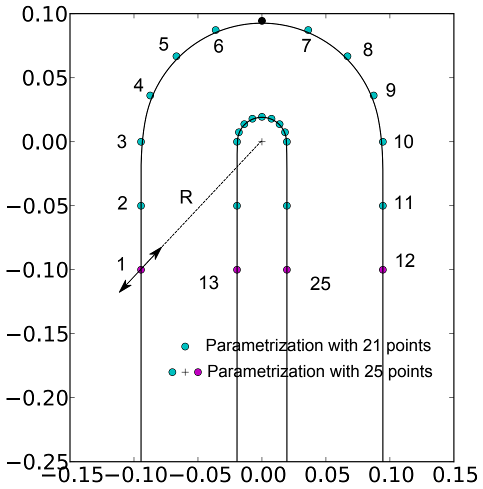

FIGURE 6. **PARAMETRIZATION OF THE B-SPLINE CURVES DEFINING THE U-BEND**

main flow behavior will still be captured with this simplification. A discussion of the flow field will demonstrate the validity of this assumption.

The inlet and outlet sections are originally 8 hydraulic diameters upstream and downstream of the U-bend. Here the inlet and outlet is moved further downstream and upstream, because instead of a velocity profile at the inlet as Verstraete *et. al.* have used for their calculations, constant values of total pressure and total temperature are specified. Therefore the flow had to be allowed to develop. The inlet is located 18 hydraulic diameters in front of the U-bend and the outlet 11 hydraulic diameters downstream. At the outlet the static pressure is specified.

The total pressure and total temperature are set to adjust the Reynolds number to 40000. The Mach number is 0.05. Also 1% turbulence is specified at the inlet.

Parametrization

In the optimization by Verstraete *et al.* the inner and outer curves are composed of four third-order Bezier curves, each defined by a polynomial with four control points. The outer curve is parametrized by a total of 12 degrees of freedom, the inner curve by 14. Finally their test case has 26 degrees of freedom. The parametrization they used for the inner curve is shown in Fig. 5.

The same parametrization was not used in this work. Instead, a parametrization that fits better into our work flow and one that would also allow the same contour was chosen. The inner curve as well as the outer curve are defined by a B-spline curve with a number of control points. Not all control points of the curves are design variables. Fig. 6 shows the B-splines and the control points that are also design variables, except for one of them: the point at 90° is not changed for the outer curve, as the design is required to remain in the limits of the bounding box (Fig. 4). The points are moved only in the radial direction, as indicated for the first parameter, so that each point has one degree of freedom. The first test case is optimized without the first and last parameters of each curve, so that it has 21 design variables (points colored in cyan). 10 of these points are on the outer curve. 11 are on the inner curve. The second test case is optimized with 25 design variables (points colored in cyan and magenta).

The step size α is set to 8% of the distance of the location of a design variable to the coordinate center ($0.08R_k$). The scale factor Δ is set to 1.2 and the limiter $\delta = 0.01R_k$.

Objective Function

The U-bend was optimized for minimum total pressure drop by Verstraete *et al.* [17]. For this study the pressure drop is normalized. The objective function is formulated as:

$$\min f(\mathbf{x}) = \frac{p_{total}^{inlet} - p_{total}^{outlet}}{0.5\rho_{inlet}|\mathbf{V}_{inlet}|^2} \tag{13}$$

Grid

The grid generation has been performed with the inhouse mesher AIGRID [19]. It consists of 344x52 cells. Fig. 7 shows a close-up on the grid at the U-bend. The dimensionless wall distance y^+ is smaller than 1. The cells also have a constant extension in the third dimension.

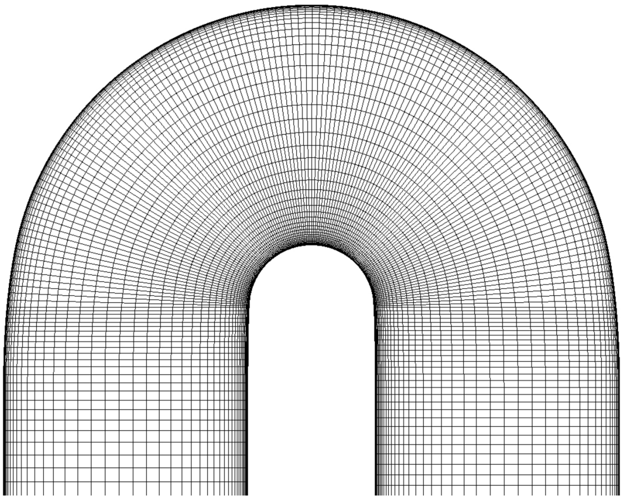

FIGURE 7. **CLOSE UP OF THE COMPUTATIONAL GRID IN THE U-BEND**

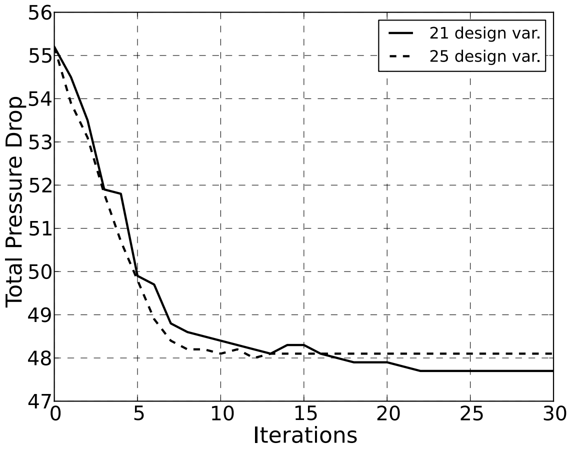

FIGURE 8. **OPTIMIZATION RESULTS WITH 21 AND 25 DESIGN VARIABLES**

Computational Method

The computations were performed with the Navier-Stokes code LINARS developed at the institute by Pecnik et al. [20], which has been successfully utilized for the solution of numerous applications. The code solves the incompressible (and compressible) Reynolds-averaged Navier-Stokes equations in conservative form by means of a fully-implicit time-marching finite-volume method. Structured grids are utilized in multiblock assignment. The inviscid fluxes are discretized with the upwind flux-difference splitting method by Roe [21]. The viscid flux vector at the cell interfaces is constructed in a central-differencing manner using Green's theorem. The incompressible equations are implemented with the artificial density formulation.The optimization is controlled by python scripts that monitor the CFD computations, check convergence and evaluate the objective function.

Turbulence models make up one of the main uncertainties of numerical simulations; and U-bend geometries are challenging to reproduce in numerical simulations due to the effects of streamlines curvature and the associated secondary flow. Flow separation further increases the uncertainty of CFD simulations. Broad trends can be captured by two equation eddy-viscosity models, but they are unable to predict the effect of streamline curvature on the turbulence structure [17]. Still, due to their lower computational cost two-equation models are employed widely in industrial applications.The calculations in this study are performed with the two-equation shear stress transport turbulence model by Menter [22].

RESULTS AND DISCUSSION

For the two test cases with 21 and 25 parameters 30 optimization iterations are performed. Each iteration corresponds approximately to the computational expense of 2 to 2.5 CFD simulations. A converged solution with new parameters needed 10000 steps of the CFD calculations. The evaluation of sensitivities demanded mostly between 500 to 700 steps for each parameter (Fig. 3).

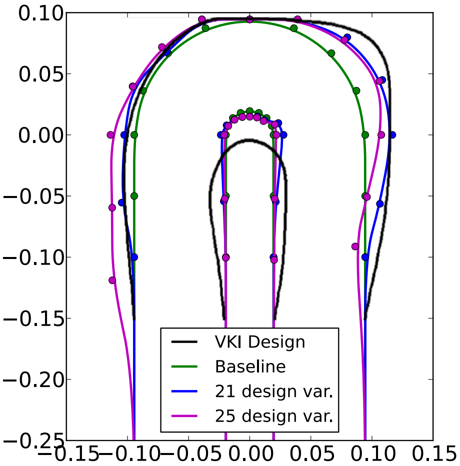

FIGURE 9. **COMPARISON OF THE OPTIMIZED DESIGNS WITH THE BASELINE DESIGN**

In Fig. 8 the results of the optimizations are shown. Most of the reduction of the pressure loss is already achieved during the first 10 steps. The optimization with 21 parameters produces a slightly better result than the optimization with 25 parameters. Consequently, the optimization using more parameters does not bring any advantage but rather a disadvantage, because of the additional computational time. The minimum pressure drop achieved with 25 parameters is 48.1 Pa, with 21 parameters we achieve 47.7 Pa. The initial total pressure drop is 55.2 Pa, so the optimizations have found solutions that reduce the pressure drop by 7.1 Pa and 7.5 Pa. The pressure drop reduction achieved by Verstraete *et al.* [17] is about 7 Pa. Although this test case is quasi-3d and Verstraete *et al.* optimized full 3d this comparison still shows the quality of the presented optimization method.

Design

The shapes of the improved U-bends are shown in Fig. 9. The baseline design and an approximation of the VKI design are also plotted. We can see considerable differences in the shape of the resulting designs with 21 and 25 parameters even though one is not significantly better than the other. But both optimizations have induced the same deformations on the standard U-bend at a different extent. Both these designs are different from the optimal shape presented by Verstraete *et al.* [17], although the direction of the induced changes are similar. The different

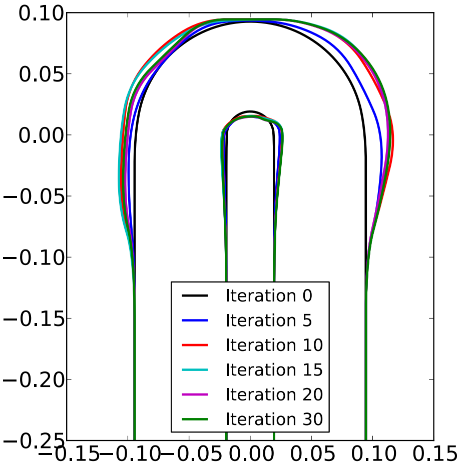

FIGURE 10. DEVELOPMENT OF THE WALL CONTOURS DURING THE OPTIMIZATION ITERATIONS FOR 21 DESIGN VARIABLES

results are reasonable as both the optimization method and, more importantly, the parametrization method are not the same.

Fig. 10 shows the U-bend geometry during the optimization with 21 design variables at chosen optimization steps. After step 10 the changes in the shape of the curves are much smaller. It converges quite directly to the optimum shape. The outer wall contour in the first half of the U-bend is in iteration 15 further away from the center at certain locations than in the optimum. This is an expected behavior of the optimization method, because parameters might be changed even if they don't improve the design at a certain step as shown Fig. 2. The constant reduction of the effective step size ensures the convergence to the optimum.

Flow Field

The flow field of the standard U-bend was investigated experimentally with particle image velocimetry (PIV) and CFD by Verstraete *et al.* [18]. They found that there is a flow acceleration near the inner wall and deceleration near the outer wall. A large recirculation region is created as the streamlines along the inner walls separate just before the half of the bend. The length of this region is about $1.6D_h$ in their experimental results. It reduces the effective cross section and contributes to the acceleration of the flow in the second half of the bend. These complex flow phenomena are not captured accurately by CFD calculations in their investigations as well as the simulations performed in this study. In their 3d simulations the separation occurs later than in the experiments with the length of the recirculation region underpredicted. Fig. 11 shows the normalized absolute velocity U/U_0 from our quasi-3d simulation in the standard geometry. The separation occurs, as in the CFD analysis by Verstraete *et al.,* later than in the measurements. The length of the separation region is not underpredicted but its thickness is.

In Fig. 12 the normalized turbulent kinetic energy (TKE) is presented. Verstreate *et al.* used the definition of TKE following Soranna *et al.* [23] with the $3/4$ coefficient to account for the contribution of the missing out-of-plane velocity component. For an easier comparison the same definition is used here:

$$k* = \frac{\frac{3}{4}(\overline{u'^2} + \overline{v'^2})}{0.5U_0^2}$$

The over bar indicates ensemble averaging used by Verstraete *et al.* [18].

Near the outer walls TKE is enhanced. This enhancement is consistent with the streamline curvature effect on turbulence properties (Bradshaw [24]) and with the PIV measurements by Verstraete *et al.* Near the inner wall TKE production is expected to be lower. The rise of TKE at the beginning of the curvature near the inner wall is more distinctive than in their PIV measurements. But the low TKE level in the middle of the channel in the U-bend is consistent with their experimental results. The large production of TKE due to separation is reproduced well by the CFD calculations.

Fig. 13 shows the normalized absolute velocity U/U_0 in the optimized geometry with 21 design variables. The resulting absolute velocity does not differ much from that of the standard geometry. The first half of the inner wall is only slightly thickened by the optimization. The cross section here is still enlarged as the outer wall boundary is widened. The separation region is moved further downstream and practically induced by a bump formed on the inner wall at the end of the bend. At the second half of the bend the duct section is considerably enlarged. This limits the acceleration of the flow. Further downstream the cross section area is reduced, causing the flow to accelerate. The separation region is thinner and shorter.

The contours of TKE are presented in Fig. 14. The production of TKE due to the curvature is reduced close to the walls with respect to the standard U-bend. The higher production of TKE by the separation bubble can still be observed. But this is also much lower than for the standard geometry.

Figs. 15 and 16 show the normalized absolute velocity and TKE for the second optimization with 25 parameters. As the optimization results suggested, the flow field is quite similar to the flow field in the U-bend optimized with 21 parameters. Only two of the extra parameters, the first parameter at the inlet of the U-bend and the last

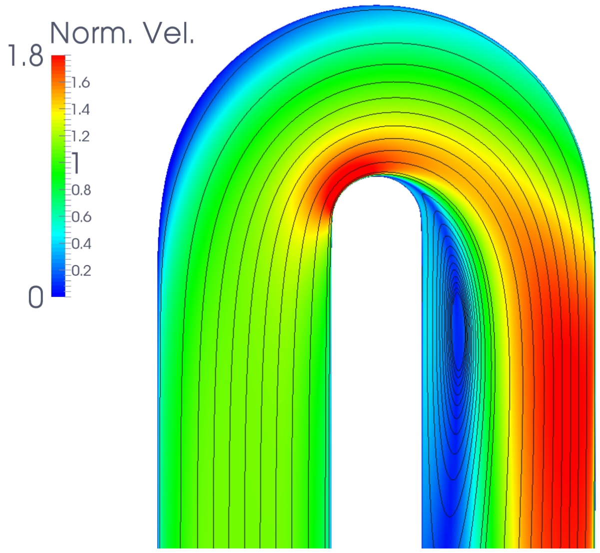

FIGURE 11. ABSOLUTE VELOCITY FIELD IN THE BASELINE DESIGN

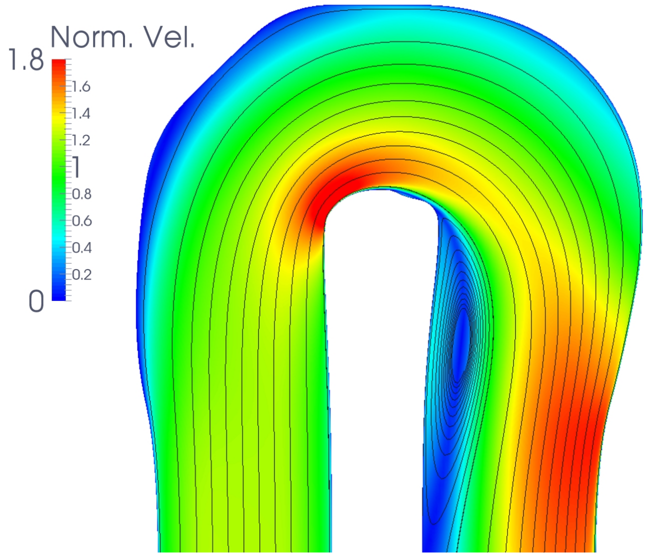

FIGURE 13. ABSOLUTE VELOCITY FIELD IN THE DESIGN OPTIMIZED WITH 21 DESIGN VARIABLES

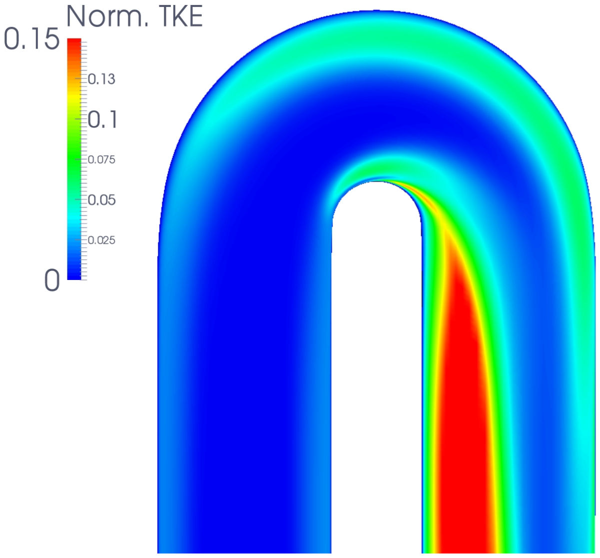

FIGURE 12. TKE CONTOURS IN THE BASELINE DESIGN

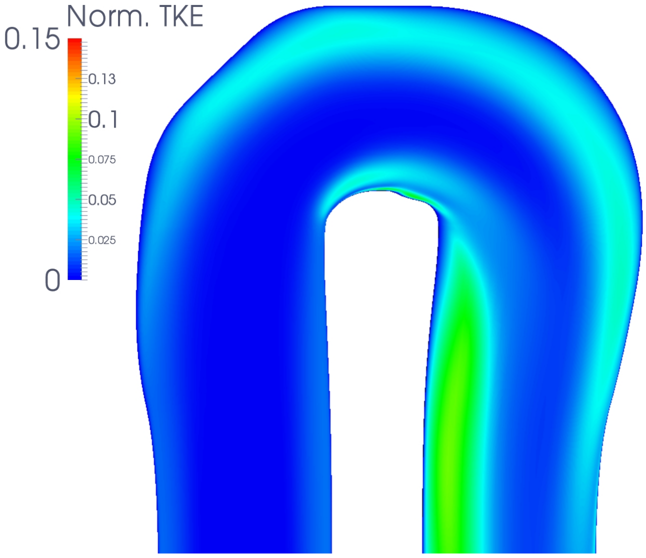

FIGURE 14. TKE CONTOURS IN THE DESIGN OPTIMIZED WITH 21 DESIGN VARIABLES

parameter at the outlet are changed significantly. It has caused the outer wall boundary to be moved outwards, so that the cross section at the inlet is enlarged. This slightly reduces the velocity at the inflow of the bend, which in turn reduces the thickness of the separation region, which allows the cross section of the bend in the second half to be smaller than in the first optimization.

OPTIMIZATION FROM ANOTHER STARTING POINT

The optimization has also been performed from another starting point using 21 parameters, as shown in Fig. 6, using the same step size α as well as scale factor Δ. Fig. 17 shows the new initial geometry (second baseline) and the first initial geometry that was used in the discussion above (first baseline). The optimized designs of both cases are also shown in the diagram. The optimizations have not converged to exactly the same geometry. The outer contours are quite similar. They mainly have the same form. In the second half of the U-Bend the cross section of the channel is smaller after the second optimization. The trend of the inner contour is also quite similar, but the curvature is more pronounced, so that the cross section of the channel is further narrowed.

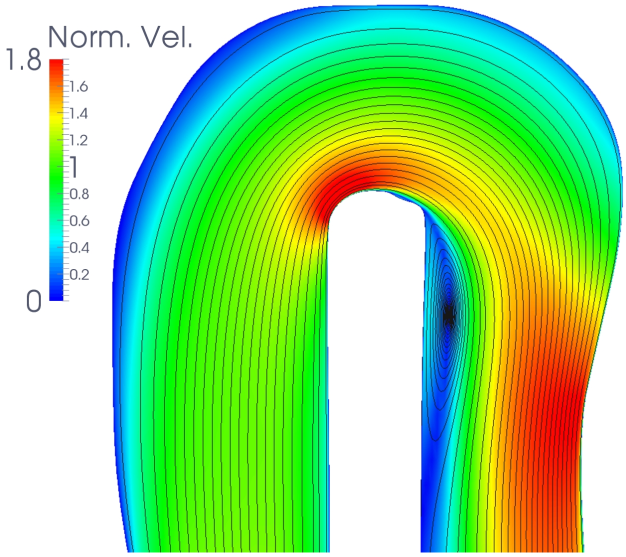

FIGURE 15. ABSOLUTE VELOCITY FIELD IN THE DESIGN OPTIMIZED WITH 25 DESIGN VARIABLES

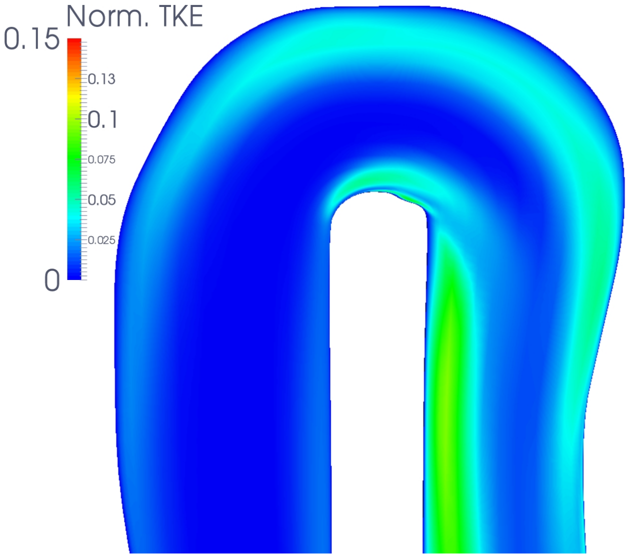

FIGURE 16. TKE CONTOURS IN THE DESIGN OPTIMIZED WITH 25 DESIGN VARIABLES

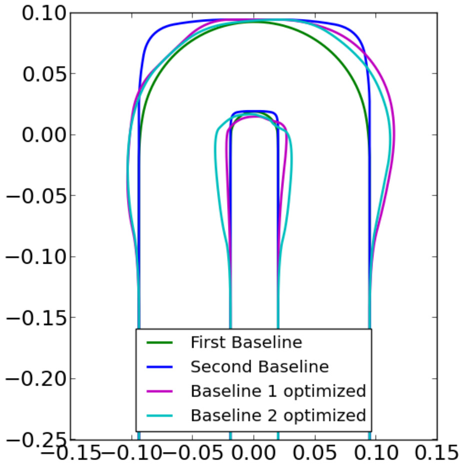

FIGURE 17. BASELINE AND OPTIMIZED CONTOURS WITH 21 DESIGN VARIABLES

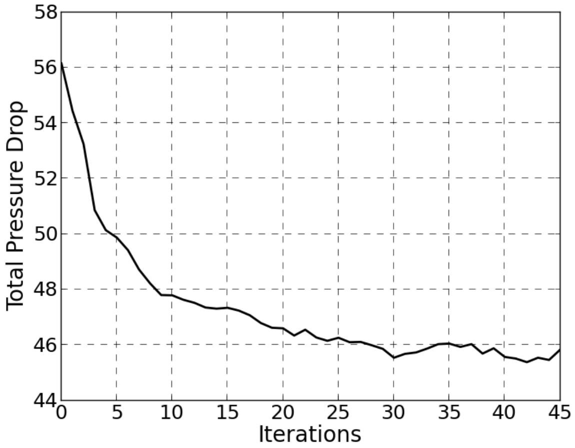

FIGURE 18. DEVELOPMENT OF THE OPTIMIZATION OF THE SECOND BASELINE DESIGN

The optimization starting from the second initial design has not found the same solution as the first optimization. But it has actually reached a better solution. The development of the objective function is shown in Fig. 18. The total pressure drop is reduced down to 46 Pa, which is approximately 1.5 Pa lower than the value achieved by the first optimization.

There can be two explanations for the different results. The first possibility is that both optimizations have found their local minimum. The second possibility is that both solutions are very close to the optimum value and the change in a single parameter does not lead to an improvement of the objective function. This can be the case if the function resembles the Rosenbrock function, which has shortly been discussed above.

SUMMARY AND CONCLUSIONS

A practical and straightforward optimization method has been introduced and demonstrated on the quasi-3d optimization of a U-bend. This test case was chosen, because the results could be compared to the optimization formerly performed at the VKI.

Similar reduction in the total pressure drop is achieved as in the reference optimization. The resulting design is not the same, but the trend of the deformations are similar. As different optimization and parametrization methods as well as different CFD solvers and turbulence models are used, and also as the optimization in this study is performed only quasi-3d, whereas the optimization by Verstraete *et al.* [17, 18] is fully 3 dimensional, achieving the same geometry is not expected. A comparable improvement of the design is pursued, which is also achieved.

An additional optimization of the U-bend starting from another baseline geometry is performed to further validate the method. Again a comparable geometry with a similar optimum value is achieved.

In future work, the method will be used to optimize the endwall of a turning mid turbine frame. Additionally, the convergence of the optimization can be improved by criteria to reduce the step size first as the solution gets close to the optimum.

ACKNOWLEDGEMENT

The authors would like to thank the Austrian Federal Ministry for Transport, Innovation and Technology who funded the project SEIKON3D within the Austrian Aeronautics Program TAKE OFF.

REFERENCES

[1] Periaux, J., and Verstraete, T., eds., 2012. *Introduction to optimization and multidisciplinary design in aeronautics and turbomachinery*. Lecture Series of the von Karman Institue for Fluid Dynamics.

[2] Goldberg, D. E., 1989. *Genetic Algorithms in Search, Optimization, and Machine Learning*. Addison-Wesley Publishing Company, Inc.

[3] Price, K., and Storn, N., 1997. "Differencial evolution". *Dr. Dobb's Journal*.

[4] Hicks, R. M., and Henne, P. A., 1978. "Wing design by numerical optimization". *Journal of Aircraft,* ***15***, pp. 407–412.

[5] Jameson, A., 1988. "Aerodynamic design via control theory". *Journal of Scientific Computing,* ***3***, pp. 233–260.

[6] Jameson, A., 1995. "Optimum aerodynamic design using CFD and control theory". AIAA 12th Computational Fluid Dynamics Conference, no. AIAA 95-1729.

[7] Kim, S., Alonso, J., and Jameson, A., 2004. "Multielement high-lift configuration design optimization using viscous continous adjoint method". *Journal of Aircraft,* ***41***, pp. 1082–1097.

[8] Wu, H., and Liu, F., 2005. "Aerodynamic design of turbine blades using an adjoint equation method". 43rd AIAA Aerospace Sciences Meeting and Exhibit, no. AIAA 2005-1006.

[9] Papadimitriou, D. I., and Giannakoglou, K. C., 2006. "A continous adjoint method for the minimization of losses in cascade viscous flows". 44th AIAA Aerospace Sciences Meeting and Exhibit, no. AIAA 2006-49.

[10] Corral, R., and Gisbert, F., 2008. "Profiled end wall design using an adjoint Navier-Stokes solver.". *Journal of Turbomachinery,* ***130(2)***.

[11] Wang, D., and He, L., 2010. "Adjoint aerodynamic design optimization for blades in multi-stage turbomachines: Part I - Methodology and verification". *Journal of Turbomachinery,* ***132(2)***.

[12] Wang, D., He, L., Li, Y. S., and Wells, R. G., 2010. "Adjoint aerodynamic design optimization for blades in multi-stage turbomachines: Part II - Methodology and verification". *Journal of Turbomachinery,* ***132(2)***.

[13] Luo, J., Xiong, J., Liu, F., and McBean, I., 2011. "Three-dimensional aerodynamic design optimization of a turbine blade by using an adjoint method". *Journal of Turbomachinery,* ***133***, January.

[14] Luo, J., Liu, F., and McBean, I., 2011. "Optimization of endwall contours of a turbine blade row using an adjoint method". ASME Turbo Expo, Vancouver, Canada, no. GT2011-46163.

[15] Akin, M. B., Sanz, W., and Pieringer, P., 2014. "Endwall contour optimization of a turning mid turbine frame using an adjoint method". ASME Turbo Expo, Düsseldorf, Germany, no. GT2014-26038.

[16] Chong, E. K., and Zak, S. H., 2001. *An Introduction to Optimization*. John Wiley & Sons, Inc.

[17] Verstraete, T., Coletti, F., Bulle, J., Vanderwielen, T., and Arts, T., 2013. "Optimization of a U-bend for minimal pressure loss in internal cooling channels - Part I: Numerical method". *Journal of Turbomachinery,* ***135***, September.

[18] Verstraete, T., Coletti, F., Bulle, J., Vanderwielen, T., and Arts, T., 2013. "Optimization of a U-bend for minimal pressure loss in internal cooling channels - Part II: Experimental validation". *Journal of Turbomachinery,* ***135***, September.

[19] Pieringer, P., 2012. Springer und Pieringer EDV Dienstleistungen OEG.

[20] Pecnik, R., Pieringer, P., and Sanz, W., 2005. "Numerical investigation of the secondary flow of a transonic turbine stage using various turbulence closures". ASME Turbo Expo 2005, Nevada, USA, no. GT2005-68754.

[21] Roe, P. L., 1981. "Approximate Riemann solvers, parameter vectors and differencing scheme". *Journal of Computational Physics,* ***43***, pp. 357–372.

[22] Menter, F. R., 1994. "Two-equation eddy-viscosity turbulence models for engineering applications". *AIAA Jounal,* ***32***(2), August, pp. 1598–1605.

[23] Soranna, F., Chow, Y.-C., Uzol, O., and Katz, J., 2006. “The effect of inlet guide vanes impingement on the flow structure and turbulence around a rotor blade”. *Journal of Turbomachinery,* ***128(1)***, pp. 82–95.

[24] Bradshaw, P., 1973. Effects of streamline curvature on turbulent flow. Tech. rep., AGARD-AG-169.